PRODUCTION AND APPLICATIONS OF LONG-LIVED POSITRON-EMITTING RADIONUCLIDES

by

Stephen A. Graves

A dissertation submitted in partial fulfillment of
the requirements for the degree of

Doctor of Philosophy

(Medical Physics)

at the

UNIVERSITY OF WISCONSIN–MADISON

2017

Date of final oral examination: 6th of January, 2017

The dissertation is approved by the following members of the Final Oral Committee:
Robert J. Nickles, Emeritus Professor, Medical Physics
Jonathan W. Engle, Assistant Professor, Medical Physics
Bradley T. Christian, Professor, Medical Physics
Onfre T. DeJesus, Professor, Medical Physics
James E. Holden, Emeritus Professor, Medical Physics
Weibo Cai, Associate Professor, Radiology

ACKNOWLEDGMENTS

I have the opportunity to write whatever I want on this page; Nothing is coerced or insincere.

Kathleen, the love of my life, has been patient with me beyond expectation. The strange hours, neurotic tendencies, and cold climate associated with being a part of my life have perturbed her minimally. It is because of her support and encouragement that I have made it this far, and continue to strive for improvement. Tom and Lori have welcomed me with open arms into a family without compare, and I thank them.

My parents have provided for my every need, made sacrifices in their life to support me, and have never doubted me. May I in my life be able to return even a fraction of their selflessness and love to those around me.

My friends are first-rate. You have challenged, consoled, advised, and supported me throughout my entire life; Kyle D., Michael , Jannik, Alex B., Josh, Eric, Adan, Erin, Debra, Kaylee, Monica, Nate, Matt, Tim, Kyle T., Kenneth, Hector S., Irena, Pat, Q, Dunks, Tobey, Shredder, Proud, Brando, Sabs, Ben, and others — thank you all dearly.

To all of the educators charged with fostering my precocious young mind, I offer my deepest gratitude. I would in particular thank Mary Jackson for her attention to the needs of individual pupils; and Mark Guthrie, Joy Wilson, and Sally Millsap for inspiring my love for the physical sciences.

To my colleagues and mentors — Todd, Reinier, Hector, Paul, Christina, Greg, and others — thank you for your wisdom, insight, friendly conversation, and contributions to this work. It has been an immense pleasure working with you.

The members of my committee — Jim Holden, Jonathan Engle, Onfre DeJesus, Brad Christian, Weibo Cai, and Jerry Nickles — have been incredibly generous with their time and expertise. I thank them for their service and guidance.

Working with Jerry is astonishing. One minute you're a doe-eyed student who's never held a transistor, and the next minute you're sitting on the back of a beam of light hurtling through the universe at three–hundred million meters per second thinking about gravitational lensing... Err – perhaps he copied Einstein, but I had a heck of a time anyway. Jerry Nickles has been the greatest positive figure in my adult life, and I thank him for the time he has spent with me. I would also thank Amy Nickles for her patience in allowing Jerry to take "just one more student."

PRODUCTION AND APPLICATIONS OF LONG-LIVED POSITRON-EMITTING RADIONUCLIDES

Stephen A. Graves

Under the supervision of Professor Robert J. Nickles
At the University of Wisconsin-Madison

Abstract

Positron emission tomography (PET) is a medical imaging modality capable of determining the in vivo spatial distribution of a biologically relevant molecule which has been labeled with a positron-emitting isotope. The use of molecules such as monoclonal antibodies and nanoparticles for therapeutic and diagnostic applications has expanded preclinically in recent years. As these larger molecules tend to have longer circulation times and slow clearance kinetics, positron-emitting isotopes with half-lives longer than conventional medical radioisotopes are required for PET applications.

This dissertation details methods for the production of ^{51}Mn ($t_{1/2}$: 45.4 min), ^{52g}Mn ($t_{1/2}$: 5.59 d), ^{64}Cu ($t_{1/2}$: 12.7 h), ^{76}Br ($t_{1/2}$: 16.2 h), ^{89}Zr ($t_{1/2}$: 3.27 d), and ^{194}Au ($t_{1/2}$: 38.0 h) on low-energy medical cyclotrons, including targetry considerations, radiochemical separation methods, and analysis of resulting purity. Pursuant to the production of these isotopes, several instrumentation developments have been made including implementation of an automatic nuclide identification library for gamma spectroscopy; development of methods for dead time correction and background estimation in auto-gamma counting; and the creation of a new linearly-filled Derenzo-type PET phantom. Measurement of the radioactive half-lives of ^{51}Mn and ^{52g}Mn are presented in addition to their use in a variety of preclinical molecular imaging applications, including immunoPET, stem cell tracking, functional β-cell mass determination, and probing the impact of isoflurane on acute pancreatic function. An analytic model of effective specific activity is formed and tested against preliminary trace metal analysis results. Measurements of excitation functions for the large-scale production of medically relevant isotopes, including ^{52g}Mn, at the Los Alamos National Laboratory Isotope Production Facility (100 MeV p^+) are presented. The results described herein have enabled and informed a variety of novel investigations in the fields of nuclear medicine and molecular imaging.

CONTENTS

Contents iii

List of Tables vii

List of Figures ix

1 Introduction 1
1.1 Organization of the Dissertation 4

2 Instrumentation in Isotope Production 6
2.1 HPGe Gamma Spectrometry 6
2.1.1 Fitzpeak library generation 7
2.1.2 FitzPeaks peak fitting evaluation 8
2.2 Auto-Gamma Counter 10
2.2.1 Background quantification and iterative subtraction methods 12
2.3 Linearly-Filled Derenzo Phantom Design 14
2.3.1 MicroPET phantom design 17

3 Isotopes of Manganese and Applications Thereof 24
3.1 Introduction: Unique divalent metal with toxicological implications 24
3.2 ^{52}Mn 28
3.2.1 Nuclear Reactions and Targetry 28
3.2.2 Cr/Mn Radiochemistry 32
3.2.3 Purity 42
3.2.4 Half-life measurement 45
3.3 ^{51}Mn 48
3.3.1 Introduction 48
3.3.2 Materials and Methods 49
3.3.3 Results 53
3.3.4 Discussion 69
3.3.5 Conclusion 73
3.4 ImmunoPET 74
3.4.1 Introduction 75
3.4.2 Methods 76

3.4.3 Results and Discussion 79
3.4.4 Rudimentary dosimetry comparison against ^{89}Zr-DFO-TRC105 84
3.4.5 Conclusion 88
3.5 DMT-1 Cell tracking 89
3.5.1 Background 89
3.5.2 Methods, Results, and Discussion 91
3.6 Quantification of Functional Beta Cell Mass 94
3.6.1 Introduction 94
3.6.2 Materials and Methods 96
3.6.3 Results 103
3.6.4 Discussion 120
3.7 Isoflurane-induced hyperglycemia 127
3.7.1 Introduction 127
3.7.2 Methods 128
3.7.3 Results and Discussion 129

4 Measurement of Fe+p nuclear excitation functions 132
4.1 Background and Motivation 132
4.2 Experimental and Analytic Methods 134
4.2.1 Target-stack design and Irradiation 134
4.2.2 Gamma spectroscopy 136
4.2.3 Initial Beam Energy Determination 136
4.2.4 Monitor Reactions 137
4.2.5 Final Energy Determination: Multiple Monitor Reaction Variance Minimization 138
4.2.6 Fluence Loss Characterization 143
4.2.7 Cross Section Calculations 145
4.3 Results and Discussion 146
4.4 Conclusions 153

5 Positron Emitting Isotopes of Gold 156
5.1 Introduction 156
5.2 ^{194}Au Production 157
5.2.1 ^{nat}Pt+p Reactions 157
5.2.2 Targetry 159

5.3 Radionuclidic Purity Results . . . 160
5.4 Thermal Diffusion . . . 160
5.5 Dissolution and Radiochemistry . . . 166
5.5.1 Review of Pt/Au Separation Methods . . . 166
5.5.2 Novel UTEVA Extraction resin method . . . 167
5.5.3 UTEVA Separation Method Results . . . 171

6 Radiobromine Production . . . 172
6.1 Background . . . 172
6.2 Target considerations and fabrication of NiSe targets . . . 174
6.2.1 Alloys of Selenium . . . 174
6.2.2 Alloy formation by heating . . . 177
6.2.3 NiSe formation by reaction with $NaBH_4$ . . . 177
6.2.4 NiSe formation by liquid ammonia–based reaction . . . 178
6.3 Target irradiation approaches . . . 178
6.4 Distillation of Radiobromine . . . 180
6.4.1 Distillation Appratus and Method . . . 180
6.4.2 Distillation Results . . . 181
6.5 Conclusion . . . 184

7 ^{64}Cu and ^{89}Zr Production . . . 185
7.1 Production Capacity . . . 185
7.2 Chemical Purity . . . 192
7.2.1 Effective Specific Activity . . . 194
7.2.2 Competitive Binding Assay . . . 197
7.2.3 Analytic Model of Effective Specific Activity . . . 199
7.2.4 Trace Metal Analysis . . . 201
7.2.5 Results . . . 203
7.3 Conclusion . . . 205

8 Directions for future work . . . 206

References . . . 208

A FitzPeaks Calibration and Operation . . . 228

B ^{51}Mn Supplemental Data . . . 236

C Beta Cell Mass Supplemental Data 240

D Measured Fe+p and Cu+p Cross Sections 245

E ^{64}Cu Effective Specific Activity History and Analysis 254

LIST OF TABLES

1.1 Properties and tracer examples of conventional PET radionuclides. 2
1.2 Long-lived positron-emitting isotopes accessible on low-energy cyclotrons . 3

3.1 Radioactive isotopes of Mn 25
3.2 Trace metal analysis of TOA-based ^{52}Mn/^{nat}Cr Separation 36
3.3 Ethanol-based anion exchange chromatographic separation of Mn/Cr results 42
3.4 Trace metal analysis of ^{52}Mn products 43
3.5 Radiomanganese yields and predicted values from literature nuclear data. . 45
3.6 ^{51}Mn irradiation yields and separation results 55
3.7 Radionuclidic purity of EoB and EoC ^{51}Mn 56
3.8 Literature measurements of the half-life of ^{51}Mn 63
3.9 ^{51}Mn half-life measurements in this work 63
3.10 ^{51}Mn OLINDA dosimetry results 69
3.11 Decay characteristics of radioisotopes of Mn 69
3.12 ^{52}Mn-DOTA-TRC105 Labeling Yield vs Time 79
3.13 Tabulated ex vivo biodistribution of ^{52}Mn-DOTA-TRC105 and $^{52}Mn^{2+}$ 85
3.14 Dosimetry comparison between ^{52}Mn-DOTA-TRC105 and ^{89}Zr-DFO-TRC105 86
3.15 Dosimetry evaluation of ^{54}Mn impurities 87

4.1 ^{nat}Fe+p Target Stack Design Specifications 141
4.2 ^{nat}Cu+p: Measured cross sections for Co reaction products 148
4.3 ^{nat}Cu+p: Measured cross sections for Cu, Mn, and Ni reaction products . . . 148
4.4 ^{nat}Fe+p: Measured cross sections 149
4.5 Nuclear decay data used for Fe+p and Cu+p σ measurements 155

5.1 Isotopes of gold which may be produced on low-energy cyclotrons 157
5.2 Radiogold yields following proton bombardment of ^{nat}Pt 160

6.1 Isotopes of Bromine 173
6.2 Binary alloys of selenium 176

7.1 ^{89}Zr production methods comparison against literature 192
7.2 NOTA, DOTA, and DFO competitive binding assay results 199
7.3 Trace metal impurities of ^{64}Cu 'hold-backs' 203

B.1 Tabulated OLINDA source organ disintigrations 236
B.2 Tabulated ^{51}Mn time activity curves (TACs) 237
B.3 Tabulated ^{51}Mn PET ROI uptake quantification. 238
B.4 Tabulated ^{51}Mn *ex vivo* biodistribution 238

C.1 Tabulated longitudinal PET results for ICR mice with intravenous ^{52}Mn. . . 241
C.2 Tabulated ex vivo biodistribution 13 days post intravenous ^{52}Mn administration242
C.3 Tabulated PET results from pharmacological manipulation of pancreatic ^{52}Mn uptake 243
C.4 Ex vivo biodistribution following pharmacological manipulation of pancreatic ^{52}Mn uptake 243
C.5 Tabulated biodistribution of ^{52}Mn in ob/ob mice 244

E.1 Tabulated history of ^{64}Cu effective specific activities at UW-Madison 255

LIST OF FIGURES

2.1 FitzPeaks automatic peak deconvolution example . . . 9
2.2 FitzPeaks manual peak deconvolution example . . . 10
2.3 Wizard 2480 Automatic Gamma Counter photograph . . . 11
2.4 Gamma counter efficiency vs. activity . . . 12
2.5 Gamma counter background measurement with ^{52}Mn. . . . 14
2.6 MicroPET Derenzo Pattern Design . . . 17
2.7 Linearly-filled MicroPET Derenzo Exploded View . . . 18
2.8 Linearly-filled MicroPET Derenzo Highlighted Fill Path . . . 20
2.9 ^{64}Cu, ^{52}Mn, ^{76}Br, ^{124}I Linearly-filled MicroPET Derenzo Images . . . 21
2.10 Conventional vs. Linearly-Filled Derenzo Fill Volume Illustration . . . 23

3.1 MEMRI Publications vs. Time . . . 27
3.2 Simultaneous PET/MRI Publications vs. Time . . . 27
3.3 ^{54}Fe(d,α)^{52}Mn excitation function . . . 29
3.4 ^{nat}Cr(p,x)^{52}Mn excitation function . . . 30
3.5 Pressed chromium target before/after irradiation . . . 31
3.6 Anion exchange chromatography elution profiles of ^{52}Mn and ^{nat}Cr . . . 34
3.7 TOA-separated Mn product TLC comparison . . . 37
3.8 Ethanol-based anion exchange chromatographic Mn/Cr separation steps . . . 40
3.9 HPGe gamma spectrum of ^{nat}Cr irradiated by 16 MeV Protons . . . 45
3.10 ^{52g}Mn half life measurement. . . . 47
3.11 ^{54}Fe target fabrication photographs and electrodeposition parameters . . . 55
3.12 Example HPGe gamma spectrum of ^{51}Mn . . . 60
3.13 Least-squares fitting of representative ^{51}Mn decay curve . . . 62
3.14 ^{51}Mn dynamic PET time-activity curves . . . 66
3.15 ^{51}Mn static PET images and biodistribution . . . 68
3.16 ^{54}Fe(p,α)^{51}Mn excitation function . . . 70
3.17 PET images of ^{52}Mn-DOTA-TRC105 and ^{52}Mn^{2+} in mice . . . 81
3.18 PET-derived TACs for ^{52}Mn-DOTA-TRC105 and ^{52}Mn^{2+} . . . 82
3.19 Ex vivo biodistribution of ^{52}Mn-DOTA-TRC105 and ^{52}Mn^{2+} . . . 84
3.20 DMT1-hNPC *in vivo* uptake of ^{52}Mn . . . 93
3.21 Serial PET images of ICR mice injected intravenously with ^{52}Mn(II) . . . 105

3.22 Serial ^{52}Mn PET ROI quantification . . . 106
3.23 Ex vivo ^{52}Mn biodistribution of mice following serial PET scanning . . . 106
3.24 Dynamic PET TACs for ^{52}Mn(II) bolus and infusion in mice . . . 108
3.25 Pharmacologic manipulation pathways for pancreatic $^{52}Mn^{2+}$ uptake . . . 111
3.26 In vitro islet uptake of ^{52}Mn . . . 112
3.27 Pharmacologic manipulation: ^{52}Mn PET image comparison . . . 113
3.28 Pharmacologic manipulation: PET ROI ^{52}Mn uptake quantification . . . 114
3.29 Pharmacologic manipulation: Ex vivo ^{52}Mn uptake . . . 115
3.30 Type-I diabetes mouse model: blood glucose and weight changes . . . 116
3.31 Type-I diabetes mouse model: ^{52}Mn-PET image comparison . . . 117
3.32 Type-I diabetes mouse model: ^{52}Mn-PET ROI quantification . . . 117
3.33 Type-I diabetes mouse model: Ex vivo ^{52}Mn biodistribution . . . 118
3.34 ^{52}Mn in Ob/Ob mice: PET image comparison . . . 119
3.35 ^{52}Mn in Ob/Ob mice: PET ROI quantification . . . 120
3.36 PET of isoflurane impact of *in vivo* pancreatic uptake of ^{52}Mn . . . 130
3.37 Gamma counting of isoflurane impact on *ex vivo* pancreatic uptake of ^{52}Mn . 131

4.1 Fe+p target stack photograph . . . 135
4.2 Energy distribution FWHM vs. Average Proton Energy . . . 137
4.3 Inter-monitor reaction fluence variance minimization . . . 140
4.4 Results of fluence variance minimization . . . 142
4.5 Beam profile measurements from Gafchromic^{TM} film exposure . . . 144
4.6 Monitor reaction-measured fluence vs profile monitor interpolation . . . 145
4.7 Cu + p: Plotted σ_c & σ_i for ^{58g}Co & ^{58m}Co vs. TALYS 2015 . . . 151
4.8 Predicted ^{52g}Mn, ^{54}Mn, ^{48}Cr, and ^{51}Cr yields from measured cross sections . 153

5.1 Literature cross sections for production of radiogold by ^{nat}Pt+p . . . 158
5.2 Photograph of ^{nat}Pt target disc . . . 159
5.3 Radio-gold thermal diffusion temperature profile . . . 164
5.4 Relative etching efficiency following thermally-assissted diffusion . . . 165
5.5 Tributyl Phosphate - HCl Distribution Coefficients for Au and Pt . . . 168
5.6 Tributyl Phosphate - HNO_3 Distribution Coefficients for Au and Pt . . . 169
5.7 Tributyl phosphate (TBP) structure . . . 169
5.8 Diamyl amylphosphonate (DAAP) structure . . . 170
5.9 Pt/Au Separation by UTEVA extraction resin . . . 171

6.1 NiSe disc target 179
6.2 Apparatus for radiobromine distillation. 181
6.3 Radiobromine distillation kinetics 182

7.1 Photograph of ^{nat}Y spot welding 189
7.2 Photograph of ^{nat}Y spot-welded target 190
7.3 Photograph of ^{nat}Y spot-welded target 191
7.4 Effective Specific Activity TLC 196
7.5 ^{64}Cu Competitive Chelation Plot 198
7.6 Model Predicted ESA vs. Measured ESA 204

A.1 Sample spectral configuration in FitzPeak 229
A.2 Energy vs. channel calibration in FitzPeak 230
A.3 Peak shape calibration in FitzPeak 232
A.4 FitzPeaks calibration source data file 233
A.5 Efficiency calibration in FitzPeak 234

B.1 ^{51}Mn *ex vivo* quantification vs. PET ROI quantification 239

C.1 Ex vivo C57BL/6J vs ob/ob $^{52}Mn^{2+}$ pancreatic uptake 240

E.1 Histogram of ^{64}Cu ESA history 254
E.2 ESA as a function of activity per sample 256

LIST OF NOTATIONS

BCM	Beta cell mass
BR	Branching ratio
CCD	Charge-coupled detector
CNS	Central Nervous System
CT	Computed Tomography
Df	Desferoxamine
DFO	Desferoxamine
DMEM	Dulbecco's modified Eagle's medium
DMT1	Divalent Metal Transporter 1
DOTA	1,4,7,10-tetraazacyclodeodecane-1,4,7,10-tetraacetic acid
DTPA	Pentetic acid, 2-[Bis[2-[bis(carboxymethyl)amino]ethyl]amino]acetic acid
EDTA	Ethylenediamineetetraacetic acid
EoB	End of Bombardment
EoC	End of Chemistry
EPA	Environmental Protection Agency
ESA	Effective Specific Activity
FDG	fluorodeoxyglucose
FOV	Field of view
hNPC	Human neural progenitor cells
HPGe	High-purity germanium detector
HPLC	High-performance liquid chromatography
%ID/g	Percent injected dose per gram
IPF	Isotope Production Facility
i.p.	Intraperitoneal
i.v.	Intravenous
K_{ATP}	ATP-Sensitive Potassium Channel
LANL	Los Alamos National Laboratory

LANSCE	Los Alamos Neutron Science Center
PBS	Phosphate-buffered saline
PET	Positron Emission Tomography
mAb	Monoclonal Antibody
MCA	Multi-channel analyzer
MEMRI	Manganese-Enhanced Positron Emission Tomography
MIP	Maximum Intensity Projection
MP-AES	Microwave Plasma Atomic Emission Spectrometry
MRI	Magnetic Resonance Imaging
NOTA	1,4,7-triazacyclononane-triacetic acid
OSEM3D	Three-dimensional ordered subset expectation maximization
p.i.	Post-injection
RfD	Reference Dose
ROI	Region of interest
SA	Specific Activity
SPECT	Single Photon Emission Computed Tomography
SPIO	Super-paramagnetic iron oxide
T_1	spin-lattice/longitudinal relaxation time
T_2	spin-spin/transverse relaxation time
TAC	Time Activity Curve
TLC	Thin layer chromatography
TOA	Tri-octyl amine
VDCC	Voltage-dependent Calcium Channel
WHO	World Health Organization

1 INTRODUCTION

Positron emission tomography (PET) operates by the detection of coincident photons following positron (β^+) decay and annihilation. The spatial distribution of these annihilation events may be reconstructed from "lines of response" for coincident events. In this way the spatial distribution of a molecule of biological significance, complexed with a radioactive isotope which decays by positron emission, may be quantified in the human body. When combined with an anatomical imaging modality, i.e. magnetic resonance imaging (MRI) or computed tomography (CT), significant diagnostic flexibility is obtained.

Over the past two decades, PET has become a mainstay diagnostic tool in modern medicine for cardiac and oncological applications. Conventional positron emitting isotopes include ^{11}C, ^{13}N, ^{15}O, ^{18}F, and ^{82}Rb, the properties of which are summarized in Table 1.1. ^{11}C, ^{13}N, and ^{15}O are typically produced at a low-energy medical cyclotron (< 20 MeV p^+) on-site while ^{18}F may be produced regionally and ^{82}Rb may be obtained from ^{82}Sr ($t_{1/2}$: 25.3 d) generators. Although these isotopes have met the needs of clinical nuclear medicine historically, the field has recently moved towards adopting radiometals such as ^{68}Ga ($t_{1/2}$: 68 min), ^{64}Cu ($t_{1/2}$: 12.7 h), and ^{89}Zr ($t_{1/2}$: 3.27 d).

Isotope	Half-life ($t_{1/2}$)	β^+ BR	β^+ Ave. Energy	Tracer examples
^{11}C	20.4 min	99.7%	0.39 MeV	PiB, Methionine, Choline
^{13}N	9.96 min	100%	0.48 MeV	Ammonia ($^{13}NH_3$)
^{15}O	2.03 min	99.9%	0.73 MeV	Water ($^{15}OH_2$)
^{18}F	109 min	96.9%	0.25 MeV	FDG, Fluoride ($^{18}F^-$)
^{82}Rb	1.27 min	96%	1.48 MeV	$^{82}RbCl_2$

Table 1.1: Properties and tracer examples of conventional PET radionuclides.

With more than 650 medical cylotrons available globally, the capacity for tracer production now far-exceeds clinical demand for [^{18}F]Fluoro-deoxy-glucose (FDG), which has enabled investigation into a broad range of novel biomedical applications. Most of these cyclotrons are located in hospitals, institutes for academic research, and commercial facilities specializing in producing and selling of radioisotopes (Schmor, 2010). The development of new biomedical applications need not be limited to these facilities however, as the potential for national and international distribution of radioisotopes has begun to be utilized recently. Positron-emitting isotopes with half-lives conducive to widespread distribution which may be produced on low-energy medical cyclotrons are listed in Table 1.2.

Isotope	Half-life ($t_{1/2}$)	β^+ BR	β^+ Ave. Energy	Production
^{48}V	16.0 d	49.9%	0.29 MeV	^{48}Ti(p,n)
^{52}Mn	5.59 d	29.6%	0.24 MeV	^{52}Cr(p,n)
^{55}Co	17.5 h	75.9%	0.57 MeV	^{58}Ni(p,α)
^{64}Cu	12.7 h	17.6%	0.28 MeV	^{64}Ni(p,n)
^{66}Ga	9.49 h	57.0%	1.75 MeV	^{66}Zn(p,n)
^{69}Ge	39.1 h	24.0%	0.49 MeV	^{69}Ga(p,n)
^{71}As	65.3 h	28.3%	0.35 MeV	^{71}Ge(p,n)
^{72}As	26.0 h	87.8%	1.17 MeV	^{72}Ge(p,n)
^{74}As	17.8 d	29.1%	0.44 MeV	^{74}Ge(p,n)
^{76}Br	16.2 h	55.0%	1.18 MeV	^{76}Se(p,n)
^{77}Br	57.0 h	0.73%	0.15 MeV	^{77}Se(p,n)
^{79}Kr	35.0 h	7.0%	0.26 MeV	^{79}Br(p,n)
^{86}Y	14.7 h	31.9%	0.65 MeV	^{86}Sr(p,n)
^{89}Zr	3.27 d	22.7%	0.47 MeV	^{89}Y(p,n)
^{90}Nb	14.6 h	51.2%	0.66 MeV	^{90}Zr(p,n)
^{124}I	4.18 d	22.7%	0.82 MeV	^{124}Te(p,n)
^{194}Au	38.0 h	1.72%	0.62 MeV	^{194}Pt(p,n)

Table 1.2: Properties and production routes of positron emitting isotopes which can be produced on low energy cyclotrons and have half-lives lending themselves to national or international distribution.

At the University of Wisconsin - Madison, fruitful research into the application and cyclotron production of new radioisotopes has been sustained for more than 45 years. Two cyclotrons are employed for radioisotope production, the legacy CTI RDS-112 (25 μA 11 MeV p^+) and the new work-horse GE PETtrace (100 μA 16 MeV p^+, 50 μA 8 MeV d^+). This dissertation deals primarily with the production of six positron-emitting radioisotopes (^{51}Mn, ^{52g}Mn, ^{64}Cu, ^{76}Br, ^{89}Zr, and ^{194}Au), five of which have half-lives conducive to distribution, but also delves into the biology and biomedical applications of radiomanganese.

1.1 Organization of the Dissertation

Chapter 2 describes a subset of the instrumentation and analytic techniques used in this work. Most notably: the generation of an extensive radionuclide identification library for HPGe gamma spectroscopy; dead time correction evaluation and background subtraction methods for auto-gamma counting; and the development of a new linearly-filled Derenzo phantom.

Chapter 3 details production and radiochemical isolation methods for ^{52g}Mn and ^{51}Mn on low-energy medical cyclotrons. Further, the use of radiomanganese is described in several applications: anti-CD105 immunoPET with ^{52}Mn-DOTA-TRC105; cell tracking by upregulation of the divalent metal transporter-1 in human neural progenitor cells; quantification of functional beta cell mass for diabetes staging, transplant monitoring, and drug development; and probing the impact of isoflurane on acute pancreatic metabolic function.

Chapter 4 describes the measurement of ^{nat}Fe+p, ^{nat}Al+p, and ^{nat}Cu+p nuclear excitation functions at the Los Alamos National Laboratory Isotope Production Facility from 30–90 MeV. These measurements may serve to inform future production strategies for medically relevant isotopes, particularly ^{58m}Co, ^{55}Co, and ^{52g}Mn. Furthermore, new analytic strategies for proton energy determination in stacked-foil type cross section measurement experiments are described.

Chapter 5 describes the production and radiochemical isolation of positron-emitting isotopes of gold by ^{nat}Pt+p. Irradiation results are detailed and a physical separation by

thermal diffusion is investigated. A novel wet-chemistry separation method employing the UTEVA extraction resin is presented.

Chapter 6 describes production strategies for radiobromine from binary alloys of selenium, and the targetry and dry distillation techniques which are currently employed at UW-Madison. Calculation of diffusion coefficients for a two-component distillation is described.

Chapter 7 describes considerations in the production capacity for ^{64}Cu and ^{89}Zr at UW-Madison, improved targetry methods for the production of ^{89}Zr, and the formation and testing of an analytic model of effective specific activity.

Appendices A–E contain: information regarding the operation and calibration of the HPGe gamma spectroscopy analysis software FitzPeaks; supplemental data regarding the biodistribution and OLINDA dosimetry of ^{51}Mn; supplemental data regarding the quantification of functional beta cell mass in murine models of diabetes using ^{52}Mn; plots comparing cross sections measured in this work against literature values; and a historical review of ^{64}Cu effective specific activity measurements, and a discussion of the limitations of these measurements.

2 INSTRUMENTATION IN ISOTOPE PRODUCTION

2.1 HPGe Gamma Spectrometry

The development of efficient radionuclide production methods depends on the accurate identification and quantification of nuclear reaction productions following irradiation. This is typically achieved by high-purity germanium (HPGe) gamma spectroscopy, but can also be achieved through alpha or beta spectroscopy, or ionization-based half-life determinations.

Gamma spectroscopy operates by determining the amount of energy deposited in a detector crystal and digitally binning that subsequent detector interaction. Semiconductor detectors (i.e. germanium detectors) having a P-I-N design rely on the production of charged particles within the intrinsic (I) region by x-rays or gamma rays, with the produced charge being proportional to incident photon energy. Electrons ejected from their atomic orbitals leave a "hole" behind, and reside in the intrinsic detector region's conduction band. These "holes" and conduction band electrons are referred to as "charge carriers." Under reverse bias, the electric field produced within the intrinsic region pushes charge carriers toward the positive (P) and negative (N) electrodes, where the charge is converted into a voltage pulse by an integral charge-sensitive preamplifier.

Due to the low band gap (low potential energy difference between the conduction band and atomic orbitals), HPGe detectors must be cooled, typically by liquid nitrogen (77 °K), to prevent excessive leakage current from thermal electron ejection. Excess

leakage current may destroy the energy resolution characteristics of an HPGe detector, or destroy the field-effect-transistor (FET) used in the preamplifier.

2.1.1 Fitzpeak library generation

Accurate radionuclide quantification depends on (1) accurate efficiency calibration as a function of energy, (2) accurate peak area quantification, and (3) sufficient counting statistics. Efficiency calibration is somewhat tied to peak area quantification, but also the accuracy and precision of calibration sources which are typically traceable to National Institute of Standards and Technology (NIST) measurements. A typical uncertainty on calibration sources is 4 - 6%, so this can be thought of as one of the limiting factors in activity quantification precision.

Motivated by the need for accurate radionuclide quantification and identification, a free version of the program "FitzPeaks" was installed and configured at UW-Madison to operate in parallel with the gamma spectroscopy data collection program "Maestro." This program is capable of automatic spectral analysis by way of storing efficiency calibrations at a variety of geometries, characterization of peak shape as a function of energy, and peak-fitting based on these understood peak shapes. This program is capable of modeling high and low-energy tailing, and is quite adept at automatic peak deconvolution. The peak-fitting subroutine is based on the SAMPO spectral analysis FORTRAN code (Routti et al., 1969), which has shown to be superior to other peak-fitting codes such as GAMMANAL, SPECANAL, GammaVision, and RAYGUN, particularly

in peak decoupling applications (Jackman et al., 2014), where peak overlap is significant. The calibration and operation of the UW-Madison FitzPeaks implementation is described in Appendix A.

In order to facilitate automatic radionuclide identification following peak quantification, we constructed a library which contains the following information:

- Half life with uncertainty
- Energies of 3-10 most prominent gamma emissions
- Gamma emission branching ratios with uncertainty

for all radionuclides (including metastable states) which meet the following criteria:

- Half life between 1 minute and 10 years
- Nuclear mass less than 130 amu

Approximately 400 radioisotopes and metastable states thereof met these conditions. Nuclear data for the construction of this library was obtained from the digital Brookhaven National Lab database, accessed July, 2015. Scripts were written to facilitate the input and analysis of Maestro-acquired spectra in FitzPeaks. Scripts were also written to expedite the calibration workflow within FitzPeaks. These implementations are further described in Appendix A.

2.1.2 FitzPeaks peak fitting evaluation

Peak-fitting by the SAMPO algorithm within FitzPeaks appears robust when calibration has been conducted properly, accounting for count-rate dependent high or low-energy

tailing. The peak fitting relies on *a priori* knowledge of the energy as a function of bin number, peak FWHM as a function of energy, and the peak shape as a function of energy. In this way, the only unconstrained parameters for each peak are the height and quadratic, linear, and constant background coefficients. When fitting the peak baseline, the algorithm is sensitive to proximal peaks and will avoid including them. If there is significant peak overlap, the algorithm is particularly adept at decoupling them. Examples of this decoupling performance are shown in Figures 2.1 and 2.2.

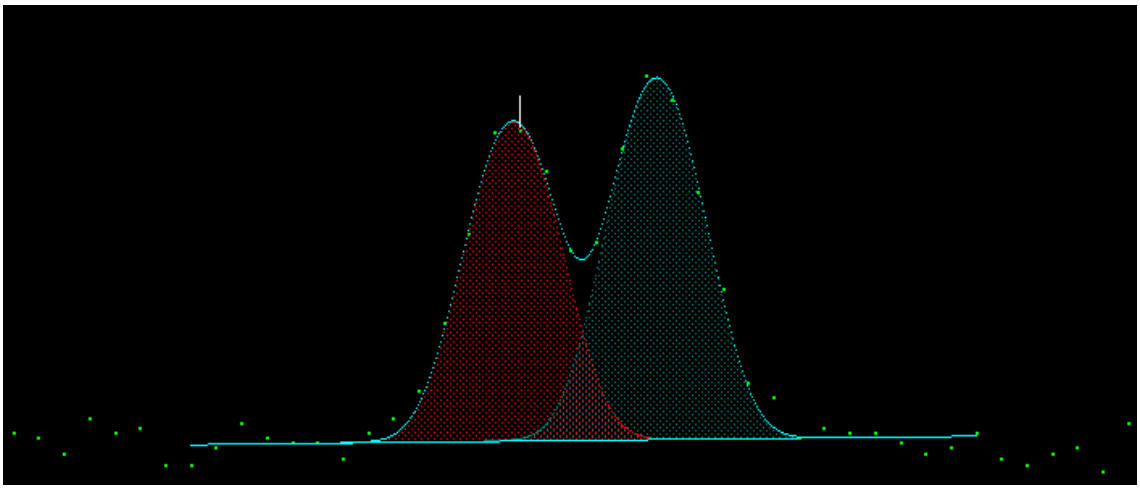

Figure 2.1: Peak area determination for the 1457.64 keV and 1460.82 lines from ^{152}Eu and ^{40}K, respectively. Peak centroids were correctly identified as 1457.6 keV and 1460.8 keV.

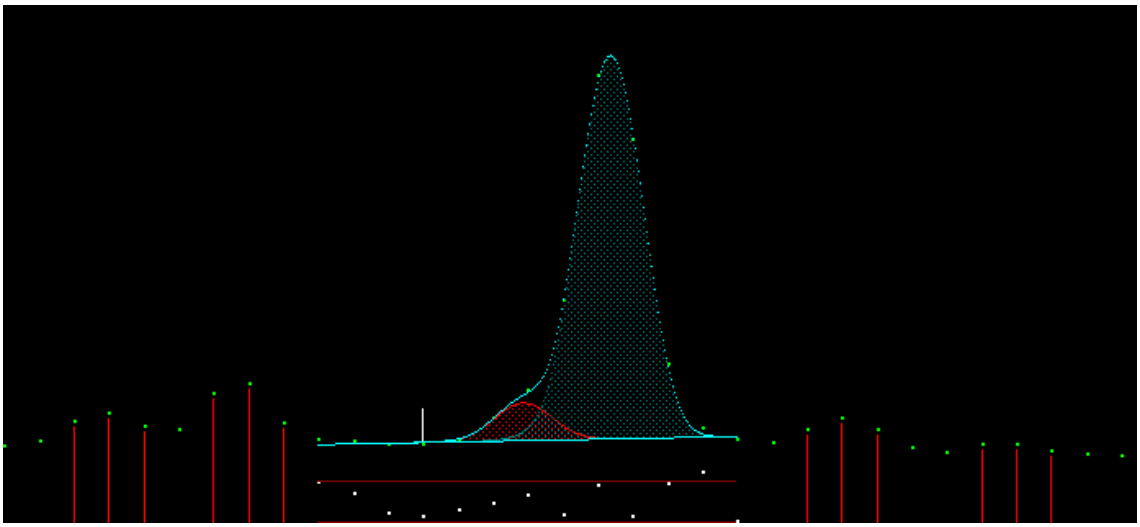

Figure 2.2: Smaller spectral peaks may be manually identified and quantified during analysis in FitzPeaks.

2.2 Auto-Gamma Counter

The use of an auto-gamma counter can be effective for the quantification of sample radioactivity, particularly in high-throughput applications such as ex vivo biodistribution studies, which often employ dozens of samples. Auto-gamma counters consist of a NaI detector shielded by lead, with a robotic mechanism for sample transfer into and out of the shielding. Typically, these counters are intended to be used with very little radioactivity (<1 μCi) and it is important to characterize the absolute efficiency as a function of isotope, sample position, and activity.

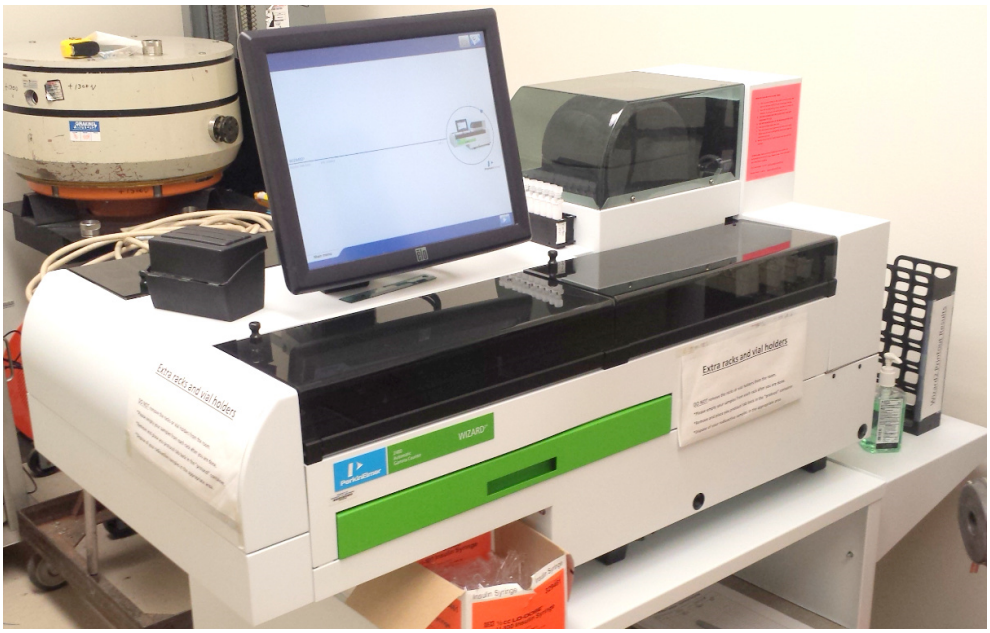

Figure 2.3: Photograph of Wizard 2480 Automatic Gamma Counter.

To this end a Perkin Elmer Wizard 2480 Automatic Gamma Counter (Figure 2.3) was characterized using varying activities and sample positions of ^{52g}Mn. Absolute activity was determined by efficiency-calibrated HPGe gamma spectroscopy, employing FitzPeaks peak-fitting. Uncertainty in efficiency was determined as the quadrature sum of the uncertainty in the gamma counter measurement, HPGe calibration efficiency uncertainty, statistical uncertainty in HPGe peak quantification, and uncertainty in the HPGe fitted peak background-subtraction.

These gamma counter efficiency measurements were used for ^{52}Mn ex vivo biodistribution studies, and similar measurements were employed in ^{51}Mn ex vivo biodistribution studies.

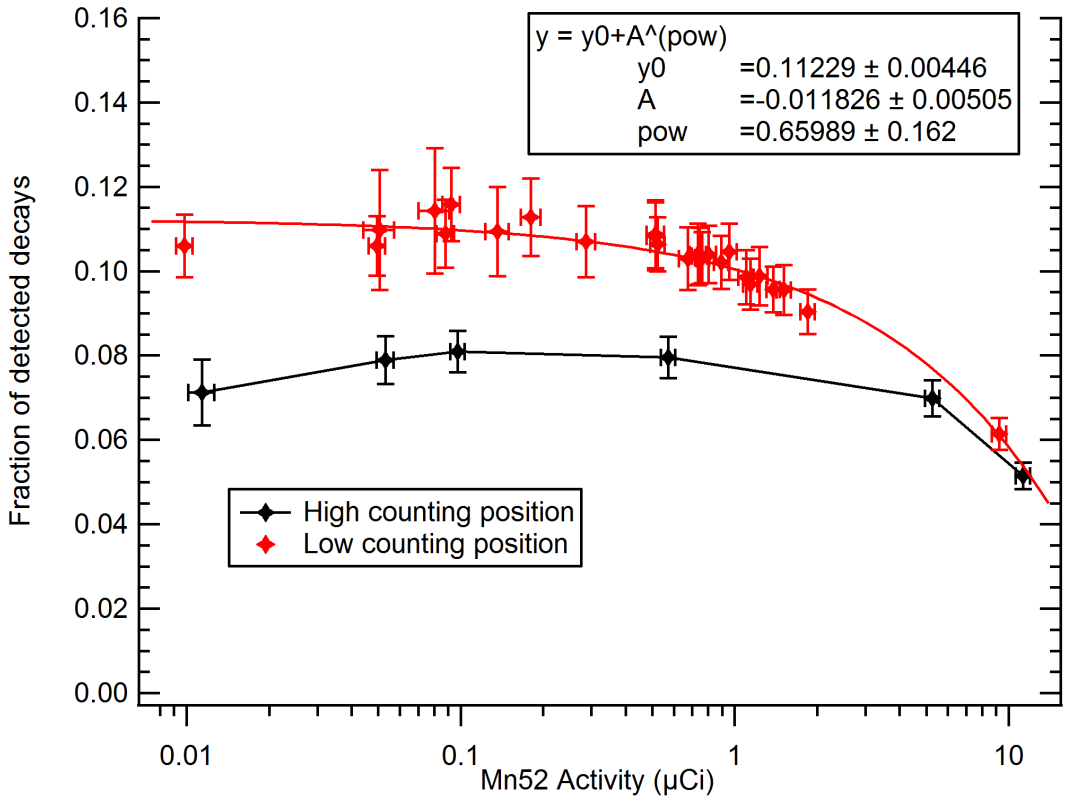

Figure 2.4: Gamma counter efficiency as a function of ^{52g}Mn activity and sample position (high and low within 10 mL test tube). Efficiency as a function of activity for the high position was fit by least-squares regression to a function of the form $f(x) = y_0 + A^{pow}$.

2.2.1 Background quantification and iterative subtraction methods

One major experimental issue with gamma counter activity quantification is the issue of background subtraction; A queue of samples (up to 10 per rack) is positioned directly outside the lead detector housing. Standard practice involves leaving one of the ten sample positions blank to acquire an approximate activity background reading from the set of proximal samples. The problem with this method is that the sample rack is in a slightly different position for each sample relative to the detector position, and also that an individual sample's background is not present while that sample is being measured.

A correct background subtraction method would involve the following steps:

1. Place a sample of known activity in position #1 and measure the background contribution for blanks in positions #2-10. Repeat this procedure until measurements have been taken with a single source in each sample position, with blanks in the remaining positions.

2. Tabulate background as function of source activity and position for the ten sample positions.

3. When a set of unknown samples is measured, subtract the background contributions of positions #2-10 from the measured activity in position #1. Repeat this subtraction for sample #2 with background contributions from samples #1, #3-10. Repeat until all samples have had a single background subtraction.

4. Repeat step #3 until all activity measurements converge to their true experimental background-subtracted values.

An example measurement (one of nine) which would be required to perform this subtraction technique is shown in Figure 2.5.

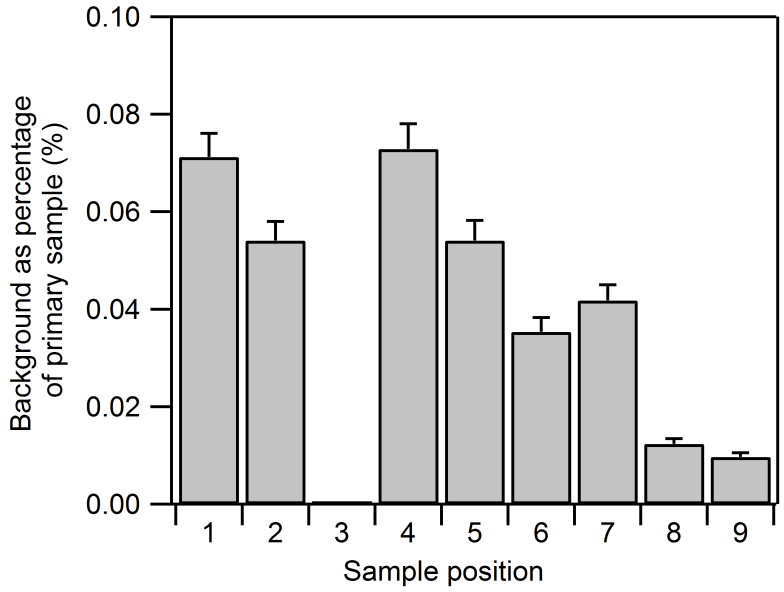

Figure 2.5: Background measurements at off-sample positions with ^{52}Mn sample (~0.1 μCi) at position 3 within a sample tray. Background is expressed as a percentage of ^{52}Mn sample count rate.

This iterative background subtraction procedure was not employed herein, as background contribution was found to be minimal (<0.1% of cumulative activity for ^{52}Mn samples), but future studies may benefit from this methodology particularly those which have a large dynamic range of sample activities.

2.3 Linearly-Filled Derenzo Phantom Design

Much of the work that follows was performed in collaboration with Benjamin Cox at the University of Wisconsin - Madison. Ben fabricated several designs, including the one described below, and deserves credit for contributions. Although not explicitly mentioned further, Ben was integral at all steps in the work described herein.

Small animal positron emission tomography (PET) imaging is widely used for devel-

opment of diagnostic agents and the identification of therapeutic markers (Cherry, 2001; Gambhir, 2002; Judenhofer et al., 2013; Larobina et al., 2006). In order to compare results between institutions or between agents labeled with different PET isotopes, scanners must be well calibrated and characterized. Several standard PET phantoms allow for inter-scanner or inter-isotope comparison. One of the most common quality control phantoms for nuclear medicine imaging is the Derenzo phantom (Derenzo et al., 1977). The phantom pattern, shown in Figure 2.6, is a series of positron emitting rods separated by twice their diameter in a triangular close-packed configuration. Several rod diameters are typically employed as a way to determine the diameter at which resolution breakdown occurs.

Derenzo phantoms are typically constructed by using two reservoirs of positron emitting isotopes in solution connected by channels making up the Derenzo design. In microPET versions of this design, some channels may be less than 1mm in diameter making it challenging to displace air bubbles when filling. One approach is to employ surfactants in the isotope solution to help with channel filling. This technique is still prone to difficulties, as surfactants in the form of detergents are prone to foaming, and organic surfactants often degrade the plastic materials from which the phantom is constructed. Another method might employ creating a vacuum within the phantom volume before filling with the isotope solution, but this adds unnecessary complexity to the filling process.

One solution to the problem of properly filling every hole in Derenzo-style phantoms

would be to design a phantom that is filled linearly, one hole at a time. This could be accomplished by creating a fluid path that snaked through a block of material by starting with a hole, then connecting it to an adjacent hole with a connecting channel on one side, connecting it to a third hole on the opposite side and continuing until all the pattern holes are filled. Such a phantom would have the additional benefit of eliminating the reservoirs used in traditional filling of these phantoms. This would reduce the overall activity needed to fill the phantom, both reducing the dose to anybody handling the phantom and increasing the quality of the resulting images by reducing noise from out-of-slice radioactivity.

Taking advantage of recent advances in three-dimensional (3D) printing (Gross et al., 2014; Schubert et al., 2014), an initial design was investigated with the fluid path winding through a single block of material. However, clearing such a long channel and cleaning out extra material from the resulting prototype, made this design impractical. Here we describe the design of a modular phantom that is filled in a linear fashion. It consists of three main pieces, a central piece, containing a hole pattern and connecting channels, and two end pieces. The piecewise design is such that it is possible to machine each component out of any desired material or use 3D printing for fabrication while still preserving the benefits of linear filling. Also shown are PET images of the hole pattern of initial prototypes of this phantom, filled with several commonly used PET isotopes in solution.

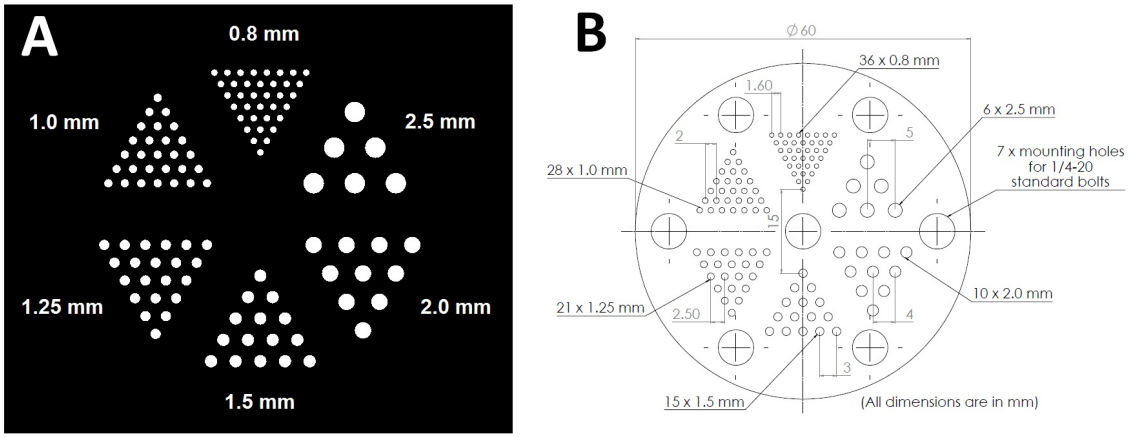

Figure 2.6: Cross-section of the Derenzo hole pattern incorporated into the prototype phantoms, shown with the activity highlighted (A) and in a technical drawing format to demonstrate how it is incorporated relative to the rest of the phantom (B).

2.3.1 MicroPET phantom design

Fabrication

All elements of the phantom assembly were designed using SolidWorks (Dassault Systemes, Velizy-Villacoublay, France), a computer-aided design (CAD) software package. The overall design of the phantom is illustrated in Figure 2.7. The central piece and two end pieces for the initial prototypes were fabricated using 3D printing on a Viper Si2 stereolithography machine (3D Systems, Rock Hill, SC, USA). The two gaskets were laser cut using a PLS 6.75 laser cutter (Universal Laser Systems, Scottsdale, AZ, USA) out of silicone sheets (McMaster-Carr, Elmhurst, IL, USA). The phantom itself is held together and sealed using glass-filled nylon nuts and bolts (McMaster-Carr).

Four initial prototypes of the final phantom design were created and assembled. To ensure proper coupling of the pieces in the assembled phantom, the mating sides of the three main phantom pieces were sanded with a series of sandpaper grits. The inlet

and outlet holes were tapped to allow for the addition of male Luer Lock fittings. A photograph of the completed assembly of one of the prototypes is shown in Figure 2.7.

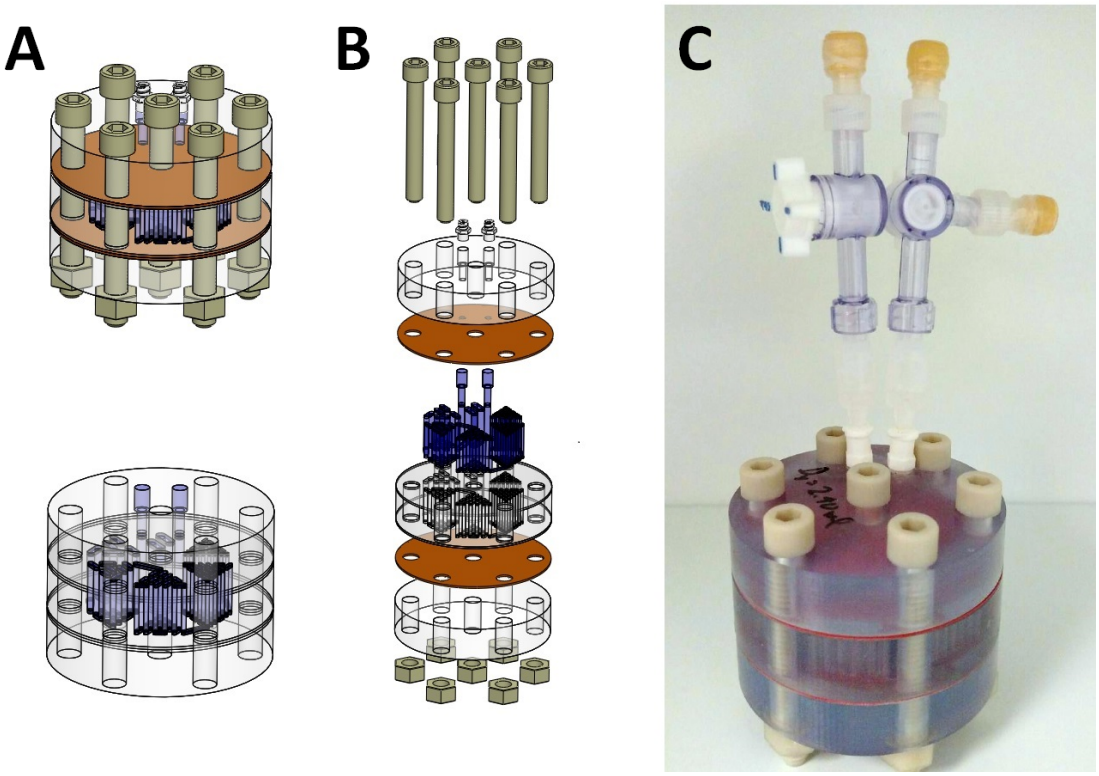

Figure 2.7: Cr3D Computer rendering of the phantom design showing all components and a rendering of the phantom design with the glass-filled nylon bolts, nuts and silicon gaskets hidden to improve visualization of the fluid volume within the phantom (A), exploded view of the phantom assembly (B) and a picture of one of the initial prototype phantoms, including the 3-way valves used during filling (C).

Filling

To facilitate filling of the phantom, an inlet and an outlet are incorporated into one of the end pieces of the phantom. In the initial prototypes, these were tapped and fitted with male Luer Lock fittings that could accept syringes. A Luer Lock syringe was filled with the appropriate volume and activity and fitted to the inlet of the phantom. An outlet

syringe was used as well for waste collection and to eliminate leaking. A three-way valve was used between the syringe and Luer Lock at both the inlet and outlet, so that the syringes could be removed after filling. A schematic of the filling path is shown in Figure 2.8.

The phantom volume was found to be approximately 2.4 mL for all four prototype phantoms. This allowed the phantoms to be filled by drawing a small volume of radioactivity into a 5mL Leur lock syringe, then drawing deionized water for a total volume of 2.4 mL in the syringe. The syringe would then be locked on the inlet port with a waste syringe on the outlet. Filling was rapid with minimal back-pressure. With the correct activity volume and filling procedure no leaks occurred.

PET Imaging

The phantom prototypes were filled with ^{52}Mn, ^{64}Cu, ^{76}Br and ^{124}I in aqueous solutions and a static PET scan was acquired on a Inveon MicroPET scanner (Siemens Healthcare, Erlangen, Germany). Greater than 400 million counts were acquired for each isotope using a 350-650 keV energy window and a 3.432 ns timing window. Isotopes were purchased commercially or produced in-house as previously described (Graves et al., 2015; McCarthy et al., 1997; Watanabe et al., 2014). Images were reconstructed by three-dimensional ordered subset expectation value maximization (OSEM3D) using a 512x512 grid size.

Axial slices along the pattern length were averaged to provide the images shown in

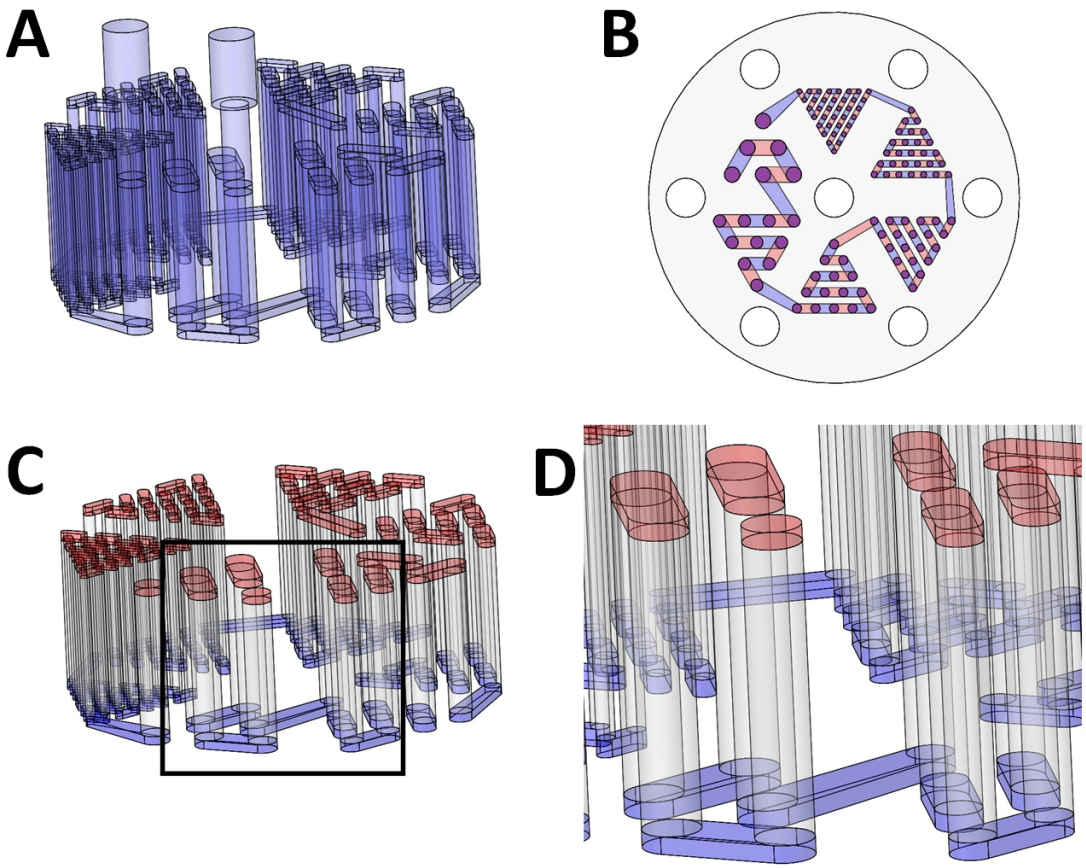

Figure 2.8: Computer rendering of the water volume within the initial prototype phantoms, including the inlet and outlet (A), a top view of the phantom with the water path through the phantom highlighted, with blue connections on one side of the phantom and red ones on the other (B), a computer rendering of the fluid path without the inlet and outlet and colored to illustrate the top and bottom connections (C) and a zoomed in view of the region indicated by the black box (D).

Figure 2.9. With scan parameters held constant, several factors can cause inter-isotope image quality variability, including positron range and confounding gamma emissions (Levin et al., 1999; Martin et al., 1995). ^{52}Mn and ^{64}Cu were found to provide the best image quality with their resolutions failing between hole diameters 0.80-1.00 mm. ^{76}Br was found to have the next best resolution failing between 1.00-1.25 mm. ^{124}I was found

to have the worse image quality with the resolution failing between 1.25-1.50 mm.

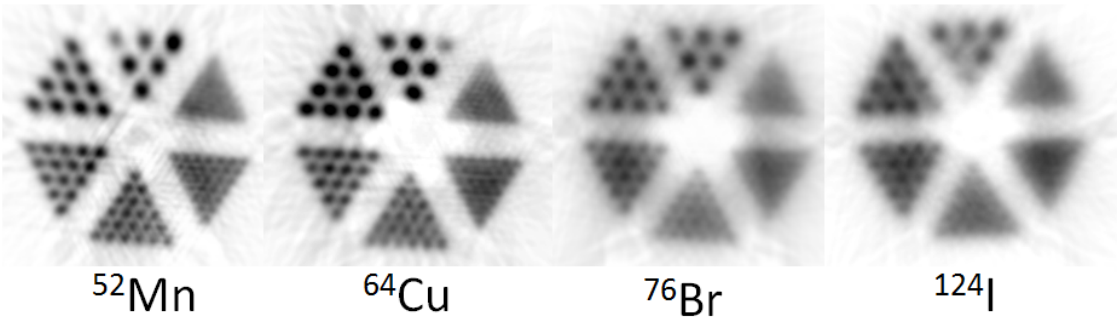

Figure 2.9: Images of the microPET phantom filled with ^{52}Mn, ^{64}Cu, ^{76}Br, and ^{124}I. Images were acquired on a Siemens Inveon MicroPET, and were reconstructed by OSEM3D.

Discussion

In this work we have demonstrated a design for the successful linear filling of a Derenzo-style hot rod microPET phantom. Linear filling makes filling phantoms of this type much easier and also without bubbles that otherwise could ruin the resulting images. This method for filling phantoms is not limited to Derenzo-style microPET phantoms. It could easily be translated to any type of phantom that utilizes a pattern of filled voids. This could include other resolution phantoms, contrast detail phantoms and uniformity phantoms, for both clinical and preclinical applications.

In addition to the linear filling of this phantom design, another key aspect is its modularity. The modularity of this design did require the use of a number of bolts to assemble the phantom, which does represent a slight drawback. The bolts that were used in the prototypes were made of glass-filled nylon to provide enough compression

to adequately seal the phantom. These bolts could lead to attenuation artifacts, although we did not observe artifacts in our reconstructed images.

The benefit of the modular design, however, is that it allows for ease of disassembly and cleaning and also allows each piece to be fabricated in a variety of ways including 3D printing as well as conventional machining techniques. While 3D printing allows for fast fabrication of prototypes and flexibility in design, a limitation is its accuracy, which depends largely on the material and printer used. This limitation can be overcome by using conventional machining techniques with a variety of materials. These techniques inherently produce parts with much higher spatial accuracy. The ability for this design to be manufactured with either 3D printing or conventional machining allows for both iterative designs of new hole patterns as well as industrial-scale manufacturing.

A major benefit of the design is the reduction in activity volume required for phantom filling, illustrated in Figure 2.10. This feature reduces isotope cost, personnel handling dose and noise from out-of-slice activity. A conservative estimate of the reduction in dose can be calculated by making a few assumptions. The whole pattern shown is approximately 40 mm in diameter, and assuming a reservoir thickness of 5 mm on each side, the total activity volume for a conventional phantom would be about 14.4 mL. This corresponds to a factor of six increase in activity volume compared to the design presented here. Therefore, incorporating a phantom like the one described here into the quality assurance (QA) protocol of an imaging facility will make the QA protocol cheaper, safer and more efficient. This constitutes a significant improvement over conventional

Derenzo phantom designs.

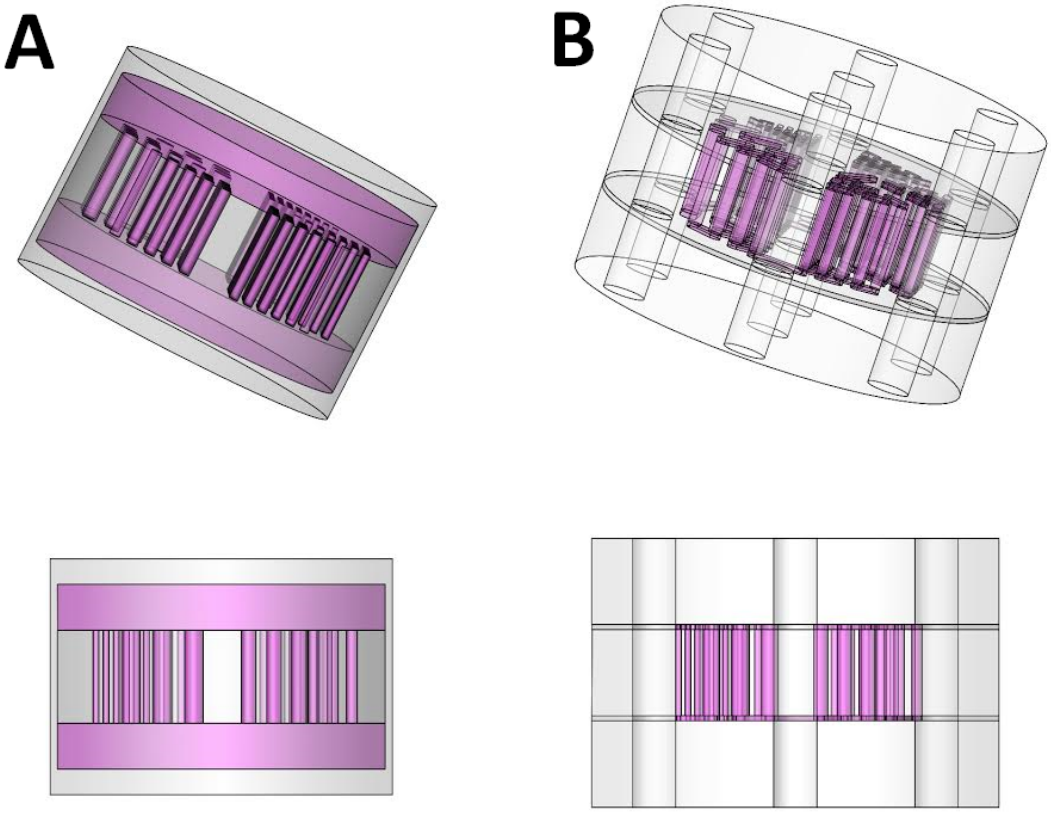

Figure 2.10: Illustration comparing a conventionally filled Derenzo style hot rod phantom (A) to the linearly filled phantom described in this manuscript (B). An isometric view (top) and a side view (bottom) are shown in both cases, with the fluid depicted in pink. The reduction in required fluid from the elimination of the reservoirs above and below the hole pattern in the conventional case is readily apparent.

3 ISOTOPES OF MANGANESE AND APPLICATIONS THEREOF

3.1 Introduction: Unique divalent metal with toxicological implications

Background

Manganese is the third most abundant transition metal in the earth's crust with a concentration of roughly 0.106% (1060 ppm), after titanium (5,600 ppm) and iron (41,000 ppm). More than 90% of globally produced manganese ores are used in steel manufacture, mostly in the form of ferromanganese. All steels contain some manganese, as it serves two purposes: (1) Manganese acts as a "scavenger," combining with sulfur to form MnS preventing the formation of FeS which leads to brittleness; (2) Manganese combines with dissolved oxygen to form MnO which prevents the formation of bubbles and pin-holes in cold steel (Greenwood et al., 1997).

Manganese has only one naturally abundant isotope, ^{55}Mn, which could prove useful for the ^{55}Mn(α,n)^{58m}Co reaction. Elemental manganese is hard and brittle, forming a bcc crystal lattice structure. The oxidation/reduction properties of Mn are complex and differ somewhat from the other metals in its group, Tc and Re. Manganate (MnO_4^{2-}) is a powerful reducing agent with many applications in chemistry. In solution, the most stable oxidation state is Mn(II) with a half-reaction standard reduction potential of -1.185 V (Greenwood et al., 1997).

Mn is found biologically in all types of bacteria, plants, and animals. In fact, it is so essential to life that the invention of the oxygen evolving complex (OEC) — containing 4

Mn atoms, responsible for catalyzing the oxidation of water to molecular oxygen — was one of the key pieces to enabling evolution of life on earth (Raymond et al., 2008). Manganese is required for photosynthesis in green plants, and forms many organometallic protein structures in mammals, such as Mn–superoxide dismutase (SOD2). Although it is an essential trace element in humans, roughly 10-20 mg in total, an excess of manganese is known to cause a variety of psychiatric and motor disturbances which closely resemble the symptoms of idiopathic Parkinson's disease. This condition is known as "manganism" and is observed in some mining and welding populations (Calne et al., 1994).

Radiomanganese

Radioactive isotopes of manganese, summarized in Table 3.1, show promise for a variety of medical applications. In particular the positron-emitting isotopes ^{52g}Mn ($t_{1/2}$: 5.59 d) and ^{51}Mn ($t_{1/2}$: 46 m, nominal) are well-suited to preclinical and clinical applications, respectively. In this work, the notation "^{52}Mn" is intended to refer to the ground state ^{52g}Mn rather than the metastable state ^{52m}Mn.

Isotope	$t_{1/2}$	Decay	Gammas >1% BR
^{51}Mn	46 m	β^+ (97.1%, E_{ave}: 0.96 MeV)	-
^{52m}Mn	21.1 m	β^+ (96.6%, E_{ave}: 1.17 MeV)	1434
^{52g}Mn	5.59 d	β^+ (29.4%, E_{ave}: 0.24 MeV)	744, 848, 935, 1246, 1333, 1434
^{54}Mn	312 d	EC (100%)	834
^{56}Mn	2.58 h	β^- (99.9%, E_{ave}: 0.83 MeV)	847, 1811, 2113

Table 3.1: Radioactive isotopes of Mn with half-lives greater than 2 minutes.

Radiomanganese was first explored as a PET agent in the late 1970's and early 1980's, particularly for use as a myocardial perfusion tracer by several groups (Lambrecht et al., 1979; Som et al., 1983; Atkins et al., 1979; Daube et al., 1985; Harper et al., 1982). In these works, ^{52m}Mn was primarily used, but some exploratory studies employing ^{51}Mn were performed. Later works continued to focus on myocardial imaging efforts while developing the ^{52}Fe/^{52m}Mn generator system for this purpose (Blaustein et al., 1997; Herscheid et al., 1983; Lubberink et al., 1999).

It was not until 2010's that ^{52g}Mn was used for PET applications — having been considered an unwelcome contaminant in early studies — with articles being published by Geoffery Topping and Lake Wooten (Topping et al., 2013; Topping et al., 2014; Wooten et al., 2015). This recent rise in interest surrounding ^{52}Mn-based PET applications is partly due to PET/MRI technological advancements and partly due to the recent success of other long-lived PET isotopes, such as ^{64}Cu and ^{89}Zr. For MRI, the T_1-relaxation shortening properties of bulk manganese are employed in a technique termed "manganese-enhanced magnetic resonance imaging" (MEMRI). The recent increase frequency of publications relating to MEMRI and PET/MRI is shown in Figures 3.1 and 3.2.

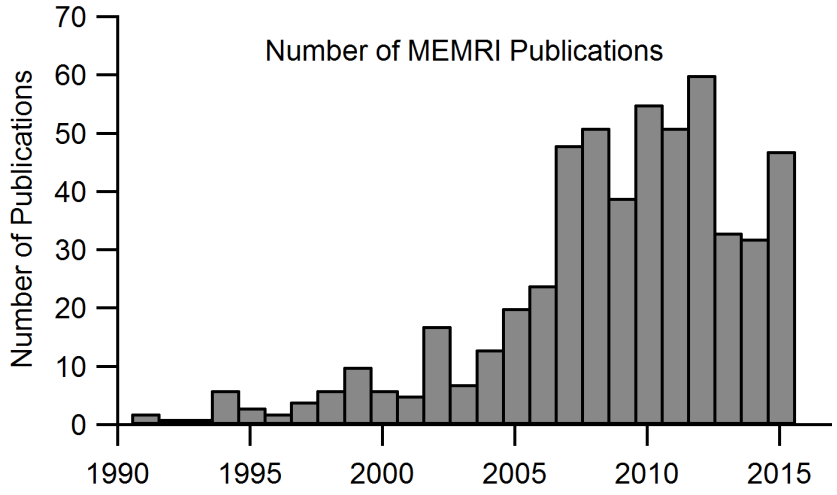

Figure 3.1: A histogram plotting the number of publications having to do with MEMRI as a function of time. The starting year of 1991 was chosen somewhat arbitrarily, as the idea of using Mn as a T1-shortening agent in MRI applications began in the 1960s.

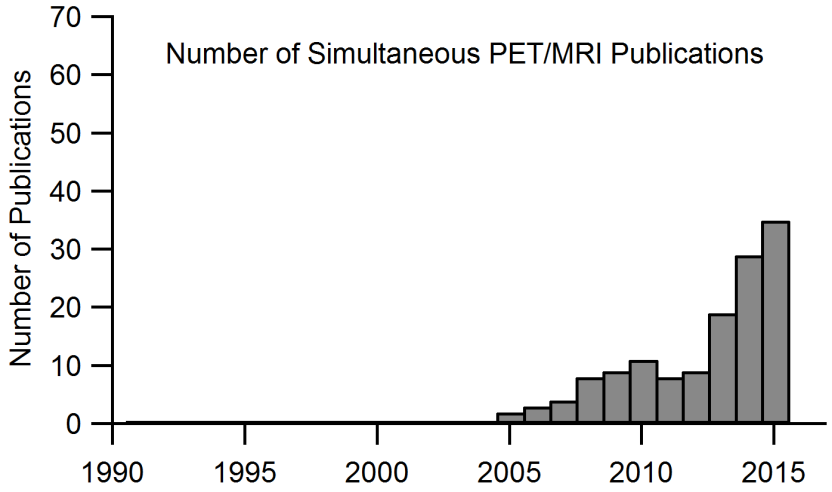

Figure 3.2: A histogram plotting the number of publications having to do with simultaneous PET/MRI as a function of time.

Although MEMRI shows promise, the biological toxicity of bulk manganese (Crossgrove et al., 2004) has hampered the development and progression of otherwise useful applications such as diffusion-tensor neuronal fiber tractography (Pirko et al., 2012;

Yamada et al., 2008; Napieczynska et al., 2015; Pautler et al., 2004), nociceptive activity detection (Jacobs et al., 2012), functional imaging of brain activation (Lin et al., 1997), diagnosis and staging of pancreatic cancer (Schima et al., 2002), heptocellular carcinoma detection (Murakami et al., 1996), cell tracking (Kim et al., 2011; Gilad et al., 2008) and evaluation of cardiac inotropic therapy (Hu et al., 2001). Manganese-based PET tracer alternatives may provide analogous imaging capabilities with reduced toxicity.

3.2 ^{52}Mn

3.2.1 Nuclear Reactions and Targetry

The production of ^{52g}Mn may be effected through a variety of nuclear reactions including high-energy protons (30 - 100 MeV) on ^{nat}Fe, intermediate energy deuterons (6–20 MeV) on ^{54}Fe, and by low-energy protons (<20 MeV) on ^{nat}Cr or ^{52}Cr. The high-energy ^{nat}Fe+p route is discussed extensively in Chapter 5, so the other routes will hereby be considered.

^{54}Fe(d,α)^{52}Mn

The idea of of radionuclidcally pure ^{52}Mn by ^{54}Fe(d,α) is intriguing, particularly due to the recent development of isotopically-enriched ^{54}Fe electrodeposition methods (described in detail in Section 3.3). Although this production route is theoretically possible, even with a thick ^{54}Fe target with an 8 MeV d^+ beam, a predicted yield of only 0.005 mCi/μAh is obtained from literature data, shown in Figure 3.3. This predicted yield agrees to within a factor of ~2 compared with experimental yields obtained by Hector

Valdovinos in ^{54}Fe(d,n)^{55}Co reaction studies at UW-Madison (yet unpublished data).

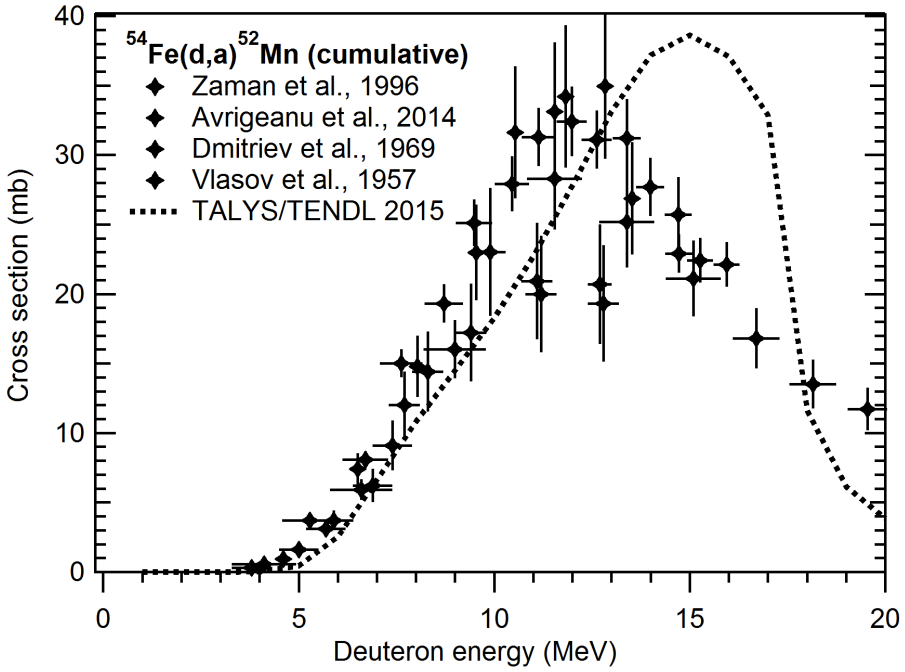

Figure 3.3: Cumulative reaction cross sections for the production of ^{52}Mn by ^{54}Fe(d,α) (Zaman et al., 1996; Avrigeanu et al., 2014; Dmitriev et al., 1969; Vlasov et al., 1957).

$^{nat/52}$Cr(p,n)^{52}Mn

The simplest method for high-yield production of ^{52}Mn is via the ^{52}Cr(p,n) reaction route. Due to the natural 83.8% abundance of ^{52}Cr in ^{nat}Cr and the low propensity for impurity formation of other Mn isotopes during proton irradiation, ^{nat}Cr, which is available in high purity from various distributors, is an inexpensive alternative to enriched target material. The main radionuclidic impurity formed from the irradiation of ^{nat}Cr is ^{54}Mn ($t_{1/2}$ = 312 d) with an energy dependent co-production rate, representing 0.1-0.4% of the ^{52}Mn activity at the end of a short bombardment at 16 MeV (Wooten et al., 2015;

Lewis et al., 2015). For 16 MeV irradiations of a thick ^{nat}Cr target, the expected yield of ^{52}Mn is approximately 9.5 MBq/μA·h (Lewis et al., 2015).

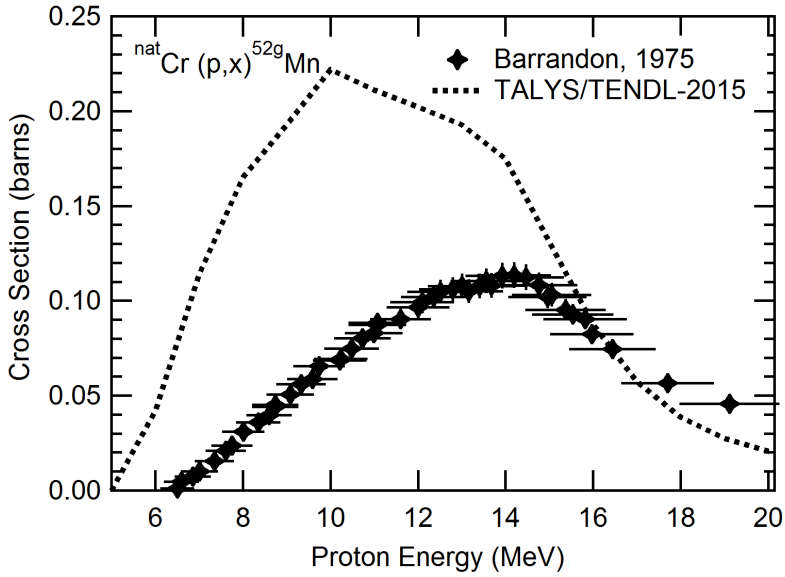

Figure 3.4: Cumulative reaction cross sections for the production of ^{52}Mn by ^{nat}Cr(p,x) (Barrandon et al., 1975).

Targets for production ^{52}Mn in this work were initially fabricated from cylindrical Cr discs (0.75" diameter, 0.4" thick, 99.95% pure, Kamis, Inc). These discs were machined to fit a cylindrical deplater for post irradiation etching. These targets were capable of withstanding high beam-currents and were able to be reused several times, but were not sufficiently pure for bioconjugate applications and required large acid volumes for etching.

More recently, targets were constructed by placing a natural chromium pellet (99.999% pure, approximately 750 mg, GFS Chemicals) on the center of a 19 mm diameter 2 mm thick silver disc (>99.9% pure, Noble Metals, Sarasota, FL) before being folded between

niobium foil and hydraulically pressed with a force of approximately 20-30 kN for ten seconds. This force is sufficient to bond the chromium metal into the silver disc without compromising the integrity of the rear target face. The bond at the Cr-Ag interface appears to be chemical rather than a physical embedding process, as this Cr granule is well adhered and in more than 50 production runs has never been observed to detach from the Ag during irradiation. The binary Ag-Cr phase diagram reveals a single quite stable alloy (BCC/ACC crystal combination) between 1–99% molar fraction of Cr with a melting point of 1235 °C (Venkatraman et al., 1990). It is likely that this alloy is being formed as a "cold weld" during target pressing. These targets have been irradiated by 16 MeV protons (GE PETtrace) with up to 60 μA of beam current with minimal discoloration.

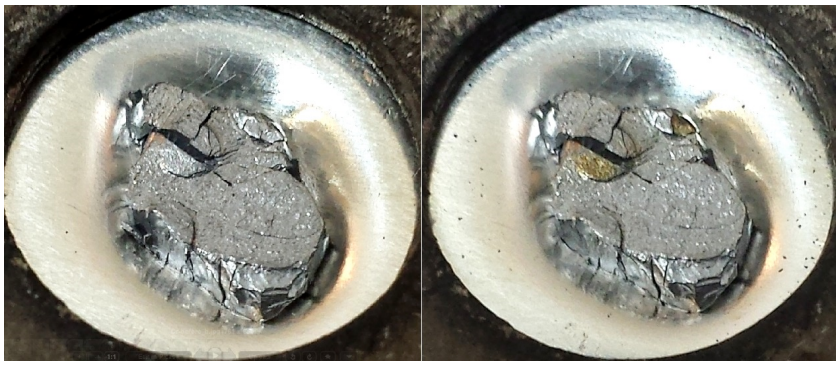

Figure 3.5: 99.999% pure chromium metal pressed in to a silver disc before (left) and after (right) irradiation with 40 μA for one hour with direct jet water cooling on the rear target face.

3.2.2 Cr/Mn Radiochemistry

It is essential that the Cr content is minimized in the final radiomanganese product, as Cr (particularly in the hexavalent form) is highly toxic. Several strategies have been explored for the separation of Mn/Cr, but in general this chemistry can be challenging due to the presence of several oxidation states of both elements and due to the similar ion chromatographic behavior of Mn(II) and Cr(III) (Knox, 1990).

In a neutral or acidic aqueous environment, manganese is predominately speciated as the pink hexaaqua ion $[Mn(H_2O)_6]^{2-}$, which is quite resistant to oxidation to Mn(III) (1.6 V standard electrode potential). In an alkaline solution however, the hydroxide $Mn(OH)_2$ is formed, which is easily oxidized to MnO_2 (-0.3 V standard electrode potential), both of which are highly insoluble in water.

Chromium is most stable as Cr(III) in acidic aqueous media, and similarly to Mn, prefers to exist as the hexaaqua ion. Three chloride forms of this ion are typically observed: the violet $[Cr(H_2O)_6]Cl_3$, the dark green trans-$[CrCl_2(H_2O)_4]Cl{\cdot}2H_2O$, and the pale green $[CrCl(H_2O)_5]Cl{\cdot}H_2O$ (Cotton et al., 1980). Dissolving elemental chromium in hydrochloric acid yields a dark green solution, implying primary speciation as the trans-$[CrCl_2(H_2O)_4]Cl{\cdot}2H_2O$. As with Mn, in aqueous alkaline solutions $Cr(OH)_3$ is the primary species, which has poor solubility resulting in bulk precipitation.

Anion Exchange Chromatography

In recent work by Geoffrey Topping (Topping et al., 2013; Topping et al., 2014) strong anion exchange chromatography was used to chromatographically separate Mn/Cr. With a concentrated hydrochloric acid mobile phase, Mn interacts more strongly than Cr with the anion exchange resin, although both interact relatively weakly. Topping et al. reported a pale yellow to colorless product and μg quantities of Cr following separation.

This separation was tested at UW-Madison using 16 mL of AG-1x8 (Bio-Rad, Hercules, CA, USA) in a 0.6" glass column. The column was equilibrated with 70 ml 12.1 M HCl. Irradiated and dissolved chromium metal (70 ± 1 mg) contained in 7 mL of 11 M HCl was loaded onto the column, and 1-5 ml fractions were eluted using 12.1 M HCl. Eluted fractions were assayed for ^{52}Mn activity using a ionization well chamber (Capintec, Ramsey, NJ, USA), and chromium content was measured by MP-AES. Activity readings were assumed to be all ^{52}Mn, based on the assumption that ^{54}Mn contributes negligibly to Capintec ionization.

The resulting elution profile shown in Figure 3.6. Combining fractions from 40 mL to 86 mL resulted in 60.1% activity recovery with 0.872 mg ^{nat}Cr metal remaining in the product, as measured by MP-AES. This corresponds to a separation factor of approximately 68. Furthermore, late fractions containing only trace chromium still eluted as a pale yellow color, suggesting the AG-1x8 resin was possibly being degraded or late Cr elution was observed — possibly due to speciation as the $[CrCl(H_2O)_5]Cl{\cdot}H_2O$ isomer.

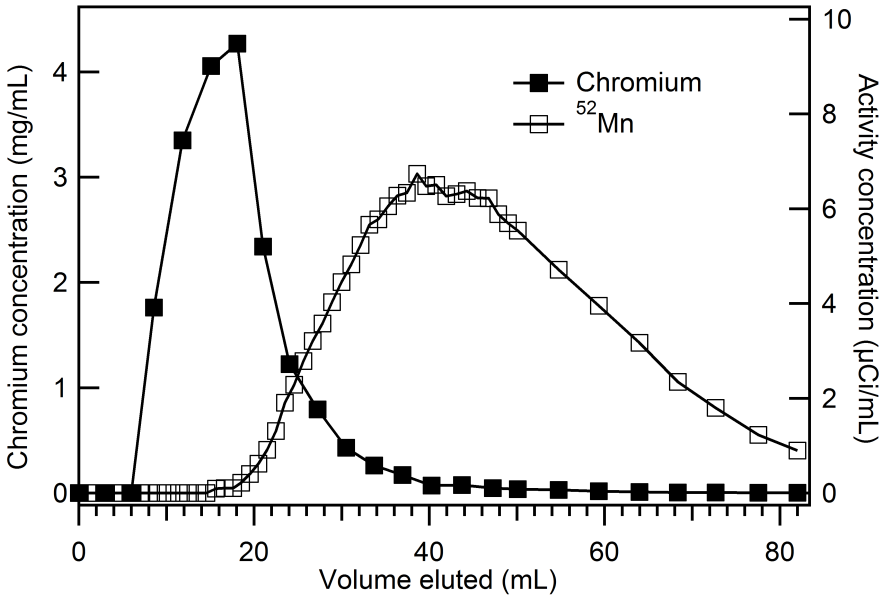

Figure 3.6: The elution profiles for bulk chromium and ^{52}Mn on an AG-1x8 column using concentrated HCl show some overlap. Chromium concentrations were measured by microwave plasma atomic emission spectrometry (MP-AES), and activity concentrations were measured by an ionization well chamber.

These results are disappointingly poor with less than 2/3 of the ^{52}Mn being recovered in 26 mL of concentrated (pale yellow) HCl. A residual 0.872 mg of Cr is unacceptable for animal studies, as ideally Cr mass would be reduced to less than 1 μg per subject. Further, this residual Cr mass is significantly higher than the mass reported by Topping et al.. This residual Cr mass might be reduced by employing a significantly larger column volume, but this approach would also increase the already vast elution and equilibration volumes. This mass might also be reduced by collecting later fractions at the expense of ^{52}Mn yield.

Trioctylamine Solvent-Solvent Extraction

A solvent extraction–based Mn/Cr separation procedure has been described by Lahiri et al., whereby Mn(II) ions are selectively extracted from 9 M HCl into 0.8 M trioctylamine (TOA) in cyclohexane (Lahiri et al., 2006). Mn is subsequently back-extracted to an aqueous media in the form of 0.001 M NH_4OH. A separation factor of up to 377 and a chemical yield of up to 60% is obtained by Lahiri et al. by these methods.

This method was tested at UW-Madison. Chromium targets were etched by 5 ml concentrated HCl for 60 minutes at 80 °C following irradiation. Mn^{2+} ions were extracted from the target solution — approximately 9 M HCl — to 10 ml of 0.8 M trioctylamine in cyclohexane. 10 ml 0.005 M NH_4OH was used to back-extract Mn(II) ions to aqueous media. This purification cycle was conducted a total of three times to reduce chromium contamination to a total mass of less than 1 μg. Trace chromium, manganese, iron, nickel, and zinc contamination was measured by microwave plasma atomic emission spectrometry (MP-AES) following the first purification cycle of this separation.

In the solvent-solvent extraction separation, for a starting bulk chromium mass of 456 ± 1 mg, a post-separation chromium mass of 5.35 ± 0.04 ng was measured by MP-AES. This mass reduction corresponds to an average separation factor of 440.1 for each of the three purification cycles. Each cycle had a ^{52}Mn recovery efficiency of 73 ± 7% (n=6), resulting in an overall separation efficiency of approximately 35%. These efficiencies and separation factors agree reasonably well with the published values by Lahiri et al.. Trace metal analysis results by MP-AES (Cr, Mn, Fe, Ni, and Zn) for the TOA extracted ^{52}Mn

product are summarized in Table 3.2. The final ^{52}Mn product was then taken to dryness under argon overflow, and then reconstituted in 0.1 M phosphate-buffered saline.

Metal	Mass Before Separation (μg)	Mass After Separation (μg)
Zn	1.51 ± 1.14	34.5 ± 0.9
Cu	1.83 ± 0.65	0.457 ± 0.006
Ni	4.54 ± 0.95	0.210 ± 0.002
Fe	26.52 ± 2.91	6.11 ± 0.06
Mn	11.47 ± 0.07	0.355 ± 0.007
Cr	126 ± 2 mg	74.3 ± 1.0

Table 3.2: Microwave plasma atomic emission spectrometry (MP-AES) measurements were taken to investigate the presence of trace metal impurities in mg of bulk chromium was separated using a single TOA extraction cycle. Zinc, copper, nickel, iron, manganese, and chromium concentrations were measured before and after separation. In the unseparated target material, iron and manganese are the most significant impurities. A modest reduction in copper, nickel, and iron are observed after separation, but a significant increase in zinc is observed. We suspect that the organic phase (trioctylamine + cyclohexane) is corrosive to the plastic vials that were used for solvent-solvent extractions, leading to an increase in ionic zinc contamination. To resolve this problem, glass separatory funnels were used in future experiments.

Due to uncertainty regarding the resulting chemical form ^{52}Mn product — as alkaline solutions are known to promote the formation of $MnOH_2$, MnO, and MnO_2 — investigative studies were performed. Thin layer chromatography (TLC) was utilized on four different samples to examine the chemical form of ^{52}Mn in the TOA extracted product. Sample 1 consisted of the TOA extracted product dried down and taken up in water. Sample 2 consisted of ^{52}Mn separated by ion exchange chromatography in HCl as a standard for $^{52}MnCl_2$. Sample 3 was created by treating $^{52}MnCl_2$ (sample 2) with OH to produce ^{52}Mn(OH)2. Sample 4 was produced by treating $^{52}MnCl_2$ with H_2O_2 to produce $^{52}MnO_x$ (x = 1, 2). These four samples were tested against five different

mobile phases: (A) H_2O, (B) 0.1 M HCl, (C) 1:1 MeOH : 10% NH_4OAc, (D) 0.05 M DTPA, and (E) 0.25 M NH_4OH. In the five mobile phases tested, samples 1 and 2 acted nearly identically, implying that the TOA product was not in the insoluble forms $Mn(OH)_2$ or MnO_x (Figure 3.7). From these TLC results, it was concluded that the TOA separated ^{52}Mn product was likely in the Mn(II)-chloride form.

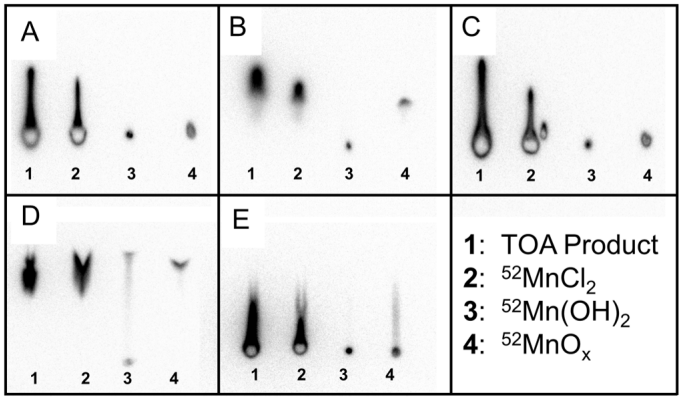

Figure 3.7: $Mn(OH)_2$ and MnO_x (x = 1, 2) were assumed to be the most likely insoluble and non-dissociative alternative chemical forms to $MnCl_2$ following separation by TOA extraction. Standards were prepared and tested against five different mobile phases using TLC. The five mobile phases were (A) H_2O, (B) 0.1 M HCl, (C) 1:1 MeOH:10% NH_4OAc, (D) 0.05 M DTPA, (E) 0.25 M NH_4OH.

Ethanol-based Anion Exchange Chromatography

As the two previous separation methods were found to be lacking, the former due to large acid volumes and poor separation; the latter due to time-consuming solvent-solvent extraction/dry-down steps and poor chemical yield — we sought to develop a new method. The ideal features of a separation method would be a high ^{52}Mn recovery efficiency, low residual chromium mass, no dry-down steps, "trap-and-release" chromatographic behavior, and a small final elution volume (<0.5 mL) in an injectable

matrix. Pursuant to these features, the separation of Mn from Cr by semi-aqueous anion exchange was explored.

The previously described methods for separating manganese from chromium involve anion exchange (except the work by Buccholz et al.) relying upon the formation of anionic chloride complexes of manganese (e.g. $MnCl_3^-$, $MnCl_4^{2-}$, $MnCl_5^{3-}$, etc.). Notably, there is a marked enhancement in the formation of anionic manganese chlorides when hydration is limited by using non-aqueous solvents. However, under similar conditions Cr^{3+} does not form anionic chloride complexes. This behavior is evident in the distribution coefficients for Mn and Cr against anion exchange resin from 97% EtOH 0.3M HCl solutions (Pietrzyk, 1960), where the resin affinities are sufficiently disparate for trap-and-release purification of ^{52}Mn from bulk Cr with small resin beds.

Targets were constructed as previously described hydraulically pressing ^{nat}Cr granules into Ag, and were irradiated by 16 MeV protons. Following irradiation, targets were etched by 2 mL of HCl (32-35%, Optima, VWR) at 75 °C for one hour, or until cessation of bubbling (typically 400 mg of the 750 mg Cr target was dissolved by this procedure). The solution was quantitatively transferred to a large centrifuge tube using a 47.5 mL rinse of ethanol (molecular biology grade, Sigma-Aldrich). To this solution, 0.5 mL of HCl was added resulting in a final target solution volume of 50 mL.

Three columns were constructed, each containing approximately 250 mg of dry AG-1x8 strong anion exchange resin (Bio-Rad Laboratories, Inc.) and were equilibrated and rinsed with 10 mL of 97:3 ethanol-HCl. The 50 mL of target solution was passed

through the first column trapping the ^{52}Mn and letting the bulk ^{nat}Cr pass through. After rinsing with 10 mL of 97:3 ethanol–HCl the activity was eluted in 1 mL of 6 M HCl. The eluted volume was diluted to 50 mL with ethanol, and then loaded on the second column. After rinsing, the activity was again eluted in 1 mL of 6M HCl and taken up to 50 mL with ethanol. With the activity loaded onto the third and final purification column, the column was rinsed, and the activity was eluted in approximately 1 mL of 0.1 M of HCl or any other desired aqueous eluent. Due to mobile-phase retention in the resin, invariably the final elution contained trace ethanol. It should be noted that for some labeling procedures, the eluted product should be dried down and reconstituted in 0.1M HCl or an appropriate aqueous buffer. These separation steps are summarized in Figure 3.8.

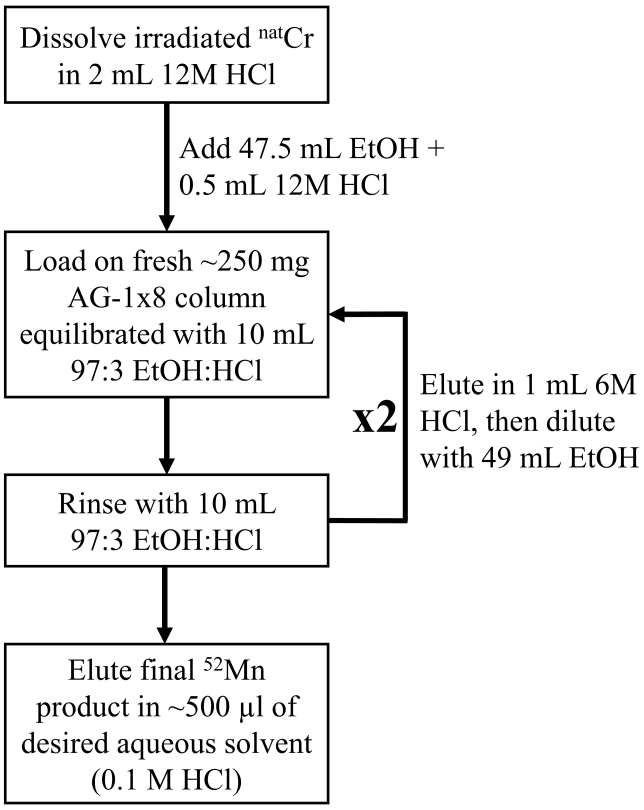

Figure 3.8: Diagram of separation steps for isolating ^{52}Mn from ^{nat}Cr using ethanol-based ion exchange chromatography. A final separation factor of $\sim 1.6 \times 10^6$ was obtained with a ^{52}Mn recovery efficiency of $62 \pm 14\%$ (n=7). Total separation duration excluding dissolution is approximately 30 minutes.

^{52}Mn extraction from ethanolic HCl onto AG-1x8 was $73 \pm 13\%$, $91 \pm 4\%$, and $92 \pm 5\%$ efficient ($n = 7$) at each of the column passes. The low first-step separation efficiency is likely due to the low HCl and ethanol concentrations for loading, approximately 0.11 M and 95% respectively, compared to the ideal concentrations of >0.3 M HCl and >97% ethanol. It is known that ^{52}Mn trapping is greatly improved by drying the dissolved target material before reconstituting in 0.3 M HCl, 97% EtOH (Fonslet et al., unpublished data). In fact, eluting in 0.1 M HCl and drying down between each of the three columns

has been shown to increase ^{52}Mn recovery to nearly 100% (Fonslet et al., unpublished data). These dry-down steps add complication, time, personnel dose, and increased probability of contamination however. Alternate methods for improving radiochemical yield might employ hydrogen chloride ethanol or dioxane solution (4.0 M HCl in dioxane, Sigma Aldrich Inc.) following target dissolution. Adding one of these solutions to the dissolved target material would result in the desired HCl concentration without the burden of added aqueous volume. The overall ^{52}Mn recovery efficiency of 62 $\pm$ 14% (n=7) was sufficient for our purposes, as it was nearly twice as efficient as the previously described based extraction approach to ^{52}Mn/^{nat}Cr separation and more easily lends itself to automation.

Chromium content in the eluted fractions fell successively at each step by factors of 601 $\pm$ 31, 80 $\pm$ 6, and 42 $\pm$ 5 ($n = 1$), as seen in Table 3.3. The overall chromium separation factor was $1.6 \times 10^6 \pm 1.0 \times 10^6$ ($n = 4$) as measured by trace metal analysis. During the first column separation, the resin became uniformly green-tinted indicating a slight retention of Cr^{3+}. This chromium did not wash off of the resin in any appreciable way with repeated rinses of the ethanolic HCl. However upon elution of ^{52}Mn, this species of Cr also co-eluted to a small degree. Similar effects were observed in the other two subsequent column separations by tracing the Cr content with MP-AES. Surprisingly this behavior contrasts with the published distribution coefficients of Pietrzyk et al., in that the extracted species of Cr was not behaving chromatographically. This is ultimately the reason why three sequential separations were required to achieve the necessary

purity for labeling, rather than repeated washings. The act of removing the Cr from the column and then re-constituting it in the ethanolic solutions appeared to reset the Cr speciation dichotomy, although with diminishing returns. This is likely due to the formation of different hydration states of Cr^{3+} in solution and their slow interchange (Knox, 1990). Regardless, the two additional column repetitions were not restrictive to rapid isolation of the product ^{52}Mn.

	Cr Mass (μg)	**Step Separation Factor**	**Cumulative Separation Factor**
Dissolved Target	$(4.05 \pm 0.04) \times 10^3$	–	–
After Column #1	360 ± 18	601 ± 31	$(6.0 \pm 0.3) \times 10^2$
After Column #2	3.82 ± 0.19	80 ± 6	$(4.8 \pm 0.4) \times 10^4$
After Column #3	0.083 ± 0.008	42 ± 5	$(2.0 \pm 0.3) \times 10^6$

Table 3.3: Summary of ^{nat}Cr reduction throughout the three-part separation method. Metals listed in this table were tested for by MP-AES trace metal analysis. All metals that samples were tested for are included in this table. A final separation factor of radiomanganese from ^{nat}Cr $(2.0 \pm 0.3) \times 10^6$ was observed.

3.2.3 Purity

Trace metal analysis

Trace metal conatmination was measured for three representative ^{52}Mn productions using our optimized target (^{nat}Cr granule pressed in Ag) and separation method (ethanol-based anion exchange). The results are listed in Table 3.4.

Element	Run 1 Mass (μg)	Run 2 Mass (μg)	Run 3 Mass (μg)
Cr	1.07 ± 0.10	0.17 ± 0.02	0.11 ± 0.01
Mn	0.11 ± 0.01	0.23 ± 0.05	0.19 ± 0.01
Fe	0.19 ± 0.02	1.26 ± 0.17	0.72 ± 0.08
Co	0.00 ± 0.01	0.00 ± 0.04	0.00 ± 0.15
Ni	0.00 ± 0.01	0.56 ± 0.16	0.18 ± 0.01
Cu	0.14 ± 0.01	0.04 ± 0.02	0.43 ± 0.06
Zn	3.30 ± 0.33	1.78 ± 0.27	1.10 ± 0.23

Table 3.4: Trace metal analysis of three ^{52}Mn productions using a pressed ^{nat}Cr granule in Ag target and ethanol-based anion exchange radiochemical separation.

Chelation and Effective specific activity

As a first test for bifunctional chelation of Mn to macromolecules, the common chelate DOTA (1,4,7,10 tetraazacyclododecane 1,4,7,10 tetraacetic acid) is an obvious choice due to its ubiquity in radiochemical applications and the reported stability of DOTA chelates with Mn(II) (Bianchi et al., 2001). ^{52}Mn complexation by an excess of DOTA was found to be rapid (<30 minutes) at room temperature under lightly acidic conditions (~pH 3.0-7.0). DTPA was also found to rapid complex ^{52}Mn, although ostensibly with a lower stability compared with DOTA.

Titration of the ^{52}Mn sample against varying concentrations of DOTA resulted in an effective specific activity of up to 2 GBq/μmol. MP-AES trace metal analysis of the final samples are given in Table 3.4. If all transition metal impurities are considered to be competitive for DOTA chelation with equal affinity, reactions at a level of about 4 GBq/μmol are predicted from the data. It is probable that a significant portion of the trace metal impurities come from the large volumes of ethanol involved in the separation

process. For example, we observed iron in the ethanol stock at a concentration of 31 ng/mL, or roughly 5 μg total iron mass in a typical production. An additional in-house distillation of commercial ethanol might be effective in producing metal-free ethanol, reducing impurities in future ^{52}Mn productions.

HPGe Gamma Spectroscopy

Gamma spectroscopy was performed on unseparated (Figure 3.9) and separated ^{52}Mn products. A small ^{51}Cr impurity is observed in the unseparated spectrum, most likely from the ^{52}Cr(p,2n)^{51}Mn$\rightarrow^{51}$Cr route. The 320 keV ^{51}Cr gamma line was not observed in spectra of separated radiomanganese samples for count durations of up to 24 hours with a detector dead time of 1–5%.

Experimentally observed ^{54}Mn impurity levels agree with predicted values from literature nuclear data, with an EoC contamination of ~ 0.4%. Thick target ^{52}Mn and ^{54}Mn production rates from 16 MeV protons are listed in Table 3.5.

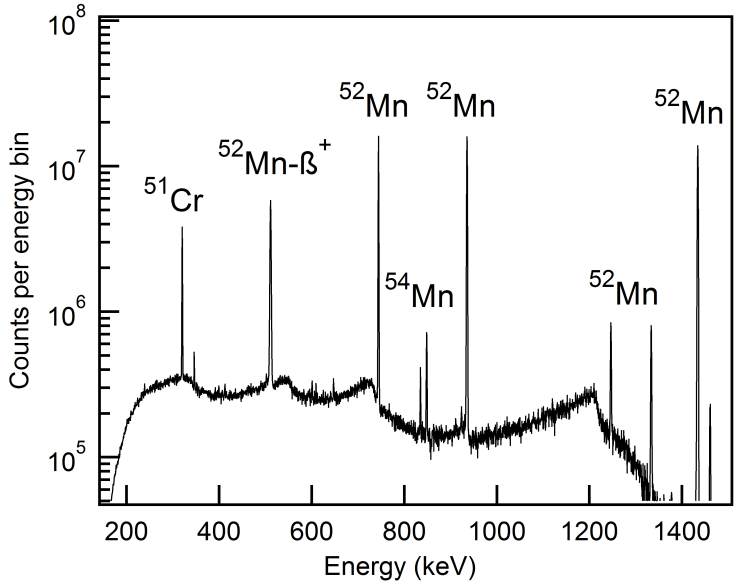

Figure 3.9: An efficiency corrected high-purity germanium (HPGe) spectrum of unseparated target material collected nine days post-irradiation shows minimal ^{54}Mn contamination.

	Experimental	**Predicted**
^{52}Mn Yield	0.256 ± 0.022 mCi/μAh	0.291 mCi/μAh
^{54}Mn Yield	1.14 ± 0.14 μCi/μAh	1.16 μCi/μAh
^{52}Mn Purity	99.55%	99.60%

Table 3.5: Radiomanganese yields and predicted values from literature nuclear data.

3.2.4 Half-life measurement

In order to measure the radioactive half-life of ^{52}Mn a sample of radiochemically isolated ^{52}Mn was placed in a well ionization chamber with data logging capabilities for 19 days. The resulting data was truncated to eliminate short-lived impurities (^{51}Mn, ^{52m}Mn). A two-component exponential function was used to fit the data as shown in Figure 3.10. The known ^{54}Mn impurity was accounted for by constraining one of the two exponentials

with a half life of 312.20(20) d. Perturbations to this constrained value of the half-life of ^{54}Mn revealed that the quantification of the half-life of ^{52}Mn was not sensitive to this constraint. The fitting was weighted by a walking standard deviation (4000 seconds width centered about relevant datum) of the fitting residual. A chi-squared per degree of freedom (χ^2/df) of 1.005 was obtained suggesting the uncertainties used for weighting are slightly underestimated compared to the true variability of the data. The fitting residuals were found to be centered about zero and are uncorrelated with time.

A final ^{52g}Mn half-life measurement of 5.593 $\pm$ 0.005 d (mean $\pm$ SD) was obtained. This agrees well with previous measurements of the half life of ^{52g}Mn (listed below) but does not improve upon their precision.

- 5.60 $\pm$ 0.01 d (Burgus et al., 1954)
- 5.60 $\pm$ 0.01 d (Nagle et al., 1977)
- 5.591 $\pm$ 0.003 d (Yaffe et al., 1977)

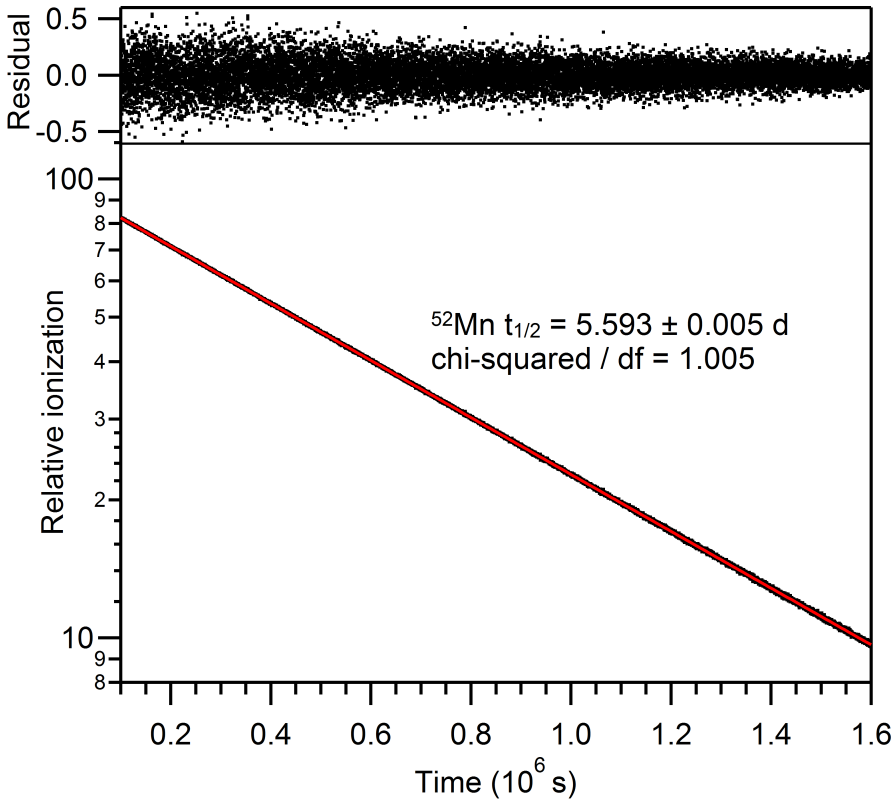

Figure 3.10: Measurement of the radioactive half-life of ^{52g}Mn by well-chamber ionization.

3.3 ^{51}Mn

3.3.1 Introduction

^{51}Mn ($t_{1/2}$: 46.2 min, β+: 97.1%, $E\beta^{+}_{ave}$: 0.96 MeV) has no prominent (>1%) gamma emissions and possesses a half-life which is suitable for clinical studies. One additional consideration though is the dose contributed by the radioactive decay daughter of ^{51}Mn, ^{51}Cr ($t_{1/2}$: 27.7 d) which emits a 320 keV gamma ray in 10% of decays. Although the clinical use of ^{51}Mn appears promising, particularly for pancreatic β cell imaging, there has been little previous work done on producing ^{51}Mn on low-energy medical cyclotrons. Daube et al., produced ^{51}Mn by the ^{50}Cr(d,n) reaction (Daube et al., 1985) for use as a myocardial perfusion tracer, using $^{50}Cr_2O_3$ powder as the irradiation target material. Likewise, Klein et al. produced ^{51}Mn by ^{50}Cr(d,n) but with a ^{50}Cr metal powder target (Klein et al., 2002; Klein et al., 2000). Manufacturing a robust target from enriched $^{50}Cr_2O_3$ powder or ^{50}Cr-metal powder is challenging however, as neither Daube et al., nor Klein et al., were able to exceed 4 μA of irradiation current (Hichwa et al., 1981). Fortunately radionuclically pure ^{51}Mn may also be obtained through the ^{54}Fe(p,α) reaction pathway. To our knowledge, this route has not been previously investigated for the production of clinically relevant quantities of ^{51}Mn. The aims of this work were to (A) develop and characterize ^{51}Mn production methods by ^{54}Fe(p,α), to (B) characterize the in vivo behavior of $^{51}MnCl_2$ in healthy mice, and to (C) evaluate the dosimetric feasibility of clinical ^{51}Mn studies.

3.3.2 Materials and Methods

Materials and Nomenclature

All reagents were obtained from commercial vendors and were used as received unless otherwise stated. Aqueous solutions were constituted in >18 MΩ/cm H_2O. Tissue uptake of radioactivity is specified in standard uptake values (SUV), defined as the product of the percent of injected dose per gram of tissue (%ID/g * 100) and the body weight (g) of the subject. Unless otherwise stated, all values are specified as mean ± standard deviation.

^{54}Fe Target Fabrication and Irradiation

Targets were prepared by electrolytic deposition of isotopically enriched ^{54}Fe metal (<100 mg) on Ag disc substrates (0.5 mm thick, 19 mm diameter), as previously described (Valdovinos et al., 2015; Valdovinos et al., 2016; Vosburgh et al., 1948). Briefly, ^{54}Fe-enriched metal (99.93%, Isoflex USA, San Francisco, CA) was dissolved in 2 - 5 mL of 6 M HCl. To this solution 100 µl of 30% H_2O_2 was added to promote the Fe(III) oxidation state. This solution was taken to near dryness (< 1 mL), before adding 15 mL of saturated ammonium oxalate solution (stock solution stored with ~1g Chelex 100 resin to minimize trace metal impurities). Approximately 100 mg of L-ascorbic acid was added to this solution to promote the reduction of Fe(III) cations. This solution was adjusted to pH ~3.0 using 6 M NaOH or 6 M HCl and transferred to a cylindrical plating cell. The platinum wire anode was positioned approximately 1 cm above the

silver disc substrate, and a potential of 7.0 $\pm$ 0.1 V was applied corresponding to an initial current of 0.09 $\pm$ 0.01 A (115 $\pm$ 13 mA/cm^2). Electrical current and pH were measured at multiple time-points during electrodeposition. 20 μL aliquots of the plating solution were also collected at multiple time-points for Fe-concentration measurements by microwave plasma atomic emission spectroscopy (MP-AES, Agilent Technologies, Santa Clara, CA). When electrodeposition had completed as determined by electrolyte becoming colorless (~24 hours), targets were dried and weighed to determine the plated ^{54}Fe mass.

Targets were irradiated by 16 MeV protons with water-jet cooling on the rear target face. Beam currents of up to 60 μA were applied without changes in target appearance. Following irradiation the short-lived ^{54}Co ($t_{1/2}$: 1.5 min) impurity was allowed to decay for 10 minutes before dismounting the target. Activities were quantified by efficiency-calibrated high-purity germanium (HPGe) gamma spectroscopy, and end of bombardment (EoB) decay correction was performed using the nominal ^{51}Mn half-life (46.2 $\pm$ 0.1 min, 95% confidence interval) (Erlandsson et al., 1970).

Mn(II) / Fe(III) Separation Chemistry

Following irradiation, targets were placed in a cylindrical dissolution cell, whereby an o-ring sealed against the front of the target face around the electrodeposited and irradiated ^{54}Fe material. After the addition of 2 mL of 11M HCl, the reaction vessel was brought to 80 °C. Dissolution was found to be complete in less than 20 minutes.

To this solution 1.8 mL H_2O + 0.2 mL 30% H_2O_2 was added before transferring to a 15 mL (1.5 cm diameter) AG-1x8 strongly-basic anion exchange column which had been equilibrated with ~5 column volumes of 5 M HCl. Using 5 M HCl as mobile phase, the first 5 mL of eluent were discarded. The following 10 mL, containing the ^{51}Mn product, were collected in a pear-shaped rotary evaporator flask. The ^{51}Mn product was taken to dryness under reduced atmosphere, and the resulting $^{51}MnCl_2$ residue was redissolved in ~500 μl of pH 6.5 0.01 M NaOAc buffer. The enriched ^{54}Fe target material was recovered from the separation column in 30-50 mL of 0.1 M HCl, which was subsequently taken to dryness (ferric chloride) by boiling under N_2 gas flow.

The Mn(II) oxidation state following separation was confirmed by thin-layer chromatographic techniques, as previously described (Lewis et al., 2015). Residual Fe impurities in the final ^{51}Mn product were quantified by MP-AES analysis. An effective specific activity was measured by competitive DOTA chelation (room temperature, 0.15 M NaOAc, pH ~6.0, 1 hour) followed by silica thin-layer chromatography (0.25 M NH_4OH). The mass of DOTA required to bind 50% of a sample's activity was interpolated from the resulting sigmoidal binding curve, and effective specific activity was calculated as the amount of activity divided by twice this mass.

Animal Model, PET/CT Imaging

All animal studies were conducted under a protocol approved by the University of Wisconsin Institutional Animal Care and Use Committee. Non-fasted healthy ICR mice

(Envigo, Indianapolis, IN) were divided into two groups. Mice in the first group (n=2) were anaesthetized by isoflurane (4% induction, 1% maintenance), tail-vein catheters were affixed, and mice were placed on the microPET/CT bed in a prone position (Inveon, Siemens Preclinical Solutions, Knoxville, TN). Dynamic PET acquisition was started and $^{51}Mn^{2+}$ was administered in a rapid bolus (3.3 MBq, 200 μl, 10% 0.01 M NaOAc / 90% PBS) through the tail-vein catheter. 60 minutes of dynamic PET data were acquired following $^{51}Mn^{2+}$ administration. Due to the impact of volatile anesthetics on voltage-dependent calcium channel (VDCC) activation (Graves et al., 2016; Diltoer et al., 1988), the second group ($n = 3$) received an intravenous bolus of $^{51}Mn^{2+}$ (1.6 MBq, 200 μl, 10% 0.01 M NaOAc / 90% PBS) while awake. 60 minutes post-injection mice were anaesthetized by isoflurane, CT scans performed, and a 10 minute static PET scan acquired. Following imaging, mice were immediately sacrificed by CO_2 asphyxiation, and organs were extracted. Ex vivo biodistribution measurements were performed by gamma counting.

Dynamic PET data were binned into 46 frames (12x5 s, 6x10 s, 6x30 s, 6x150 s, 6x300 s) and frames were reconstructed using non-scatter-corrected 3D ordered-subset expectation maximization followed by maximum a posteriori reconstruction (OSEM3D/MAP). Static PET data were reconstructed into a single frame by OSEM3D/MAP.

Dosimetry Calculations

Due to the rapid blood clearance of Mn^{2+}, OLINDA (Organ Level INternal Dose Assessment) dosimetry calculations (Stabin et al., 2005) were performed assuming instant compartment localization with organ activity fractions equal to those measured by ex vivo biodistribution herein. Based on the previously measured lengthy organ residence times of Mn^{2+} (Graves et al., 2015), it was also assumed that the effective organ clearance half-life (T_{eff}) was equal to the radioactive half-life of ^{51}Mn ($t_{1/2}$: 46.2 min). It was assumed that ^{51}Mn injections were 100% radionuclidically pure. In regards to the daughter isotope, ^{51}Cr ($t_{1/2}$: 27.7 d), it was assumed that the activity remained in same organ compartments as the parent ^{51}Mn biodistribution without biological clearance. It is possible that ^{51}Cr organ residence times could be obtained by sacrificing mice injected with i.v. ^{51}Mn at late time-points, however this was not performed as a part of this work. Standard radiation weighting factors were used ($\gamma = 1$, $\beta = 1$). Source-organ integrated decays for ^{51}Mn and ^{51}Cr are tabulated in Table B.1. Based on these assumptions, effective dose (ED) and effective dose equivalent (EDE) (units of mSv/MBq) were calculated for a standard adult male and female.

3.3.3 Results

^{54}Fe Target Fabrication and Irradiation Results

Electrodeposition was found to be complete in approximately 24 hours with residual Fe concentration dropping to <0.04 mg/mL (~0.5 mg ^{54}Fe unplated). Changes in plating

metrics are shown in Figure 3.11. The electroplated ^{54}Fe material appeared dark grey in color, rough in texture, and strongly adhered to the Ag substrate. Occasionally slight oxidation could be seen near the periphery of the electroplated area, but this appeared to reduce during target irradiation. Precipitation was observed during pH adjustment in solutions containing greater than ~100 mg of Fe. This may indicate that larger electrolyte volumes are needed in order to produce high-mass targets. Targets were irradiated with up to 60 μA of 16 MeV protons, and no change in target appearance was observed. Targets of thicknesses 46.2–64.4 mg/cm^2 were irradiated by 30 μA of 16 MeV protons for one hour, and end of bombardment (EoB) yield was 1.21–1.66 GBq, as measured by efficiency-calibrated HPGe gamma spectroscopy.

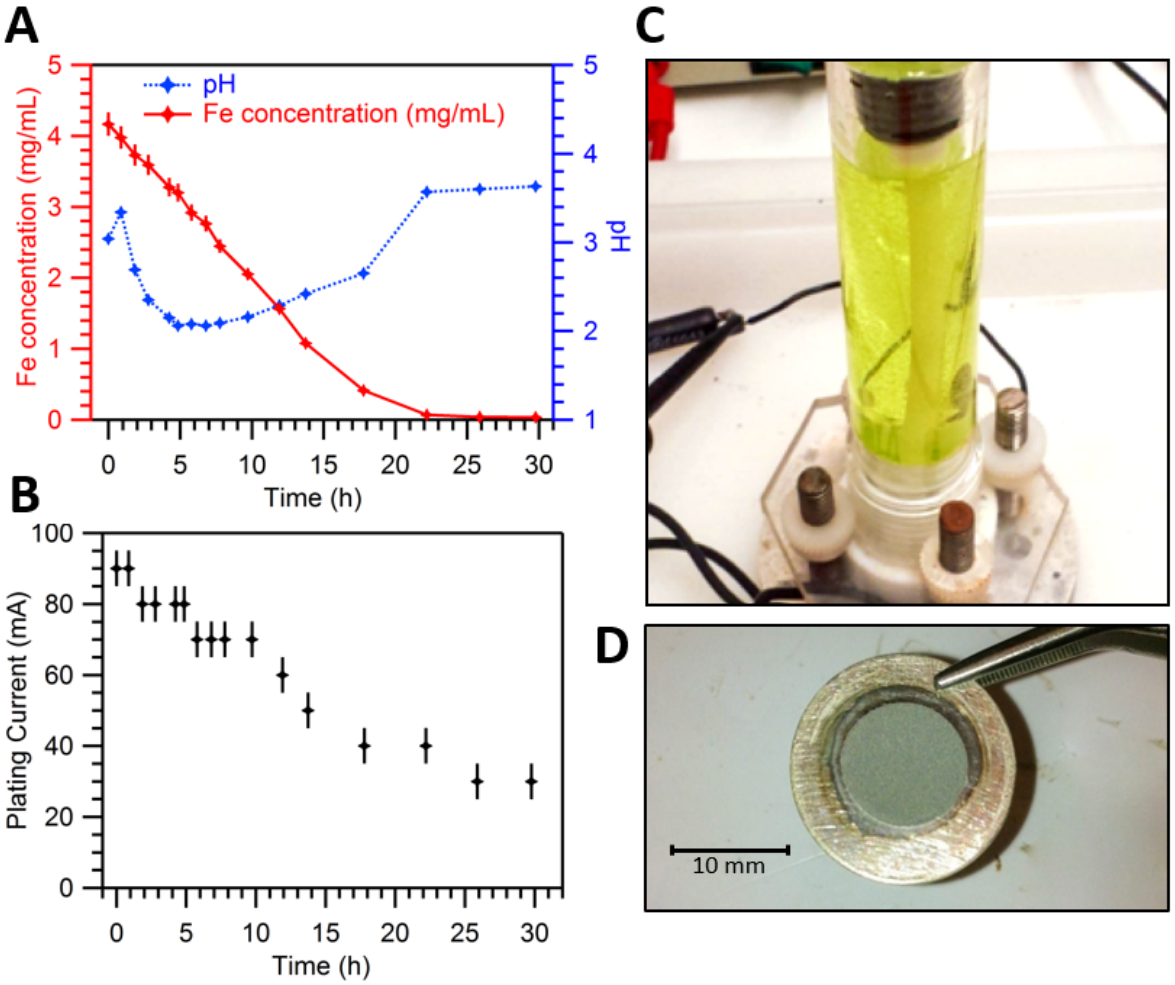

Figure 3.11: (A) Concentration of Fe in electrodeposition solution as a function of time (red) and solution pH as a function of time (blue). Fe concentration was measured by microwave plasma atomic emission spectroscopy (MP-AES). (B) Plating current as a function of time with plating potential held constant at 7.0 ± 0.1 V. (C) Photograph of plating cell at the start of plating. During plating the light green color becomes colorless. (D) Photograph of electroplated ^{54}Fe target on Ag disc substrate.

Trial #	Target Thickness (mg/cm^2)	EoB Yield (GBq)	Final Fe Impurity Mass (μg)	Separation factor
1	64.4	1.66 ± 0.08	8.89 ± 0.08	$(3.92 \pm 0.03) \times 10^3$
2	58.1	1.31 ± 0.07	0.72 ± 0.01	$(3.42 \pm 0.05) \times 10^4$
3	46.2	1.21 ± 0.06	0.043 ± 0.001	$(6.67 \pm 0.15) \times 10^5$

Table 3.6: ^{51}Mn irradiation yields and separation results from three production trials.

^{51}Mn Separation and ^{54}Fe Recovery

Total chemistry duration including dissolution, separation, dry-down, and final formulation was found to be approximately 90 minutes. Decay-corrected ^{51}Mn yield was 67.3 $\pm$ 12.6% ($n = 3$). Recovery yields could be improved by collecting more than 10 mL of eluent at the expense of increased separation and dry-down duration. For targets of thicknesses 46–64 mg/cm^2 ($n = 3$) irradiated by 30 μA of 16 MeV protons for one hour, end of chemistry (EoC) yield was found to be ~185–370 MBq (n=3).

Final Fe impurity masses for three production trials are listed in Table 3.6, along with corresponding separation factors. ^{54}Fe recovery efficiency between productions was found to be 94.3 $\pm$ 4.2% (n=3). The final ^{51}Mn product, decay-corrected to EoB, was found to be >99.9% radionuclidically pure by HPGe gamma spectroscopy with the ^{51}Cr daughter being the largest impurity (0.08%). Trace radionuclidic impurities are listed in Table 3.7. An EoB effective specific activity of 7.4 GBq/μmol (1.9 GBq/μmol at EoC, n=1) was measured by titration with DOTA.

Isotope	**$t_{1/2}$**	**EoB Activity Fraction**	**EoC Activity Fraction**
^{51}Mn	46.2 m	99.91%	99.34%
^{52}Mn	5.59 d	0.00%	0.00%
^{51}Cr	27.7 d	0.08%	0.61%
^{55}Co	17.5 h	0.01%	0.05%
^{56}Co	77.2 d	0.00%	0.00%
^{57}Co	272 d	0.00%	0.00%

Table 3.7: Radionuclidic purity of separated ^{51}Mn product measured by HPGe gamma spectroscopy.

Half-life measurements

During experimentation with ^{51}Mn, we observed that the half-life was shorter than the specified value of 46.2 $\pm$ 0.1 min from the most recent A=51 *Nuclear Data Sheets* evaluation (Xiaolong, 2006). Previous ^{51}Mn half-life measurements (Livingood et al., 1938; Miller et al., 1948; Burgus et al., 1950; Gilbert et al., 1966; Erlandsson et al., 1969; Ferrer et al., 1973) are summarized in Table 3.8. In light of the observed discrepancy from these values, we designed a dedicated experiment to measure the half-life of ^{51}Mn.

^{51}Mn was produced by 16 MeV proton irradiation (GE PETtrace) of isotopically enriched ^{54}Fe (30–60 mg, 99.93% enriched, Isoflex USA), which had been electrodeposited over an area of ~1 cm^2 on 0.5 mm thick, 21 mm diameter Ag discs. ^{51}Mn was radiochemically isolated from the target material by dissolution of the ^{54}Fe material followed by anion exchange chromatography. An aliquot of ^{51}Mn (1–2 MBq in 20-100 μl) was then prepared for spectroscopic measurements.

A high-purity germanium (HPGe, Canberra C1519) gamma detector was calibrated for efficiency and energy response using point sources of ^{241}Am, ^{133}Ba, ^{137}Cs, and ^{60}Co obtained from the National Institute of Standards and Technology (NIST, Gaithersburg, MD, USA) and an in-house quantified point source of ^{152}Eu. Consecutive gamma spectra were for acquired with a ^{51}Mn sample in an unperturbed geometry for 25–60 hours. Acquisition lengths were set to 100 seconds live-time, resulting in 1000–2200 time-points per measurement ($n = 4$). Due to the low branching ratio of the primary gamma emission of ^{51}Mn (749.07 keV, 0.265%), the 511 keV annihilation photon was utilized for half-life

determination. Peak area was calculated by subtraction of an average background continuum determined from bins above and below the peak energy. Sensitivity of the measured half-life to changes in the count durations was evaluated by retrospectively re-binning spectral data into 500 second count durations.

Early spectral acquisitions were associated with up to 7% detector dead-time, resulting in ~107 seconds elapsing (T_{real}) for a 100 second live-time (T_{live}) acquisition. In order to correct for radioactive decay during each acquisition, the initial 511 keV "incidence rate" (I_0) was obtained. If it is assumed that dead-time does not change significantly during a single acquisition, and that the nominal decay constant (λ) is sufficiently close to the true value, then the relationship between N and I_0 is described by Equation 7.1.

$$N = \int_0^{T_{real}} \frac{T_{live}}{T_{real}} I_0 e^{-\lambda t} dt \tag{3.1}$$

Evaluating this integral we obtain:

$$I_0 = \left(\frac{N}{T_{live}}\right)\left(\frac{\lambda T_{real}}{1 - e^{-\lambda T_{real}}}\right) \tag{3.2}$$

For early time-points where dead-time was greater than 5%, this correction for radioactive decay and detector dead-time was 1.33%. For intermediate time-points where dead-time was less than 1% (511 keV peak area still ^{51}Mn-dominated), this corrective factor was reduced to 1.0126. At late time-points where ^{51}Mn had decayed below background levels, the decay constant for ^{55}Co was employed for this correction. During

these late time-points, this correction was found to be less than 0.06%.

Radioactive contaminants were identified by summing the acquired spectra and identifying characteristic gamma emissions. Contaminants with direct contribution to the 511 keV peak included ^{55}Co, ^{56}Co, ^{208}Tl, and ^{106}Ag. Contaminants with indirect contribution to the 511 keV peak through pair production included ^{65}Zn, ^{214}Bi, ^{60}Co, ^{22}Na, ^{40}K, and ^{88}Y. Given that the half-lives of these contaminants are significantly greater than that of ^{51}Mn, the majority are well approximated by linear or constant background fitting components to the 511 keV incidence rate decay curve. ^{55}Co, likely produced from the (p,2n) reaction on ^{56}Fe impurities in the target material, was treated independently in decay fitting due to its shorter half-life and relatively high abundance.

Decay curve least-squares fitting was performed using the model described by Equation 3.13, where A_1, λ_1, A_2, λ_2, M, and C were fitting parameters. To specifically account for the presence of ^{55}Co, λ_2 was constrained to $\ln(2)/(63108\ \text{s})$. Sensitivity of this constraint to the uncertainty in the nominal ^{55}Co half-life was evaluated. Fitting was performed over the full set of data for each run, without temporal truncation.

$$f(t) = A_1 e^{-\lambda_1 t} + A_2 e^{-\lambda_2 t} + Mt + C \tag{3.3}$$

Initial least-squares fitting was weighted by the square-root of the measured 511 keV count-rate divided by the count duration. After this first-pass of curve fitting, fitting was performed weighted by a floating standard deviation of the first-pass fitting residuals. The width of this variance estimation window was nominally chosen to be

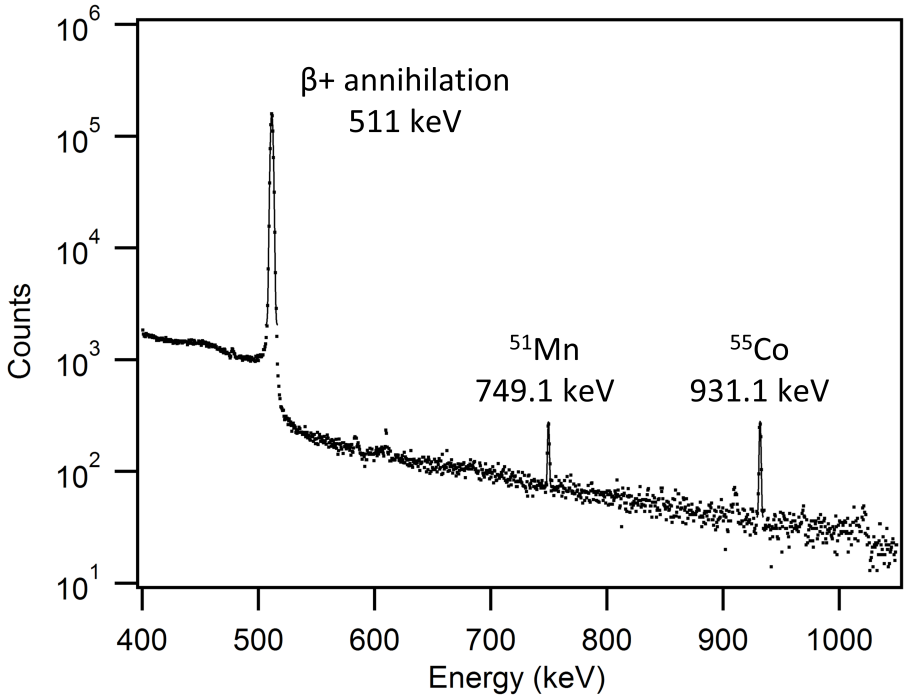

Figure 3.12: Example HPGe gamma spectrum of ^{51}Mn with 3600 second count duration.

3000 seconds, centered at the sample of interest. It is not obvious that this window should be sample-centered, however application of the mean value theorem over 3000 seconds to an approximation of the uncertainty function (square root of count rate) reveals that this is appropriate. Fitting was performed iteratively using this weighting method until changes in obtained fitting parameters were negligible.

To ensure that data were not affected by drift in the digital acquisition clock, the CPU clock was compared against the web-based NIST clock. We observed a maximum drift of -7.6 ± 0.3 seconds in the CPU clock compared with the web-based NIST clock during a 68 hour acquisition. This deviation results in a correction to the measured ^{51}Mn half-life of less than 0.002 min, which is herein considered negligible.

All measurement and statistical uncertainty was assumed to be normally distributed for propagation calculations. All uncertainties in this work are presented as $\pm$ one standard deviation (σ).

An example gamma spectrum is shown in Figure 3.12 and a representative decay curve and corresponding fit are shown in Figure 3.13. A final ^{51}Mn radioactive half-life value for ^{51}Mn of 45.59 ± 0.07 min was obtained. Results from individual measurements are listed in Table 3.9, and the final result is compared against literature values in Table 3.8.

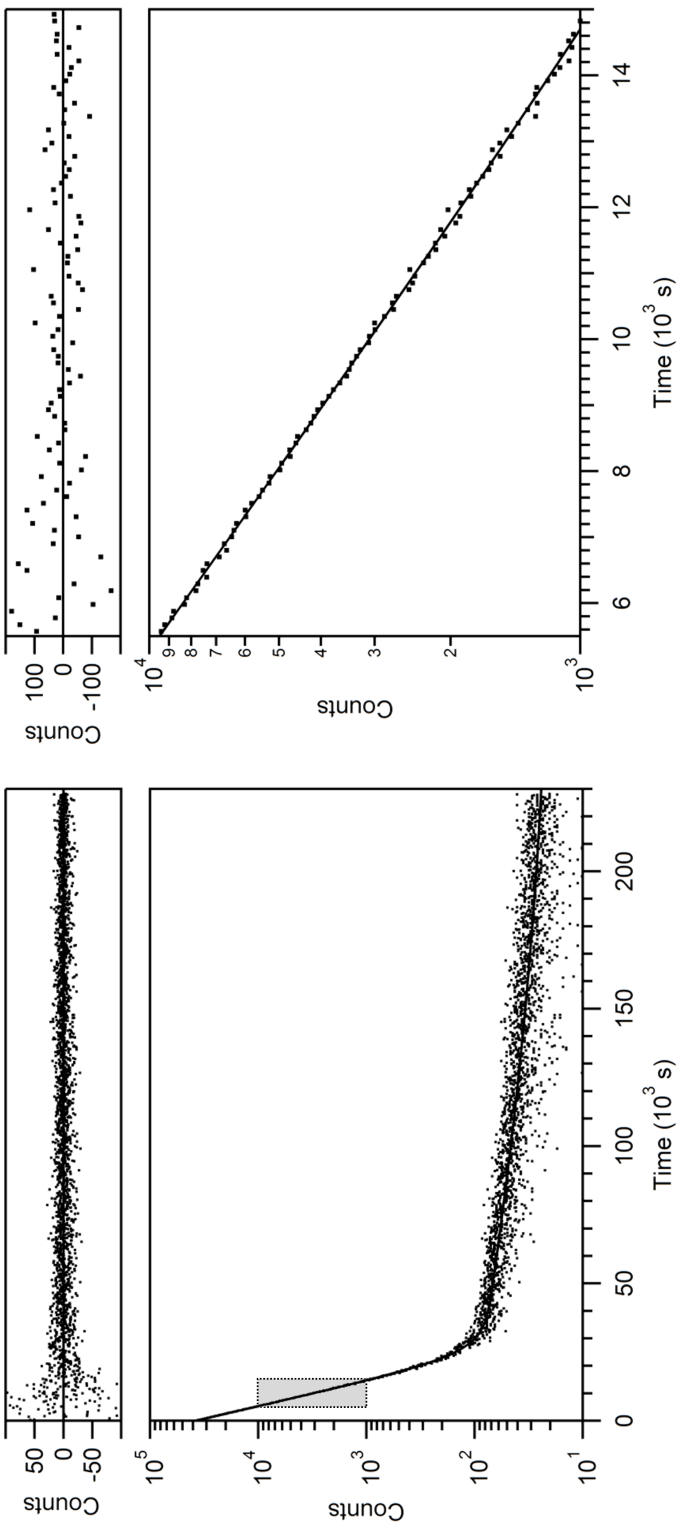

Figure 3.13: Decay curve fitting for one representative measurement and associated fitting residuals. Serial spectroscopic measurements were acquired over approximately 230,000 seconds and the 511 keV peak fit by a two-component exponential and linear component decay curve. The right plot shows a subset of the full data set, over one decade of ^{51}Mn decay, indicated by the rectangle in the left plot.

Reference	$t_{1/2} \pm \sigma$ (min)
Livingood, 1938	46 ± 2
Miller, 1948	45
Burgus, 1950	44.3 ± 0.5
Gilbert, 1966	46.5 ± 0.2
Erlandsson, 1969	46.2 ± 0.1
Ferrer, 1973	$[46.2 \pm 0.1]^{a}$
This work	45.59 ± 0.07

Table 3.8: Previous measurements of the radioactive half-life of ^{51}Mn, including the result from this work. [a]Authors state that their measurement is “in agreement with" Erlandsson et al..

Measurement	$t_{1/2} \pm \sigma$ (s)	χ^2/dof
1	45.63 ± 0.06	1.004
2	45.56 ± 0.04	0.995
3	45.53 ± 0.04	1.001
4	45.66 ± 0.04	0.992
Average	45.59 ± 0.07	–

Table 3.9: ^{51}Mn half-life measurements in this work.

This obtained half-life value does not agree with the most precise previous measurement, made by Erlandsson et al. in 1969, of 46.2 ± 0.1 min, which is also the currently accepted value. In their work, Erlandsson et al. produced radioisotopically pure ^{51}Mn by ^{50}Cr(p,γ), and performed serial annihilation photon spectroscopic measurements — NaI(Tl) detector, 400–600 keV window — over approximately 6600 seconds. A single-component exponential model was used for decay fitting, which ignored contributions from background contaminants, such as the annihilation photons following pair production from the 1461 keV ^{40}K γ-emission.

Without considering other possible confounding factors, a plausible explanation for

the shorter half-life result obtained herein is the presence of ^{52m}Mn in our radioactivity samples, however the 1434 keV characteristic ^{52m}Mn γ-emission was not observed.

In order to investigate this discrepancy, a truncated set of our data was created (0 – 20,000 s) and was fit to a single-component exponential model. The half-life result from this fitting (46.13 $\pm$ 0.04 min) is in excellent agreement with the literature value of 46.2 $\pm$ 0.1 min. However, if we fit this truncated data set to the full model described by Equation 3.13 constraining A_2, λ_2, M, and C to values obtained from fitting the full data set, a ^{51}Mn half-life value of 45.70 $\pm$ 0.04 min is obtained, which is in agreement with the value reported here. This constrained fit on data from t = 0 – 20,000 s also qualitatively improved the “goodness of fit" from 15,000 – 20,000 s compared with the unconstrained fit.

The robustness of radioisotopic impurity quantification in our regression model was examined. The most significant impurity, ^{55}Co, was quantified by fitting the decay of its characteristic 931 keV gamma over the collected serial spectra. ^{55}Co radioactivity at t $= 0$ was quantified by correcting for branching ratio and detector efficiency. This secondary quantification was in excellent agreement with the ^{55}Co radioactivity quantification obtained from the A_2 fitting parameter in 511 keV fitting, 12.8 $\pm$ 1.1 kBq and 12.3 $\pm$ 0.8 kBq respectively. This suggests that explicit fitting of ^{55}Co in the 511 keV regression model is appropriate and robust.

^{51}Mn half-life measurements did not depend strongly on the constrained half-life of ^{55}Co in decay curve fitting. Perturbing the constrained half-life of ^{55}Co (nominally

17.53 $\pm$ 0.03 h) for one measurement dataset by 10% to 15.77 h or 19.28 h results in a change to the measured ^{51}Mn half-life of less than 0.0002%. Furthermore, ^{51}Mn half-life measurements were not sensitive to changes in count duration. Retrospectively re-binning the acquired spectra into 500 second count durations resulted in no significant change to the measured half-life values.

In summary the half-life of ^{51}Mn has been measured to be 45.59 ± 0.07 min. This is the most precise measurement to date, and disagrees with the Nuclear Data Sheets (NDS) value by over 6σ. Due to the improved fitting model and data acquisition duration in this work, we believe that this measurement is more accurate than previous literature values.

PET results

Rapid ^{51}Mn accumulation in the heart, liver, kidneys, pancreas, and salivary glands were observed in ICR mice (n=5) following a rapid intravenous bolus injection. PET time-activity curves (TACs) are shown in Figure 3.14, and tabulated data is listed in Appendix A. Following initial distribution (< 1 min), uptake was observed to be stable over 30 minutes of PET imaging, which is consistent with previous findings employing $^{52g}Mn^{2+}$ (Graves et al., 2015; Hernandez et al., 2016; Brunnquell et al., 2016). A heart blood-pool clearance half-life of 7.7 $\pm$ 0.7 seconds was determined by weighted exponential least squares regression of the heart TAC from 0.375 to 3.25 minutes post-injection.

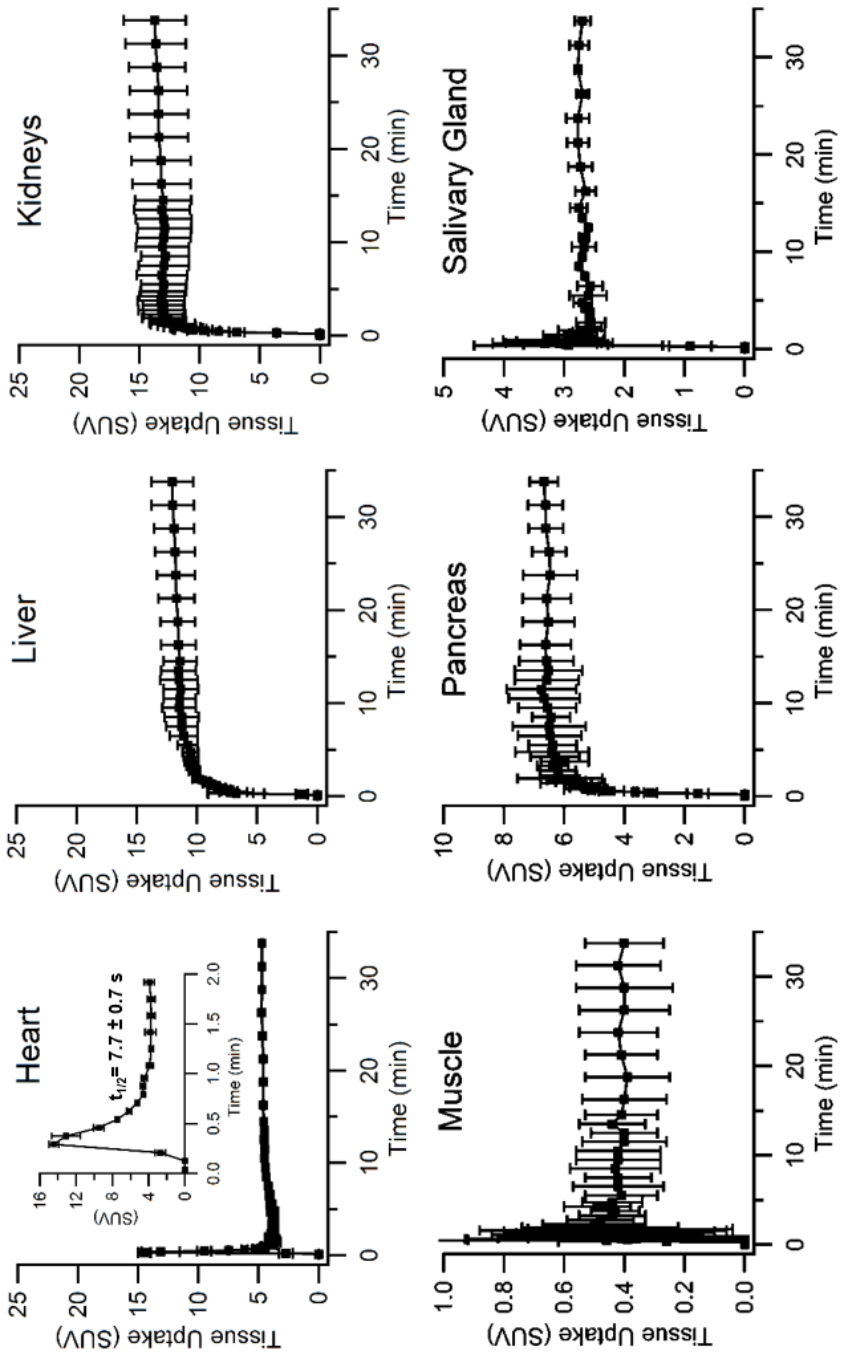

Figure 3.14: Dynamic PET time-activity curves (TACs) of organ ROIs in ICR mice (n=2, mean ± SD) injected with a rapid intravenous bolus of ^{51}Mn(II), imaged for 30 minutes post-injection.

Delineation of the pancreas from the surrounding organs (e.g. kidneys) was readily

achieved in static PET images (Figure 3.15A). PET ROI quantification (Figure 3.15B) and ex vivo biodistribution by gamma counting (Figure 3.15C) show little activity in the muscle and blood, which is consistent with results from dynamic PET imaging. Tabulated PET and ex vivo biodistribution data are listed in Appendix B. Ex vivo biodistribution shows highest ^{51}Mn uptake in the kidneys (9.2 $\pm$ 0.7 SUV), followed by the pancreas (7.0 $\pm$ 1.3 SUV) and the heart (5.6 $\pm$ 1.8 SUV). Comparing dynamic PET subjects (n = 2, I.V. $^{51}MnCl_2$ bolus under isoflurane) with static PET subjects (n = 3, I.V. $^{51}MnCl_2$ non-anaesthetized) reveals significantly higher kidney uptake in anaesthetized dynamic PET subjects, 13.7 $\pm$ 2.6 vs. 7.7 $\pm$ 1.1 ($p = 0.03$).

Good agreement was observed between in vivo PET quantification and ex vivo gamma counting in all tissues with the exception of the heart. As tissues are rinsed and patted dry prior to weighing and gamma counting, this discrepancy in measured heart uptake is likely due to the inclusion of low-activity blood mass in heart PET ROIs. Intersubject biodistribution variability was found to be minimal when using the SUV uptake metric despite highly varied subject weights (37.6, 48.3, and 22.1 g). As expected, greater intersubject biodistribution variability was observed when using the %ID/g uptake metric.

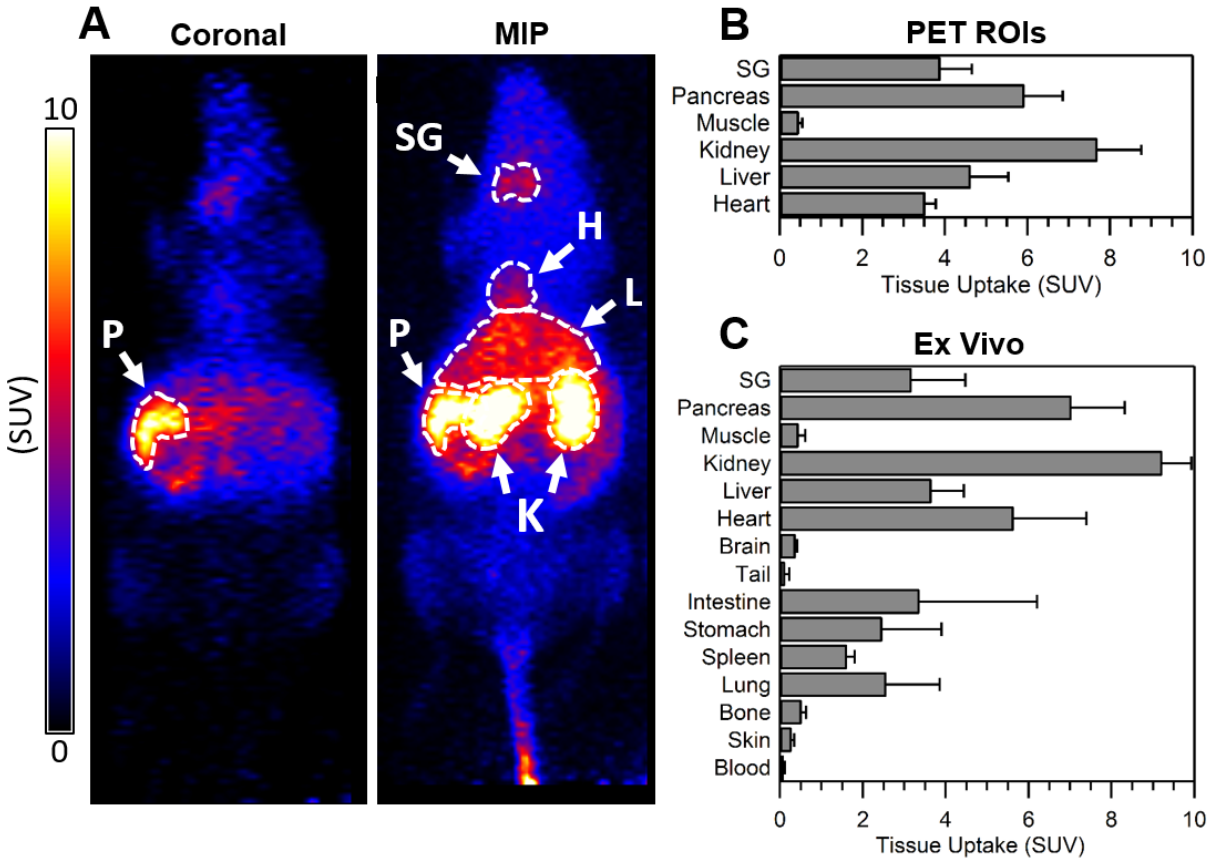

Figure 3.15: (A) Coronal slice and maximum intensity projection (MIP) static PET images of a representative ICR mouse injected intravenously with ^{51}Mn(II) (non-anaesthetized during injection). PET images were acquired one hour post-injection. Pancreas (P), salivary gland (SG), heart (H), liver (L) and kidneys (K) indicated by arrows. (B) ^{51}Mn tissue uptake quantification of hand-drawn PET ROIs in ICR mice (n=3, mean ± SD) injected with a rapid intravenous bolus of ^{51}Mn(II). (C) Ex vivo ^{51}Mn biodistribution in ICR mice (n=3, mean ± SD) immediately following PET imaging, measured by gamma counting.

Dosimetry Calculation Results

^{51}Mn was found to have an EDE of 0.0362 mSv/MBq and 0.0422 mSv/MBq for the standard male and female human model respectively. The daughter isotope ^{51}Cr was found to have an EDE of 0.267 mSv/MBq and 0.324 mSv/MBq for the standard male and female model respectively. OLINDA dosimetry predictions for a typical clinical

dose (370 MBq, 10 mCi) are listed in Table 3.10.

Contribution	Male (mSv)	Female (mSv)
^{51}Mn	13.4	15.6
^{51}Cr	0.11	0.14
Total	13.5	15.8

Table 3.10: Effective dose equivalent (EDE) for a 370 MBq intravenous injection of radionuclidically pure $^{51}Mn^{2+}$ in the standard adult human male and female.

3.3.4 Discussion

Manganese is an essential trace element in mammalian biology (Santamaria et al., 2010) and has many prospective applications as an imaging agent in medicine. Of the three positron-emitting isotopes of manganese, ^{51}Mn is best suited to clinical PET based on decay characteristics, which are detailed in Table 3.11. Robust methods for the preparation of ^{51}Mn are essential to the investigation of basic science and clinical questions relating to the biological role of manganese in disease.

	^{51}Mn	^{52m}Mn	^{52g}Mn
Half life	46.59(7) min	21.1(2) min	5.591(1) d
β^+ Branch	97.08(7)%	96.6(6)%	29.4(4)%
β^+ Mean Energy	962.8(10) keV	1172(9) keV	242(5) keV
Gamma Energies and Branching Ratios	749 keV, 0.26% 1148 keV, 0.078% 1164.4, 0.076% 2001 keV, 0.037% 603.5 keV, 0.015%	1434 keV, 98.3% 378 keV, 1.7% 1728 keV, 0.216% 1531 keV, 0.046% 1334 keV, 0.029%	1434 keV, 100.0% 936 keV, 94.5% 744 keV 90.0% 1334 keV, 5.07% 1246 keV, 4.21%

Table 3.11: Decay characteristics of ^{51}Mn, ^{52m}Mn, and ^{52g}Mn.

To our knowledge, this work constitutes the first attempt at ^{51}Mn production via ^{54}Fe(p,α) and radiochemical isolation in clinically-relevant quantities. Cross sections for this production route are shown in Figure 3.16, peaking at approximately 45 mb at ~18 MeV. A thick target for this reaction (16 MeV → 10 MeV p^+) would be approximately 250 g/cm^2. The electrodeposition method described here has proved effective for the quantitative reduction of ^{54}Fe(III) to ^{54}Fe-metal, with the electroplated Fe metal being strongly adhered to the Ag disc substrate. From Figure 3.11A, it may be inferred that ^{54}Fe(III) reduction follows zero-order kinetics for the majority of the plating duration. This suggests that plating time may vary depending on the ^{54}Fe mass in solution. The plating solution pH was found to be highly variable during electrodeposition, with the solution rising above pH 3.0 upon completion. This acute rise in pH near plating completion may enable non-colorimetric automation methods.

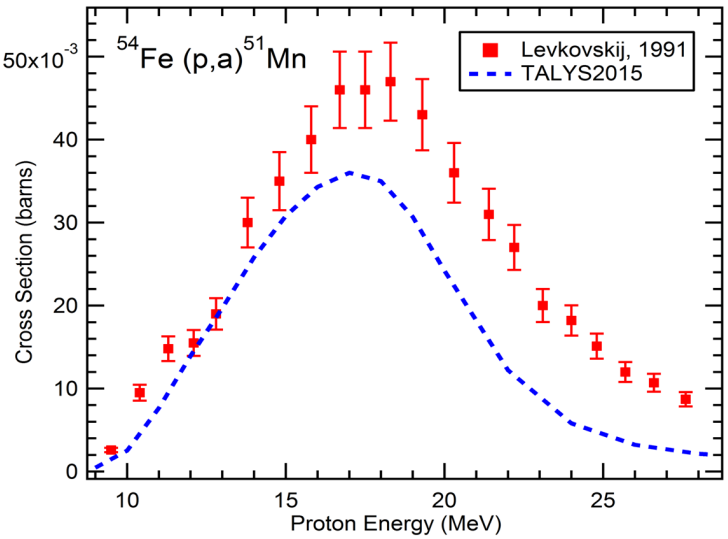

Figure 3.16: TALYS predictions and empirical (Levkovski et al., 1991) measurements of the ^{54}Fe(p,α)^{51}Mn excitation function.

The fabricated ^{54}Fe targets were robust, withstanding relatively high beam currents (16 MeV, 60 μA) without changes in appearance. The target thicknesses (~45–65 mg/cm^2) and irradiation parameters (30 μA for 1 h) used in this work were sufficient to provide enough EoC activity (~185–370 MBq) for several small animal studies or approximately one human study. EoC yield could readily be increased to 1.5–2.0 GBq by employing target thicknesses of approximately 100 mg/cm^2 and irradiating with a beam current of 60 μA for 2 hours. Based on these yields, a total chemistry duration of ~90 minutes is sufficiently short for production purposes. However at institutions without solid-target capabilities, a solution-target of $^{54}Fe(NO_3)_2$ or $^{50}Cr(NO_3)_3$ could provide alternative production routes. Although the chemical isolation of ^{51}Mn from bulk Fe metal is simpler than ^{51}Mn from bulk Cr, the production cross section for ^{50}Cr(d,n) is significantly higher than ^{54}Fe(p,α) which may help compensate for the reduced target atomic fraction (Klein et al., 2000; Cogneau et al., 1966; Levkovski, 1991).

PET imaging of pancreatic beta cells with $^{51}MnCl_2$ appears promising due to the rapid blood clearance and significant pancreatic accumulation. Further studies are needed to determine the feasibility and optimal study methodology for beta cell mass quantification by ^{51}Mn-PET. To this end, non-specific exocrine uptake could possibly be quantified by co-injection of VDCC blocking agents such as nifedipine. Furthermore, serial studies are warranted for monitoring the decline in beta cell mass in a streptozotocin-induced mouse model of type-I diabetes (Like et al., 1976; Deeds et al., 2011). Other positron-emitting divalent metals such as $^{63}Zn^{2+}$ ($t_{1/2}$: 38.5 min β+: 92.7%, Eβave= 0.92 MeV)

may also prove useful for beta cell related investigations, as VDCCs are permeable to Zn^{2+} and significant ^{63}Zn pancreatic uptake has been observed in mice by Degrado et al. (DeGrado et al., 2014; Engelbrecht et al., 2013, Lubag et al., 2011).

The heart blood-pool clearance half-life of $^{51}Mn^{2+}$ found in this work (7.7 ± 0.7 s) is astonishingly rapid, suggesting first-pass tissue localization kinetics. It is likely that this measured clearance half-life significantly differs from a true blood clearance half-life, as the assumption of uniformly-distributed tracer within the blood pool is likely inaccurate with such rapid clearance kinetics. Rapid blood clearance and stable accumulation offers experimental flexibility with regards to PET imaging duration and timing following tracer administration. Tracer kinetics such as these also support the use of the SUV uptake metric for ^{51}Mn-PET studies, as tracers without significant tissue clearance, i.e. [^{18}F]-FDG, lend themselves well to such analytic methods. Furthermore, the rapid blood clearance of ^{51}Mn may enable multiple-injection protocols within a single patient study. Techniques such as these may prove useful in beta cell mass (BCM) quantification studies for the subtraction of non-specific exocrine pancreas uptake by stimulation or blocking (i.e. glibenclamide or nifedipine) of beta cell VDCCs following baseline imaging. On the other hand, the pulsatile nature of calcium transport (Hellman et al., 1994; Rorsman et al., 2003) may increase test-retest variability for bolus injection techniques. This effect could possibly be mitigated by administering $^{51}MnCl_2$ as an intravenous infusion over 5–15 minutes.

The mean positron energy emitted during the decay of ^{51}Mn (962 keV) is significantly

higher than that of ^{18}F (250 keV) or ^{52g}Mn (242 keV) which leads to poorer spatial resolution in PET images. Regardless the resolution of ^{51}Mn has still proven to be sufficient for whole-organ-ROI microPET studies, and positron range is not typically the limiting factor of clinical PET resolution (Sanchez-Crespo et al., 2004).

^{51}Mn dosimetry appears favorable, even when accounting for the long-lived daughter ^{51}Cr, and making the conservative assumption that this daughter is not biologically excreted. In this work, a cumulative effective dose equivalent of ~15 mSv for a 370 MBq ^{51}Mn PET study was calculated. This result is comparable to the average dose for an [^{18}F]-FDG study of 14.1 mSv (Mettler et al., 2008). This suggests that it would be possible to perform up to three repeat PET studies in healthy or type-I diabetic volunteers without exceeding the annual non-stochastic International Commission on Radiological Protection (ICRP) limit of 50 mSv for research subjects (Huda et al., 1989; ICRP, 2007).

3.3.5 Conclusion

Methods for the efficient production and isolation of ^{51}Mn by $^{54}Fe(p,\alpha)$ followed by anion exchange chromatography have been described. Initial $^{51}MnCl_2$ pharmacokinetic characterization in mice and predicted human dosimetry show promise for a variety of PET applications, including VDCC activation imaging in pancreatic beta cells.

3.4 ImmunoPET

The extension of ^{52}Mn to bioconjugated antibody imaging requires sufficiently high specific activity ^{52}Mn in a state suitable for macromolecule labeling. Using the previously described ethanolic anion exchange radiochemistry methods, effective specific activities by DOTA chelation of up to 0.05 Ci/μmol were obtained. The goal of this work to investigate the potential of ^{52}Mn-immunoPET using the well established preclinical TRC105 model, an anti-CD105 mAb.

To summarize, ^{52}Mn was produced by 60 μA, 16 MeV proton irradiation of natural chromium metal pressed into a silver disc support. Radiochemical separation proceeds by strong anion exchange chromatography of the dissolved Cr target, employing a semi-organic mobile phase, 97:3 (v:v) ethanol: HCl (11M, aqueous). The method was $62 \pm 14\%$ efficient ($n = 7$) in ^{52}Mn recovery, leading to a separation factor from Cr of $(1.6 \pm 1.0) \times 10^6$ (n = 4), and an average effective specific activity of 0.8 GBq/μmol ($n = 4$) in titration against DOTA. ^{52}Mn-DOTA-TRC105 conjugation and labeling demonstrate the potential for chelation applications. In vivo images acquired using PET/CT in mice bearing 4T1 xenograft tumors are presented. Peak tumor uptake was 18.7 ± 2.7 %ID/g at 24 hours post injection and ex vivo ^{52}Mn biodistribution validates the in vivo PET data. Free $^{52}Mn^{2+}$ (as chloride or acetate) was used as a control in additional mice to evaluate the non-targeted biodistribution in the tumor model.

3.4.1 Introduction

^{52}Mn may offer advantages over traditional ^{64}Cu or ^{89}Zr immunoPET in situations where treatment response monitoring at late time-points (2-3 weeks) is desired. In cases where radioimmunotherapy is initiated with long-lived nuclides such as ^{177}Lu, the full time-course of treatment could be monitored by ^{52}Mn PET. Further, due to the abundance of coincident high energy gamma rays, ^{52}Mn is one of relatively few nuclides that can be used in third-gamma coincidence PET for either dual nuclide event tagging or combined Compton telescope PET tomography (Lang et al., 2014). Despite this, clinical translation should proceed with caution due to the preponderance of coincident high energy gammas: 744 keV (90%), 935 keV (95%) and 1434 keV (100%). Coupled with the myriad biological roles of manganese, which may lead to prolonged retention of radiomanganese in critical organs, careful dosimetry prior to translation should be considered.

Because the long physical half-life of ^{52}Mn ($t_{1/2}$: 5.591 days) lends itself well to the long biological circulation times in radioimmunoPET applications, a demonstration of the stable chelation of ^{52}Mn using bifunctionalized DOTA conjugated to a monoclonal antibody proves the usefulness of ^{52}Mn as a radiotracer. For this study TRC105, a chimeric human/murine immunoglobulin G (IgG1) monoclonal antibody (mAb) which binds to the angiogenic marker CD105 with very high specificity, was chosen as the model compound due to the extensive body of data available that describes its biodistribution with other radiometals and chelates (Engle et al., 2012; Hong et al., 2012; Zhang et al.,

2011). This antibody is currently associated with seventeen phase I and II multi-center clinical trials which are planned, underway, or already completed investigating the therapeutic efficacy in a variety of solid tumors either alone or as an adjunct to other treatment techniques.

The purpose of this report is to describe a methodology for the production and purification of ^{52}Mn that is amenable to bioconjugate chemistry. A simple cyclotron target made of chromium metal is described, and the procedure for extracting ^{52}Mn from the Cr matrix is given. The chemical purity of the produced ^{52}Mn is demonstrated by trace metal analysis and chelation with DOTA. Finally, the suitability of DOTA as a bifunctional chelate for Mn is investigated by in-vivo experiments of ^{52}Mn-DOTA-TRC105 in 4T1 xenograft-bearing mice, and comparison with the biodistribution of weakly coordinated $^{52}Mn^{2+}$. To our knowledge, the formation of ^{52}Mn-DOTA-TRC105 constitutes the first bioconjugate radiomanganese PET agent, and acts as a benchmark of the purity of ^{52}Mn required for targeted PET.

3.4.2 Methods

Materials

All reagents were obtained from commercial vendors and were used as received unless otherwise stated. TRC105 (mAb) was provided by TRACON Pharmaceuticals Inc. 4T1 murine breast cancer cells were obtained from the American Type Culture Collection (ATCC). Aqueous solutions were constituted in >18 MΩ/cm water. Unless noted, the

term HCl refers to 32-35% aqueous hydrochloric acid Ethanol-HCl mixtures were made in v:v proportion using ethanol (molecular biology grade, Sigma Aldrich) and 32-35% aqueous HCl (untitrated, Optima grade, VWR).

Preparation of "Free $^{52}Mn^{2+}$" Injections

Eluted ^{52}Mn fractions were taken to dryness under reduced atmosphere at 70 °C to remove H^+ ions and EtOH contamination. $^{52}MnCl_2$ injections were prepared by reconstituting the dried ^{52}Mn in phosphate-buffered saline and ^{52}Mn-Acetate injections were prepared by reconstituting the dried ^{52}Mn in pH 7.5 0.1 M NaOAc.

DOTA-TRC105 Conjugation and ^{52}Mn Labeling

A solution containing TRC105 was adjusted to pH 8.5-9.0 with 0.1 M Na_2CO_3. p-SCN-Bn-DOTA (Macrocyclics) previously dissolved in DMSO was added to this solution in a 25:1 (DOTA : TRC105) molar ratio. Following this addition, the pH was measured and adjusted to pH 8.5-9.0 with Na_2CO_3. The conjugation reaction was allowed two hours to complete at room temperature before DOTA-TRC105 was purified by size exclusion chromatography (PD-10, GE-Healthcare) using phosphate-buffered saline (PBS) mobile phase.

2-3 mCi of ^{52}Mn in ~200 μl 0.1 M HCl was added to 500 μl 0.1 M pH 4.5 NaOAc. To determine the appropriate quantity of DOTA-TRC105, labeling was initially tested with 100, 250, 500 and 1000 μg/mCi. ^{52}Mn labeling with these samples was monitored by radio-TLC using 50 mM pH 4.5 EDTA mobile phase over the course of one hour at room

temperature. TLC peak discrimination was used to distinguish between bound and unbound ^{52}Mn, and peak integration was used for quantification following a background subtraction.

For animal experiments, 150 μg of DOTA-TRC105 per mCi ^{52}Mn was added to the buffered activity solution and allowed to react for 60 minutes at 37 °C. After labeling, EDTA was added such that the resulting concentration was 1 mM. Labeling yield was quantified by radio-TLC, and the ^{52}Mn-DOTA-TRC105 was purified by size exclusion chromatography using PBS mobile phase. The resulting fraction was collected and passed through a 0.2 μm syringe filter prior to in vivo experiments.

Imaging and Biodistribution Studies

Mice were anesthetized with 2% isofluorane and 60-120 μCi of ^{52}Mn-DOTA-TRC105 ($n = 3$), $^{52}MnCl_2$ ($n = 2$), or ^{52}Mn-Acetate ($n = 2$) was injected by tail vein in a rapid bolus. PET/CT imaging was performed (Inveon microPET/CT, Siemens Inc.) at five time-points between 4 and 128 hours in the ^{52}Mn-DOTA-TRC105 group, and five time-points between 4 and 96 hours in the $^{52}Mn^{2+}$ control groups with at least 40 million coincident counts per PET acquisition. Static images were reconstructed using OSEM3D.

Following the last PET time-point, each animal was sacrificed. In addition to a blood draw, samples from the following tissues were extracted, washed in saline, and weighed: 4T1 tumor, skin, muscle, bone (femur, inferior half), heart, lung, liver, kidney, spleen, pancreas, stomach, intestine, tail, brain, and salivary gland. ^{52}Mn activity in each sample

was measured by auto-gamma counting (Wizard 2480, PerkinElmer).

The results of both PET region of interest (ROI) and ex vivo biodistribution quantitative analysis were expressed as percent of the injected dose per gram of tissue (%ID/g ± SD).

3.4.3 Results and Discussion

TRC105 conjugation, labeling, imaging, and biodistribution

A lower average ^{52}Mn-DOTA effective specific activity of 0.8 GBq/μmol compared to that of the typical ^{89}Zr-DFO assay (~30 GBq/μmol) motivated an increase in the bifunctional-chelate to antibody ratio (25:1) during conjugation. The resulting DOTA-TRC105 had excellent radiolabeling properties as shown in Table 3.12. 150 μg/mCi of DOTA-TRC105 was sufficient to reach ^{52}Mn complexation efficiencies greater than 95% after 60 minutes at 37 °C.

mAb mass (μg/mCi)	**20 min**	**40 min**	**60 min**
100	85%	89%	95%
250	98%	93%	99%
500	99%	95%	98%
1000	99%	93%	100%

Table 3.12: Radiolabeling efficiency of ^{52}Mn-DOTA-TRC105 as a function of antibody mass and time as measured by thin layer chromatography. Reactions took place at 37 °C in a pH 4.0-4.5 0.1 M NaOAc solution.

Injections of ^{52}Mn-DOTA-TRC105 were administered to Balb/c mice bearing 4T1 xenografts and PET data were collected. MIP PET images are shown in Figure 3.17. ROI quantification of the ^{52}Mn-DOTA-TRC105 PET images yielded the time activity curves

shown in Figure 3.18. Finally, the ex vivo biodistribution results shown in Figure 3.19 confirm the accuracy of image-based ROI quantification.

Tumor uptake peaked at the 24-hour PET time-point with an average value of 19 $\pm$ 3 ID/g ($n = 3$). The ^{52}Mn-DOTA-TRC105 time activity curves measured in this work agree well with those seen with ^{89}Zr-labeled TRC105 via desferrioxamine in the same animal and xenograft model (Hong et al., 2012) indicating a stable conjugate. Furthermore the increased DOTA conjugation ratio does not seem to perturb CD105 binding affinity. When comparing the ex vivo biodistribution of ^{89}Zr-DF-TRC105 to ^{52}Mn-DOTA-TRC105 the most significant difference is the slower blood clearance rate of ^{52}Mn-DOTA-TRC105 to ^{89}Zr-Df-TRC105. Assuming the same conjugate distribution, dosimetrically, ^{52}Mn is less favorable for injection compared to ^{89}Zr for immunoPET (see supplemental materials). However in some instances the higher dose from ^{52}Mn may be justified for longer-term scanning, or its use in novel triple coincidence PET cameras.

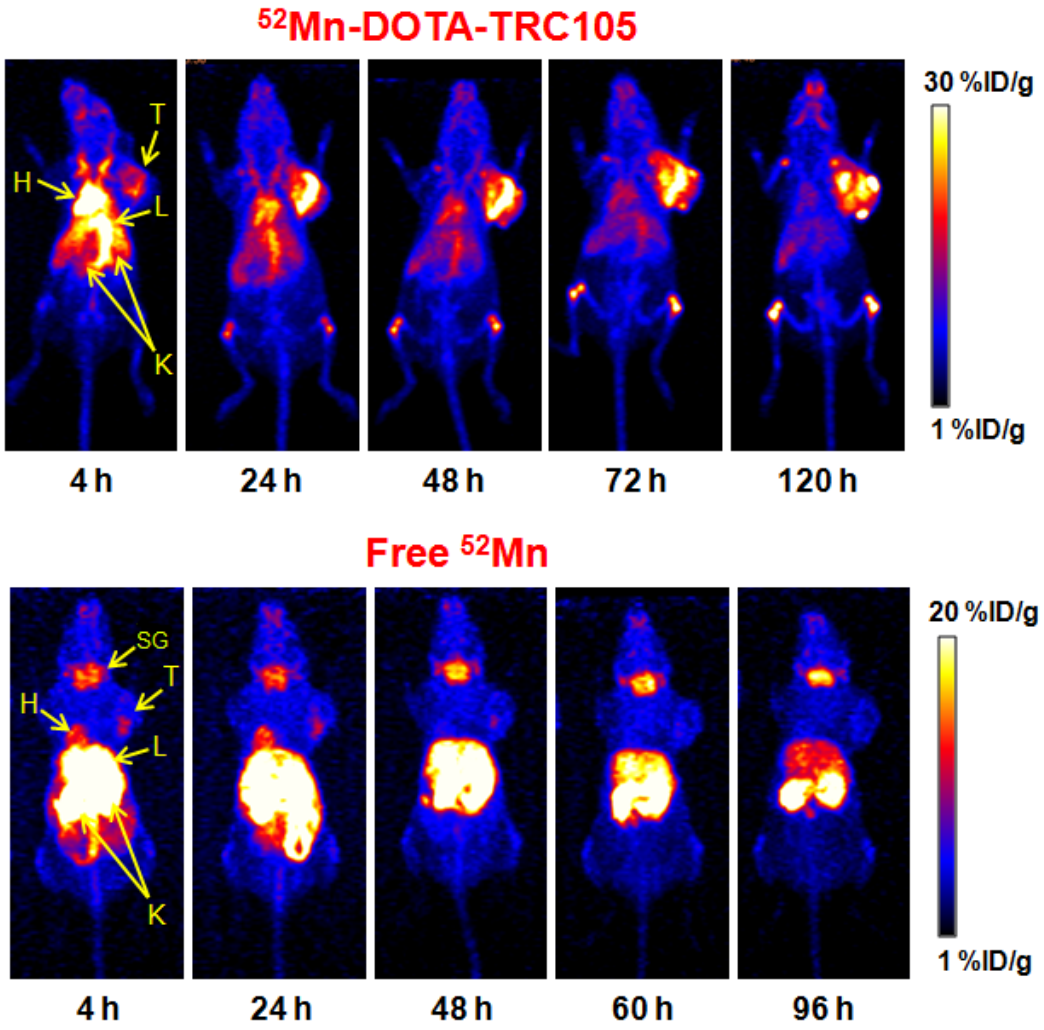

Figure 3.17: Serial maximum intensity projection (MIP) PET images of mice injected with ^{52}Mn-DOTA-TRC105 and $^{52}MnCl_2$. Significant salivary gland accumulation in the $^{52}MnCl_2$ images contrasting the lack of uptake in the ^{52}Mn-DOTA-TRC105 images indicates highly stable DOTA chelation of $^{52}Mn^{2+}$ even at late time-points. Note, H: Heart, L: Liver, K: Kidneys, T: Tumor, SG: Salivary glands. Significant accumulation was also observed in the pancreas for free ^{52}Mn images, but this is not readily visible on a MIP with this %ID/g window.

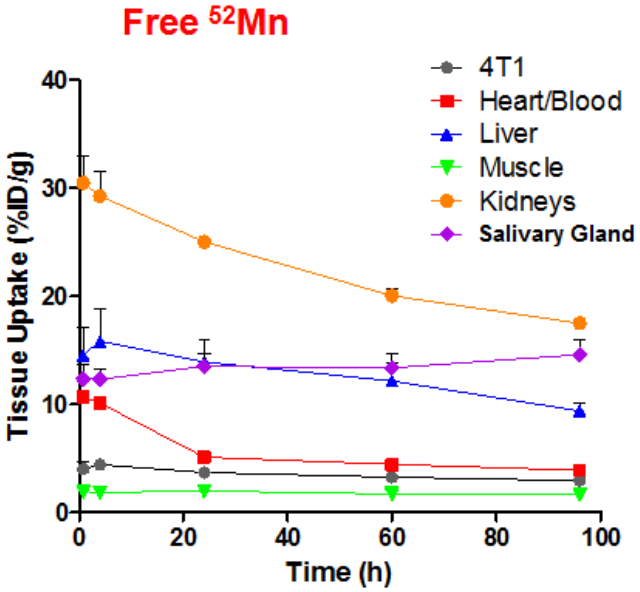

Figure 3.18: TACs acquired from ROI analysis of PET images obtained in subjects injected with ^{52}Mn-DOTA-TRC105 ($n = 3$) and with Free ^{52}Mn ($n = 4$). Error bars represent the standard deviation, and are displayed one-sided for visual clarity. The Heart/Blood TAC uses an ROI drawn over the left ventricle and does not differentiate specific uptake in the myocardium from the blood pool.

Comparing ^{52}Mn-DOTA-TRC105 with the "Free ^{52}Mn" PET images, there are clear differences in the distribution pattern. The most pronounced differences include a lack of salivary gland uptake in the ^{52}Mn-DOTA-TRC105 images, and a lack of tumor uptake in the $^{52}MnCl_2$ images. These features support that the DOTA chelation of ^{52}Mn is stable, even 120 hours post-injection. However, there is an enhanced signal in the bones with the targeted injections, but not in the free-ion case. Typically bone uptake in immunoPET is associated with instability of the metal-chelate pair. If this is the case in the present study, it is clear that the slow-dissociating manganese displays a pharmacokinetic profile that is distinct from the free manganese. One possible explanation is a direct interaction between the bone and the DOTA-bound manganese rather than a hydrolysis mechanism

for chelate instability. Further investigation into the in vivo behavior of manganese salts may help determine the impact that slow dissociation has upon PET quantification, as has been done for ^{89}Zr (Severin et al., 2015).

Impurities

Prior to translation there are many important considerations, especially concerning radionuclidic and chemical purity. The injections in this study contained approximately 0.5% radionuclidic impurity from ^{54}Mn, which contributes only in a small way to personal dosimetry (see supplemental material), but the long half-life (biological and physical) may be an important factor in deciding whether or not to use enriched ^{52}Cr as an alternative target material, thereby eliminating production of ^{54}Mn. Chemically, the use of chromium in a pharmaceutical production may raise concerns of toxic effects. However, the amount of Cr that remains after purification is extremely low, at most 1μg for an entire production (150-250 MBq). This Cr has no propensity to form a stable complex with functionalized DOTA (Asti et al., 2012) and would be further removed during the size exclusion purification step. For comparison, the EPA reference dose(RfD, dose below which no effects are observed) for Cr(IV), is 3 μg/kg in rats (USEP, 1999), a level much higher than would be reached following injection of a purified ^{52}Mn-immunoconjugate.

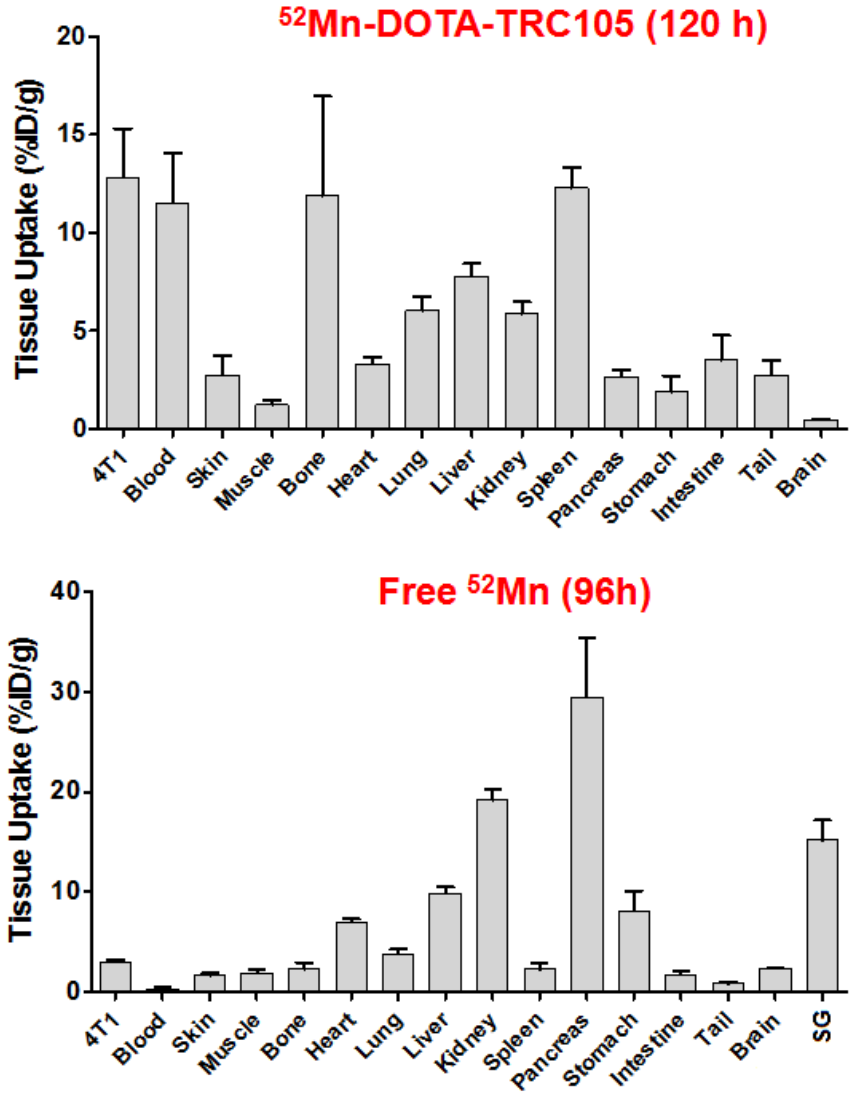

Figure 3.19: Ex vivo ^{52}Mn-DOTA-TRC105 ($n = 3$) and $^{52}MnCl_2$/^{52}Mn-acetate ($n = 4$) biodistribution data obtained following the last PET time point. Animals were sacrificed, and tissue samples were isolated, washed with saline, dried, weighed, and gamma counted.

3.4.4 Rudimentary dosimetry comparison against ^{89}Zr-DFO-TRC105

In order asses the acceptability of ^{52}Mn as an immunoPET label, it is useful to make a dosimetric comparison to ^{89}Zr. Due to the high energy gammas from both isotopes, a

Tissue	Free ^{52}Mn (%ID/g) ($n = 4$)	^{52}Mn-DOTA-TRC105 (%ID/g) ($n = 4$)
4T1 Tumor	2.9 ± 0.2	12.8 ± 2.5
Blood	0.27 ± 0.14	11.5 ± 2.5
Skin	1.6 ± 0.2	2.7 ± 1.0
Muscle	1.9 ± 0.3	1.2 ± 0.2
Bone	2.3 ± 0.6	11.9 ± 5.1
Heart	7.0 ± 0.3	3.3 ± 0.4
Lung	3.8 ± 0.5	6.0 ± 0.7
Liver	9.9 ± 0.6	7.8 ± 0.6
Kidney	19.2 ± 1.1	5.9 ± 0.6
Spleen	2.2 ± 0.6	12.3 ± 1.0
Pancreas	29.4 ± 6.0	2.6 ± 0.3
Stomach	8.1 ± 2.0	1.9 ± 0.8
Intestine	1.7 ± 0.3	3.5 ± 1.3
Tail	0.8 ± 0.2	2.8 ± 0.7
Brain	2.30 ± 0.07	0.46 ± 0.06
Salivary Gland	15.1 ± 2.0	-

Table 3.13: Ex vivo free ^{52}Mn and ^{52}Mn-DOTA-TRC105 biodistribution data obtained following the last PET time point. Animals were sacrificed, and tissue samples were isolated, washed with saline, dried, weighed, and gamma counted.

good first order evaluation is to evaluate the dose to the whole body, liver, and bone marrow due to accumulations in two common accumulating structures, namely the liver and bone. Clearly before translation more data and detailed dosimetry is required, however this analysis aims at providing a reasonable estimate.

The biological half-life of Zr and Mn in mice tibia are 97 days and 263 days respectively (Ishini et al., 1969; O'Neal et al., 2014), therefore the residence time in the bone is assumed to be entirely determined by the physical decay. For the liver, the clearance half-life observed in mice for TRC105 is approximately 50 h for ^{89}Zr-DFO-TRC105 and 173 h for ^{52}Mn-DOTA-TRC105. Using these numbers without allometric scaling however makes a distorted picture for the human dosimetry. One possibility to estimate residence times

in humans is to assume that any activity in the bones is transchelated from the initial tracer, and any activity in the liver will eventually be metabolized into a bio-available state. Therefore the clearance half-lives of the free elements for the bones, 21 years (Greiter et al., 2011) for Zr and 8.5 years (O'Neal et al., 2014) (scaled) for Mn, can be used to determine the residence time in the bone, and the slow-phase biological half-life for the free elements, 7 days (Mealey et al., 1957) for Zr and 39 days (Mahoney et al., 1968) for Mn, can be used to calculate the liver residence times. This liver clearance half-life may be underestimated for tracer levels of Mn^{2+} however, as Daube et al. observed a clearance half-life of 165 days for ^{54}Mn (Daube et al., unpublished data, 1985). Regardless, by these approximations, OLINDA is used to calculate effective dose per MBq in each organ with the results shown in Table 3.14 (note: uptake phase is ignored as it is short compared to the clearance time).

	Eff. half-life (d)		Dose to Liver (mSv/MBq)		Dose to Red Marrow (mSv/MBq)		Whole Body (mSv/MBq)	
	^{52}Mn	^{89}Zr	^{52}Mn	^{89}Zr	^{52}Mn	^{89}Zr	^{52}Mn	^{89}Zr
1MBq Liver	4.9	2.2	30.6	6.5	1.4	0.2	2.7	0.5
1MBq Bone	5.6	3.3	0.9	0.2	5.5	2.3	1.6	0.5

Table 3.14: Effective dose in mSv to liver, bone marrow, or whole body per MBq accumulated activity in either the liver or bone as the source organ (after uptake phase). Calculations were performed with OLINDA, using the 70 kg adult male phantom. The effective half-life of the nuclides in the liver was calculated using the slow phase of the biological half-life of the free metals, 7 days for Zr, and 39 days for Mn. As bone desorption rates for these elements are very slow (8.5 years for Mn and 21 years for Zr) the effective half-life for each nuclide in the bone is simply the physical half-life.

In general, the results in Table 3.14 demonstrate that the patient dose is approximately 5 times higher when using ^{52}Mn compared to equal activity accumulation of ^{89}Zr. In

practice this will be mitigated to a small degree by the slightly higher abundance of positron emission from ^{52}Mn (29.6% for ^{52}Mn vs. 22.7% for ^{89}Zr) meaning that less injected activity is needed for the same detector response. Additionally, if injected activities are scaled for a desired response at a late time-point, equivalent imaging will require less injected activity of ^{52}Mn compared to ^{89}Zr due to the half-life difference. As an example, to get the same positron rate at 10 days post-injection, three times more ^{89}Zr would need to be injected than ^{52}Mn. Therefore if imaging is intended to be done at late time points, and the injected activity is scaled accordingly, the dosimetry difference is not quite as pronounced.

Turning to the influence of ^{54}Mn on the dosimetry, on average ^{54}Mn comprised 0.4% of the overall activity at EOB. As a reasonable estimation we assume that at injection this has grown to 0.5%, meaning that for every 1 MBq of ^{52}Mn injected there is also 5 kBq of ^{54}Mn injected in the same chemical form. Using the biological half-lives as above, it is possible to calculate the influence of ^{54}Mn upon the dosimetry, as presented in Table 3.15.

	Eff. half-life (d)	Dose to Liver (mSv/5 kBq)	Dose to Red Marrow (mSv/5 kBq)	Whole Body (mSv/5 kBq)
5 kBq Liver	35	0.25	0.01	0.02
5 kBq Bone	283	0.06	0.07	0.09

Table 3.15: Effective dose to target organs from 5 kBq ^{54}Mn accumulated in either the liver or bone (corresponding to 1 MBq of ^{52}Mn accumulated).

From Table 3.15 it is clear that a safe estimate considering the presence of ^{54}Mn is that it will not alter the personal dosimetry of a patient by more than about 5%, making

it a minor contribution. However there are other quality-of-life considerations with injections of long-lived radioactivity (e.g. trouble at security screenings in airports, or cultural stigma) which might prompt the use of enriched ^{52}Cr as a target material in order to limit ^{54}Mn. As with any patient care, there is a delicate balance between cost, benefit, and quality of life that must be met on an individual basis. However, the dose from ^{54}Mn should not weigh heavily, especially if the dose from ^{52}Mn is deemed acceptable.

3.4.5 Conclusion

The results above and methodology below are intended to provide an easily reproducible path towards investigating bioconjugate systems using ^{52}Mn. The example of ^{52}Mn-DOTA-TRC105 shows that stable chelation of manganese via bifunctionalized DOTA is suitable for tracing macromolecules with PET over the course of several days, with imaging characteristics that compare favorably to ^{89}Zr. Additionally, the effective specific activity of ^{52}Mn that results from anion-exchange separations from ethanol-HCl mixtures is sufficient to conduct antibody imaging.

3.5 DMT-1 Cell tracking

Much of this work was performed in collaboration with, or solely by, Christina (Lewis) Brunnquell, and is further described in our recent *Theranostics* publication (Lewis & Graves et al., 2015) and in Christina's dissertation (Brunnquell, 2016). As such the entirety of this work is not reproduced here; Rather, the research is introduced and key findings discussed.

3.5.1 Background

The growing field of stem cell therapy is moving toward clinical trials in a variety of applications, particularly in cardiac and neurological diseases (Makkar et al., 2012; Feldman et al., 2014). This translation of cell therapies into humans has prompted a need to assess the location, survival, and dynamics of transplanted cells non-invasively and longitudinally.

In recent years, a variety of in vivo cell tracking methods have been developed and applied in animals and humans, including direct labeling with super-paramagnetic iron oxide nanoparticles (SPIONs) (Li et al., 2014; Janowski et al., 2014) and radiolabelled molecules such as ^{111}In-oxine, ^{18}F-FDG (Lang et al., 2013; Arbab et al., 2012), and ^{89}Zr-DFO-NCS (Bansal et al., 2015). The direct labeling approach for cell tracking is relatively straightforward, clinically applicable, and well suited for short-term studies to investigate the initial distribution of cells. However, the potential for long-term cell tracking can be compromised by radiolabel decay, label dilution upon cell division, non-specific contrast

if the label leaves the cell, and label persistence upon cell death (Cianciaruso et al., 2014). Reporter genes present an alternative approach to stem cell tracking that can offer greater depth of functional information regarding cell survival and differentiation (Bernau et al., 2014; Ahn et al., 2014). Several reporter genes have been extensively investigated for this purpose, most notably firefly luciferase for bioluminescence imaging (BLI), herpes simplex virus-1 thymidine kinase (HSV-TK) for PET, and ferritin for MRI (Bernau et al., 2014; Koehne et al., 2003; Velde et al., 2012). These reporters have had varying success, and they each have their own strengths and weaknesses in terms of sensitivity, clinical applicability, soft tissue contrast, resolution, and applicability in the central nervous system (Rodriguez-Porcel et al., 2008).

In this work, we investigate the divalent metal transporter 1 as a reporter gene for cell tracking in the central nervous system. The DMT1 protein transports divalent metals such as Cd^{2+}, Fe^{2+}, Co^{2+}, and Mn^{2+} (Illing et al., 2012). This protein is ubiquitously expressed and plays important roles in metal transport in the brain and gut, with relatively lower expression levels in the brain (Au et al., 2008). As a reporter gene, DMT1 over-expression enables increased manganese (Mn) incorporation, resulting in selective signal enhancement and detection in MRI (Bartelle et al., 2012). Although several groups of researchers have investigated Mn-based MRI for cellular imaging (Bartelle et al., 2012; Odaka et al., 2011), we hypothesize that ^{52}Mn-based PET could offer increased sensitivity, reduced bulk manganese dose, and provide valuable complementary information when paired with MEMRI.

The objective of this work was to develop the foundation for Mn-based PET and MRI and establish proof of concept regarding the potential of DMT1 as a dual-modality reporter gene for stem cell imaging in the brain. With the complementary strengths of PET and MRI available, this approach may offer increased flexibility for *in vivo* cell tracking compared to other cell tracking approaches.

3.5.2 Methods, Results, and Discussion

^{52}Mn was produced as previously described by irradiation of thick ^{nat}Cr and separation by TOA extraction. DMT1 expression was enhanced in a line of human neural progenitor cells (hNPC; G010) by transfection of a cytomegalovirus promoter (SLC11A2 HaloTag Fusion FlexiVector) using the Basic Primary Neurons Nucleofection system (Lonza Group, Basel, Switzerland). Immunocytochemistry was used to examine the expression of human DMT1 protein in these cells. Cell viability was assessed by trypan blue staining and counting before and after exposure to macroscopic quantities of $^{nat}MnCl_2$ (0, 100, and 1000 μM). Having been exposed to a range of $^{nat}MnCl_2$ concentrations, *in vitro* transfected and wild-type cells were imaged by MRI using a 4.7 T preclinical scanner (Agilent Technologies) using a T1 mapping sequence. Uptake of radiomanganese was compared between *in vitro* transfected and wild-type cells by incubation with $^{52}MnCl_2$ followed by gamma counting of the rinsed cells. Adult wild-type male and female Sprague-Dawley rats were used for cell transplantation and imaging experiments. Transfected and wild-type cells (2-3 μl, 150,000 cells/μl) were injected bilaterally into two striatal sites using a

stereotactic frame. One day following surgeries, animals were administered $^{nat}MnCl_2$ (50 mg/kg) by intravenous infusion and imaged by MRI. On separate subjects, PET/CT (Siemens Inveon) was performed 24 hours following intravenous infusion of ^{52}Mn (~ 0.85 mCi) with and without $^{nat}MnCl_2$ carrier added. Following scanning, animals were sacrificed; ex vivo ^{52}Mn biodistribution was quantified; and 0.3-1.0 mm brain sections were used for autoradiography and histology.

In transfected cells, up to 42% of cells were found to overexpress DMT1 after one day. This percentage decreased somewhat linearly to approximately 5% at 7 days post-transfection. 100 μM $^{nat}MnCl_2$ (expected levels in the rat brain following administration) did not decrease cell viability *in vitro* compared with baseline, but at 1000 μM increased cell death was observed. Transfected cells showed significantly shorter T1 relaxation in *in vitro* MRI images compared with wild-type cells following incubation with $^{nat}MnCl_2$, suggesting uptake was enhanced by DMT1 overexpression. This was also seen with an increase in ^{52}Mn uptake *in vitro*, with an enhancement of approximately 500%. Rats with bilateral cell transplants showed a modest increase in R1-map signal in MRI images on the transfected side, but one subject showed a decrease in signal — likely due to surgery-induced hemorrhage-related iron accumulation. No significant difference between the wild-type and transfected regions was observed in *in vivo* ^{52}Mn-PET images (Figure 3.20A), however a PET scan of an *ex vivo* isolated brain (Figure 3.20B) showed a modest increase in signal on the side of transfected cells. This modest increase was also observed in autoradiography of a sagittal section (Figure 3.20C) near the site of transfected cell

transplantation.

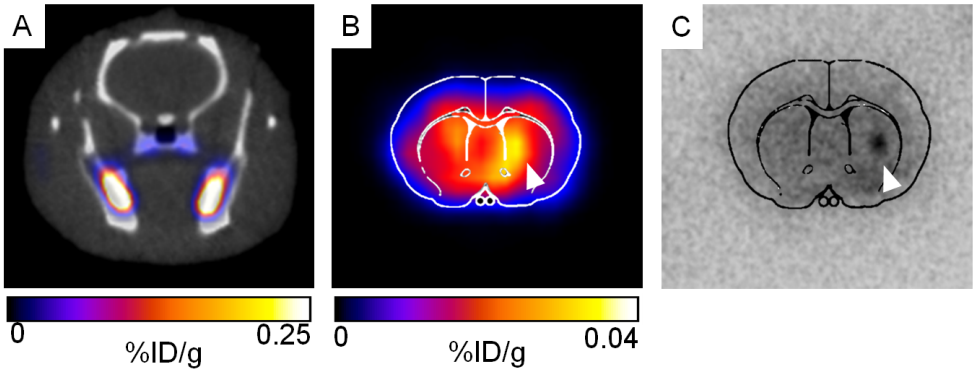

Figure 3.20: *In vivo* uptake of ^{52}Mn by transplanted human neural progenitor cells with upregulated DMT1 expression in a rat striatium. Wild-type cells are transplanted on the left side and transfected cells on the right. (A) *In vivo* PET images reveal very low brain uptake of ^{52}Mn, and no detectable difference between wild-type and transfected cells. (B) PET of the *ex vivo* brain reveals slight signal enhancement in the region of transfected cells, which is corroborated by (C) autogradiography of sagittal brain sections.

The results of this study are mixed, but overall somewhat promising. DMT1 over-expression by transfection was readily accomplished, however this overexpression is quite transient. For future studies, a line of cells stably expressing DMT1 needs to be developed for long-term cell tracking and detection of cell graft rejection. *In vitro* MRI and gamma counting experiments indicate that manganese is taken up in significantly higher amounts in transfected cells compared with wild-type cells, however *in vivo* MRI signal was weak and any radiomanganese signal enhancement was overwhelmed by proximal activity in the submandibular salivary glands of the rat. These results suggest that Mn^{2+} transport across the blood brain barrier is insufficient for significant tracer accumulation, and these techniques might be better suited to cell tracking within other organs or tissues such as the heart, liver, pancreas, or kidneys.

3.6 Quantification of Functional Beta Cell Mass

3.6.1 Introduction

Type 1 diabetes mellitus caused by the autoimmune destruction of insulin producing pancreatic β-cells affects approximately 0.2% of the world's population (Onkamo et al., 1999). Pancreatic islet transplantation combined with immune suppression has been shown to temporarily allow for partial or full insulin independence in patients with type 1 diabetes mellitus, but no permanent treatment yet exists. An imaging modality capable of monitoring the decline of functional β-cell mass and the viability of islet or stem-cell derived β-cell transplants would be invaluable to future therapeutic investigations

Human pancreatic islets occupy approximately 4.5% of the pancreas volume, and are composed of a mixture of β, α, γ, δ, and ϵ cells (Ionescu-Tirgoviste et al., 2015; Kim et al., 2009). As individual islets vary in size from 25 to 400 μm in diameter (Kim et al., 2009; von Mach et al., 2003; Kilimnik et al., 2012) and are non-uniformly distributed throughout the pancreas, quantification is challenging through noninvasive anatomical imaging techniques such as magnetic resonance imaging (MRI) or computed tomography (CT) (Virostko et al., 2009). Alternatively, positron emission tomography (PET) is a technique that typically involves quantifying the in vivo distribution of a biologically relevant moiety via tracking with a positron emitting radioisotope. Compared with MRI and CT, PET has significantly greater imaging sensitivity and inherently probes physiology rather than anatomy (Paulus et al., 2001), which may prove useful in the clinical quantification

of functional β-cell mass.

Mn^{2+}, in a behavior that mimics Ca^{2+}, is freely transported through voltage dependent Ca^{2+} channels (VDCCs) (Au et al., 2008; Silva et al., 2004; Shibuya et al., 1992). Since VDCC activation is required for the release of insulin from β-cells, Mn^{2+} has been proposed as a molecular imaging agent for probing β-cell function and mass using manganese-enhanced magnetic resonance imaging (MEMRI) (Antkowiak et al., 2013; Antkowiak et al., 2009; Antkowiak et al., 2012; Lamprianou et al., 2011; Rorsman et al., 1982; Rorsman et al., 1983). However, this technique is limited by the significant cellular toxicity and slow biological clearance of manganese, which prevents the possibility of repeated contrast administration (Silva et al., 2004; Crossgrove et al., 2004). This technique stands to benefit greatly from the ~10^9 times higher relative sensitivity of PET. The objective of this work was to assess the feasibility of using Mn-PET to probe β-cell mass and function.

Herein, we take advantage of the exceptional sensitivity and quantitation of PET and the availability of radiomanganese (^{52}Mn and ^{51}Mn) to noninvasively image β-cells in mice. When intravenously injected in mice, $^{52}Mn^{2+}$ ($t_{1/2}$: 5.6 d) showed rapid and prominent accumulation in the mouse pancreas, which was confirmed to be specific to β-cells by several in vitro and in vivo blocking studies. We also explored the potential of ^{52}Mn-PET to detect changes in β-cell mass in mouse models of type 1 and type 2 diabetes. Overall, our results point to the significant potential for radiomanganese to overcome several limitations of other β-cell imaging agents and potentially become a

method of choice for studying β-cell physiology noninvasively.

3.6.2 Materials and Methods

Manganese-52 production and purification

^{52}Mn was produced as previously described (Graves et al., 2015). Briefly, ^{nat}Cr granules (99.999% pure, Alfa Aesar) were hydraulically pressed into silver discs (0.75" diameter, 2mm thick), and irradiated by 60 μA of 16 MeV protons (GE PETtrace) for 1-3 hours (~0.2–0.9 GBq end of bombardment ^{52}Mn yield). Following irradiation, targets were dissolved by 2 mL HCl at ~70°C for one hour. The dissolved target material was diluted with 50 mL ethanol + 0.5 mL concentrated HCl, and was passed over a 200-300 mg AG-1x8 anion exchange column. The column was rinsed with 10 mL ethanol, and ^{52}Mn activity was eluted in 1 mL of 6M HCl. This separation procedure was repeated two additional times with the final activity being eluted in <1 mL of 0.01M pH 6.5 NaOAc buffer. Aliquots of this activity solution were diluted to the desired injection volume (~200 μl) with phosphate-buffered saline (PBS), typically 2–4 MBq (50–100 μCi) per subject.

Animal models

Two strains of mice, ICR (Envigo, Indianapolis, IN) and C57BL/6J (The Jackson Laboratory, a Harbor, ME), were employed for in vivo imaging studies. All mice were approximately ten weeks of age at the time of the experiments. Pre-diabetic C57BL/6J ob/ob mice carrying the homozygous obese spontaneous leptin mutation were obtained

from the Jackson Laboratory. Mice had access to food and water ad libitum, except under fasting condition when access to food was restricted for 6–12 hours. All animal experiments were performed under the approval of the University of Wisconsin Institutional Animal Care and Use Committee.

PET imaging

The acquisition of PET images was performed in the Inveon μPET/μCT scanner (Siemens Preclinical Solutions, Knoxville, TN). To study the long-term biodistribution and clearance of $^{52}Mn^{2+}$ in the mouse body, approximately 3.7 MBq (100 μCi) of $^{52}Mn^{2+}$ was injected intravenously (IV) in female ICR mice. Due to the long physical half-life of ^{52}Mn ($t_{1/2}$: 5.6 d), PET scans were recorded at multiple time-points between 1 hour and 13 days post injection of the radiotracer. Before each scan, mice were anesthetized with isoflurane (4% induction; 1% maintenance) and placed in the scanner in prone position. 30–40$\times 10^6$ coincidence events per mouse static PET scans were acquired (time window, 3.432 ns; energy window, 350–650 keV) and the PET images were reconstructed in Inveon Acquisition Workplace (Siemens Preclinical Solutions, Knoxville, TN) workstation using a non-scatter-corrected three-dimensional Ordered Subset Expectation Optimization/-Maximum a Posteriori (OSEM3D/MAP) algorithm. Region-of-interest (ROI) analysis was performed after organs were manually delineated on the PET images. Tissue uptake values were reported as standardized uptake value (SUV), which is normalized to whole body radiomanganese concentration.

To acquire dynamic PET scans, mice were anesthetized with isoflurane and the lateral tail vein was catheterized. Simultaneous with the administration of 1.7 MBq (50 μCi) of $^{52}Mn^{2+}$ as a fast IV bolus, one-hour scans were recorded and list-mode files were binned into 46 frames (12x5 s, 6x10 s, 6x30 s, 10x60 s, 6x150 s, 6x300 s) and the images reconstructed using a non-scatter-corrected OSEM3D/MAP algorithm. In another study, 1.7 MBq (50 μCi) of $^{52}Mn^{2+}$ was continuously infused with a syringe pump (Kd Scientific, Model 780100) over a period of 30 min, starting at the beginning of the PET scan. List-mode files were framed into 30 x 2 min frames and reconstructed using the above-mentioned algorithm.

To investigate the specificity of $^{52}Mn^{2+}$ for β-cells, a series of studies were performed where $^{52}Mn^{2+}$ uptake was manipulated through the pharmacologic stimulation or inhibition of the insulin secretory pathway. In these experiments, 0.74–1.85 MBq (20-50 μCi) of $^{52}Mn^{2+}$ was administered IV into either female ICR or C57BL/6J mice and static PET scans were acquired at 1 h post injection. During tracer administration, mice were awake. Mice were only anaesthetized by isoflurane (1%) immediately before PET imaging.

Ex vivo biodistribution studies

Ex vivo biodistribution studies were performed in all groups of mice in order to validate the results of PET imaging and obtain a more complete biodistribution profile of $^{52}Mn^{2+}$. Following the last imaging time point, mice were euthanized by CO_2 asphyxiation

and the organs of interest were removed, wet-weighed, and counted on an automated gamma-counter (Wizard 2480, Perkin Elmer). The tissue uptake of $^{52}Mn^{2+}$ was reported as SUV (mean $\pm$ SD).

Islet isolation

Mouse pancreatic islets were isolated by collagenase digestion (Gregg et al., 2016). Briefly, mice were placed under shallow anesthesia and sacrificed via cervical dislocation. The mouse common bile duct was cannulized and 3–5 mL of an ice-cold solution containing type XI collagenase (0.5 mg/mL; Sigma Aldrich, St. Louis, MO) and bovine serum albumin (BSA; 0.2 mg/mL; Sigma Aldrich, St. Louis, MO) in Hank's balanced salt solution (HBSS; Invitrogen, Carlsbad, CA) was injected into the mouse pancreas. After inflation, the pancreas was removed, placed in a glass vial containing 5 mL of the collagenase solution, and incubated in a shaking water bath at 37 °C. Samples were digested for approximately 30 min after which the digests were centrifuged at 50$\times$g for 2 min and islet pellets were washed three times with 30 mL of an ice-cold BSA (0.2 mg/mL) in HBSS solution. The pellet was resuspended and islets handpicked into 35 mm petri dishes. Following isolation, islets were placed in RPMI1640 media supplemented with penicillin (100 U/mL; Invitrogen), streptomycin (100 μg/mL; Invitrogen), and FBS (10% (wt/vol); Sigma) and incubated overnight at 37 °C in a 5% CO_2 atmosphere.

Pharmacological disruption of $^{52}Mn^{2+}$ uptake in islets of Langerhans

The uptake of $^{52}Mn^{2+}$ by murine islets of Langerhans was determined under several stimulatory or inhibitory conditions. Batches of 50 islets were transferred into 0.45 μm filtered bottom 1 mL centrifuge vials (Thermo Fisher Scientific, Grand Island, NY), 500 μL of Krebs-Ringer buffer (KRB: 118 mM NaCl, 5.4 mM KCl, 2.4 mM CaCl, 1.2 mM $MgSO_4$, 1 mM KH_2PO_3, 20 mM HEPES; pH 7.4) containing a low glucose concentration (1 mM D-glucose) were added and the islets incubated for 30 min at 37 °C. After removing the supernatant following centrifugation at 50g for 5 min, 250 μL of KRB containing glucose, diazoxide (50 μM; Tocris Biosciences, Bristol, UK), or tolbutamide (250 μM; Selleckchem, Houston, TX) were added, and the vials were spiked with 370 kBq (10 μCi) of $^{52}Mn^{2+}$. After 15 min of incubation, the solutions were filtered and islets were washed three times with KRB. The $^{52}Mn^{2+}$ radioactivity in the islet pellets were measured in an automated gamma counter (Perkin Elmer).

Stimulatory effect of glucose and glibenclamide on β-cell uptake of $^{52}Mn^{2+}$ in vivo

To corroborate the correlation between $^{52}Mn^{2+}$ pancreatic uptake and the mechanism of insulin release in β-cells, the insulin secretory pathways were stimulated in vivo using glucose and glibenclamide (Tocris Biosciences, Bristol, UK), which is known to promote insulin release in β-cells via blockade of ATP-sensitive potassium channel (K_{ATP}). Mice were injected intraperitoneally (IP) with 100 μL of glucose (1g/kg) or glucose (1g/kg) +

glibenclamide (5 mg/kg) in PBS, 15 min before the IV injection of 0.74–1.85 MBq (20–50 μCi) $^{52}Mn^{2+}$. Static PET scans were acquired 1 h after the injection of the radiotracer, after which ex vivo biodistribution was performed.

Inhibitory effect of diazoxide and nifedipine on β-cell uptake of $^{52}Mn^{2+}$ in vivo VDCC blockade was achieved in vivo via a 20 mg/kg IP injection of 3,5-dimethyl 2,6-dimethyl-4-(2-nitrophenyl)-1,4-dihydropyridine-3,5-dicarboxylate (nifedipine; MP Biomedicals, LLC, Santa Ana, CA) in dimethyl sulfoxide. To activate K_{ATP} channels, mice received an IP injection of a 20 mg/kg dose in PBS of 7-Chloro-3-methyl-4H-1,2,4-benzothiadiazine 1,1-dioxide (diazoxide; Tocris Biosciences, Bristol, UK), a clinically used potent K_{ATP} agonist. Both groups of mice were injected with 0.74 MBq (20 μCi) of $^{52}Mn^{2+}$, 15 min after the administration of either nifedipine of diazoxide. Whole-body PET scans were acquired at 1 h post injection, after which ex vivo biodistribution was performed.

PET studies in type 1 diabetes model

Type 1 diabetes was induced in female ICR mice via a single IP injection of 180 mg/kg streptozotocin (STZ; MP Biomedical, LLC, Santa Ana, CA), a toxin which selectively destroys pancreatic β-cell (Lenzen, 2008). The injectable STZ solution (12.5 mg/mL) was prepared freshly in phosphate buffered saline (PBS). The weight of each mouse was measured daily, and blood glucose levels were recorded every other day with a glucometer (TRUEresult, Trividia Health Inc., Fort Lauderdale, FL) using blood samples collected from the tail vein. Mice were considered diabetic after two consecutive blood

glucose readings above 250 mg/dL and were used for PET imaging studies one week after the injection of STZ. To evaluate $^{52}Mn^{2+}$ pancreatic uptake on diabetic mice, 0.74 MBq (20 μCi) of activity were administered IV and static PET images recorded 1h after administration of the tracer. Ex vivo biodistribution was carried out following PET acquisition.

PET studies in pre-type 2 diabetes model

Given the altered glucose metabolism in obese mice, we compared the pancreatic uptake of $^{52}Mn^{2+}$ in lean (wild-type) and obese (ob/ob) mice on the C57BL/6J background. For PET imaging, 0.74 MBq (20 μCi) of $^{52}Mn^{2+}$ was IV injected into obese mice or lean controls, 1 h prior to PET scan acquisition. Subsequent $^{52}Mn^{2+}$ accumulation in the pancreas and other organs of interest were quantified.

Statistical analysis

A minimum sample size of three (n=3) was used in all in vitro and in vivo experiments. The uptake of $^{52}Mn^{2+}$ in the different tissues was reported as SUV (mean ± SD) and the differences between groups were evaluated for significance using a two-tailed Student's t-test. Differences were considered statistically significant at $P < 0.05$.

3.6.3 Results

^{52}Mn production and separation

Production yields of up to 5.92 MBq/μAh (355 MBq/h @ 60 μA) were achieved using a ^{nat}Cr pellet pressed into a silver disc substrate. ^{52}Mn was eluted in <1mL of 0.01 M NaOAc buffer (pH ~6.5) from a ~150 mg AG-1x8 column which had been previously rinsed with ethanol. As previously described (Lewis et al., 2015), thin layer chromatographs confirmed the Mn(II) oxidation state following elution. End of bombardment radionuclidic purity was measured to be >99.5% by efficiency-calibrated high-purity germanium (HPGe) gamma spectrometry measurements. The only radionuclidic impurity observed was <0.5% ^{54}Mn ($t_{1/2}$= 312.1 d), which does not decay by positron emission.

In vivo whole-body PET and biodistribution of $^{52}Mn^{2+}$ in normal mice

The in vivo biodistribution of $^{52}Mn^{2+}$ was investigated noninvasively with PET and ex vivo gamma counting. Figure 3.21 shows coronal planes intersecting the pancreas of ICR mice, in PET scans acquired between 1 hour and 13 days after the IV injection of 3.7 MBq (100 μCi) of $^{52}Mn^{2+}$. A fast and prominent accumulation of $^{52}Mn^{2+}$ was observed in the pancreas, kidneys, liver, heart, and salivary glands (5.13 $\pm$ 0.38, 5.13 $\pm$ 0.02, 3.27 $\pm$ 0.36, 2.11 $\pm$ 0.20, and 2.30 $\pm$ 0.26 SUV at 1 h post injection, respectively; $n = 3$; Figure 3.22). In the subsequent time points during the longitudinal study, $^{52}Mn^{2+}$ accretion gradually declined in all organs except the salivary gland where uptake remained at around 3 SUV (Figure 3.22, Table C.1). $^{52}Mn^{2+}$ uptake in the pancreas, which was highest at 1 h

post injection, was notably higher than in the liver and kidneys at all time points, with pancreas-to-normal organ contrast ratios peaked 3 days after $^{52}Mn^{2+}$ administration. Uptake in the muscle was very low and had little variation during the whole study. Ex vivo biodistribution was performed after the last PET scan 13 days after injection, confirming a marked accumulation of $^{52}Mn^{2+}$ in the salivary gland, pancreas, kidneys, and to a lesser extent, the heart and liver (Figure 3.23, Table C.2). Other organs including the brain, lungs, bones, intestines, stomach, and spleen displayed low $^{52}Mn^{2+}$ uptake, typically less than 0.5 SUV.

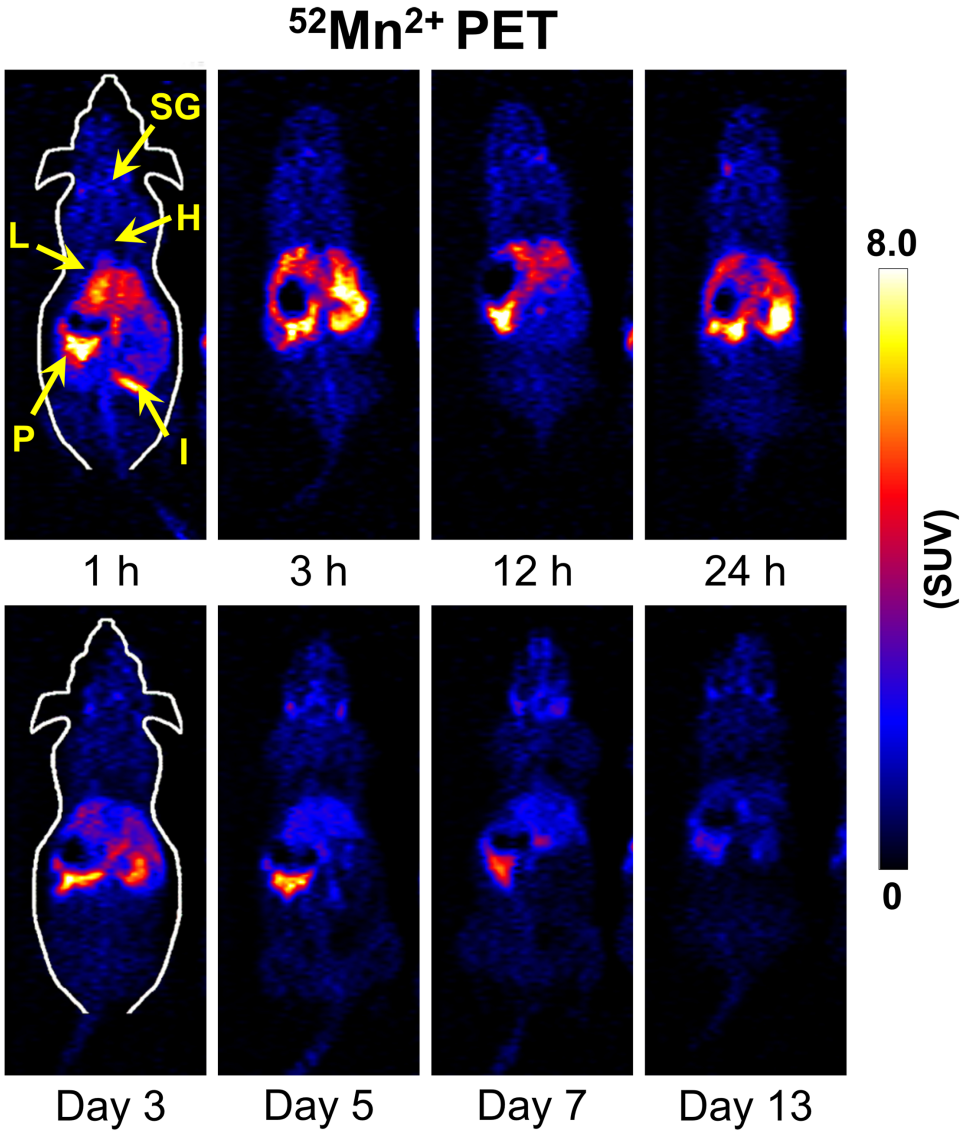

Figure 3.21: Serial PET images of a representative ICR mouse injected intravenously with ^{52}Mn(II) (no anesthesia except during the PET scans). Coronal PET image slices were selected to best show pancreatic uptake. Arrows point to P: pancreas, H: heart, L: liver, I: intestines, and SG: salivary gland.

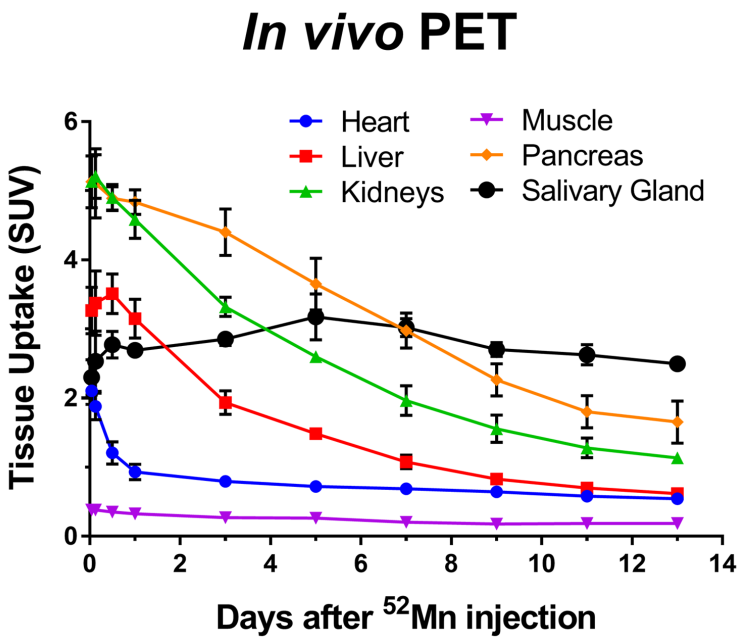

Figure 3.22: ROI-based ^{52}Mn(II) uptake quantification of the heart, liver, kidneys, muscle, pancreas, and submandibular salivary gland in serial PET images. Values represent mean $\pm$ SD. n = 4

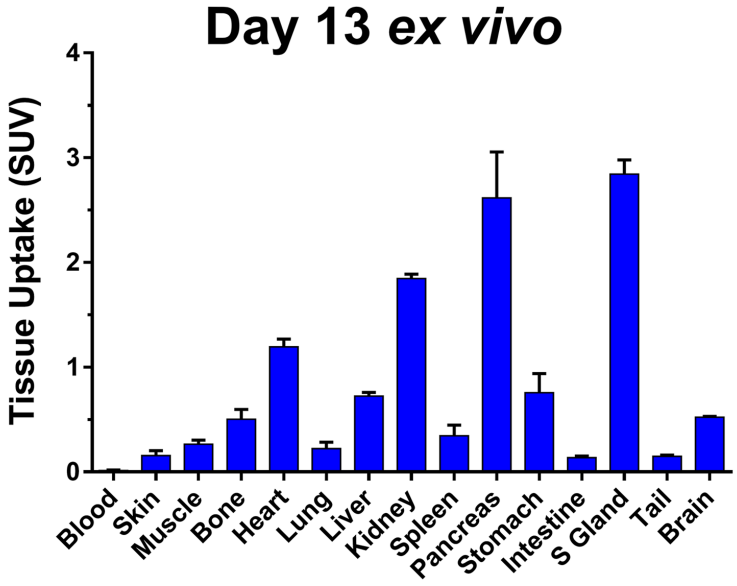

Figure 3.23: Ex vivo ^{52}Mn biodistribution of sacrificed mice following last PET time-point, determined by gamma counting. S Gland: salivary gland. Values represent mean $\pm$ SD. n = 4.

Because the whole-body distribution of $^{52}Mn^{2+}$ occurred largely within the first hour after IV administration, a dynamic PET study was designed to investigate the first hour of $^{52}Mn^{2+}$ kinetics. Figure 3.24 shows the time-activity curves (TACs) resulting from ROI analysis of the dynamic PET data corresponding to the heart, liver, kidneys, pancreas, salivary gland, and muscle under two administration regimes: IV rapid bolus injection and IV continuous infusion over 30 minutes. The analysis of the myocardial TAC revealed extremely fast blood extraction kinetics with a blood circulation half-life of 10.7 ± 3.5 s in mice administered a rapid IV $^{52}Mn^{2+}$ bolus. Consequently, $^{52}Mn^{2+}$ uptake was stabilized in the organs of interests within 5 minutes post injection. A residual radioactivity of 2.60 ± 0.41 SUV was observed in the heart at 1 h post injection, which was consistent with the specific uptake on Mn^{2+} ions by myocardial tissue. Compared to the static 1 h post injection PET scans, similar $^{52}Mn^{2+}$ uptake values were observed in the heart (2.11 ± 0.20 vs. 2.60 ± 0.41 SUV) and muscle (0.38 ± 0.03 vs 0.16 ± 0.02 SUV), while liver (3.27 ± 0.34 vs. 5.16 ± 1.46 SUV) and kidneys (5.13 ± 0.02 vs. 7.81 ± 0.51 SUV) were much higher at the end of the dynamic scan. Interestingly, a ~50% reduction in pancreatic uptake from 5.13 ± 0.38 to 2.74 ± 0.59 SUV was observed in the dynamic studies.

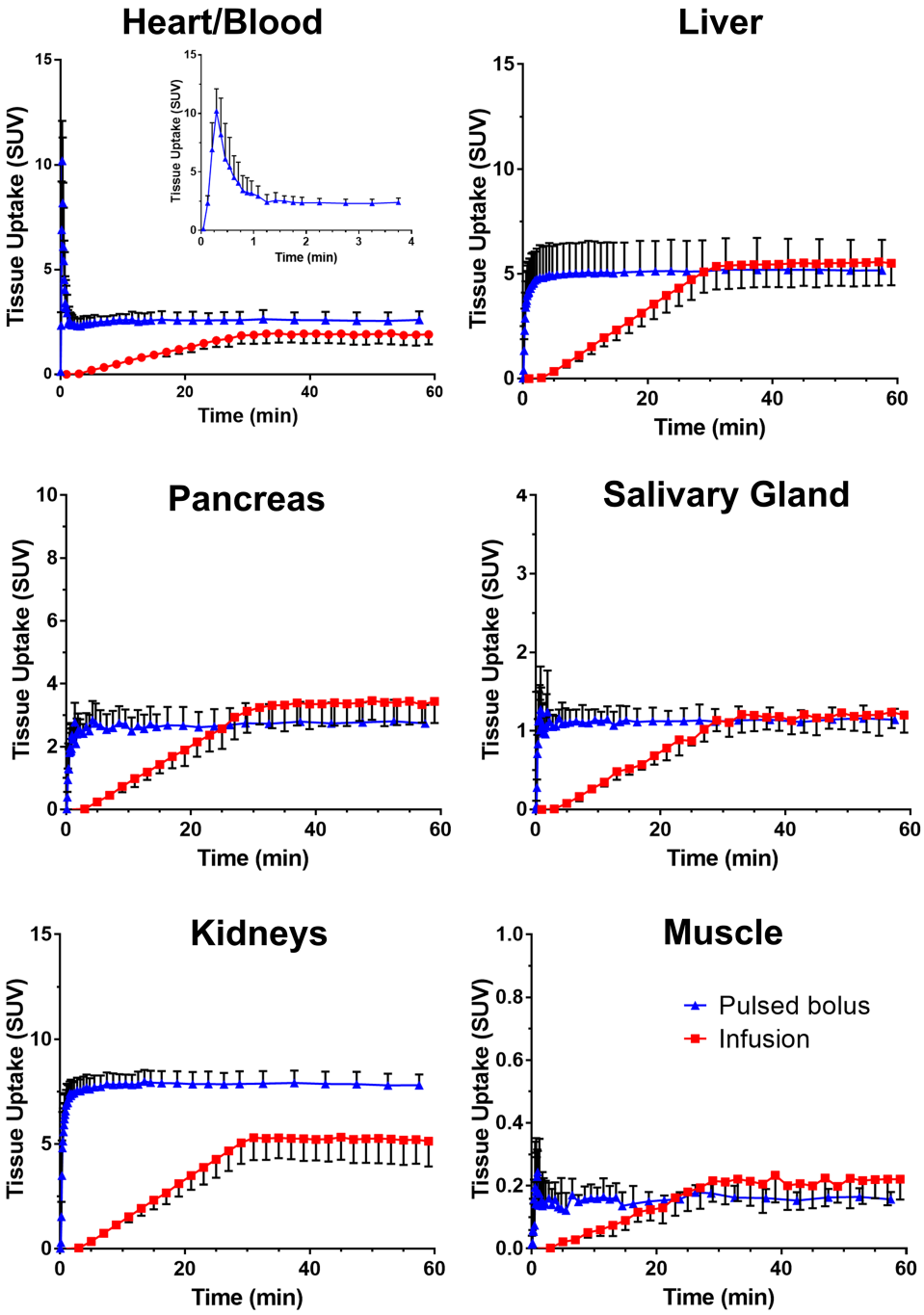

Figure 3.24: Dynamic PET time-activity curves (TACs) derived from hand-drawn ROIs for the heart/blood, liver, kidneys, pancreas, salivary gland, and muscle. Blue curves indicate TACs in mice injected by a rapid IV bolus of ^{52}Mn(II), while red curves indicate an intravenous infusion of ^{52}Mn(II) over 30 minutes.

As clearly depicted in Figure 3.24 (red curves), a continuous injection of the $^{52}Mn^{2+}$ over a 30 min time period resulted in a linear ramping in organ radioactivity, followed by an immediate plateau upon infusion termination. This corroborated the rapid distribution kinetics of $^{52}Mn^{2+}$. Comparable results were obtained by either rapid bolus or continuous infusion of $^{52}Mn^{2+}$ in terms of organ uptakes at equilibrium. Only the kidney displayed higher radioactivity at 1 h post injection in mice administered the rapid bolus vs. mice receiving continuous $^{52}Mn^{2+}$ infusion, 7.81 ± 0.51 vs. 5.14 ± 1.21 SUV, respectively ($n = 4$). During the continuous infusion regime, pancreas reached an uptake of 3.44 ± 0.69 SUV which, similar to the rapid bolus injection, was also significantly lower than that in the static PET scans at 1 h post injection (5.13 ± 0.38 SUV).

Previous reports have shown that most volatile anesthetics, including isoflurane impair insulin secretion by inhibiting the deactivation of K_{ATP} channels (Tanaka et al., 2009; Desborough et al., 1993). Plausibly, the observed decrease in pancreatic uptake of $^{52}Mn^{2+}$ resulted from mice being anesthetized through the full extent of the studies during the dynamic PET scans. The impact of isoflurane on acute pancreatic metabolic function is described further in Section 3.7.

Uptake of $^{52}Mn^{2+}$ in isolated islets

To corroborate the mechanism of $^{52}Mn^{2+}$ uptake in the pancreas and its specificity for β-cells, an in vitro $^{52}Mn^{2+}$ uptake study was performed in islets isolated from obese (ob/ob) mice. Due to the similarities between Mn^{2+} and Ca^{2+} ions, Mn^{2+} uptake by

β-cells occurs via influx through VDCC (Figure 3.25). Isolated islets were incubated with 0.37 MBq (10 μCi) of $^{52}Mn^{2+}$ under several stimulatory/inhibitory conditions (Figure 3.26). $^{52}Mn^{2+}$ was readily taken up by islets, even under low glucose (1 mM) resting conditions. $^{52}Mn^{2+}$ uptake was significantly enhanced ($P < 0.05$) when the islets were stimulated with 10 mM glucose. This effect was blocked by the further addition of diazoxide (50 μM), which inhibits the opening of VDCC via activation of K_{ATP} channels. As expected for intracellular Ca^{2+} (Merrins et al., 2016), $^{52}Mn^{2+}$ uptake declined to levels well under the basal conditions. Conversely, glucose and the K_{ATP} channel blocker tolbutamide (250 μM) resulted in significantly higher $^{52}Mn^{2+}$ retention. Overall, these experiments demonstrate that pancreatic islet uptake of $^{52}Mn^{2+}$ depends on the activation status of β-cells.

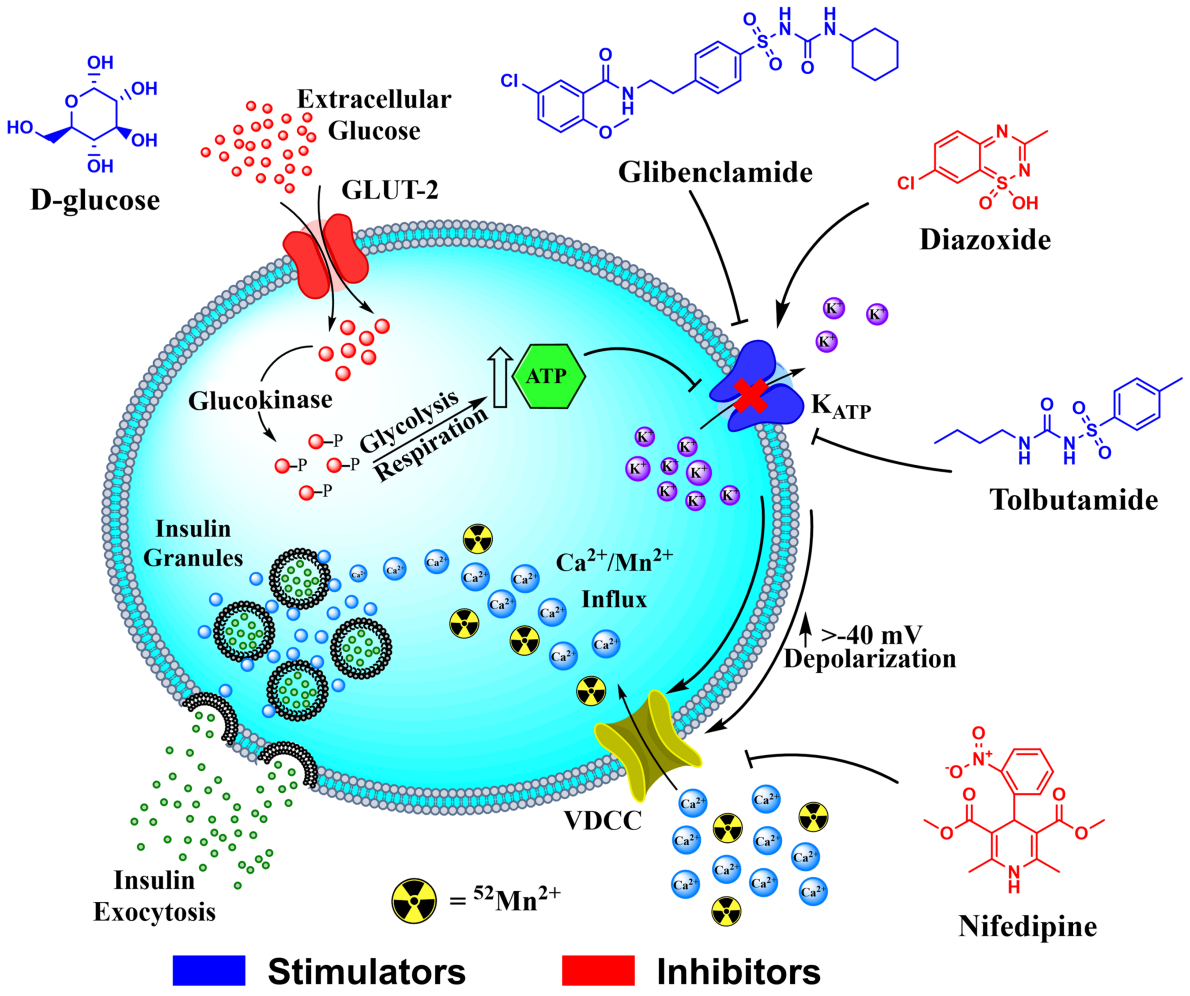

Figure 3.25: Pharmacologic manipulation of the insulin secretory pathway in β-cells. Molecular structures in blue indicate compounds which activate calcium influx through VDCC, while those in red are inhibitory.

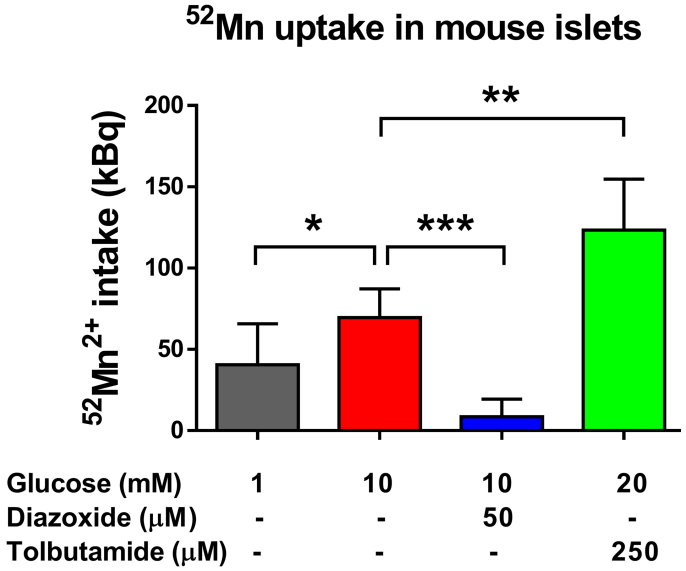

Figure 3.26: Uptake of ^{52}Mn by isolated ob/ob mouse islets. Groups of 50 islets from 3 independent islet preparations were incubated with $^{52}Mn(II)$ (370 kBq) in the presence of glucose and K_{ATP} channel modulators as indicated. Mean ± SD; *, $P < 0.05$; **, $P < 0.01$; ***, $P < 0.001$.

Pharmacological manipulation of $^{52}Mn^{2+}$ pancreatic uptake in vivo

To verify the specificity of $^{52}Mn^{2+}$ accretion in the pancreas noninvasively using PET imaging, $^{52}Mn^{2+}$ pancreatic uptake was pharmacologically manipulated in vivo through the inhibition or stimulation of insulin secretion. In line with the in vitro results, inhibition of VDCC by direct blockade with nifedipine, or activation of K_{ATP} with diazoxide resulted in a significant ($P < 0.0001$) abrogation of the PET signal within the pancreas. Figure 3.27 shows coronal PET slices of the pancreas of ICR mice receiving 20 mg/kg IP injections of nifedipine or diazoxide, 10-15 min before the administration of an intravenous $^{52}Mn^{2+}$ bolus. Compared to the control group, a clear decrease in pancreatic PET signal was observed 1 h following injection of $^{52}Mn^{2+}$. PET quantification revealed

a 44% (5.13 ± 0.36 vs. 2.85 ± 0.92 SUV) and 54% (5.13 ± 0.36 vs. 2.36 ± 0.61 SUV) decline in $^{52}Mn^{2+}$ uptake in groups administered diazoxide and nifedipine, respectively (Figure 3.28 and 3.29). On the contrary, mice administered glibenclamide (5 mg/kg) exhibited a significant enhancement in pancreatic SUV values. The distribution of $^{52}Mn^{2+}$ in other organs of interest including the heart, liver, kidneys, spleen and salivary gland remained largely unaltered among groups (Tables C.3 and C.4).

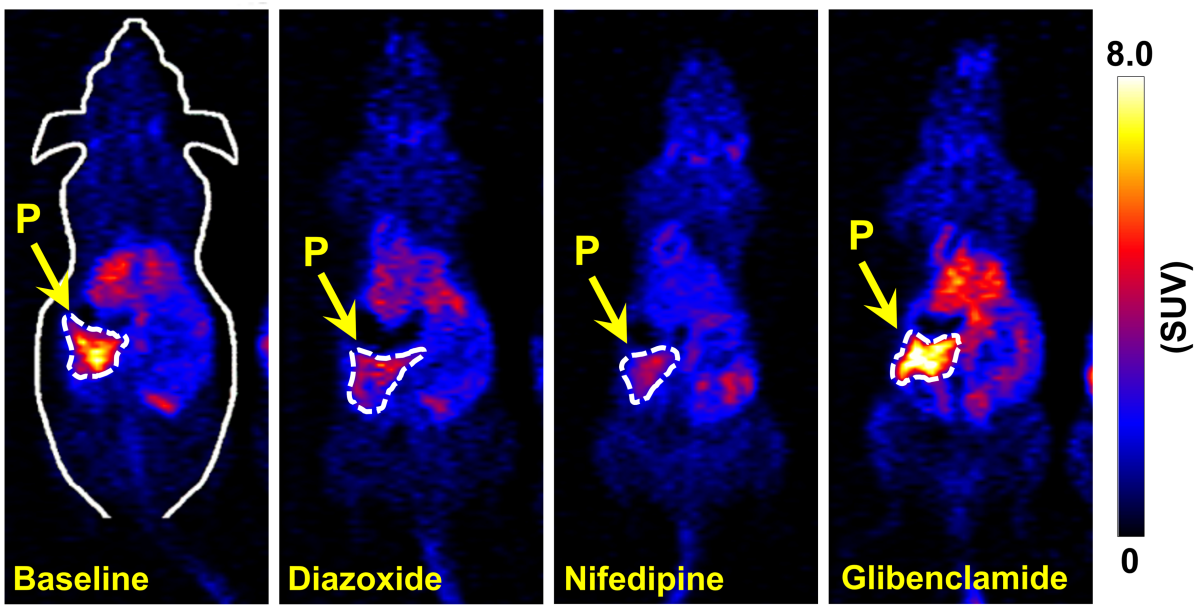

Figure 3.27: In vivo pharmacological modulation of $^{52}Mn^{2+}$ pancreatic uptake in ICR mice. Coronal PET images 1 h post injection showing the pancreas of mice given IP injections of diazoxide (20 mg/kg), nifedipine (20 mg/kg), or glibenclamide (5 mg/kg) prior to the administration of a $^{52}Mn(II)$ rapid bolus. Yellow arrows point to white contours demarcating the pancreas.

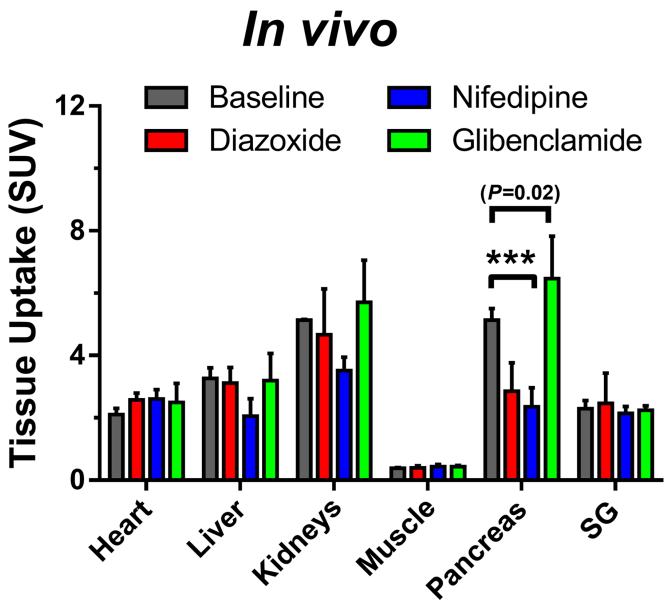

Figure 3.28: In vivo pharmacological modulation of $^{52}Mn^{2+}$ pancreatic uptake in ICR mice. Hand drawn ROI-based quantification of static PET images acquired 1 h post injection.

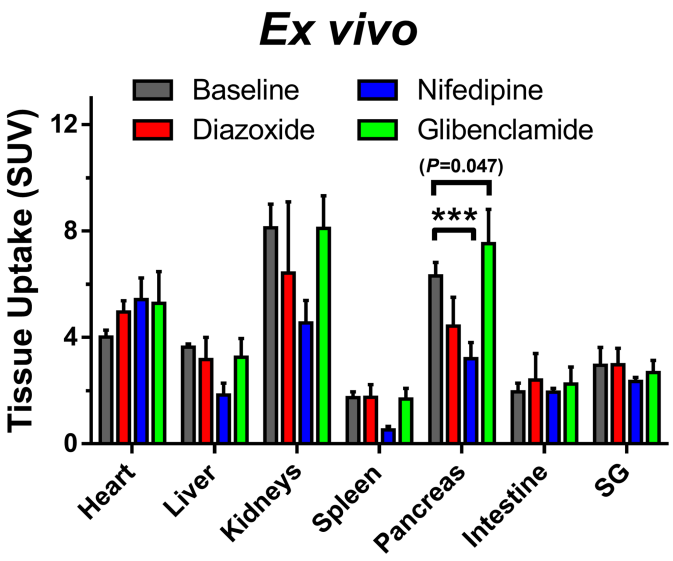

Figure 3.29: In vivo pharmacological modulation of $^{52}Mn^{2+}$ pancreatic uptake in ICR mice. Results from ex vivo biodistribution studies following PET imaging. Significantly reduced pancreatic uptake of $^{52}Mn^{2+}$ is observed in mice that received nifedipine and diazoxide ($P < 0.0001$) prior to radiotracer administration. Mice which received glibenclamide (5 mg/kg) prior to radiotracer administration had significantly higher pancreatic uptake of ^{52}Mn than the control mice, in both PET ($P = 0.02$) and biodistribution ($P = 0.047$) studies. SG: salivary gland.

$^{52}Mn^{2+}$ uptake in type 1 diabetic mice

We further investigated the correlation between pancreatic $^{52}Mn^{2+}$ uptake and β-cell functionality in a murine model of type 1 diabetes. Diabetes was induced in ICR female mice via injection of a single STZ (180 mg/kg) dose. As observed in Figure 3.30, four days after induction, mice presented signs of hyperglycemia (blood glucose > 250 mg/dL) and weight loss that indicated a diabetic status. As seen in the PET images (Figure 3.31), $^{52}Mn^{2+}$ accretion within the pancreas of diabetic mice was significantly ($P < 0.0001$) reduced from 5.13 ± 0.38 SUV (n=3) in normal mice to 2.04 ± 0.81 SUV (n=3) in diabetic mice (Figure 3.32, Tables C.3 and C.4). Ex vivo biodistribution corroborated a > 58%

decrease in pancreatic accumulation of $^{52}Mn^{2+}$ (Figure 3.33). These results further demonstrated the specificity and the potential of radiomanganese PET imaging to detect changes in β-cell mass noninvasively.

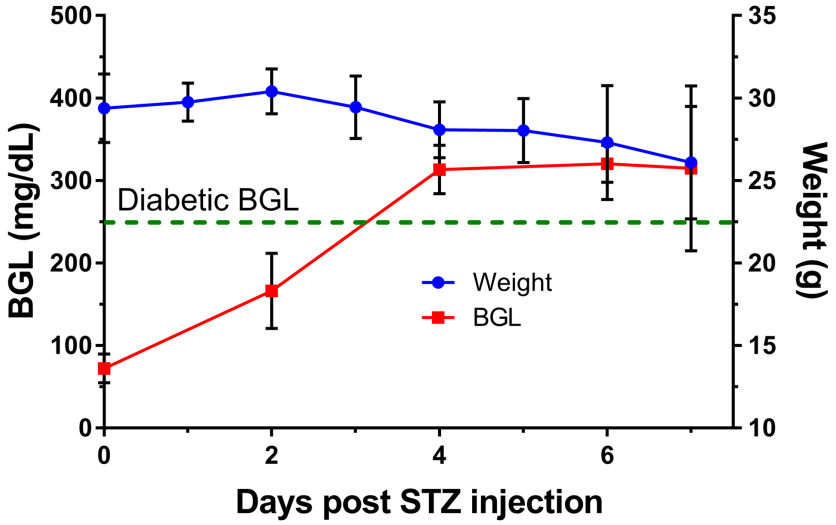

Figure 3.30: Following the administration of an acute dose of streptozotocin (STZ, 180 mg/kg), ICR mice started to show symptoms of diabetes: reduced weight and high blood glucose level (BGL; > 250 mg/dL).

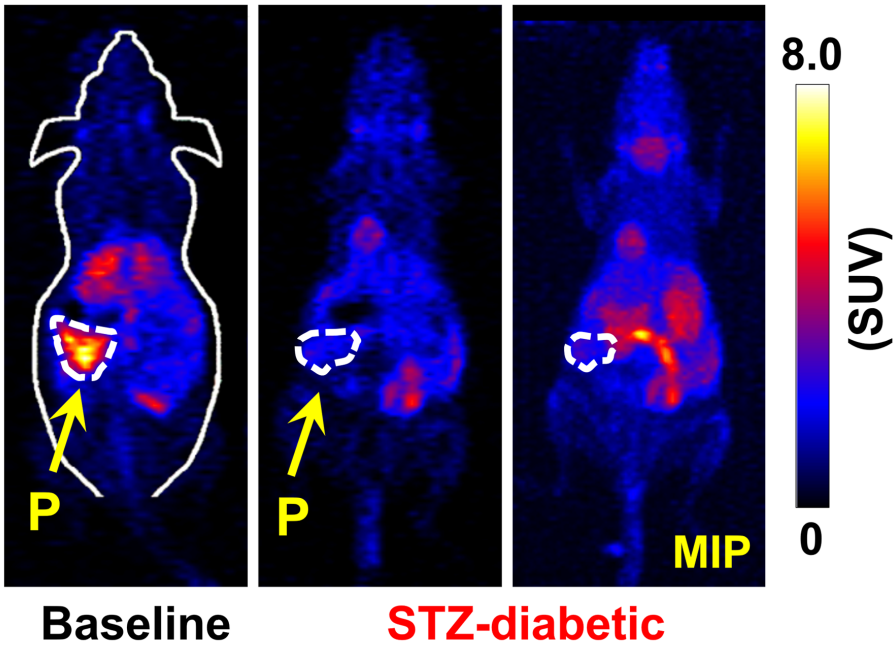

Figure 3.31: ^{52}Mn-PET imaging in a mouse model of type 1 diabetes. One-hour post injection coronal PET images of healthy (left panel) or diabetic (center/right panels) ICR mice showing a clearly reduced PET signal in the pancreas of the diabetic mice.

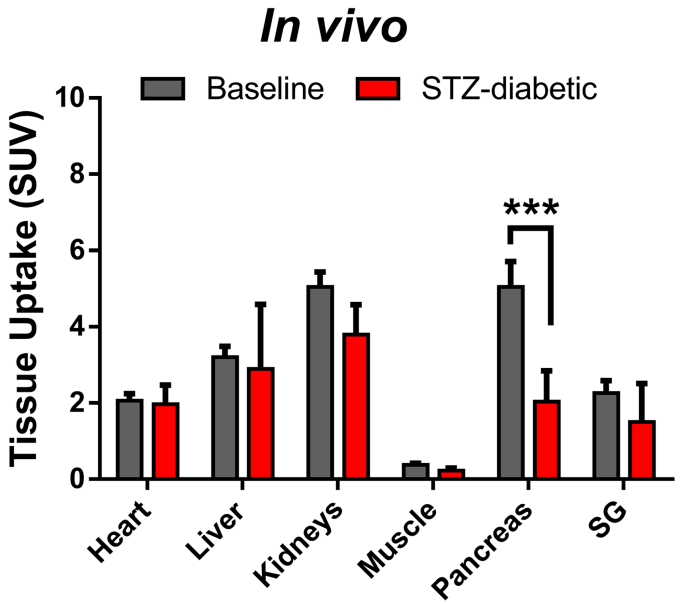

Figure 3.32: PET ROI analysis of ^{52}Mn uptake in type 1 diabetes mouse model. A significant ^{52}Mn uptake reduction is seen in STZ-treated mice. Values represent mean $\pm$ SD; *** $P < 0.0001$; $n = 3$

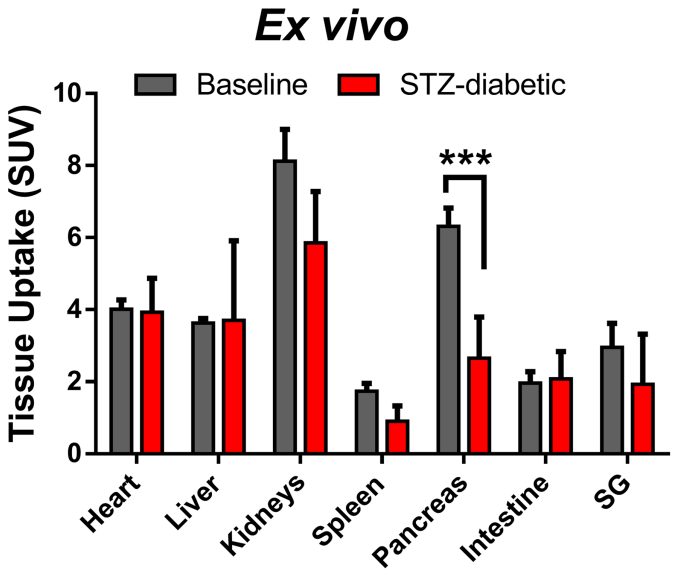

Figure 3.33: Ex vivo quantification of ^{52}Mn biodistribution in type 1 diabetes mouse model. A significant ^{52}Mn uptake reduction is seen in STZ-treated mice. Values represent mean ± SD; *** P < 0.0001; n = 3

$^{52}Mn^{2+}$ uptake in pre-type 2 diabetic mice

Imaging studies were also performed in C57BL/6J mice carrying the lepob (ob/ob) spontaneous mutation that result in animal obesity and pre-diabetic syndrome (i.e. pre-type 2 diabetes). Increased $^{52}Mn^{2+}$ accumulation in the pancreas of pre-type 2 diabetic ob/ob mice was observed in the PET data (Figure 3.34). Pancreatic uptake was 4.89 ± 0.68 SUV in lean mice and 7.27 ± 1.03 SUV in the pre-type 2 diabetic ob/ob mice (Figure 3.35), 1 h after administration of $^{52}Mn^{2+}$ (n=3). Ex vivo biodistribution corroborated the statistically significant differences in pancreatic SUV between the groups (P < 0.0001; Figure C.1 and Table C.5). Uptake in the liver and salivary gland was very similar in obese and lean animals with SUVs of 3.68 ± 0.25 vs. 3.40 ± 0.73 and 2.40 ± 0.20 vs. 3.11 ± 1.05, respectively.

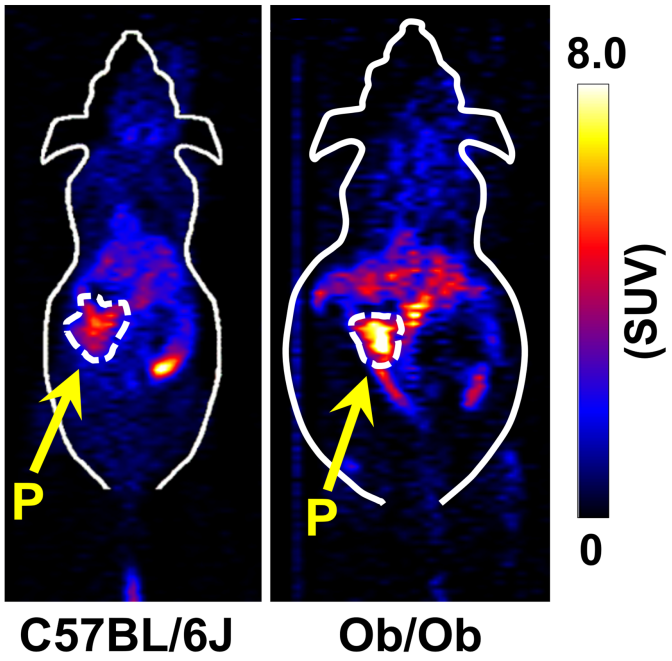

Figure 3.34: ^{52}Mn-PET imaging in pre-type 2 diabetic ob/ob mice. Coronal PET images acquired 1 h after ^{52}Mn(II) administration. The pancreas can be readily delineated in the images of both obese (ob/ob) mice and lean (C57BL/6J) controls. Yellow arrows point to hand-drawn contours of the pancreas.

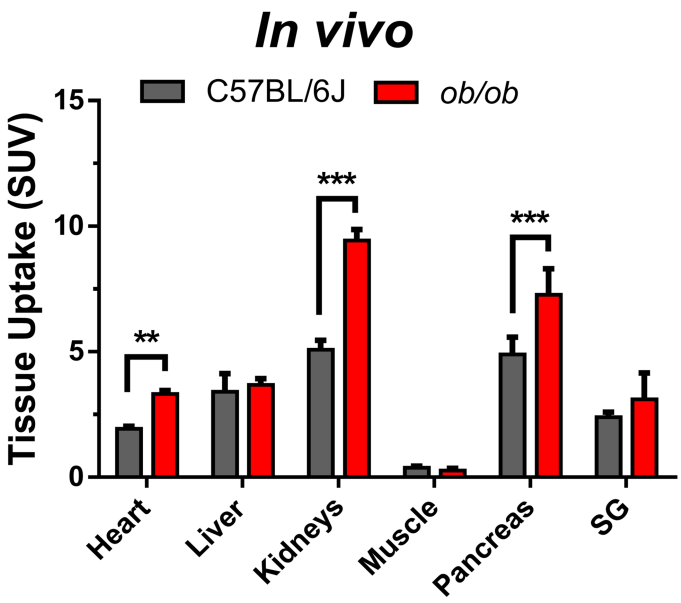

Figure 3.35: ^{52}Mn in pre-type 2 diabetic ob/ob mice. PET ROI quantification expressed as SUV indicated a significant difference in $^{52}Mn^{2+}$ pancreatic uptake between groups. Values represent mean ± SD; *** $P < 0.0001$; n = 3; SG: salivary gland.

3.6.4 Discussion

The loss/dysfunction of pancreatic β-cells is the cornerstone of both type 1 and type 2 diabetes (Weir et al., 2004). The ability of β-cells to sequester divalent metal ions (e.g. Ca^{2+}, Mn^{2+}, Zn^{2+}, and Co^{2+}) is essential to the production and release of insulin. While β-cell function has been widely investigated based on the measurement of Ca^{2+} currents in vitro (Atwater et al., 1979), little progress has been achieved in exploring β-cell divalent metal intake for measurement of function in vivo. Part of this is due to the lack of effective methods to track the distribution of most of these metals in vivo. Fortunately, Mn^{2+} has both magnetic and nuclear properties that facilitate its noninvasive detection by both MRI and PET. In the present work, we report the use of radioactive manganese for noninvasive

PET imaging of the mouse pancreas. When injected intravenously, $^{52}Mn^{2+}$ accumulated largely into pancreatic tissue with exceptionally fast blood extraction kinetics. $^{52}Mn^{2+}$ uptake in the pancreas, which peaked within minutes following administration in healthy mice, was on the order of 5-6 SUV with slow clearance half-life of approximately 8 days.

Two isotopes of manganese present themselves as excellent candidates for manganese-based PET, ^{52}Mn ($t_{1/2}$: 5.6 d, β+: 29.6%, $E\beta_{ave}$: 0.24 MeV) and ^{51}Mn ($t_{1/2}$: 46.2 min, β+: 97.1%, $E\beta_{ave}$: 0.96 MeV). Due to its high energy gamma emissions and relatively long half-life, ^{52}Mn is best suited to preclinical small animal research. ^{51}Mn on the other hand has excellent decay properties which are more amenable to clinical applications. With its longer half-life, ^{52}Mn can be easily shipped nationally or internationally whereas ^{51}Mn must be produced and utilized on-site. The most common production strategy for ^{52}Mn involves the low energy (E_{p+} < 20 MeV) proton irradiation of ^{nat}Cr metal targets. Several recent publications have addressed the radiochemical isolation of ^{52}Mn from ^{nat}Cr (Lewis et al., 2015; Buchholz et al., 2015; Graves et al., 2015; Lahiri et al., 2006; Topping et al., 2013; Buchholz et al., 2013). In this work, we employed an ethanol/HCl-based anion exchange chromatography that allows for a ^{52}Mn recovery efficiency of greater than 60% in less than 2 hours. Overall, contamination including heavy metals such as ^{nat}Cr (< 0.1 μg) was very low, making the isolated ^{52}Mn suitable for preclinical investigations.

A key finding of our work was that the observed pancreatic radioactivity was a result of the specific uptake of $^{52}Mn^{2+}$ by pancreatic β-cells. By pharmacologically

manipulating the mechanism of insulin secretion in isolated islets in vitro, we were able to correlate the uptake of radioactive $^{52}Mn^{2+}$ with Ca^{2+} uptake. This agrees with other in vitro/ex vivo studies using non-radioactive Mn^{2+} that reported a correlation between Mn^{2+} uptake and β-cell functional capacity (Rorsman et al., 1982; Rorsman et al., 1983; Gimi et al., 2006; Antkowiak et al., 2011). Similarly, in vivo studies demonstrated that the chemical inhibition of insulin release, using nifedipine or diazoxide, resulted in a drastic decline in the accumulation of $^{52}Mn^{2+}$ within the pancreas. In addition, the stimulation of insulin secretion with glibenclamide (5 mg/kg) led to an increase in $^{52}Mn^{2+}$ uptake in the pancreas. Overall, our results indicated that the $^{52}Mn^{2+}$ uptake observed in the pancreas was largely mediated by and dependent on the functional β-cell mass.

Our next question was if this method was sensitive enough to detect changes in β-cell mass that occur during diabetes progression and disease. First, we employed an experimental animal model of STZ-induced type 1 diabetes, which showed a ~60% reduction in the pancreatic accumulation of $^{52}Mn^{2+}$, while uptake in other organs remained unaltered. This indicates the ability of radiomanganese PET imaging for revealing extreme cases of β-cell loss. Probing the gradual loss of β-cell mass under chronic exposure to low doses of STZ using $^{52}Mn^{2+}$ ($t_{1/2}$= 5.6 d) was not feasible due to its long radioactive half-life. To this end, future longitudinal studies employing ^{51}Mn ($t_{1/2}$= 46 min) are warranted.

Equally relevant results were observed in the obese mouse (ob/ob) model of pre-type 2 diabetes, where significant ($P < 0.0001$) enhancement in pancreatic uptake of

$^{52}Mn^{2+}$ was observed. These results agree with previous reports showing that ob/ob mice do not progress to type 2 diabetes, but rather present markedly higher β-cell mass compared with lean mice, at 10 weeks of age (Bock et al., 2003; Golson et al., 2010). An increased β-cell mass in this population is consistent with the increased pancreatic uptake of $^{52}Mn^{2+}$ that we have observed herein, which demonstrate the potential of radiomanganese PET for noninvasively quantifying variations in β-cell mass within the context of type 2 diabetes, particularly at the early stage of disease progression.

As there can be significant changes in β-cell function long before changes in mass are observed (Ha et al., 2016), it is advantageous that the relative uptake of $^{52/51}Mn^{2+}$ in vivo depends on the functional β-cell mass. This ability has the potential to shed light on the survival of β-cell transplants, and on the rate of functional β-cell mass decline in asymptomatic type 1 diabetic patients. Whether or not $^{52/51}$Mn-PET is capable of measuring subtle changes in this parameter is the pivotal question to its clinical significance. The diffusion of Mn^{2+} through β-cell VDCCs depends on functional activation by glucose or drug-based stimulation. This has been shown here through in vitro and in vivo functional suppression and enhancement studies. For a given state of glucose activation, the amount of Mn^{2+} cellular internalization is relative to the number of available VDCCs, which should be proportional to functional β-cell mass. Furthermore, accurate quantification of β-cell mass will require subtraction of nonspecific exocrine pancreas tracer uptake of the radiotracer. This may be accomplished through pharmacological manipulation to acutely suppress β-cell uptake using nifedipine, isoflurane, diazoxide,

or other suppressing agents.

Our studies also provided valuable information on the kinetics of the whole-body distribution of $^{52}Mn^{2+}$. Besides specifically accreting in pancreatic islets, $^{52}Mn^{2+}$ also accumulated in the liver, heart, kidneys, and salivary gland. Despite the significant kidney uptake, no clear sign of renal excretion was observed and most of the $^{52}Mn^{2+}$ clearance occurred through the hepatobiliary system. From the analysis of the image-derived dynamic TAC of the heart, we estimated a $^{52}Mn^{2+}$ circulation half-life of 10.7 $\pm$ 3.5 s following a rapid bolus injection, which aligned with previous studies showing an extremely fast (~0.8 min) blood clearance of ^{54}Mn in dogs (Atkins et al., 1979). Such fast extraction kinetics and the lack of evidence of $^{52}Mn^{2+}$ metabolites in blood indicate that compartmental modeling could be used to describe $^{52}Mn^{2+}$ uptake in a more quantitative manner. A stable residual myocardial uptake was observed after complete blood clearance, approximately 1 min after injection. Of note was the marked underestimation of myocardial uptake by PET compared to biodistribution results, with an average recovery coefficient of 0.54. This is an inherent limitation of the PET imaging-based quantification of small volumes such as the myocardial wall, which in mice is affected by severe partial volume effects (Erlandsson et al., 2012; Gargiulo et al., 2012).

We faced several challenges during our preclinical PET imaging. Besides the partial volume effect which affects image-derived quantitation, pancreas delineation was difficult due to the lack of anatomical reference and the proximity of the pancreas to kidneys. Furthermore, the observed pancreatic uptake during the dynamic studies was

significantly lower compared to the static scans. Through further investigation we determined that this was due to the mice being anaesthetized by isoflurane during $^{52}Mn^{2+}$ administration, as isoflurane is suggested to prevent K_{ATP} inhibition (Desborough et al., 1993; Graves et al., 2016). These experiments are detailed in the Supplementary Materials Section 3.7. These challenges are largely confined to small animal research, however, as accurate pancreas delineation, reduced impact of partial volume effects, and non-anaesthetized subjects are all possible by scaling up to humans.

Several PET tracers have been studied as potential β-cell imaging agents. [^{11}C]-Dihydrotetrabenazine (DTBZ) and the ^{18}F-labeled DTBZ analog FP-(+)-DTBZ have been shown to have high affinity for the type 2 vesicular acetylcholine transporter (VMAT2), which is expressed on the surface of rodent β-cells but appears to be entirely absent from pancreatic exocrine tissue (Eriksson et al., 2010; Kung et al., 2008; Simpson et al., 2006; Singhal et al., 2011). Unfortunately, primate models have shown very low pancreatic uptake of [^{11}C]-DTBZ, which suggests that the degree of VMAT2 expression is species-dependent (Schafer et al., 2013; Murthy et al., 2008; Moore 2009). More work is needed in quantifying human β-cell expression of VMAT2, and how expression density is related to β-cell function. Another category of tracers includes radiolabeled (e.g. ^{18}F, ^{68}Ga, ^{64}Cu, ^{111}In) derivatives of exendin-4, a glucagon-like protein-1 receptor (GLP-1R) agonist (Brom et al., 2014; Kiesewetter et al., 2012; Kirsi et al., 2014; Selvaraju et al., 2013; Wu et al., 2011). Fluorescence microscopy has shown that GLP-1R is only located on β-cells within the human pancreas (Tornehave et al., 2008), making it an attractive

molecular imaging target due to its specificity. Unfortunately, exendin-4 also suffers from low pancreatic uptake (less than 0.3 %ID/g in Sprague-Dawley rats at 1 h post injection whereas proximal kidney uptake was greater than ~25% ID/g) (Bandara et al., 2016). In general, the implementation of tracers targeting surface receptors of β-cells is extremely challenging, considering the low total mass of β-cells, diffuse pancreatic distribution, and heterogeneous receptor expression.

Aside from following the decline in β-cell mass of type 1 diabetic patients, there is a pressing need for a noninvasive method for longitudinal imaging of pancreatic islet transplants. Islet transplantation has been shown to lead to insulin independence for several years in patients with type 1 diabetes (Eter et al., 2015; Paty et al., 2004), but has not been widely adopted due to the need for donor tissues. Recent advances in selective stem cell differentiation techniques will likely lead to wider clinical adoption of β-cell transplantation therapies (Vegas et al., 2016). The ability to noninvasively track the survival and function of transplanted β-cells would enable research into the patient-specific efficacy of immune-modulating therapies and the development of new therapeutic strategies (Gotthardt et al., 2014). The use of ^{51}Mn-PET for monitoring islet transplant survival is compelling, since it can be performed repeatedly over time.

In conclusion, the prominent pancreatic uptake, rapid localization kinetics, and well characterized metabolic pathways of $^{51/52}Mn^{2+}$ make it a promising molecular imaging agent for the noninvasive assessment of β-cell function and its correlation with β-cell mass.

3.7 Isoflurane-induced hyperglycemia

3.7.1 Introduction

Isoflurane, halothane, desflurane, and sevoflurane are widely used as general anesthetics, and all have a molecular structure consisting of highly-fluoridated organic backbones. Isoflurane and halothane are so ubiquitous that they are on the World Health Organization's list of essential medicines (DiPiro et al., 2002). Volatile anesthetics have excellent safety records overall, and have a rapid onset and offset following administration and cessation making them ideal candidates for outpatient anesthesia and veterinary applications, although volatile anesthetics are also frequently used for long-duration surgical procedures (Landoni et al., 2008).

Although largly considered safe, volatile anesthetics are known to inhibit the secretion of insulin during administration (Kehl et al., 2002; Camu, 1976; Diltoer et al., 1988). During extended procedures this reduction in blood insulin has been shown to lead to intraoperative hyperglycemia, which increases the risk of intraoperative myocardial infarction. The exact mechanism of action for suppression of insulin secretion is not well established, but the leading theory is that volatile anesthetics directly activate ATP-sensitive potassium channels of beta cells (Tanaka et al., 2003). The mechanism for suppression of insulin secretion is debated, but one prominent theory is that isoflurane directly prevents inhibition of adenosine triphosphate-sensitive potassium channels (K_{ATP}) preventing β-cell membrane depolarization. Without plasma membrane depo-

larization, voltage dependent calcium channels (VDCCs) do not open which prevents activation of insulin exocytosis.

In the previous chapter, ^{52g}Mn was shown to behave chemically like Ca^{2+} allowing for rapid VDCC transport, making it well suited for β-cell function investigations. The objective of this work was to demonstrate the suppressive effect that isoflurane has on mouse pancreatic uptake of ^{52}Mn, confirming the prevention of β-cell membrane depolarization.

3.7.2 Methods

^{52}Mn was produced as previously described by irradiation of ^{nat}Cr separation by ethanol-based anion exchange chromatography. The final ^{52}Mn product was eluted in 0.01 M pH 6.0 NaOAc. 1.0-1.5 MBq of ^{52}Mn was used for each subject. Fasted ICR mice were divided into three treatment groups:

- Group 1 received an intravenous (IV) bolus of ^{52}Mn.
- Group 2 received an intraperitoneal (IP) injection of glucose (1 mg/kg), then an IV bolus of ^{52}Mn after 10 minutes had elapsed.
- Group 3 received an IV bolus of glucose (1 mg/kg), then an IV infusion of ^{52}Mn from 5-15 min post-glucose.

Half of each group received treatment while awake ($n = 3$–6), and half received treatment under isoflurane anesthesia ($n = 3$). After a total of one hour had elapsed a static PET scan was collected, subjects were sacrificed, and ex vivo ^{52}Mn biodistribution

was measured by gamma counting. On a subset of subjects, dynamic PET data was acquired during ^{52}Mn IV bolus injection for kinetic analysis. PET regions of interest (ROIs) were manually placed over organs with significant ^{52}Mn uptake.

3.7.3 Results and Discussion

Pancreatic uptake of ^{52}Mn was found to be significantly lower in all three groups under the influence of isoflurane anesthesia compared to non-anesthetized controls, as shown in Figure 3.37. In mice injected with only an IV bolus of ^{52}Mn, pancreatic uptake decreased from 20.4 ± 3.23 %ID/g to 7.3 ± 1.7 %ID/g ($p = 0.0002$) under isoflurane. In mice injected with IP glucose 10 minutes prior to a bolus injection of ^{52}Mn, uptake decreased from 20.0 ± 4.35 %ID/g to 13.2 ± 2.04 %ID/g ($p = 0.028$). In the third group, with mice injected with IV glucose 5 minutes prior to a ^{52}Mn IV infusion lasting 10 minutes pancreatic uptake was found to be reduced from 24.0 ± 2.5 %ID/g to 13.5 ± 2.0 %ID/g ($p = 0.001$) while under isoflurane anesthesia. PET ROI quantification was found to be in good agreement with ex vivo biodistribution results.

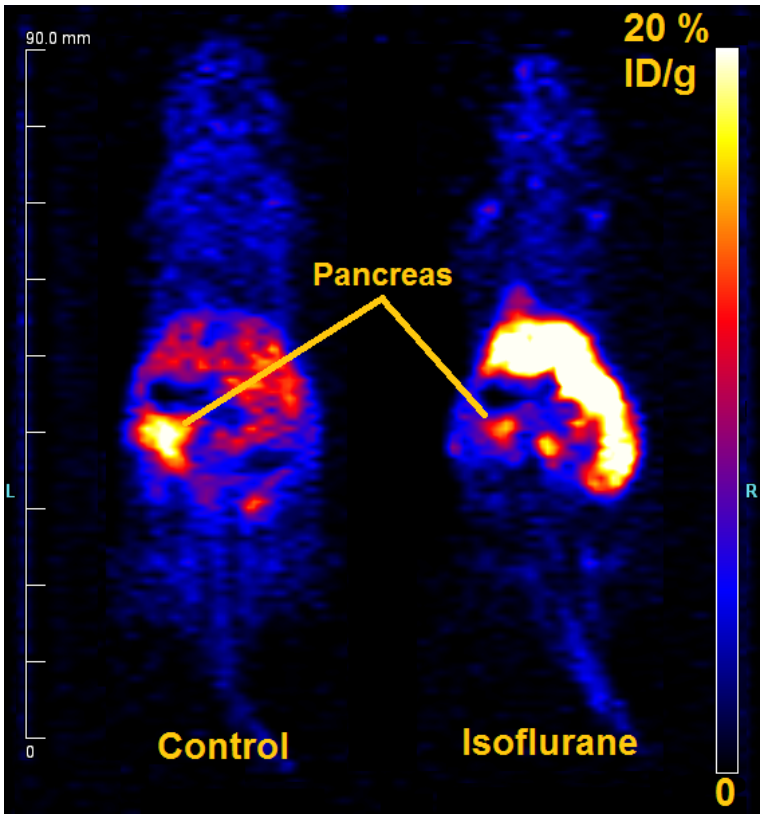

Figure 3.36: Sagittal PET slice comparison of ICR mice injected with a rapid bolus of ^{52}Mn while awake (A) and while under isoflurane anaesthesia (B). Significantly higher ^{52}Mn accumulation is observed in awake subjects.

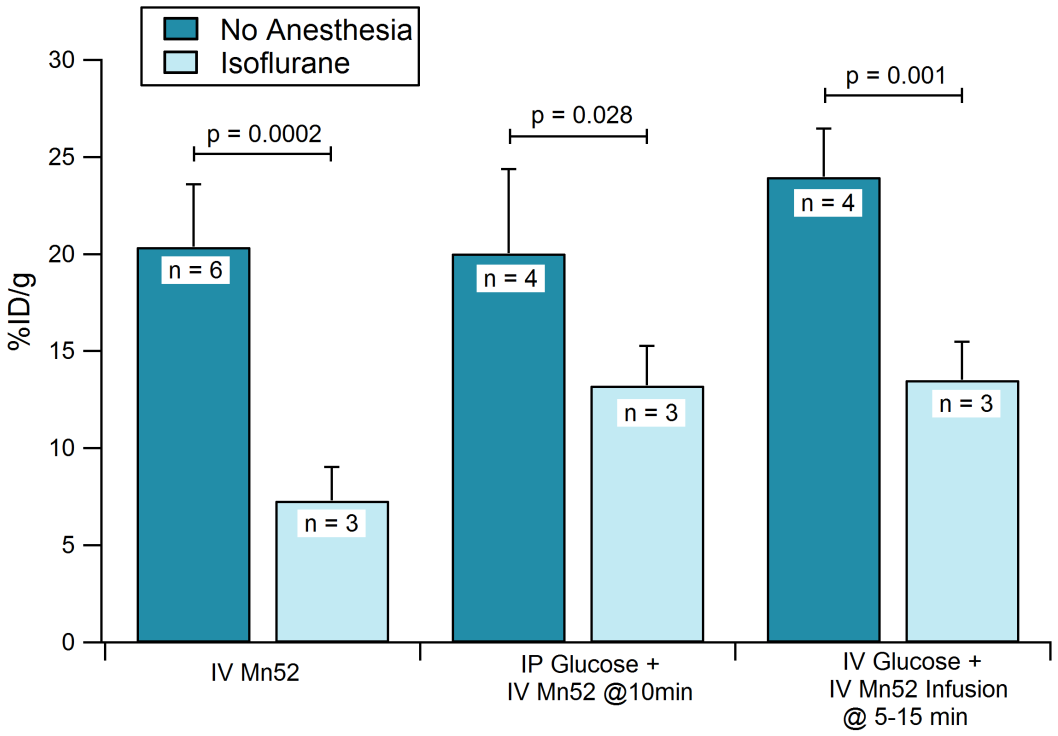

Figure 3.37: *Ex vivo* gamma counting of ^{52}Mn uptake in the ICR mouse pancreas following three treatments with and without isoflurane. In all three cases, pancreatic uptake of ^{52} is significantly inhibited.

In conclusion, significant suppression of pancreatic ^{52}Mn uptake by isoflurane was observed for all three groups. This result supports the theory that isoflurane prevents β-cell plasma membrane depolarization by activating ATP-sensitive potassium channels. To our knowledge, this work constitutes the first direct VDCC-based evidence for this theory.

4 MEASUREMENT OF FE+P NUCLEAR EXCITATION FUNCTIONS

4.1 Background and Motivation

Radioisotopes of medical interest which can be produced using intermediate-energy proton accelerators ($30 < E_p < 200$ MeV) include the parent nuclides in generator systems $^{82}Sr/^{82}Rb$, $^{68}Ge/^{68}Ga$, $^{44}Ti/^{44}Sc$, $^{72}Se/^{72}As$, as well as direct production of ^{225}Ac. Both the Los Alamos Neutron Science Center's (LANSCE's) Isotope Production Facility (IPF) and the Brookhaven National Lab's (BNL's) Brookhaven Linac Isotope Producer (BLIP) are well suited to producing these isotopes. The national clinical supply for $^{82}Sr/^{82}Rb$ and $^{68}Ge/^{68}Ga$ generators is currently shared between these facilities by employing alternating six month run-cycles. Research tracers and generator radionuclides are produced intermittently depending on demand and the needs of the isotope program. The large-scale production of these isotopes is necessarily preceded by accurate nuclear excitation function measurements at appropriate energies.

Recently ^{52}Mn ($t_{1/2}$ = 5.59 d, β^+ = 29.6%, $E\beta^+_{ave}$= 0.24 MeV) and ^{55}Co ($t_{1/2}$ = 17.5 h, β^+ = 76%, $E\beta^+_{ave}$ = 0.57 MeV) have been investigated preclinically as positron emission tomography (PET) imaging tracers due to their favorable physical, chemical, and biological properties (Graves et al., 2015; Lagunas-Solar et al., 1979; Mastren et al., 2015; Topping et al., 2013; Valdovinos et al., 2014). Mn^{2+} has been shown to behave biologically like Ca^{2+}, making it an excellent candidate for applications such as neural tract tracing and pancreatic β-cell mass determination (Graves et al., 2016; Hernandez et al., 2016). For

intravenous injections of $^{52g}Mn^{2+}$, a blood clearance of under 5 minutes suggests that $^{51}Mn^{2+}$ ($t_{1/2}$ = 46.2 m, β^+ = 97.1%, $E\beta^+_{ave}$ = 0.962 MeV) could be a clinically desirable surrogate for ^{52g}Mn from a dosimetry and pharmacokinetic perspective (Graves et al., 2016; Hernandez et al., 2016). Both ^{52}Mn and ^{55}Co have well established chelation chemistries, and are rapidly and stably coordinated by DOTA at a neutral pH. With established chelation methods, both ^{52}Mn and ^{55}Co may be employed in a variety of molecular imaging applications, such as in vivo tracking of monoclonal antibodies (Graves et al., 2015). Mn^{2+} is also a versatile T1-shortening magnetic resonance imaging (MRI) contrast agent, which could enable future dual modality PET/MR applications (Brunnquell et al., 2016; Lewis et al., 2015). In addition to ^{52g}Mn and ^{55}Co, ^{58m}Co has been suggested to have decay properties suitable for Auger electron therapeutic applications, and to this end several preclinical studies are underway (Bernhardt et al., 2001; Valdovinos et al., 2016; Valdovinos et al., 2016).

The radioactive half-lives of ^{55}Co and ^{52}Mn are conducive to national and international transport, respectively. Some issues which need to be addressed prior to considering large-scale production of these isotopes include preclinical demand, target design considerations, radionuclide yield, radionuclidic purity, and methods for radiochemical isolation. The goal of this work was to measure the nuclear formation cross sections of ^{52}Mn, ^{54}Mn, ^{55}Co, and others from ^{nat}Fe and ^{nat}Cu foils in an attempt to address expected radionuclide yield and purity. Furthermore, we employ multiple monitor reactions to correct for beam energy inaccuracies derived from proton transport simulations and

calculations.

4.2 Experimental and Analytic Methods

4.2.1 Target-stack design and Irradiation

A target stack was constructed using 50 μm and 25 μm ^{nat}Fe foils (99.99%, GoodFellow Metals, Coraopolis, PA, 15108-9302, USA), 100 μm and 30 μm ^{nat}Cu foils (99.9%, Good-Fellow Metals), and 100 μm ^{nat}Al foils (99.997%, Alfa Aesar, Ward Hill, MA, 01835, USA). Foils were cut into 2.5 cm squares and weight measurements were taken. Degrader foil widths and heights were each measured with a Vernier caliper in three places. Target foil thicknesses (atoms/cm2) were calculated from width, height, and weight measurements. Foils were then sealed in 25 μm Kapton® polyimide tape with a silicone-based adhesive backing. The resulting encapsulated target foils were affixed to frames and placed within a water-proof target stack box, containing degrader layers, shown in Figure 4.1. Degrader densities were calculated by dimensional measurements and weighing, prior to being affixed to the target box by electron beam welding. Each target stack compartment contained two ^{nat}Fe foils, one ^{nat}Cu foil, and one ^{nat}Al foil. At the front and rear of the target stack, 130 μm thick stainless steel layers were employed as beam profile monitors. Details of this target stack design are listed in Table 1.

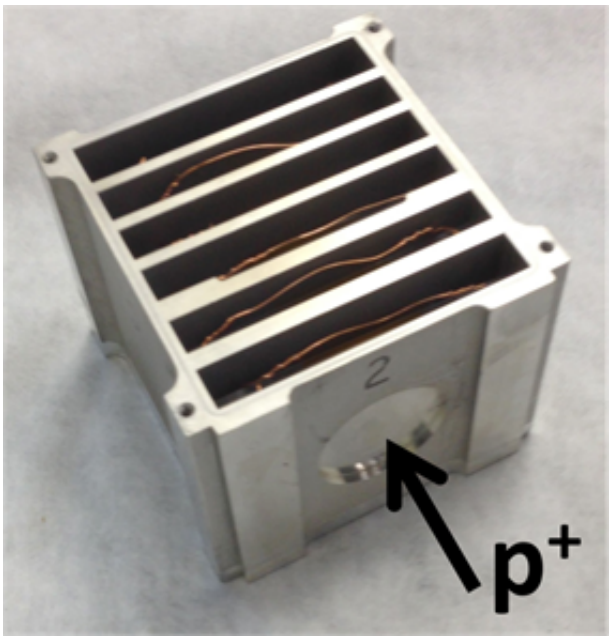

Figure 4.1: Photograph of target stack before being sealed with o-ring bearing lid. Beam entrance window is shown, as are Al degrader layers between stack compartments. Degrader layers were measured and weighed before being electron-beam welded into place. Target frame bundles are held together by copper wire, as shown.

The assembled target stack was irradiated at the Los Alamos National Laboratory (LANL) Isotope Production Facility (IPF) with approximately 99 nA of incident protons for one hour. Nominal proton energy was 100 MeV, but time-of-flight measurements during the irradiation indicated an average incident proton energy of 99.7 MeV. This measured incident energy was used for further calculations and simulations. After passing through an entrance window, a layer of cooling water, and the target window, the average beam energy was approximately 90 MeV. Following irradiation, the target-stack was disassembled, and the encapsulated foils were wiped clean of surface contamination. Foils were monitored for gamma emissions beginning approximately 24 hours following irradiation.

4.2.2 Gamma spectroscopy

Following irradiation, gamma spectroscopy was performed using two high-purity germanium (HPGe) detectors at LANL (p-type Al-window ORTEC GEM detectors) and one detector at the University of Wisconsin - Madison (UW) (Canberra C1519). Early post-irradiation assays were done at LANL, and later assays were done at UW-Madison. In the case of LANL data, spectral peak areas were determined using the SPECANAL code, which is an in-house revised version of the legacy GAMANAL code (Gmmink et al., 1972). In the case of UW data, spectral peak areas were determined using the SAMPO code, which employs particularly sophisticated peak-fitting methods (Aarnio et al., 1992). Decay-corrected comparisons between UW and LANL quantification agreed within 5%. Uncertainty in activity quantification was calculated as the quadrature sum of (1) the statistical counting uncertainty, (2) uncertainty in literature branching ratio data, and (3) uncertainty in the HPGe efficiency calibrations.

4.2.3 Initial Beam Energy Determination

Average beam energy for each target position was estimated using the Monte Carlo N-Particle (MCNP6) code and by in-house calculations using Anderson & Ziegler (A&Z) analytic formalisms (Ziegler, 1999; Goorley et al., 2012). A&Z calculations provide reasonable estimations of average beam energy, but MCNP6 simulations yield both average energy and the energy distribution at each target position (Marus et al., 2015). A plot of proton energy distribution full-width half-max (FWHM) vs. average proton energy

from MCNP6 results, shown in Figure 4.2, was used for further FWHM calculations.

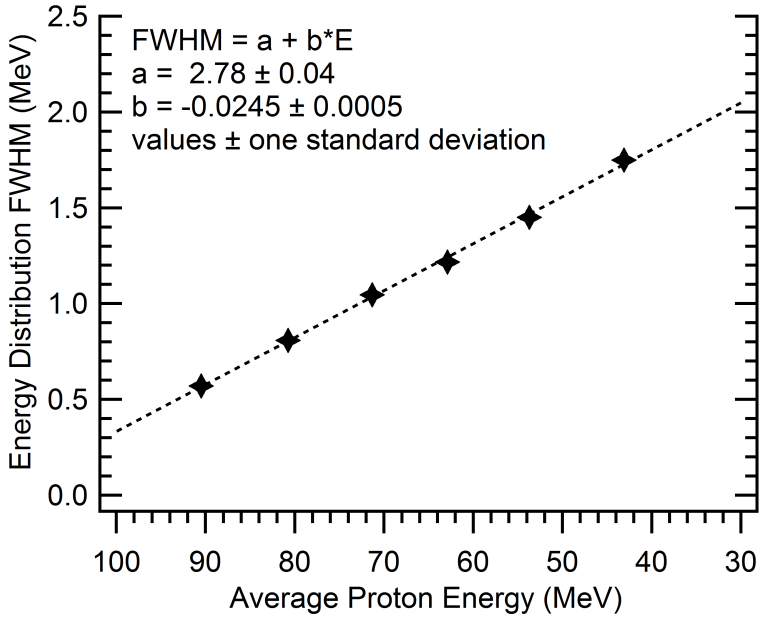

Figure 4.2: MCNP6 simulation results showing energy distribution full-width half-max (FWHM) as a function of average proton energy in each target stack compartment. A linear least-squares fit was used for determining proton energy FWHM at non-simulated energies.

4.2.4 Monitor Reactions

Four monitor reactions were selected in an attempt to provide accurate measures of proton fluence with minimal neutron contamination: $^{nat}Cu(p,x)^{56}Co$, $^{nat}Cu(p,x)^{62}Zn$, $^{nat}Cu(p,x)^{65}Zn$, and $^{nat}Al(p,x)^{22}Na$. These reactions have been extensively characterized, and are recommended by the IAEA as proton monitor reactions (Tarkanyi et al., 2001). For fluence calculations, recommended IAEA cross section values were used. In-house evaluated data were used above 60 MeV for the $^{nat}Cu(p,x)^{62}Zn$ reaction. Proton fluence uncertainty was calculated as the quadrature sum of (1) the uncertainty in recommended

monitor reaction cross sections, (2) monitor reaction isotope quantification uncertainty, (3) uncertainty in the target foil areal density, and (4) the uncertainty in the "effective cross section" from the proton energy distribution FWHM at each monitor foil. Note that uncertainty (1) and (4) both have an energy dependence which must be accounted for in subsequent calculations.

4.2.5 Final Energy Determination: Multiple Monitor Reaction Variance Minimization

Making the assumptions that monitor reaction-derived proton fluence should agree across multiple monitor reactions within the same target stack compartment and that the proton energy distribution FWHM values predicted by MCNP6 simulations are accurate, then it is possible to use multiple monitor reactions to determine the average proton energy at each monitor foil. This approach has the potential to greatly reduce proton energy uncertainties toward the rear of a target stack. Monitor reaction-derived fluence discrepancies have previously been described (Marus et al., 2015), pointing to uncertainties in degrader thickness, degrader density, incident beam energy, and proton stopping power data.

In this work, agreement in the proton fluences derived from the four monitor reactions on ^{nat}Cu and ^{nat}Al foils in the final stack compartment was obtained by minimizing variance in the calculated fluence as a function of Al degrader density in analytic A&Z proton transport calculations. Varying degrader density has little effect on average beam

energy near the front of the stack, but changes the average proton energy greatly toward the rear of the stack. This minimization method, shown in Figure 4.3, is a straightforward and effective way of estimating average beam energy. An average proton energy of 35.1 MeV entering the last compartment was found, approximately 8 MeV lower than MCNP6 simulations and approximately 6 MeV lower than A&Z calculations with a nominal Al density. The impact of this variance minimization process on monitor reaction-derived proton fluence is shown in Figure 4.4. Although only degrader density was varied in this approach, it is likely that the source of this energy discrepancy is a combination of uncertainty in incident beam energy, literature stopping powers, target geometry, and degrader density.

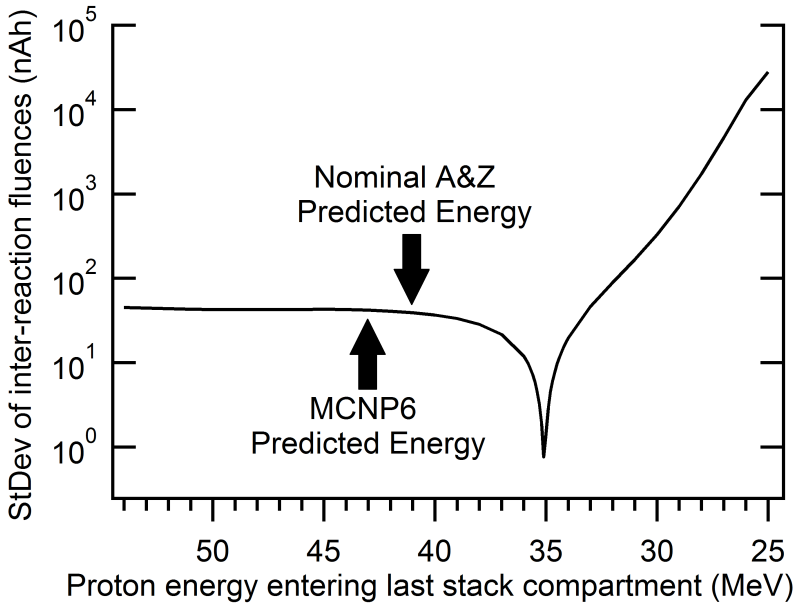

Figure 4.3: Results of varying degrader density in analytic A&Z calculations on inter-monitor reaction fluence standard deviation. Varying degrader density has the effect of non-linearly varying the average beam energy in each compartment. This non-linear dependence on density has nearly the same functional impact as variations in the incident beam energy. Arrows indicate the predicted average beam energy in the last stack compartment by MCNP6 simulation and nominal A&Z calculations. A clear minimum from this approach is seen at 35.1 MeV, suggesting the initial beam energy estimations by nominal A&Z calculations and by MCNP6 simulation are significantly higher than what was experimentally observed.

Target layer	Nominal Thickness	Measured Thickness (atoms/cm^2)	Thickness Uncertainty (%)
SS Profile Monitor	130 μm	-	-
Fe-1	50 μm	3.56×10^{20}	0.09%
Al-1	100 μm	5.88×10^{20}	0.33%
Cu-1	100 μm	9.26×10^{20}	0.18%
Fe-2	50 μm	3.88×10^{20}	0.17%
Al Degrader-1	4.983 mm	-	-
Fe-3	50 μm	3.48×10^{20}	0.18%
Al-2	100 μm	5.94×10^{20}	0.05%
Cu-2	30 μm	2.23×10^{20}	0.87%
Fe-4	50 μm	3.78×10^{20}	0.19%
Al Degrader-2	4.394 mm	-	-
Fe-5	50 μm	3.41×10^{20}	0.05%
Al-3	100 μm	5.94×10^{20}	0.11%
Cu-3	30 μm	2.24×10^{20}	0.41%
Fe-6	50 μm	3.80×10^{20}	0.14%
Al Degrader-3	3.468 mm	-	-
Fe-7	25 μm	1.87×10^{20}	0.25%
Al-4	100 μm	5.93×10^{20}	0.12%
Cu-4	30 μm	2.27×10^{20}	1.24%
Fe-8	25 μm	1.77×10^{20}	0.55%
Al Degrader-4	3.460 mm	-	-
Fe-9	25 μm	1.86×10^{20}	0.44%
Al-5	100 μm	5.90×10^{20}	0.14%
Cu-5	30 μm	2.21×10^{20}	0.98%
Fe-10	25 μm	1.69×10^{20}	0.21%
Al Degrader-5	3.465 mm	-	-
Fe-11	25 μm	1.78×10^{20}	0.17%
Al-6	100 μm	5.92×10^{20}	0.14%
Cu-6	30 μm	2.23×10^{20}	1.27%
Fe-12	25 μm	1.84×10^{20}	0.48%
SS Profile Monitor	130 μm	-	-

Table 4.1: Target stack order and foil thicknesses, where the proton beam travels through the stack in the order shown in the table. Uncertainty in areal density is calculated from uncertainties in the width, height, and mass of individual foils. Degrader thickness measurements are omitted due to the proton transport methods used herein.

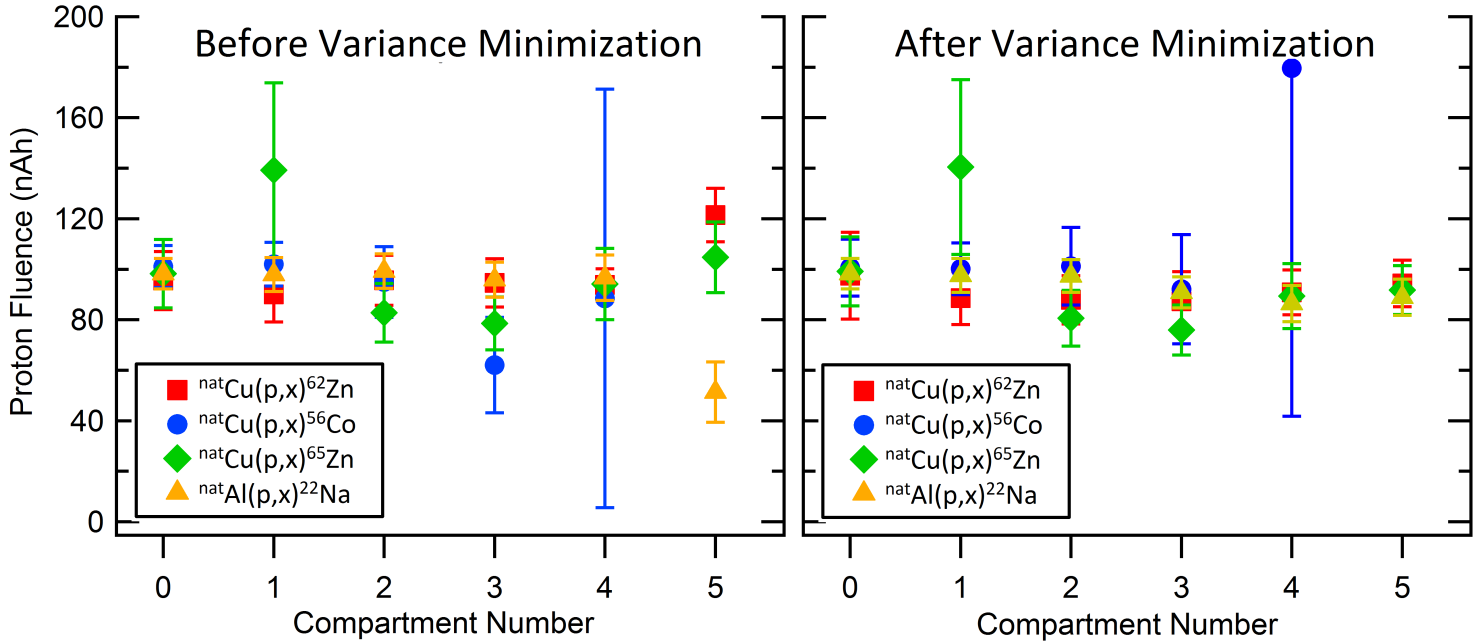

Figure 4.4: Results of varying degrader density in analytic A&Z calculations on inter-monitor reaction fluence variance. Compartment #0 resides at the front of the target stack, while compartment #5 resides at the rear. A significant reduction in monitor reaction variance throughout the entire stack is seen after employing the variance minimization approach in compartment #5. This result is further evidence that multiple monitor reaction variance minimization has the potential to significantly reduce energy uncertainties in stacked-foil cross section measurement experiments. The variability of $^{nat}Cu(p,x)^{56}Co$ in compartment 4 and absence in compartment #5 is due to the rapid drop off in this excitation function at these energies.

4.2.6 Fluence Loss Characterization

As the beam travels through the stack, small angle deflections cause a broadening in the beam profile. Using the activated stainless steel profile monitors from the front and rear of the target stack, Gafchromic film was exposed and analyzed yielding beam profile measurements, shown in Figure 4.5. These profile measurements were used to determine a theoretical fluence loss based on the finite target foil areas. This theoretical fluence loss agreed within error compared with monitor reaction derived fluence loss, as shown in Figure 4.6.

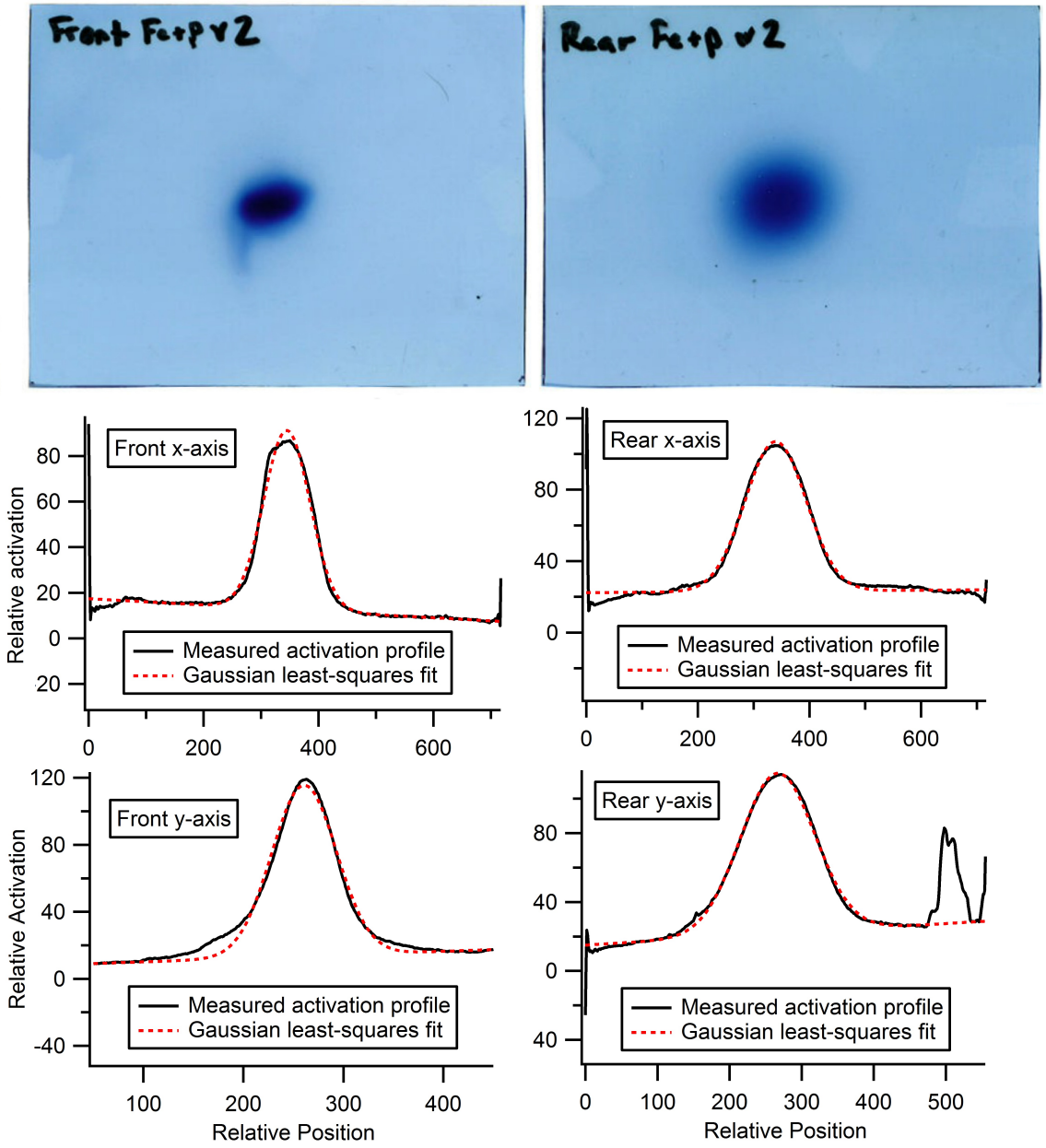

Figure 4.5: Front and rear target stack beam profile measurements. Stainless steel profile monitors were used to expose Gafchromic™ film, which was analyzed in ImageJ. Thin rectangular ROI's were placed across each beam spot, and the collapsed profile was modeled by ordinary least-squares fitting using a Gaussian function with linear background offset.

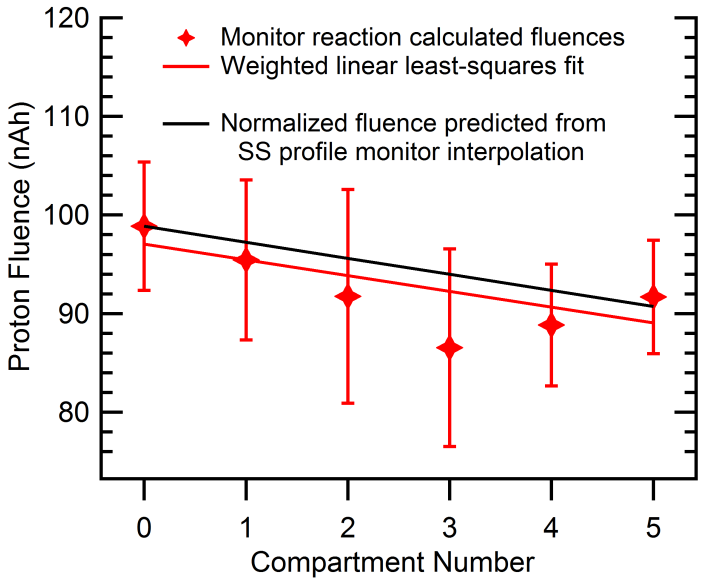

Figure 4.6: Final fluence measurements as a function of target stack compartment number following monitor reaction derived proton fluence variance minimization. The red line represents a weighted linear line of regression indicating a drop in proton fluence of 7.2% as the beam travelled through the target stack. The black line is the estimated fluence loss determined by analysis of the stainless steel (SS) beam profile foils at the front and rear of the stack, normalized to the proton fluence measured in the first compartment.

4.2.7 Cross Section Calculations

Where possible, activation products were quantified at multiple time-points. End of bombardment (EoB) activities and uncertainties were determined by extrapolation of decay curve regression, weighted by quantification uncertainty for individual time-points. Radioactive half-lives and gamma branching ratios were obtained from the Brookhaven National Laboratory National Nuclear Data Center (NNDC). For posterity, these values are listed in Appendix A. For indirectly produced daughter isotopes, EoB activity quantification was achieved by least-squares fitting with solutions to the first and second-order Bateman differential equations. One example of this relationship is the

^{nat}Fe(p,x)^{48}Cr reaction, where ^{48}Cr ($t_{1/2}$=21.56 h) subsequently decays to 48V ($t_{1/2}$=15.97 d). Cross sections were calculated as the EoB activity (s^{-1}) divided by the areal target density (cm^{-2}), proton fluence (unitless), and the radioactive decay constant (s^{-1}). For purposes of analysis, cumulative cross sections (σ_c) were defined as the sum of all independent formation cross sections (σ_i) leading to that particular radionuclide. This distinction is relevant in cases of decay chains or the formation of metastable states.

4.3 Results and Discussion

The target-stack box remained water-tight during irradiation, and foils were not thermally deformed. The layer of Kapton® tape surrounding each foil bubbled slightly on the front and rear of each foil near the beam spot. From irradiated Al foils, ^{22}Na was the only isotope quantified. From irradiated Cu foils ^{55}Co, ^{57}Co, ^{58}Co, ^{60}Co, ^{61}Cu, ^{64}Cu, ^{59}Fe, ^{52}Mn, ^{54}Mn, ^{56}Ni, and ^{57}Ni were quantified, but ^{59}Fe was excluded from cross section calculation due to insufficient counting statistics (Tables 4.2 & 4.3). From Fe foils, ^{55}Co, ^{56}Co, ^{57}Co, ^{58}Co, ^{48}Cr, ^{51}Cr, ^{52}Fe, ^{52}Mn, ^{54}Mn, and ^{48}V were quantified, but ^{57}Co and ^{58}Co were excluded from cross section calculation due to limited counting statistics and concerns over background contamination (Table 4.4). The nuclear cross sections measured in this work are compared to literature values in Appendix D. From the four monitor reactions used herein, proton fluence entering the target stack was measured to be 98.9 $\pm$ 6.5 nAh. This is in excellent agreement with the 99 nAh nominal fluence from IPF operation logs, which is based on non-destructive proton current measurement. By the

final target stack compartment, measured proton fluence had dropped by approximately 7.2% to 91.7 $\pm$ 5.8 nAh.

^{nat}Cu + p	^{55}Co	^{57}Co	^{58g}Co	^{58g}Co	^{58m}Co	^{60}Co
E_p (MeV)	σ_c (mb)	σ_c (mb)	σ_c (mb)	σ_i (mb)	σ_i (mb)	σ_c (mb)
89.4 ± 0.6	1.60 ± 0.11	36.8 ± 2.4	51.7 ± 3.4	20.8 ± 5.2	30.9 ± 5.6	10.2 ± 0.8
78.6 ± 0.9	0.788 ± 0.069	31.2 ± 2.7	45.7 ± 3.9	18.8 ± 6.5	27.2 ± 6.8	10.1 ± 0.9
69.1 ± 1.1	0.108 ± 0.014	34.3 ± 4.1	36.4 ± 4.3	12.4 ± 6.1	24.2 ± 6.7	10.2 ± 1.2
58.6 ± 1.4	-	49.6 ± 5.8	30.3 ± 3.6	6.0 ± 5.8	24.4 ± 6.5	11.3 ± 1.3
48.0 ± 1.6	-	36.6 ± 2.6	42.8 ± 3.1	18 ± 11	25.3 ± 11.2	8.59 ± 0.74
35.1 ± 1.9	-	40.0 ± 4.3	44.5 ± 2.9	7.4 ± 10.3	36.9 ± 10.6	3.72 ± 0.29

Table 4.2: Measured cross sections for ^{nat}Cu+p radiocobalt reaction products. σ_c denotes cumulative cross section values, while σ_i denotes independent cross sections.

^{nat}Cu + p	^{61}Cu	^{64}Cu	^{52g}Mn	^{54}Mn	^{56}Ni	^{57}Ni
Ep (MeV)	σ_c (mb)	σ_c (mb)	σ_c (mb)	σ_c (mb)	σ_c (mb)	σ_c (mb)
89.4 ± 0.6	58.9 ± 4.7	37.4 ± 2.8	1.45 ± 0.01	6.36 ± 0.40	0.0824 ± 0.0056	1.31 ± 0.09
78.6 ± 0.9	65.6 ± 5.8	40.5 ± 4.0	0.376 ± 0.035	3.93 ± 0.37	0.0878 ± 0.0077	0.985 ± 0.086
69.1 ± 1.1	78.4 ± 7.6	41.3 ± 5.3	-	4.76 ± 0.52	0.0762 ± 0.0091	1.35 ± 0.16
58.6 ± 1.4	85.4 ± 9.1	48.2 ± 6.1	-	4.92 ± 0.53	0.0169 ± 0.0025	2.09 ± 0.25
48.0 ± 1.6	118 ± 13	52.9 ± 5.4	-	0.907 ± 0.095	-	0.981 ± 0.075
35.1 ± 1.9	168 ± 23	68.7 ± 6.4	-	0.066 ± 0.012	-	-

Table 4.3: Measured cross sections for ^{nat}Cu+p radiocopper, radiomanganese, and radionickel reaction products.

^{nat}Fe + p	^{55}Co	^{56}Co	^{48}Cr	^{51}Cr	^{52}Fe	^{52g}Mn	^{54}Mn	^{48}V
E_p (MeV)	σ_c (mb)	σ_c (mb)	σ_c (mb)	σ_c (mb)	σ_c (mb)	σ_c (mb)	σ_c (mb)	σ_c (mb)
90.2 ± 0.6	4.77 ± 0.32	6.21 ± 0.58	0.749 ± 0.050	78.1 ± 5.1	2.42 ± 0.16	35.3 ± 2.3	73.7 ± 4.9	15.8 ± 1.0
89.0 ± 0.6	4.48 ± 0.30	6.49 ± 0.59	0.666 ± 0.044	74.0 ± 4.9	2.36 ± 0.16	36.7 ± 2.4	75.1 ± 5.0	14.8 ± 1.0
79.3 ± 0.8	5.40 ± 0.46	8.07 ± 0.89	0.398 ± 0.034	61.9 ± 5.3	2.55 ± 0.22	39.3 ± 3.4	78.3 ± 6.7	7.20 ± 0.62
78.3 ± 0.9	5.39 ± 0.46	7.68 ± 0.82	0.392 ± 0.034	61.0 ± 5.2	2.64 ± 0.23	43.1 ± 3.7	82.9 ± 7.1	7.03 ± 0.60
68.8 ± 1.1	6.52 ± 0.77	8.37 ± 1.12	0.372 ± 0.044	48.6 ± 5.8	2.28 ± 0.27	37.1 ± 4.4	88.0 ± 10.4	5.16 ± 0.61
67.8 ± 1.1	6.48 ± 0.77	9.32 ± 1.26	0.371 ± 0.044	50.7 ± 6.0	2.21 ± 0.26	38.5 ± 4.6	94.3 ± 11.2	5.50 ± 0.65
59.3 ± 1.3	8.09 ± 0.94	13.2 ± 1.8	0.304 ± 0.035	63.9 ± 7.4	1.67 ± 0.19	21.0 ± 2.4	110 ± 13	6.77 ± 0.79
58.3 ± 1.4	8.07 ± 0.94	12.5 ± 1.8	0.263 ± 0.031	65.0 ± 7.6	1.57 ± 0.18	19.6 ± 2.3	113 ± 13	6.87 ± 0.80
48.8 ± 1.6	10.1 ± 0.7	14.4 ± 1.4	0.0406 ± 0.0046	97.2 ± 6.8	1.64 ± 0.12	13.9 ± 1.0	148 ± 10	5.34 ± 0.38
47.6 ± 1.6	10.1 ± 0.7	14.5 ± 1.5	0.0136 ± 0.0045	95.1 ± 6.7	1.62 ± 0.11	14.6 ± 1.0	152 ± 11	4.82 ± 0.35
36.1 ± 1.9	18.3 ± 1.2	20.9 ± 2.0	-	48.0 ± 3.0	1.31 ± 0.08	26.9 ± 1.7	147 ± 9	0.139 ± 0.024
34.6 ± 1.6	22.3 ± 1.4	18.8 ± 1.7	-	36.3 ± 2.3	2.10 ± 0.14	31.4 ± 2.0	136 ± 9	-

Table 4.4: Measured cross sections for ^{nat}Fe+p reaction products.

Uncertainty in calculated cross sections was typically driven by uncertainty in proton fluence derived from monitor reactions (± 6-12%) and HPGe calibration uncertainty (± 5%). In a few particular cases, uncertainty was driven by activity quantification uncertainty due to limited counting statistics. Target foils had thickness uncertainties less than 1.3%, indicating that foil characterization uncertainty did not contribute significantly to overall cross section uncertainty.

The prospect of producing positron emitting isotopes of nickel is intriguing from the perspective of essential trace-element biological research or as a possible theranostic pair with ^{66}Ni ($t_{1/2}$= 54.6 h, β^- = 100%, $E\beta^-_{ave}$ = 73.4 keV), which decays by soft β^- emission that could bridge the gap between Auger emitting nuclides and conventional therapeutic β-emitting isotopes. The production cross section for ^{56}Ni by ^{nat}Cu(p,x)^{56}Ni is insufficient for medical relevance at energies below 100 MeV (max of 0.085 mb), but production cross section for ^{57}Ni ($t_{1/2}$= 35.6 h, β^+ = 43.6%, $E\beta^+_{ave}$= 354 keV) is more reasonable with a peak of approximately 2.2 mb at 57 MeV.

Production of cobalt isotopes from ^{nat}Cu+p could be useful as experimental monitor reactions (^{nat}Cu(p,x)^{56}Co in particular), but otherwise there are relatively few potential applications for this production route. One notable feature of this work however is the first reported independent cross section data for ^{nat}Cu(p,x)^{58m}Co and ^{nat}Cu(p,x)^{58g}Co. The calculated cumulative cross section values from these independent measures agree well with measured cumulative data. The production of ^{58m}Co appears to be more probable than the direct production of ^{58g}Co at the energies probed here. In Figure 4.7 these

measured independent and cumulative cross are compared against TALYS/TENDL-2015 code predictions (Koning et al., 2007). The code agrees with measured independent $^{nat}Cu(p,x)^{58g}Co$ cross sections, but seems to underestimate $^{nat}Cu(p,x)^{58m}Co$ cross sections. This underestimation is also reflected in the cumulative $^{nat}Cu(p,x)^{58g}Co$ TALYS predictions.

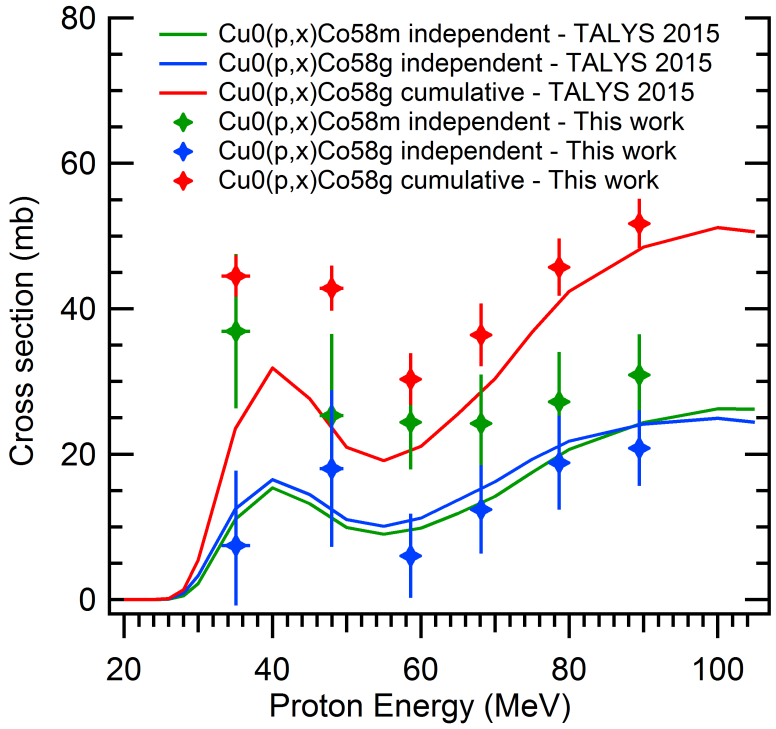

Figure 4.7: Comparison between TALYS 2015 predictions and measured independent $^{nat}Cu(p,x)^{58g}Co$ and $^{nat}Cu(p,x)^{58m}Co$ and cumulative $^{nat}Cu(p,x)^{58g}Co$ cross sections. TALYS predicted values for the independent $^{nat}Cu(p,x)^{58g}Co$ agree with values measured in this work, but TALYS appears to underestimate $^{nat}Cu(p,x)^{58g}Co$ reaction cross sections. This underestimation is also reflected in the cumulative $^{nat}Cu(p,x)^{58g}Co$ TALYS predicted values.

Production of ^{52g}Mn by $^{nat}Cu+p$ appears impractical due to the large co-production of ^{54}Mn (approximately 4:1 atomic ratio, ^{54}Mn:^{52g}Mn at 90 MeV) and because the cross

section is significantly lower than ^{nat}Fe(p,x)^{52g}Mn at intermediate energies (30 - 100 MeV) or ^{nat}Cr(p,x)^{52g}Mn at low energies (10-20 MeV). Producing ^{52g}Mn at intermediate energies by ^{nat}Fe(p,x) is possibly viable, depending on the required radionuclidic purity. The instantaneous production rates for ^{52g}Mn, ^{54}Mn, ^{48}Cr, and ^{51}Cr as a function of energy are shown in Figure 4.8. These results suggest that a ^{nat}Fe target that degrades a proton beam from 90 to 70 MeV would initially yield approximately 47 MBq/μAh of ^{52}Mn with an overall post-separation radionuclidic purity of 96.5%. With low energy production approaches (i.e. ^{nat}Cr(p,x)^{52g}Mn) being capable of radionuclidic purities greater than 99.6% (Wooten et al., 2015), this production route does not appear practical. An enriched ^{54}Fe target could possibly be employed to prevent ^{54}Mn co-production. Unfortunately, the dominant reaction from this route to the $A = 52$ isobar, ^{54}Fe(p,3n)^{52}Co, leads entirely to ^{52m}Mn rather than ^{52g}Mn through ^{52}Co $\rightarrow$ ^{52g}Fe $\rightarrow$ ^{52m}Mn (Junde et al., 2007). There is a need for ^{54}Fe(p,x)^{52g}Mn thick target yield experiments to evaluate the feasibility of this production route for radionuclidically pure ^{52g}Mn. For production schemes from Fe metal, radiomanganese could be easily isolated from radiocobalt by anion exchange chromatography, but separating Mn and Cr typically requires more elaborate radiochemistry approaches, such as ethanol-based anion exchange chromatography, trioctylamine solvent extraction, or acetic acid/methanol based anion exchange chromatography (Graves et al., 2015; Lewis et al., 2015; Lahiri et al., 2006; Buchholz et al., 2015).

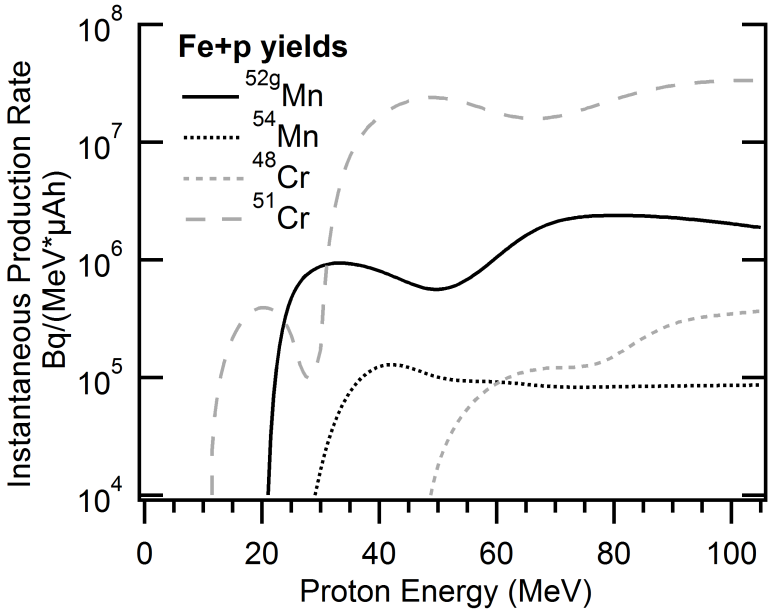

Figure 4.8: Instantaneous production rate for ^{52g}Mn, ^{54}Mn, ^{48}Cr, and ^{51}Cr, including indirect production routes. Production rate is specified in units of Bq/(MeV μAh) where MeV is the amount of beam energy lost in the target. For thin targets, production rate can be determined directly from this plot, but for thick targets an average production rate must first be calculated over the relevant energy region.

The use of ^{nat}Cu(p,x)^{62}Zn and ^{nat}Cu(p,x)^{65}Zn as monitor reactions has proven quite effective in this work. These reactions are already recommended by the IAEA who has evaluated literature data for this purpose. Unlike ^{nat}Al(p,x)^{22}Na and ^{nat}Cu(p,x)^{56}Co, these monitor reactions are not confounded by neutron induced reactions. As neutron flux may be significant toward the rear of a target stack, this trait should be considered when selecting monitor reactions for future studies.

4.4 Conclusions

From this work, we present twenty sets of cross section measurements from Fe+p and Cu+p at energies between 34.6 MeV and 90.2 MeV, including the first reported

independent $^{nat}Cu(p,x)^{58g}Co$ and $^{nat}Cu(p,x)^{58m}Co$ measurements. Furthermore, we have described monitor reaction variance minimization methods which can effectively reduce proton energy uncertainties in stacked-foil cross section measurement experiments.

Isotope	Half Life	Gamma Energy (keV)	Branching Ratio (%)
^{22}**Na**	2.6018(22) y	1274.5	99.944(14)
^{24}**Na**	14.997(12) h	1368.6	99.9936(15)
		2754	99.855(5)
^{48}**V**	15.9735(25) d	983.5	99.98(4)
		1312.1	98.2(3)
		944.1	7.870(7)
^{48}**Cr**	21.56(3) h	308.3	100
		112.4	96.0(20)
^{51}**Cr**	27.7010(11) d	320.1	9.910(10)
^{52g}**Mn**	5.591(3) d	1434.1	100.0(14)
		935.5	94.5(13)
		744.2	90.0(12)
^{54}**Mn**	312.20(20) d	834.8	99.9760(10)
^{52g}**Fe**	8.275(8) h	168.7	99.2(19)
		377.7	1.643(19)
^{55}**Co**	17.53(3) h	931.3	75
		477.2	20.2(14)
		1408.4	16.88(8)
^{56}**Co**	77.27(3) d	846.8	100
		1238.3	67.6(4)
		2598.5	17.28(15)
^{57}**Co**	271.79(9) d	122.1	85.60(17)
		136.5	10.68(8)
		14.4	9.16(15)
^{58g}**Co**	70.86(7) d	810.8	99
^{60}**Co**	5.2714(5) y	1332.5	99.9856(4)
		1173.2	99.9736(7)
^{56}**Ni**	6.077(12) d	158.4	98.8(10)
		811.9	86.0(9)
		750	49.5(12)
^{57}**Ni**	35.60 h	1377.6	81.7(16)
		127.2	16.7(3)
		1919.5	12.26(25)
^{61}**Cu**	3.333(5) h	283	12.2(3)
		656	10.77(18)
		67.4	4.23(13)
^{64}**Cu**	12.700(2) h	1345.8	0.473(10)
^{62}**Zn**	9.186(13) h	596.6	26
		40.8	25.5(13)
		548.3	15.3(8)
^{65}**Zn**	244.26(26) d	1115.5	50.04(24)

Table 4.5: Nuclear decay data used in this work, including radioactive half-life, prominent gamma energies, and branching ratios. Data was obtained from the National Laboratory National Nuclear Data Center (NNDC), accessed May 1st, 2016.

5 POSITRON EMITTING ISOTOPES OF GOLD

5.1 Introduction

Gold nanoparticles (AuNPs) have demonstrated their incredible versatility in applications such as in vitro and in vivo imaging, cancer therapy, and drug delivery (Huang et al., 2016; Zhang et al., 2008; Liu et al., 2008). These AuNPs come in many shapes including nanospheres, nanorods, nanoshells, and nanocages. Their versatility stems from the ability to construct or conjugate a single AuNP with many surface-bound functional ligands. Many types of AuNPs are inherently fluorescent, allowing for ex vivo microscopy applications as well as small animal fluorescence imaging (Cai et al., 2008). High atomic number and physical density allow for the possibility of using AuNPs as computed tomography (CT) contrast agents, especially in dual energy applications (Ducote et al., 2011).

Some attempts have been made to bring AuNPs into the realm of nuclear medicine, mostly involving the extrinsic labeling of chelated radiometals. Although these strategies have brought some success, an intrinsic labeling strategy could reduce concerns of in vivo instability, and changes in pharmacokinetic behavior (Zhou et al., 2012). Intrinsic radiolabeling strategies involve synthesizing the nanoparticles in the presence of a gold radioisotope, which is thereby structurally incorporated. The choice of isotope for this technique has typically been ^{198}Au ($t_{1/2}$ = 2.7 days, E_γ = 411.8 keV) as it is reactor produced by ^{197}Au(n,γ) and is therefore commercially available. However with such a

high energy gamma emission, SPECT image quality is quite poor.

Three positron-emitting isotopes of gold, ^{191}Au, ^{192}Au, and ^{194}Au, present themselves as potentially useful in this and other molecular imaging contexts. Their decay properties and potential production routes are listed in Table 5.1, along with other Au isotopes accessible by low-energy cyclotron facilities. Half-lives of 3.2, 4.94, and 38.0 h, respectively, could allow for a variety applications depending on the targeting moiety pharmacokinetics.

Isotope	$t_{1/2}$	**Decay Mode**	**Prominent γ's (keV)**	**Production Route**
^{191}**Au**	3.18 h	ϵ/β^+(0.254 %)	586, 278, 674, ...	^{192}Pt(p,2n)
^{192}**Au**	4.94 h	ϵ/β^+(5.6 %)	317, 296, 2237, ...	^{192}Pt(p,n)
^{193}**Au**	17.7 h	ϵ	186, 256, 268, ...	^{192}Pt(d,n), ^{194}Pt(p,2n), ^{196}Hg(p,α)
^{194}**Au**	38.0 h	ϵ/β^+(1.72 %)	328, 296, 1469, ...	^{194}Pt(p,n)
^{195}**Au**	186.1 d	ϵ	99, 130, 31, ...	^{nat}Pt(p,x)
^{196}**Au**	6.17 d	ϵ/β^-(7 %)	356, 333, 426, ...	^{196}Pt(p,n), $^{197/nat}$Au(γ,n)
^{198}**Au**	2.69 d	β^-(100 %)	412	^{198}Pt(p,n), $^{197/nat}$Au(n,γ)
^{199}**Au**	3.14 d	β^-(100 %)	158, 208	202Hg(p,α), ^{198}Pt(d,n)

Table 5.1: Isotopes of gold which may be produced by low-energy p^+ or d^+ accelerators. Note that $^{197/nat}$Au refers to the 100% naturally abundant isotope of gold, ^{197}Au.

5.2 ^{194}Au Production

5.2.1 ^{nat}Pt+p Reactions

With the accessibility of 16 MeV protons and 8 MeV protons on a GE PETtrace, the choice of radio-gold production routes is limited to (p,x) reactions on natural-abundance Pt-metal or (p,n) reactions on isotopically enriched ^{192}Pt or ^{194}Pt; deuterons below 8 MeV have insufficient energy for the (d,2n) reaction required to access ^{191}Au, ^{192}Au, or ^{194}Au

(Tarkanyi et al., 2004). Although proton-induced excitation functions for isotopically enriched Pt-targets have not been measured, aside from ^{198}Pt(p,n)^{198}Au, literature data is available for ^{nat}Pt+p reactions. Literature cross sections (Tarkanyi et al., 2004) are shown in Figure 5.1. From these excitation functions, we see that the production of ^{191}Au from 16 MeV protons is not possible, and that the cross section for production ^{192}Au is too low to have any practical value. Production of ^{194}Au on the other hand is quite possible with 16 MeV protons however, with an initial cross section of 320 mb, albeit with the significant co-production of ^{193}Au and ^{195}Au.

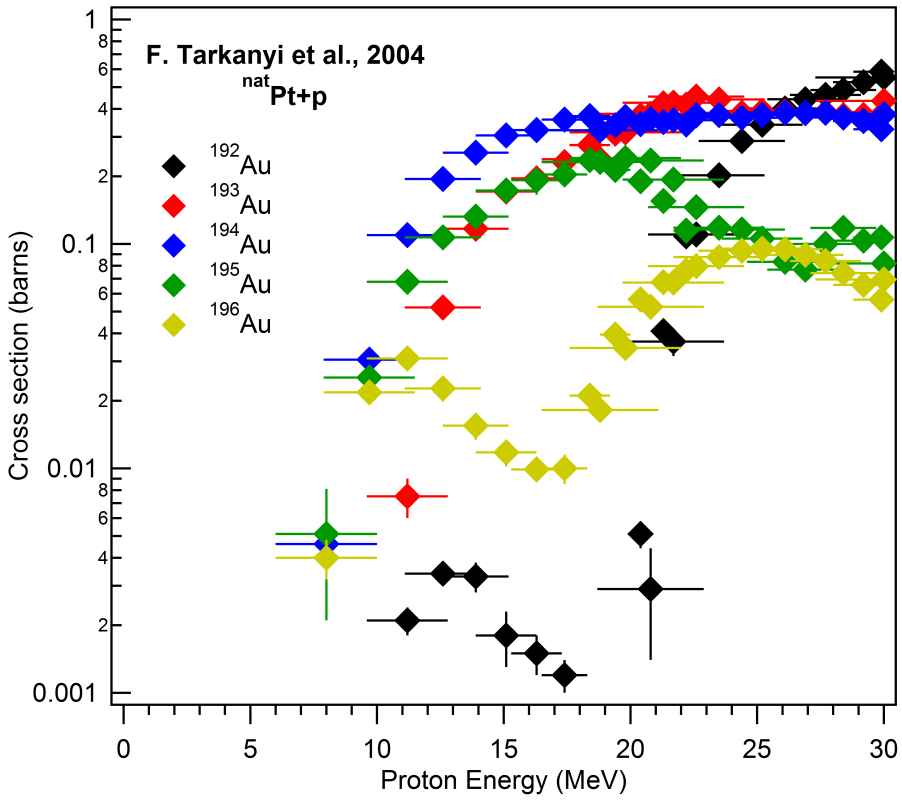

Figure 5.1: Literature cross sections for production of ^{192}Au, ^{193}Au, ^{194}Au, ^{195}Au, and ^{196}Au, by ^{nat}Pt+p.

5.2.2 Targetry

^{nat}Pt is an excellent target material due to its high melting point (1768 °C) and reasonably high thermal conductivity (71.6 $W/m \cdot K$). The projected range of a 16 MeV proton in platinum is 0.722 g/cm^2. Based on the density of 21.45 g/cm^3, a target thickness of approximately 0.34 mm would be required to stop 16 MeV protons. For the work described herein, 0.75" diameter and 0.23 mm thick ^{nat}Pt coins were used, which corresponds to a mass of approximately 1.5 grams of platinum. A photograph of this target following irradiating is shown in Figure 5.2. At current platinum prices (Oct., 2016), this amounts to a raw target material value of approximately $47 USD.

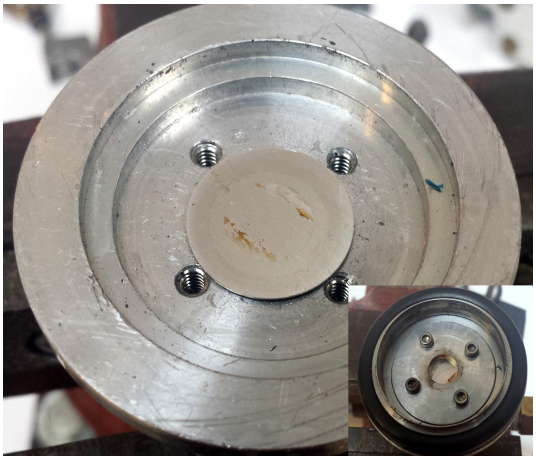

Figure 5.2: Photograph of ^{nat}Pt following irradiation by 30 μA for 1 h.

Isotopically enriched ^{192}Pt (41.6% enrichment, $166/mg) and ^{194}Pt (91.45% enrichment, $5.53/mg) are available as a metallic powders (Oak Ridge National Lab, NIDC). If a thermal diffusion radiochemical separation proved feasible, these enriched isotopes could be formed into a self-supporting target and re-used without lengthy post-

separation recycling.

5.3 Radionuclidic Purity Results

^{nat}Pt targets were irradiated by 16 MeV protons, and assayed by serial HPGe gamma spectroscopy. EoB radionuclide yields are listed in Table 5.2. The ^{194}Au purity is far from ideal, but for preclinical imaging applications, radionuclidic purity is only a concern insofar as it impacts PET quantitation. Careful scanner calibration at several post-EoB time-points can effectively mitigate this concern.

Isotope	$t_{1/2}$	**Dominant Route**	**Yields on ^{nat}Pt**
^{193}Au	17.6 h	^{194}Pt(p,2n)	10.7 MBq/μAh
^{194}Au	37.9 h	^{194}Pt(p,n)	10.7 MBq/μAh
^{196}Au	6.17 d	^{196}Pt(p,n)	0.159 MBq/μAh

Table 5.2: Radiogold yields following proton bombardment of 0.23 mm thick ^{nat}Pt for 1h.

5.4 Thermal Diffusion

Background

Radiochemical separation by thermal diffusion is a relatively new procedure, although it could be considered a sub-case of dry distillation methods, i.e. radioiodine distillation from tellurium-based alloys. Methods for the thermal diffusion-based separation of $^{110/115m}$In from ^{nat}Cd foils was first described by Lundqvist et al. in 1995 (Lundqvist et al., 1995), followed shortly by an article from the same group (Tolmachev et al., 1996) describing the separation of $^{66/67}$Ga from ^{nat}Zn foils. The general method for

performing these separations involves heating the target to just below its melting point for an extended period (30-120 min) followed by rinsing the target briefly with weak acid.

This technique depends on a large difference in melting point between the target and radioactive element, whereby the radioactive element's melting point is well below the melting point of the bulk substrate. Tolmachev et al. postulate that as the radioactive element (i.e. gallium) reaches the target surface (i.e. zinc), the radioactive atoms create a new "phase." Due to tracer amounts of radioactive atoms, the new "phase" is not what is meant by the classical macroscopic definition, but regardless, the atoms are removed from the bulk target solid-phase. This effectively creates a "zero-concentration" boundry condition, which causes a concentration gradient leading to thermal diffusion and accumulation of the radioactive element on the target surface. This assumes that the vapor pressure of the radioactive element is not so high at the diffusion temperature as to have significant evaporative losses.

The time-dependence of linear diffusion takes a form similar to the heat equation, where the rate of concentration change ($\partial C/\partial t$) may be expressed as a diffusivity constant (D) multiplied by the negative of the linear concentration gradient ($-\partial^2 C/\partial x^2$), as shown below.

$$\frac{\partial C(x,t)}{\partial t} = -D\left(\frac{\partial^2 C}{\partial x^2}\right) \tag{5.1}$$

Although this equation may be generalized to three-dimensions by way of the ∇^2

operator, a thin target foil may be thought of as a semi-infinite plane of uniform activation. This geometry lends itself well to a one-dimensional diffusion treatment. The solution to this treatment takes the form of a normalized Gaussian convolution against the spatial activity distribution, the width of which is proportional to $\sqrt{Dt}$.

The atomic diffusivity constant (D, units of cm^2/s) is an empirical quantity that depends on temperature, lattice structure, and chemical interaction between the trace element and the macroscopic substrate. The diffusion coefficient (D) for trace gold (MP: 1064 °C) in platinum metal (MP: 1768 °C) is approximately 1.1×10^{-9} cm^2/s at 926 °C and 6.9×10^{-9} cm^2/s at 1055 °C (Bolk, 1961). Linear extrapolation from these values to 1250 °C yields a diffusion coefficient of 1.6×10^{-8} cm^2/s. As diffusion coefficients in solids typically have a temperature dependence given by the exponential Arrhenius equation, this linear extrapolation likely underestimates the diffusion coefficent significantly. Regardless, if we assume that an irradiated ^{nat}Pt foil is held at 1250°C for 8 hours, the approximate width of the gaussian smoothing is given by:

$$\text{width} \approx \sqrt{Dt} = \sqrt{(1.6 \times 10^{-8}\,\text{cm}^2/\text{s})(2.88 \times 10^4\,\text{s})} = 0.021\,\text{cm} \tag{5.2}$$

This width suggests that for a foil of thickness $\ll 210$ μm, the majority of radio-gold activity would be found on the platinum surface and for a foil of thickness $\gg 210$ μm, very little activity would be localized to the platinum surface.

Pt/Au Thermal Diffusion Results

A ^{nat}Pt disc target (0.75" diameter, 230 μm thick) was irradiated by 60 μA of 16 MeV protons for 15 min, and cut into four quarters. One quarter of the target was placed in a tube furnace under argon flow, and another quarter was kept at room temperature as a control. The tube furnace was heated to a temperature of 1250 °C for 8 hours and then allowed to cool following the temperature profile shown in Figure 5.3.

The relative activities in the baked and control foils were assayed by Capintec measurement, and each foil was placed in approximately 5 mL of fresh concentrated aqua regia (1 part HNO_3 : 3 parts HCl) were agitated and allowed to sit for 6.25 hours. The foils were removed from the aqua regia, rinsed three times with 5 mL of H_2O, and dried. The combined etching and rinse solutions were assayed by Capintec. This etching was sufficient to remove approximately 2% of the samples' mass.

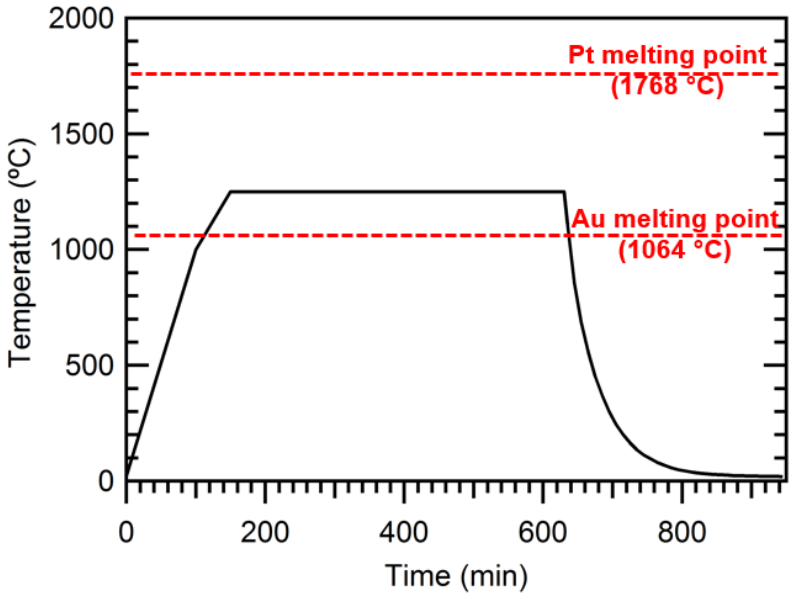

Figure 5.3: Temperature as a function of time for $^{193/194/196}$Au/^{nat}Pt separation by thermal diffusion.

The relative etching efficiency was defined as the percentage of extracted activity divided by the percentage of mass lost during etching as shown in Equation 5.3.

$$\epsilon = \frac{A_{etch}/(A_{etch} + A_{tgt})}{(m_{final} - m_{inital})/m_{initial}} = \frac{\%\ \text{Activity etched}}{\%\ \text{Mass lost}} \tag{5.3}$$

If activity were uniformly distributed throughout the target, one would expect a relative etching efficiency of 1, whereas if the activity were distributed on the target surface, one could expect a value significantly greater than 1. Relative etching efficiencies for the control and heated foil were 2.5 ± 1.2 and 1.2 ± 0.2, respectively, as shown in Figure 5.4. A two-tailed student's t-test reveals that neither of these values are significantly ($p < 0.05$) different from unity, and that they were not significantly different from each other ($p = 0.23$). Measured etching efficiency uncertainty was dominated by uncertainty

in etched mass, as the change in mass was on the order of a few milligrams.

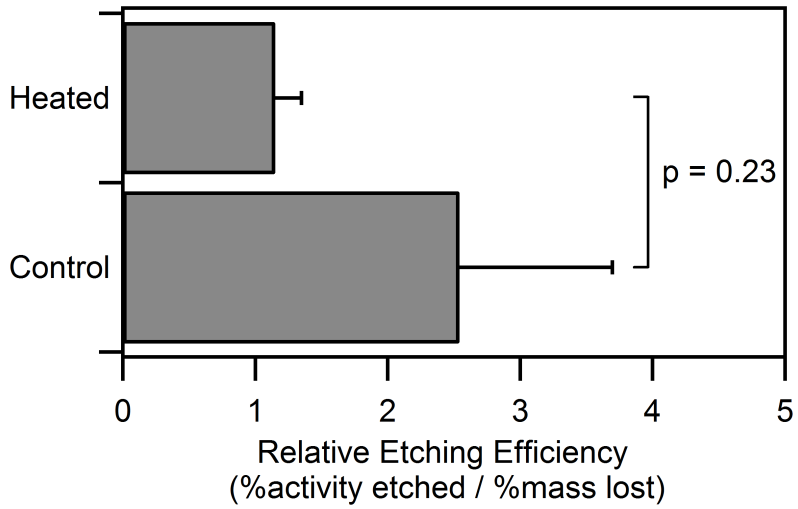

Figure 5.4: Relative etching efficiencies for proton-irradiated ^{nat}Pt heated and control foils.

These results suggest that the use of thermally-assisted diffusion as described herein for the physical separation of platinum and gold is not feasible. Although diffusion calculations suggest a significant accumulation of radiogold on the target surface, the underlying assumption is that once the surface is encountered, the gold is removed from the "macroscopic platinum solid phase" thus enabling a diffusion boundary condition resulting in accumulation. This assumption appears false under the diffusion conditions described herein. It may be possible to perform this thermally-assisted diffusion method in a reactive atmosphere, i.e. oxygen, whereby upon encountering the target surface gold ions are oxidized and removed from diffusion consideration.

5.5 Dissolution and Radiochemistry

Without a facile physical separation, the use of wet-chemistry dissolution methods are required for the isolation of radiogold from bulk ^{nat}Pt. The only common reagent for the dissolution of platinum metal is the highly oxidizing aqua regia (nitro-muriatic acid: 3 parts concentrated hydrochloric acid, 1 part concentrated nitric acid). This reagent must be prepared fresh and never stored in sealed containers as it reacts spontaneously to form NO and NO_2 gas. Even with concentrated aqua regia, the dissolution of platinum is slow; this is evidenced in the previous section by the fact that only ~2% of the Pt samples' mass was etched by aqua regia after 6.25 hours at room temperature.

Heat has been shown to accelerate this process considerably. For example, we have achieved more than 50% dissolution of a 1.5 g Pt target disc after ~16 hours at 75 °C. Although this is sufficient for radiochemistry development, such a lengthy and incomplete dissolution is unacceptable for large-scale radionuclide production. This dissolution rate could assuredly be improved by electrolytic methods, such as those described by Serhiy Cherevko et al. in 2014 (Cherevko et al., 2014).

5.5.1 Review of Pt/Au Separation Methods

A variety of solvent extraction techniques exist for gold, several of which are capable of isolation from platinum. (Das et al., 1976; Emery et al., 1961) Two of the more prominent and effective methods include the selective extraction of Au^{3+} from 2 M hydrobromic acid into isopropyl ether, first described by McBryde et al. in 1948, and extraction of

Au^{3+} from 6.9 M hydroiodic acid into diethyl ether, described by West et al., in 1952 (McBryde et al., 1948; West et al., 1952). Although these extractions are quite efficient for the separation of Au from Pt, the reconstitution of radiogold in hydrobromic or hydroiodic acid following dissolution in aqua regia is inconvenient, as is the formulation following extraction.

It is also known that gold complexes in all concentrations of hydrochloric acid, ostensibly $AuCl_4^-$, are strongly absorbed ($K_D \approx 10^4 - 10^6$) by strongly basic anion exchange resins (Kraus et al., 1954). The presence of NO_3^- anions however limits the efficacy of this method, and Kraus et al. did not describe elution methods.

5.5.2 Novel UTEVA Extraction resin method

The ideal separation method for Pt/Au would involve extracting directly from the aqua regia dissolution matrix (HNO_3 / HCl mixture) onto a relatively small-volume solid-phase column, followed by elution in a small (< 2 mL) volume which may be taken to dryness prior to final formulation.

Braun and Ghersini in their book entitled "Extraction Chromatography" show high distribution coefficients ($\sim 10^4$) for the solvent extraction of Au from HCl at all concentrations into 100% tributyl phosphate (TBP) and relatively low extraction ($K_D \approx 10^0$) of Pt (Braun et al., 1975). Likewise when extracting from weak nitric acid into TBP high distribution coefficients are seen for Au and low distribution coefficients are seen for Pt. Distribution coefficients for both Au and Pt decrease at higher nitric acid concentrations.

These distribution coefficients have been transcribed and plotted in Figures 5.5 and 5.6. This distribution behavior would, in theory, lend itself well to the selectrive extraction of Au from Pt from dilute (3:1) aqua regia. After isolating the TBP, the Au could be back-extracted by concentrated nitric acid.

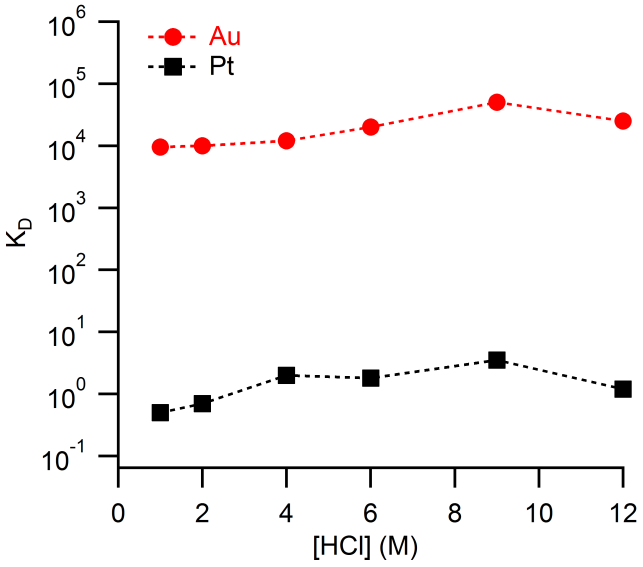

Figure 5.5: Distribution cofficients (K_D) for Pt and Au between hydrochloric acid and 100% tributyl phosphate (TBP) (Braun et al., 1975).

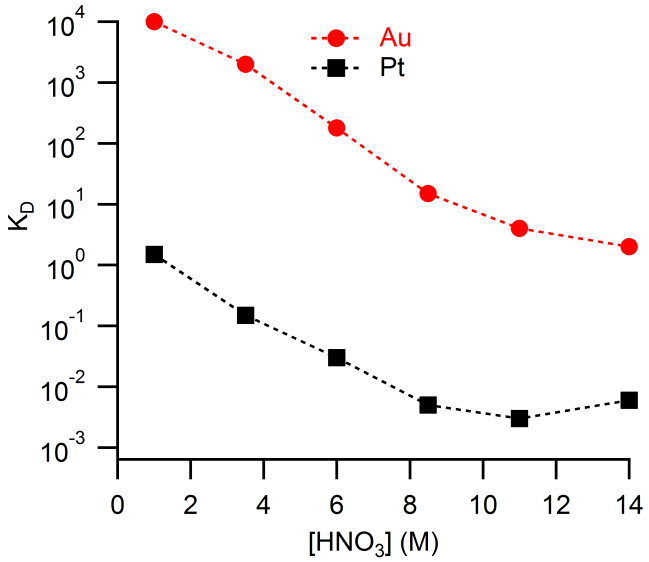

Figure 5.6: Distribution cofficients (K_D) for Pt and Au between nitric acid and 100% tributyl phosphate (TBP) (Braun et al., 1975).

Based on the structure of TBP (Figure 5.7), we hypothesized that the extraction resin UTEVA (Eichrom Technologies LLC, Lisle, IL, USA) would behave similarly due the structural similarity of its functional group, diamyl amylphosphonate (DAAP, Figure 5.8), to TBP. This resin has previously been suggested as a possibly suitable alternative to TBP in actinide separation applications (Moyer, 2009).

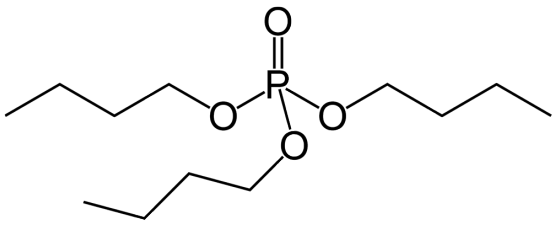

Figure 5.7: Structure of the organophosphorus extractant tributyl phosphate.

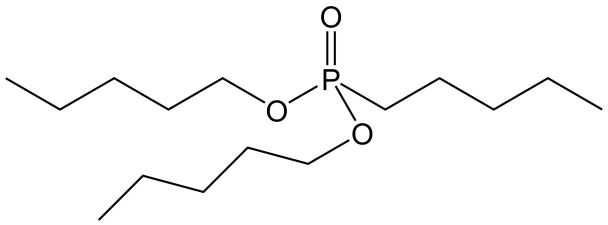

Figure 5.8: Structure of the UTEVA functional group, diamyl amylphosphonate (DAAP)

To test the hypothesis that UTEVA would make a suitable solid-phase extraction resin for the separation of Au from Pt, ^{nat}Pt target material was irradiated by 16 MeV protons, and was etched by 5 mL of fresh concentrated aqua regia. The resulting solution was diluted to 20 mL with water and was passed over 50-100 mg of UTEVA resin (mesh size, column diameter, etc.) equilibrated with 1 M HNO_3 at a flow-rate of approximately 20 mL/min. The column was rinsed by ~10 mL of 1M HNO_3 and the radiogold product eluted in ~ 0.5 mL of concentrated HNO_3.

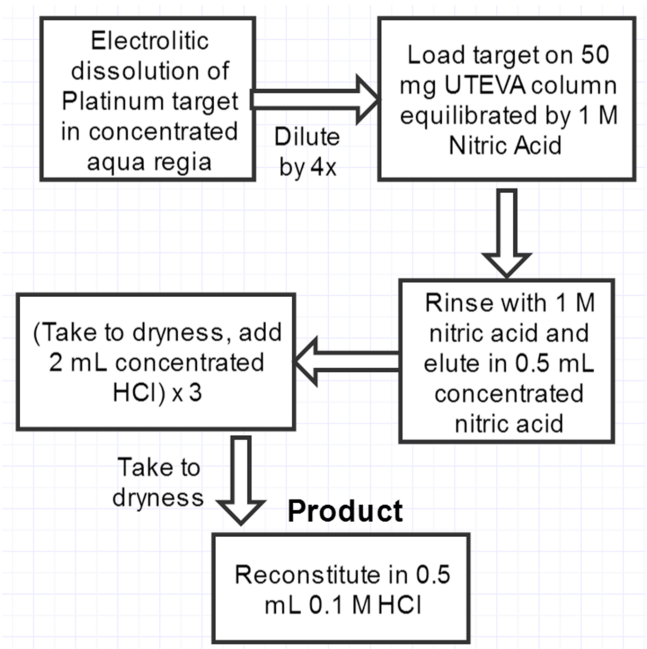

Figure 5.9: Method for the separation of radiogold from ^{nat}Pt following dissolution in aqua regia.

5.5.3 UTEVA Separation Method Results

Loading and elution was found to be nearly quantitative, with an average separation efficiency of of 97.6 $\pm$ 1.0 % (mean $\pm$ SD, n = 2) as determined by well-chamber ionization assay (Capintec). Although dissolution is quite time consuming, the separation procedure itself can be accomplished in approximately 5 minutes by hand. Electrolytic dissolution of the ^{nat}Pt target followed by an automated separation method could enable the rapid and high-yield isolation of radiogold.

6 RADIOBROMINE PRODUCTION

6.1 Background

Halogens present unique radiochemistry opportunities which are not afforded by conventional radiometal labeling schemes. Most notably, radio-halogens may be directly incorporated into small molecules which have a biodistribution sensitive to size and structure. Large macrocyclic chelators are not a suitable labeling scheme for most small molecule–based PET tracers. Furthermore, extensive literature exists on the synthesis of ^{18}F-containing tracers; These methods may be readily translated to the synthesis of radiobromine-based compounds, although the stability and properties of the resulting compounds may differ from their fluorinated analogues.

Much like iodine, bromine has several isotopes which are potentially useful in medical applications. This is in contrast with fluorine, which has only two isotopes with possible medical applications (^{18}F: $t_{1/2}$ = 11.8 h, β^+; ^{17}F: $t_{1/2}$ = 64 s, β^+), and chlorine, which has only two isotopes with possible medical applications (^{34m}Cl: $t_{1/2}$ = 32 m, β^+; ^{38}Cl: $t_{1/2}$ = 37 m, β^-). The advantage of bromine over iodine, aside from differences in decay characteristics, is the inherently smaller covalent radius of bromine which results in decreased structural modification of the tracer compound. Additionally the C-Br bond strength is is greater than that of C-I leading to greater *in vivo* stability.

A list of the potentially useful isotopes of bromine is summarized in Table 6.1. Bromine offers positron emitting isotopes (^{74}Br, ^{75}Br, ^{76}Br, ^{77}Br, ^{80}Br), beta emitting

isotopes (^{80}Br, ^{82}Br), Auger electron emitting isotopes (^{77}Br, ^{80m}Br), and a SPECT-energy gamma emitting isotope (^{77}Br). Because of this, radiobromine-based compounds may be used for both diagnostic and therapeutic applications. Elements with isotopes exhibiting these "theranostic" properties are considered favorable as nuclear-medicine moves toward a personalized approach to diagnosis and therapy.

Isotope	$t_{1/2}$	**Decay modes**	**Low-energy production routes**
^{74}Br	25.4 m	β^+ (91%)	^{74}Se(p,n)
^{75}Br	96.7 m	β^+ (75%)	^{74}Se(d,n), ^{76}Se(p,2n)
^{76}Br	16.2 h	β^+ (55%)	^{76}Se(p,n)
^{77}Br	57.0 h	β^+ (0.73%), augers & SPECT-energy gamma	^{77}Se(p,n), ^{80}Kr(p,α)
^{78}Br	6.45 m	β^+ (93%)	^{78}Se(p,n)
^{80}Br	17.7 m	β^- (92%), β^+ (2.2%)	^{80}Se(p,n)
^{80m}Br	4.4 h	IT, augers + x-rays	^{80}Se(p,n), ^{83}Kr(p,α)
^{82}Br	35.3 h	β^- (101%)	^{82}Se(p,n), ^{84}Kr(d,a)

Table 6.1: Isotopes of bromine with potential medical applications.

The use of radiobromine in nuclear medicine began primarily in late 1970s, with ^{77}Br being distributed to Universities and research hospitals on the 100's of mCi scale, being produced at the LANL Meson Physics Facility (LAMPF) by irradiation of metallic Mo targets (Grant et al., 1981). Although this production capacity was not sustained at LANL, the demand for Auger electron–emitting radionuclides has grown in recent years. Recent work has also shown that ^{76}Br in place of ^{18}F in various compounds allows for imaging at significantly later time-points. (Burkemper et al., 2015) This opportunity is important for the evaluation of pharmacodynamics of pharmaceuticals, particularly

those with long circulation times or slow biological clearance.

6.2 Target considerations and fabrication of NiSe targets

Aside from the production of radiobromine by high-energy Mo+p, various production methods have been explored using low-energy medical cyclotrons, typically employing As or Se targets. Nunn and Waters described the production of carrier-free ^{77}Br by ^{75}As(α,2n) in 1975 (Nunn et al., 1975). Madhusudhan et al., described the production of large quantities of ^{77}Br by ^{78}Se(p,2n) in 1979 (Madhusudhan et al., 1979), using a target in the form of a 4π water-cooled encapsulated metallic ^{78}Se or ^{78}Se-Pb alloy. Since these early advances in production there have been many institutions seeking to produce preclinical quantities of ^{76}Br and ^{77}Br.

Without an alpha-particle accelerating cyclotron, the main production route for radiobromine is by the proton irradiation of Se, which as a particularly low melting point (221 °C) and thermal conductivity (0.52 W/m·K). Because of these properties, the irradiation of metallic Se or Se-oxide requires low currents to prevent target failure.

6.2.1 Alloys of Selenium

Due to the low melting point of elemental Se, the use of binary alloys has the potential to greatly increase target durability at the expense of decreased radiobromine yield. Common binary alloys of Se are listed in Table 6.2. From a purely physical perspective, $TaSe_2$ shows the highest melting point (1872 °C) with a reasonably high Se mass fraction

(47%). $NbSe_2$ offers the highest Se mass fraction (62%) with a reasonably high melting point (>1316 °C). CrSe offers and an excellent compromise between these two with a melting point of 1500 °C and a Se mass fraction of 60%.

The down-side to selecting a binary alloy with a high melting point (>1000 °C) is the added difficulty of target formation and dry-distillation, requiring larger and more powerful sources of heat. For these reasons and due in part to availability, NiSe was chosen as the desired target alloy for preliminary radiobromine production experiments. In previous work by other groups, Cu_2Se has also been employed.

Alloy	Melting point (°C)	Mass Fraction Se
CrSe	1500	60%
MnSe	1460	59%
FeSe	965	59%
CoSe	1055	57%
NiSe	959	57%
Cu_2Se	1113	38%
CuSe	550	55%
ZnSe	1525	55%
GaSe	960	53%
GeSe	667	52%
As_2Se_3	360	20%
SrSe	1600	47%
$NbSe_2$	>1316	63%
$MoSe_2$	>1200	62%
Ag_2Se	880	27%
CdSe	1268	41%
In_2Se_3	890	51%
SnSe	861	40%
Sb_2Se_3	661	49%
$TaSe_2$	1872	47%
WSe_2	>1200	46%
HgSe	1000	28%
TlSe	381	16%
PbSe	1078	28%
Bi_2Se_3	710	36%

Table 6.2: Common binary alloys of selenium.

In the interest of maximizing ^{80m}Br yield, it may be beneficial to minimize the production of short-lived contaminant radionuclides, so the target may be manually dismounted and processed following irradiation. ^{nat}Ni^{nat}Se is commercially available, but for the purposes of minimizing ^{60}Cu ($t_{1/2}$ = 23.7 m) and ^{62}Cu ($t_{1/2}$ = 9.7 m) production, methods for the "in house" formation of ^{58}NiSe were explored. These methods if successful may also enable the use of enriched isotopes of selenium, i.e. ^{76}Se, ^{77}Se, and ^{80}Se.

6.2.2 Alloy formation by heating

One method for the formation of binary alloys is heating stoichiometric quantities of elemental constituents above the alloy's melting point — assuming the melting point of the alloy is above one or both of the constituents melting points — under an inert atmosphere (i.e. N_2, Ar, or vacuum).

In the case of NiSe, the melting point of nickel (1455 °C) is well above that of the melting point of NiSe (980 °C), which is well above the melting point of Se (221 °C). This means that if held at 1000-1100 °C, mixed powders of Ni and Se will form molten NiSe. However as the boiling point of Se is 685 °C, significant Se mass loss has been observed. Unfortunately, NiSe may not be quantitatively formed at temperatures below 980 °C, as the periphery of Ni particles may form NiSe below this temperature, but the core of the particle would theoretically be protected the solid NiSe coating. For these reasons, furnace-based NiSe formation is not suitable for enriched selenium isotopes, however this method may still be useful for the formation of $^{58}Ni^{nat}Se$.

6.2.3 NiSe formation by reaction with $NaBH_4$

The formation of NiSe nanoparticles has been described by Moloto et al. in 2009 (Moloto et al., 2009). Briefly, 1 g of Se powder and 1 g of $NaBH_4$ (dissolved in methanol) are combined and stirred for 60 min at room temperature. To this mixture, 1 g of $NiCl_2$ is added and stirred for 60 minutes. The resultant greyish-black precipitate is filtered, washed several times acetone, and is dried under vacuum. The advantage of this method

is the formation of NiSe under mild conditions. The disadvantage of this approach is the co-formation of NaCl within the NiSe crystal structure. Performing this reaction in H_2O rather than methanol in order to prevent NaCl precipitation results in the formation of Ni_3Se_4 according to Moloto et al., rather than the desired NiSe.

6.2.4 NiSe formation by liquid ammonia–based reaction

A third method for the formation of NiSe involves the stoichiometric mixing of Ni metal powder and Se metal powder in a pressure vessel submerged in liquid-N_2 or solid-CO_2. NH_3 gas is streamed into the vessel condensing to NH_3 liquid below -33.3 °C. Once a sufficient volume of liquid ammonia has been trapped, the vessel is sealed and brought to room temperature (~10 bar). This method was originally described by Henshaw et al. in 1997 (Henshaw et al., 1997). Based on recent work by Paul Ellison at UW-Madison, it seems that this method is effective for the formation of NiSe, with approximately 100 hours of reaction time at room temperature.

6.3 Target irradiation approaches

Once the desired metal-selenide alloy has been obtained, it may be formed into a target and irradiated in a variety of ways. One method that has been attempted at UW Madison is annealing NiSe powder along a horizontal target, which is irradiated with 15 ° or 30° incidence angles. Without a more elaborate substrate, the NiSe powder seems to "ball up" during annealing or irradiation, so we have employed a nickel mesh on the target

surface such that molten NiSe moves to fill the interstitial space within the mesh. These targets have been irradiated with up to 12 μA on a PETtrace beamline resulting in target failure (scorched surface, melted target material). During this irradiation, radiobromine was "autodistilled" and trapped on a quartz tube surrounding the irradiated target. Unfortunately at these temperatures Se boil-off resulted in significant contamination of the trapped radiobromine.

The best targetry method for NiSe that has been employed to date is the formation of NiSe discs by pressing NiSe powder (~500 mg) into a boron nitride crucible. A well-fitting lid is pressed on top of the crucible which is heated to 1050 °C. The resulting targets are shown in Figure 6.1. These targets have been placed in 4π water-cooled geometry (190 mL per minute flow, ~130 μm Nb window) for irradiation, withstanding greater than 20 μA of 16 MeV protons without failure.

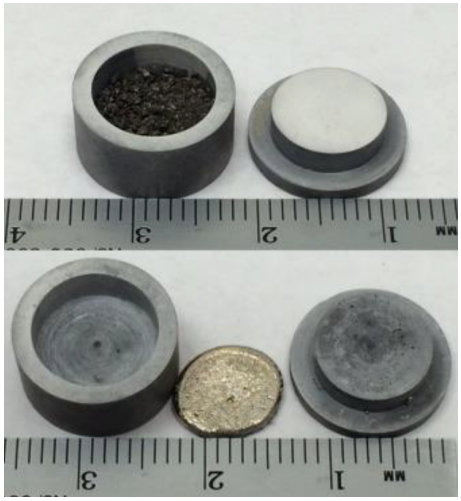

Figure 6.1: Formation of a NiSe disc target by heating within a BN cruicible to 1050 °C. Method and photograph courtesy of Paul Ellison.

6.4 Distillation of Radiobromine

Much like the separation of radioiodine from tellurium-based alloys, dry thermal distillation is an effective isolation strategy. By separating using dry distillation at sub-melting temperatures, targets could potentially be irradiated multiple times minimizing enriched isotope reclamation efforts.

6.4.1 Distillation Appratus and Method

An apparatus for the distillation of radiobromine from irradiated NiSe discs (~9 mm diameter, 1.2-2.4 mm thick) was constructed using a 0-1000 °C Carbolite tube furnace and quartz containment tube (10 mm ID, 12 mm OD). Quartz capillary tubes (1 mm ID, 6 mm OD) were fit with boron nitride tips to effectively reduce the outer tube's diameter to 1 mm on either side of the target disc. Both ends of the quartz tubes were sealed with pieces of machined Teflon, as shown in Figure 6.2. Ar sweep gas (5-50 mL/min) was used to carry distilled radiobromine downstream outside of the tube furnace, where the quartz capillary tube was cooled by ice. Further downstream, the Ar sweep gas was bubbled through a NaOH solution to trap residual radiobromine.

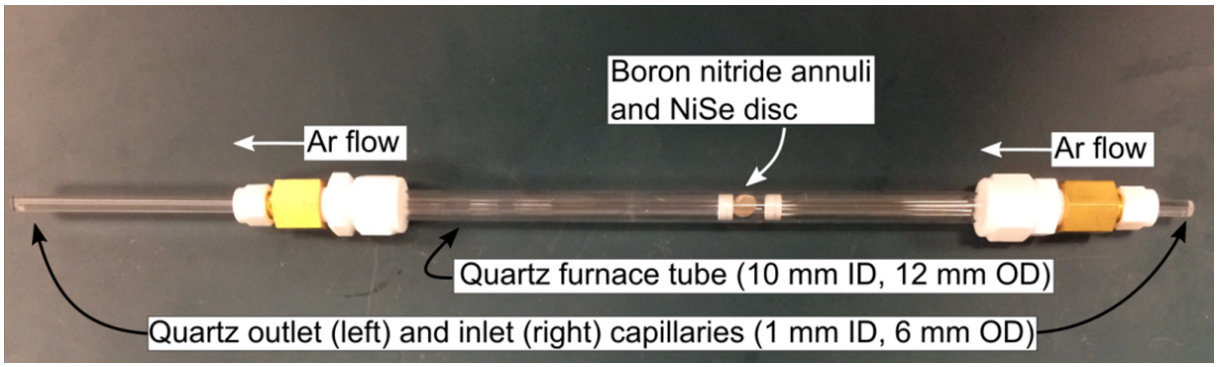

Figure 6.2: Apparatus for the distillation of radiobromine. This quartz distillation tube is placed inside a 0-1000 °C Carbolite tube furnace with a collimated CsI(Tl) detector pointed at the NiSe target. As the furnace heats and radiobromine is distilled, Ar sweep gas carries the bromine and deposits in the quartz capillary tube outside of the furnace.

External to the tube furnace, a collimated CsI(Tl) detector was used to monitor radioactivity level within the target disc. Count rate and temperature as a function of time were recorded during distillation. For distillation, the furnace was raised to 900 °C over 10-20 minutes, and was held at that temperature for 30-120 minutes. Following distillation, the furnace is allowed to cool. The downstream capillary tube is removed and rinsed of radiobromine with a small volume of warm water. This water is then passed through a 0.5 μm filter to remove residual Se particulate.

6.4.2 Distillation Results

The results of this dry distillation procedure are shown in Figure 6.3. Upon reaching approximately 800 °C, radiobromine begins to distill from the NiSe target material. As the furnace reaches its set point of 900 °C, the distillation accelerates and takes what initially appears to be an exponential decline, but after roughly 1000 seconds at this temperature a second distillation 'exponential distillation event' begins.

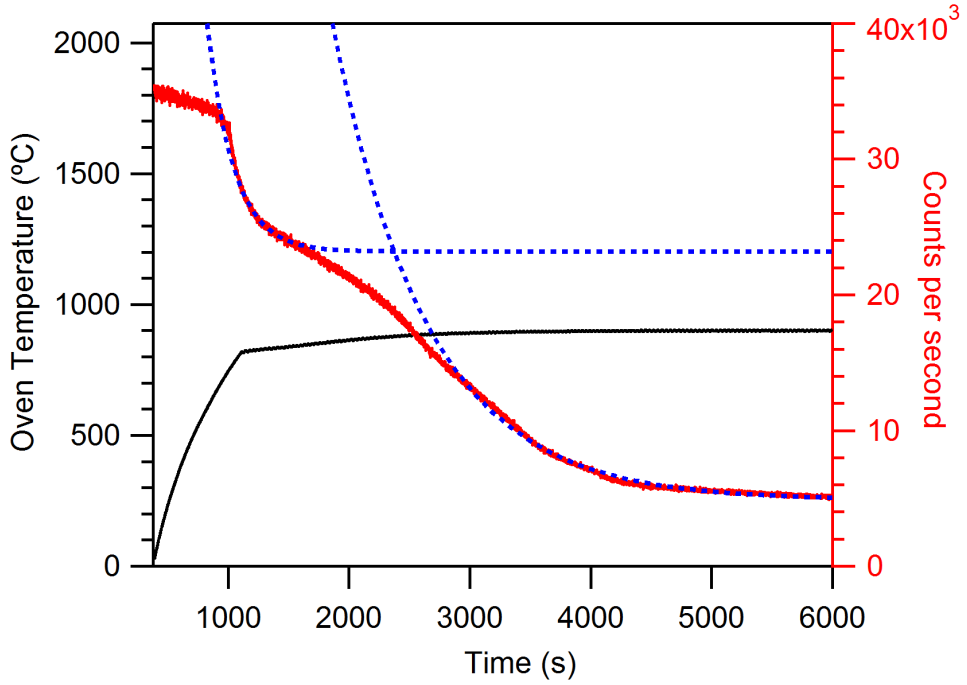

Figure 6.3: Distillation of radiobromine as a function of time, and furnace temperature as a function of time. A distinct two-component distillation is observed, indicated by the dotted blue lines of fit.

Following distillation a pink/brown residue was observed inside and just outside the furnace within the quartz tubes. This is likely due to residual Se boil-off. Approximately 70% was trapped in the outlet capillary tube. Of this 70% approximately 80% was easily dissolved into ~250 μL of warm water. This corresponds to an overall isolation yield of approximately 50-60%. The location of radiobromine deposition in the outlet capillary was observed to be highly dependent upon the Ar sweep gas flow rate, and upon the distillation time. It was determined that longer distillation times (>90 min) allowed radiobromine to be trapped further outside the tube furnace, away from the Se deposit.

This two-step exponential distillation is unusual, with roughly 1/3 of the bromine being distilled in the early component and 2/3 distilling during the late component. For

this observation we posit the following two explanations:

1. Populations of radiobromine exist with different activation energies due to lattice interactions within the non-stoichiometric NiSe crystal structure.
2. A subset of distilled radiobromine rapidly interacts with the proximal quartz enclosure, creating a secondary distillation process.

The interplay between temperature, lattice effects, and convective currents is well described by Beyer et al., 2000 (Beyer et al., 2000), in the context of radioiodine diffusion from molten tellurium dioxide. Although the distillation of radiobromine from NiSe does not follow the simple form $A = A_0 \exp(-\lambda t)$, it is still possible to calculate diffusion coefficients for each distillation component, assuming hypothesis #1 is correct — that all radiobromine is distilling from within the NiSe matrix.

Diffusion within a solid is given by the differential equation:

$$\frac{\partial C(x,t)}{\partial t} = -D\left(\frac{\partial^2 C}{\partial x^2}\right) \tag{6.1}$$

This diffusion constant D is generally described by the Arrhenius equation, $D = D_0 e^{E_a/kT}$, where E_a is defined as the activation energy, k is the Boltzmann constant, and T is temperature. Beyer et al., 2000, shows that the relationship describing the diffusion coefficient of radioiodine from tellurium dioxide takes the form:

$$D = \frac{\ln(\pi^2/16)}{t_{1/2}\pi^2} h^2 \quad \left[\frac{cm^2}{sec}\right] \tag{6.2}$$

Here, h is defined as the target thickness. From the exponential lines of fit shown in Figure 6.3, $t_{1/2}$ values of 152 ± 4 sec and 545 ± 2 sec are obtained for the fast and slow components, respectively. From Equation 6.2 and a target thickness of 0.12 ± 0.02 cm, these values yield diffusion coefficients of $(4.6 \pm 1.6) \times 10^{-6}$ cm^2/s and $(1.3 \pm 0.4) \times 10^{-6})$ cm^2/s for the fast and slow components respectively.

In order to determine D_0 and E_0 for this target geometry, this distillation procedure could be repeated at different temperatures. $\ln(D)$ plotted against inverse temperature has a linear relationship with a slope of E_0/k and a y-intercept of $\ln(D_0)$ according to the Arrhenius equation.

6.5 Conclusion

Isotopes of bromine have well-varied decay characteristics and show promise for several theranostic applications. Methods for the preparation and irradiation of isotopically-enriched selenium-based targets have been developed at UW-Madison. These targets have been shown to withstand greater than 20 μA of 16 MeV protons. Dry distillation of radiobromine from irradiated NiSe targets has been accomplished in yields sufficient for preclinical studies.

7 ^{64}Cu and ^{89}Zr production

^{64}Cu and ^{89}Zr have recently taken their place as the flagships of PET radiometals by being employed in a variety of clinical trials. These radioisotopes are particularly well-suited to national and international transport due to their half lives of 12.7 hours and 3.27 days, respectively. The reliable translation of radiopharmaceuticals employing these compounds depends on sufficient and reliable supply, and a chemical purity reliably suitable for conjugation chemistry. To this end, this work seeks to improve the production capacity and purity of ^{64}Cu and ^{89}Zr at UW-Madison

7.1 Production Capacity

^{64}Cu

The production of ^{64}Cu from enriched ^{64}Ni (>99.10%) target material has been previously characterized and developed. Briefly, $^{64}NiCl_2$ is converted to $^{64}Ni(NO_3)_2$ by two iterations of drying/rehydrating in 6M HNO_3. The final dried sample is treated with 300 µl of concentrated H_2SO_4, is diluted with 2 mL H_2O, and is pH adjusted to 9.05 ± 0.05 with NH_4OH. 0.25 g $(NH_4)_2SO_4$ is added, and the volume is adjusted to approximately 5 mL. Metallic ^{64}Ni targets are plated from this solution onto gold disk supports using a platinum wire anode with 2.4–2.6 V potential between the electrodes, resulting in a current of 10–30 mA. Plating has been found to be nearly quantitative and these targets have been shown to withstand 40 µA for several hours of irradiation with no visible

aberration. Targets material is dissolved by 12 M HCl, and is separated by anion exchange chromatography. The final ^{64}Cu product is taken to dryness, and then rehydrated in 0.1 M HCl. $NiCl_2$ is collected in later fractions and is dried once again as a first step for target preparation.

In recent years, increased demand has pushed the capacity for production of ^{64}Cu at UW-Madison to its limits. On the GE PETtrace, beam current is constrained by the molybdenum degrader foil (0.010" = 0.259 g/cm^3) used to attenuate the average proton energy from 16 MeV to 10.9 MeV for the optimal ^{64}Ni(p,n) reaction cross section. Black-body radiation calculations for a 1.25 cm^2 beam area on molybdenum (emissivity = 0.218, T_{melt} = 2623 °C) suggest a maximum radiated power of 216 watts (forward direction only), which allows for a beam current of 43 μA, assuming negligible conductive or convective cooling. Up to this point, 25 μA irradiations have been used for ^{64}Cu production on our PETtrace. End of chemistry activities on the order of 600 mCi require 6+ hours of irradiation on a target of approximately 70 mg ^{64}Ni. Diminishing returns with irradiation duration suggest that an increase in beam current or target thickness would be preferred to increase production capacity.

Active cooling methods for degrader foils have the potential to increase degrader durability beyond the output capacity of a GE PETtrace (100 μA), but this adds complication the target system. If a ^{nat}Ni on Au electroplated target is shown to consistently withstand greater than 40 μA of protons, then it may be useful to employ a direct water-cooled degrader design. Considerations for such a design include the following:

- **Ease of degrader change.** Quick-change designs increase complexity (reducing reliability) but add flexibility. Integrated foil (slow-change) designs allow for damaged degrader foils to be replaced, but do not facilitate the use of different degrader foils for different isotopes. Permanent machined degrader thicknesses allow for very simple design strategies, however damaged degrader foils would necessitate the construction of an entirely new holder.
- **Vacuum pass-through.** Without vacuum on the target-face, oxidation may occur during irradiation. This has the potential to limit dissolution and enriched isotope material recovery.
- **Degrader material and proximity to target.** Degrader materials of low atomic number (i.e. Aluminum, 13) cause less angular proton scattering, while high atomic number materials (i.e. Tantalum, 73). Higher atomic number transition metals tend to also have higher melting points, so a compromise must be made between degrader melting point, atomic number, and activation products. In all cases, having the degrader foil as close as possible to the target-face is beneficial.

These considerations, along with the durability of electroplated ^{64}Ni targets will be used for future degrader foil implementations on the GE PETtrace.

An alternate strategy for increasing ^{64}Cu production capacity, ^{64}Ni targets could be plated with larger target masses. This method is somewhat less desirable than increasing beam current as the cost of enriched isotopes is significant, and the mass loss for each production can be expressed as a percentage of the total target mass. Increasing target

mass results in higher ^{64}Cu yield, but also in greater financial overhead. This scheme for meeting production demand may prove viable if increased demand is sustained or frequent. An array of available target thicknesses would be ideal, such that a suitable target could be selected based on specific production demands.

^{89}Zr

The production of ^{89}Zr is accomplished by irradiation of natural Yttrium metal in the form of commercially available foils (99.9%, 0.64 mm, Goodfellow Inc.). Radiochemical separation is achieved using a hydroxamic acid chelate ion exchange resin (hydroxamate resin) which can by synthesized from a silica-based weak cation exchange resin, 2,3,5,6-tetrafluorophenol (TFP), 1-ethyl-3-(3-dimethylaminopropyl) carbodiimide hydrochloride (EDAC), and hydroxylamine HCl (Holland et al., 2009). This functionalized resin is now also commercially available (Eichrom Technologies). The irradiated yttrium foil is dissolved in 6 M HCl, is diluted to less than 2 M HCl, and is then loaded on a pre-washed hydroxamate column containing approximately 100 mg of resin. The column is washed with 2 M HCl, then activity is eluted in a small volume of 1.0 M oxalic acid. If desired, this ^{89}Zr-oxalate may be reconstituted as $^{89}Cl_2$ by trapping the activity on a small C-18 Sep-Pak, followed by rinsing with H_2O, and elution in ~0.5 mL 1 M HCl. (Sato et al., 2015)

As with ^{64}Cu, the rate of production of ^{89}Zr largely depends on the beam current which the target can withstand. At UW-Madison, Yttrium foils have historically been

pressed against a water cooled silver surface, and are irradiated by 15 μA of 14 MeV protons (0.125 mm molybdenum degrader). A direct water-cooled yttrium target could withstand significantly higher beam currents, but at the risk of contaminating the cyclotron chilled water supply. Electrodeposition of Y-metal is promising, however there is little literature describing plating methods for the quantitative reduction of large ^{nat}Y masses onto Ag or Au.

Novel ^{nat}Y targetry

In the interest of manufacturing a more robust target, ^{nat}Y foils were resistively spot welded to a 0.5 mm thick tantalum backing. The spot welder (White Dog, CHIFW040) was fitted with copper or silver electrodes, shown in Figure 7.1, in order to minimize contamination to the target face by metals which might interfere with DFO chelation of ^{89}Zr.

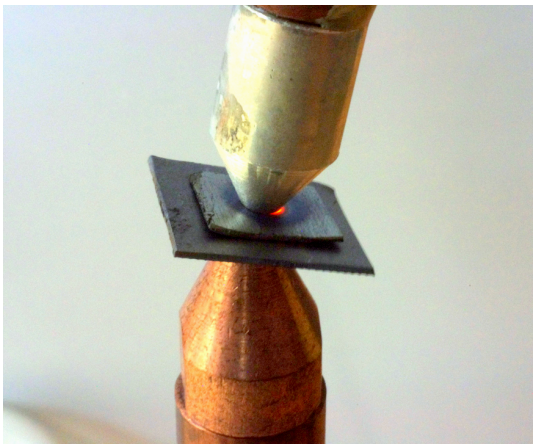

Figure 7.1: Spot welding ^{nat}Y to Ta. A silver electrode on the target-side ostensibly prevents contamination by metals which may interfere with DFO chelation.

Resistive spot-welding operates by joining two metal surfaces by the transport of high-current electricity through a small area. This electral current causes a rapid increase in local temperature, rising above the melting point of the two metals. This success of this technique seems to depend on several material and metallurgical properties, including melting point, electrical resistivity, and binary alloy phase behavior. In particular, it is helpful for the backing material to have a significantly higher melting point than the target material. In this way, yttrium (MP = 1522 °C, $\rho = 60$ μΩ·cm) was well matched to tantalum (MP = 3017 °C, $\rho = 13$ μΩ·cm).

These properties allowed for successful spot welding of ^{nat}Y to Ta, resulting in the target preparation shown in Figure 7.2. Roughly twenty spots along the target faced were welded in a sequential raster pattern. In order to provide more control, the input voltage of the spot welder was reduced to 80 VAC from 120 VAC. Welds performed with 120 VAC created a significantly cratered or perforated Y foil, and weld spots obtained at 20-60 VAC did not sufficiently bond the Y and Ta.

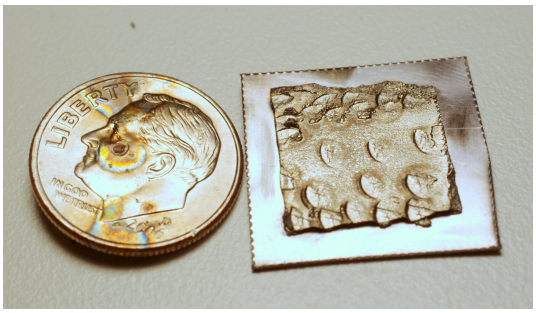

Figure 7.2: Spot welded ^{nat}Y to Ta. Welds were conducted in a raster pattern across the target face.

The water-jet-cooled Ta-welded Y target and Mo/Ta degrader assembly shown in

Fig. 2 was irradiated with successively intense proton beams: 20, 30, 40, and 50 μA for 1–2 h. These spot welded ^{nat}Y targets were irradiated with successively intense proton beams: 20, 30, 40, and 50 μA of protons with water-jet cooling on the rear tantalum face, as shown in Figure 7.3C. Irradiation durations ranged from 1–2 h. Both gamma and neutron flux scaled linearly with beam current, with "blank" targets of a water-jet-cooled Ta target and Ta degrader assembly producing roughly half of the measured Y+Ta flux.

For test targets prepared at too low of a welding-voltage, post-irradiation inspection revealed a portion of yttrium peeled away from the tantalum substrate, while showing signs of deformation and melting. These target failures were mitigated by increasing the welding-voltage and total number of welds across the target face. A well-prepared target irradiated by 50 μA of protons for 2 hours is shown in Figure 7.3A and 7.3B.

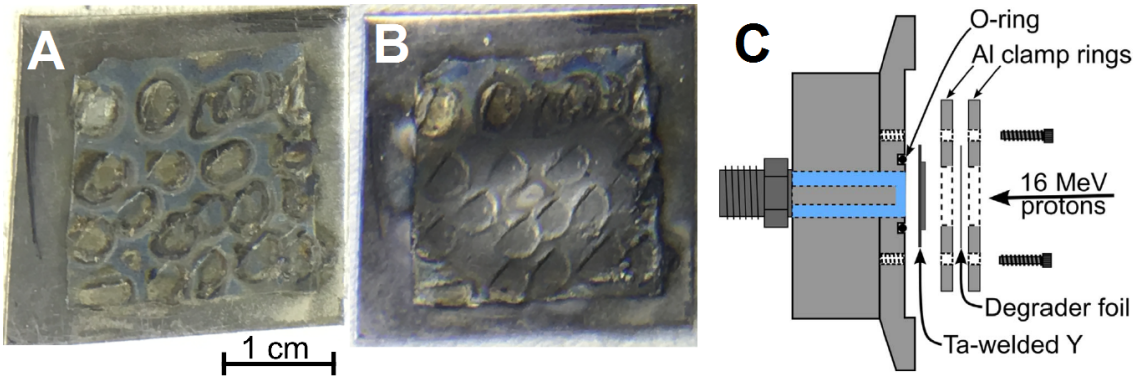

Figure 7.3: Spot welded ^{nat}Y to Ta before (A) and after (B) irradiation by 50 μA of 14 MeV protons for 2 hours. Targets were o-ring sealed on the rear face with direct jet water cooling. On the front face, the degrader foil was clamped between two rings, approximately 1 mm from the target face (C).

EoB ^{89}Zr production yields of 48 ± 4 MBq/μAh were consistent regardless of irradiation current and in good agreement with those observed with previous target methods.

Dissolution and radiochemical isolation of ^{89}Zr proceeded similarly to productions employing previous target methods, allowing for ~90% radiochemical yield. Effective specific activity measured by DFO chelation was found to be 60 ± 70 GBq/μmol ($n = 10$), which is in good agreement with previous production methods providing an effective specific activity of 60 ± 50 GBq/μmol ($n = 124$). A comparison of this work to literature production methods is provided in Table 7.1. This spot welding method and irradiation results have also been published in great detail in Applied Radiation and Isotopes by Ellison et al., 2016.

Max. proton current (μA)	**^{89}Zr yield (MBq/μAh)**	**DFO ESA (GBq/μmol)**	**Reference**
50	48 ± 4	60 ± 70	This work
45	49 ± 4	n/a	Siikanen et al., 2014
30	$14 - 16$	n/a	Dabkowskia et al., 2015
35	21 ± 2	n/a	Ciarmatori et al., 2011
15	56 ± 4	$17 - 44$	Holland et al., 2009
15	34 ± 6	4 ± 4	Wooten et al., 2013

Table 7.1: Maximum proton current, ^{89}Zr production rates, and DFO-based effective specific activities for published ^{89}Zr production methods.

7.2 Chemical Purity

Specifying the chemical purity of a radionuclide product following radiochemical isolation in a meaningful way presents several challenges. The concept of "specific activity" (SA) is designed to address this need, being generally defined as the amount of radioactivity per unit mass. This definition is quite lacking however, as described by an article by de Goeij and Bonardi, 2005, entitled "How do we define the concepts specific activity,

radioactive concentration, carrier, carrier-free and no-carrier-added?" (DeGoeij et al., 2005) This article published more than 40 years after the beginnings of modern nuclear medicine, and more than 100 years after the beginnings of radiochemistry evidences the ambiguity in defining the chemical purity of radiochemical products.

For the production of organic (i.e. ^{11}C-based) or halogenated (i.e. ^{18}F-based) radiotracers, the definition of specific activity is less nuanced, as typically the only chemical competitors are stable atoms of the same element. In these cases, the definition of activity divided by mass or molar mass is suitable.

For transition-metal-based radiotracers, chelation chemistry allows for the competition of a variety of metals and oxidation states. Further, these competeing metals experience varying affinities and stabilities for chelation, and these affinities and stabilities are dependent upon pH and temperature. With these considerations it becomes clear that the concept of specific activity in any of the conventional definitions are insufficient. Listed below are some of these conventional definitions using ^{64}Cu as an example.

- SA: Activity(^{64}Cu)/Mass(^{nat}Cu)
- SA: Activity(^{64}Cu)/Mass(^{nat}Cu + ^{64}Ni)
- SA: Activity(^{64}Cu)/Mass of all metal impurities
- SA: Activity(^{64}Cu)/Molar mass of all impurities

7.2.1 Effective Specific Activity

In order to address this ambiguity in the chemical purity of a radiochemically isolated radiometal product, the field as adopted the concept of "Effective Specific Activity" (ESA). The intention of this quantity is to specify how pure a radionuclide product "behaves" given a particular chelator and set of labeling conditions (concentration, temperature, pH, time). This metric is particularly relevant to subsequent tracer labeling radiochemistry, assuming said radiochemistry is performed with the same chelator at similar labeling conditions. Given a well-measured ESA and a known amount of radioactivity, the amount of precursor/chelate required for quantitative labeling may be calculated.

This approach loses value when a single radionuclide production supplies many users employing a variety of radiolabeling schemes, as is often the case with the production of long-lived PET radiometals. An effective specific activity may be measured for a single set of labeling conditions, and the absolute mass of contaminating metals may be measured using conventional analytic chemistry trace-metal analysis methods, but there is a gap between these metrics and the actual labeling efficacy that an end user experiences under alternate labeling conditions.

There are two possible approaches to address this problem:

1. Create a "perturbation model" which modifies the experimentally measured ESA based on differences between the reference radiochemistry conditions and end-user radiochemistry conditions. For example, an increase in labeling temperature

of 10 °C might typically be associated with an increase in ESA of 5%, or performing chelation at pH 4.5 rather than pH 6.5 might result in 20% lower ESA on average.

2. Create an analytic model which can be used to directly predict ESA from trace metal quantification results. Each contaminating metal would have a "contribution weight" as a function of chelate and labeling conditions.

In this work, we address the treatment of approach #2 by forming this analytic model, measuring preliminary "weights", and presenting preliminary prediction results.

^{64}Cu ESA Measurement

At the UW - Madison, we have measured the purity of our weekly ^{64}Cu product by chelation with 1,4,7-Triazacyclononane-1,4,7-triacetic acid (NOTA). To perform a ^{64}Cu effective specific activity measurement A sample of ^{64}Cu in 0.1 M HCl is split among samples containing varying NOTA quantities (0 – 100 ng) buffered by NaOAc to approximately pH 6.0. Thin layer chromatographs (TLCs, 1:1 MeOH : 0.25 M NaOAc mobile phase) are used to determine the fraction of ^{64}Cu bound by NOTA, then sigmoidal interpolation is used to determine the quantity of NOTA required to chelate 50% of the ^{64}Cu. The activity of the sample divided by twice this resultant mass is defined to be effective specific activity, with units of Ci/μmol.

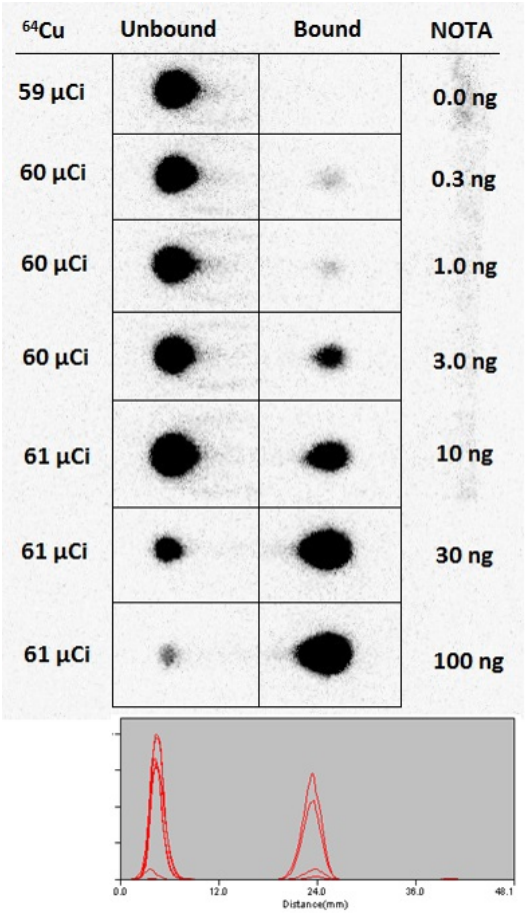

Figure 7.4: Example of effective specific activity measurement by TLC separation. Increasing concentrations of NOTA lead to increasing bound fractions of ^{64}Cu. The activity of ^{64}Cu, in this case 61 µCi, divided by twice mass of the interpolated point of 50% binding, in this case 18 ng, is defined as the effective specific activity.

These measurements are useful, but have been highly variable over the years. As an example, the average effective specific activity from June 24th, 2013 to Nov. 14th, 2016 was 9.8 $\pm$ 12.1 Ci/µmol ($\bar{x} \pm$ SD, n = 104). A complete listing of these measurements with further analysis and discussion is contained with Appendix E.

^{89}Zr ESA Measurement

To measure effective specific activity with ^{89}Zr, a chelation assay is performed using desferoxamine (DFO). Much like the ^{64}Cu method, ^{89}Zr is added to a series of buffered samples containing increasing concentrations of DFO. After an hour has elapsed, an excess of DTPA is added to conjugate any un-bound ^{89}Zr in solution. The ^{89}Zr-DFO and ^{89}Zr-DTPA species are separated by thin layer chromatography (0.05 M DTPA mobile phase), and the quantity of DFO required to bind 50% of the added activity is calculated by sigmoidal interpolation. Due to periodic degradation in measured effective specific activities of ^{89}Zr over the past several years, it has become clear that DFO stock solutions should be stored in a cool environment, approximately 3° C, and should be re-diluted from a concentrated stock solution at least once per year.

7.2.2 Competitive Binding Assay

In order to determine which trace metals have the largest impact on the chelation of ^{89}Zr and ^{64}Cu , competitive binding experiments were performed. Samples were created containing increasing competitive burdens (X) of $CuCl_2$, $ZnCl_2$, $FeCl_2$, $NiCl_2$, $CrCl_3$, $CoCl_2$, $MnCl_2$, and YCl_3. High-specific activity ^{64}Cu was added to each sample, and the pH was adjusted to appropriate labeling conditions (50 pmol of NOTA was added following the activity aliquots of ^{64}Cu. Labeling efficiencies (^{64}Cu-NOTA) were measured using TLC's, and were fit by linear regression to the form $f(X) = y_0/(1 - AX)$, where A is the chelation affinity (inverse of dissociation constant) and X is the molar ratio of the

metallic impurity to the amount of chelate. The results of this experiment are shown in Figure 7.5. As a competitor, natural copper metal had the largest impact on ^{64}Cu, which is comforting in the sense that the selectivity of NOTA for copper is affirmed. After copper, zinc contamination had the largest impact on chelation. The overall results for these experiments are shown in Table 7.2.

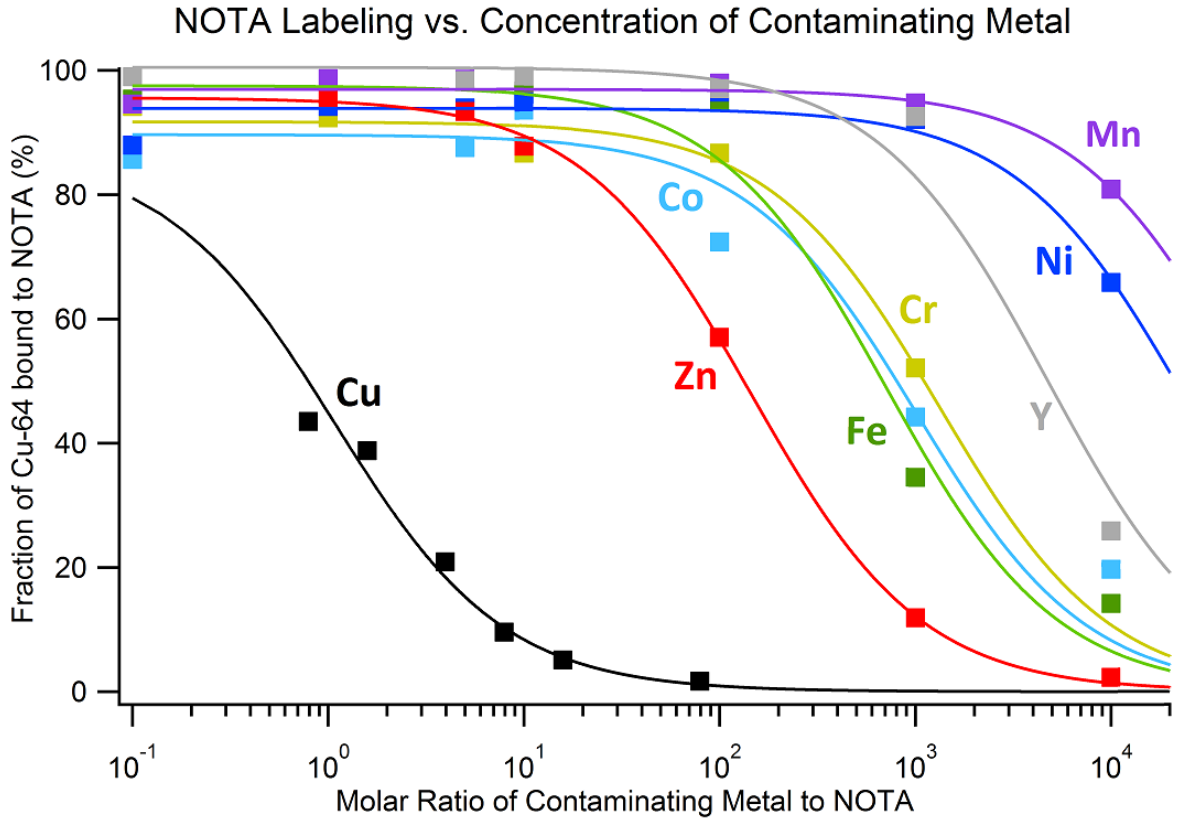

Figure 7.5: Competitive chelation plots with increasing Cu, Zn, Co, Fe, Cr, Y, Ni, and Mn impurities. Copper has the largest impact on ^{64}Cu-NOTA binding, followed by Zn, Fe, Co, Cr, Y, Ni, then Mn.

Metal	NOTA	DOTA	DFO
Cu	1.06 ± 0.15	5.22 ± 3.15	125 ± 107
Zn	266 ± 13	152 ± 31	16076 ± 8132
Fe	715 ± 187	$1.4\text{x}10^{6} \pm 5.8\text{x}10^{7}$	76552 ± 16700
Ni	24237 ± 4128	2789 ± 967	13477 ± 897
Co	1056 ± 373	476 ± 203	88489 ± 181802
Cr	1326 ± 189	11660 ± 3475	$2.1\text{x}10^{12} \pm 9.3\text{x}10^{19}$
Y	4257 ± 1031	30 ± 22	40 ± 15

Table 7.2: Chelation results for several metals with NOTA, DOTA, and DFO from competitive binding assays.

7.2.3 Analytic Model of Effective Specific Activity

In order to form a model allowing for direct calculation of effective specific activity from the affinity values measured herein, the following definitions are made:

- $f_i \equiv$ fraction of chelate occupied by metal *i*
- $A_i \equiv$ affinity of metal for given chelate and labeling conditons
- $x_i \equiv$ moles of metal *i*
- $c \equiv$ moles of chelate
- $X_i \equiv$ molar ratio of metal *i* to chelate = x_i/c
- $L_i \equiv$ fraction of metal *i* bound by chelate

First, we start with the receptor binding form:

$$f_1 = \frac{\frac{X_1}{A_1}}{1 + \frac{X_1}{A_1} + \frac{X_2}{A_2} + \frac{X_3}{A_3} + ...} \tag{7.1}$$

Note that the end behaviors of this form are appropriate; As the molar ratio of contaminating metals to chelate ($X_2, X_3, ...$) increases, the fraction of chelate occupied by metal 1 (f_1) approaches zero. Likewise, when the molar ratio of contaminating metals to chelate ($X_2, X_3, ...$) decreases, the fraction of chelate occupied by metal 1 (f_1) approaches $1/((A_1/X_1)+1)$, which for $X_1 = A_1$ results in 50% of the chelate being occupied by metal 1.

Next, substituting the definition $X_i = x_i/c$ into Equation 7.1:

$$f_1 = \frac{\frac{x_1/c}{A_1}}{1 + \frac{x_1/c}{A_1} + \frac{x_2/c}{A_2} + \frac{x_3/c}{A_3} + ...} = \frac{\frac{x_1}{A_1}}{c + \frac{x_1}{A_1} + \frac{x_2}{A_2} + \frac{x_3}{A_3} + ...} \tag{7.2}$$

As x_i may be measured by trace-metal quantification, this equation approaches a meaningful form. The quantity which is measured during an ESA assay though is the fraction of radiotracer (metal 1) which is bound by chelate, rather than the fraction of chelate which is occupied by metal 1. To this end, the substitution is made:

$$L_1 = \frac{c}{x_1} f_1 = \frac{\frac{c}{A_1}}{c + \frac{x_1}{A_1} + \frac{x_2}{A_2} + \frac{x_3}{A_3} + ...} \tag{7.3}$$

Next, we can define c_{50} as the amount of chelate required to allow for 50% of radiotracer binding ($L_1 = 0.5$). From this, effective specific activity may be notated as:

$$SA_{eff} = \frac{\text{Activity}}{2 * c_{50}} \tag{7.4}$$

Solving for c_{50} such that $L_1 = 0.5$:

$$0.5 = \frac{\frac{c_{50}}{A_1}}{c_{50} + \frac{x_1}{A_1} + \frac{x_2}{A_2} + \frac{x_3}{A_3} + ...} \tag{7.5}$$

Simplifying,

$$c_{50} = \left(\frac{2}{A_1} - 1\right)^{-1} \left(\frac{x_1}{A_1} + \frac{x_2}{A_2} + \frac{x_3}{A_3} + ...\right) = \left(\frac{2}{A_1} - 1\right)^{-1} \sum_{i=1}^{n} \frac{x_i}{A_i} \tag{7.6}$$

Based on assumption that $A_1 = 1$, this can be simplified and substituted into Eq. 7.4. This assumption is equivalent to stating that equal amounts of chelate and metal 1 would result in 50% binding at equilibrium. This is consistent with empirical Cu-NOTA results, as shown in Figure 7.5. This substitution yields our desired form:

$$\boxed{SA_{eff} = \frac{\text{Activity}}{2 * c(L_1 = 0.5)} = \frac{\text{Activity}}{2 \sum_{i=1}^{n} \frac{x_i}{A_i}}} \tag{7.7}$$

This form describes the theoretical relationship between the measured affinities of contaminating metals, their masses in the final radionuclide product, and effective specific activity under the same labeling conditions.

7.2.4 Trace Metal Analysis

In order to measure trace metal impurities during and follow radiochemistry, an microwave-plasma atomic emission spectrometer (Agilent, MP-AES 4200) was acquired and used. This device operates by forming a nitrogen-based plasma above a quartz injection

tube, which is diffusely filled with nebulized sample. Within the plasma, elemental constituents emit their characteristic fluorescence which are selectively measured by refracting the light source, extending the pathlength of the desired refracted angle with mirrors, and detection by a segmented charge-coupled detector. Quantification is achieved by calibration with known concentrations of the desired metals in an identical chemical matrix, typically 0.1 M HCl.

In order to evaluate the analytic model of ESA described herein, 'hold-backs' from ^{64}Cu productions (9/23/13 – 4/14/14, $n = 24$) were collected and tested for the most probable trace-metal impurities (Zn, Cu, Ni, Fe) by MP-AES assay. EoC activities of these samples ranged from 1.7 – 18.4 mCi, and volume ranged from 0.89 – 1.18 mL of 0.1 M HCl. The quantification results from these samples are listed in Table 7.3.

Date	Zn (ng)	Cu (ng)	Ni (ng)	Fe (ng)	% of total
9/23/2013	119.8 ± 2.5	34.1 ± 0.3	10.7 ± 2.3	104.9 ± 63.8	2.3%
9/30/2013	61.9 ± 0.4	11.8 ± 0.1	13.8 ± 1.4	127.4 ± 176.5	2.8%
10/7/2013	42.7 ± 1.4	37.1 ± 0.9	11.0 ± 1.2	229.5 ± 115.4	2.6%
10/14/2013	73.1 ± 2.7	19.8 ± 0.4	101.6 ± 2.2	266.3 ± 232.7	2.4%
10/21/2013	5513.0 ± 41.7	19.8 ± 0.1	74.9 ± 2.1	20.8 ± 20.8	3.1%
10/28/2013	87.5 ± 6.2	15.1 ± 0.4	12.5 ± 2.0	106.2 ± 125.6	–
11/11/2013	11.2 ± 3.4	11.9 ± 0.5	9.6 ± 1.6	283.3 ± 256.1	2.5%
11/18/2013	2458.3 ± 80.4	53.8 ± 0.5	24.6 ± 0.8	54.0 ± 120.1	3.2%
11/18/2013	21954.4 ± 79.7	77.8 ± 1.0	194.6 ± 3.9	1196.0 ± 16.4	3.2%
11/25/2013	281.7 ± 44.0	30.2 ± 0.4	68.6 ± 1.0	0.0 ± 24.7	5.7%
12/2/2013	144.9 ± 0.6	14.9 ± 0.4	20.1 ± 2.5	14.5 ± 44.5	0.3%
12/9/2013	289.9 ± 0.2	25.3 ± 0.5	30.8 ± 2.5	16.4 ± 91.0	1.0%
12/10/2013	757.9 ± 7.0	11.6 ± 0.7	13.9 ± 1.6	0.0 ± 55.4	–
12/16/2013	26.2 ± 4.8	30.4 ± 0.4	85.8 ± 4.1	0.0 ± 37.4	0.6%
1/6/2014	4.4 ± 0.8	11.7 ± 0.2	17.9 ± 2.8	121.1 ± 2.5	1.9%
1/14/2014	139.3 ± 0.8	16.3 ± 0.3	67.0 ± 0.8	41.6 ± 5.1	1.7%
1/21/2014	43.6 ± 2.7	135.2 ± 1.1	67.1 ± 3.1	136.8 ± 2.5	0.9%
1/27/2014	388.1 ± 5.0	159.7 ± 1.3	69.2 ± 1.3	277.1 ± 21.6	4.9%
2/3/2014	157.8 ± 2.3	95.0 ± 1.0	186.8 ± 2.2	0.0 ± 77.3	4.1%
2/10/2014	8.6 ± 1.2	7.8 ± 0.4	24.5 ± 1.1	0.0 ± 30.6	1.1%
2/17/2014	11.6 ± 0.9	7.2 ± 0.3	29.6 ± 2.0	25.1 ± 47.5	1.7%
2/24/2014	35.1 ± 3.1	10.4 ± 0.1	36.8 ± 0.4	186.2 ± 2.3	2.1%
4/7/2014	81.7 ± 0.4	9.0 ± 0.5	25.4 ± 1.6	0.0 ± 72.9	1.0%
4/14/2014	88.4 ± 0.7	24.5 ± 0.3	30.2 ± 0.6	26.2 ± 81.3	4.8%

Table 7.3: MP-AES trace metal quantification of ^{64}Cu production 'hold-back' samples. Uncertainties listed are the standard deviation between test replicates, and does not include calibration uncertainty (~5%).

7.2.5 Results

In order to evaluate our measured NOTA affinities and the model described in Section 7.2.3, ESA values were predicted from trace metal quantification results for ^{64}Cu productions from 9/23/2013 – 4/14/2014. Further, a physical specific activity — simply the activity of the sample (Ci) divided by the sum of measured impurities (μmol) — was

also calculated for each production. These two values are plotted against measured effective specific activity by competitive NOTA chelation assays, our gold standard for ESA, in Figure 7.6.

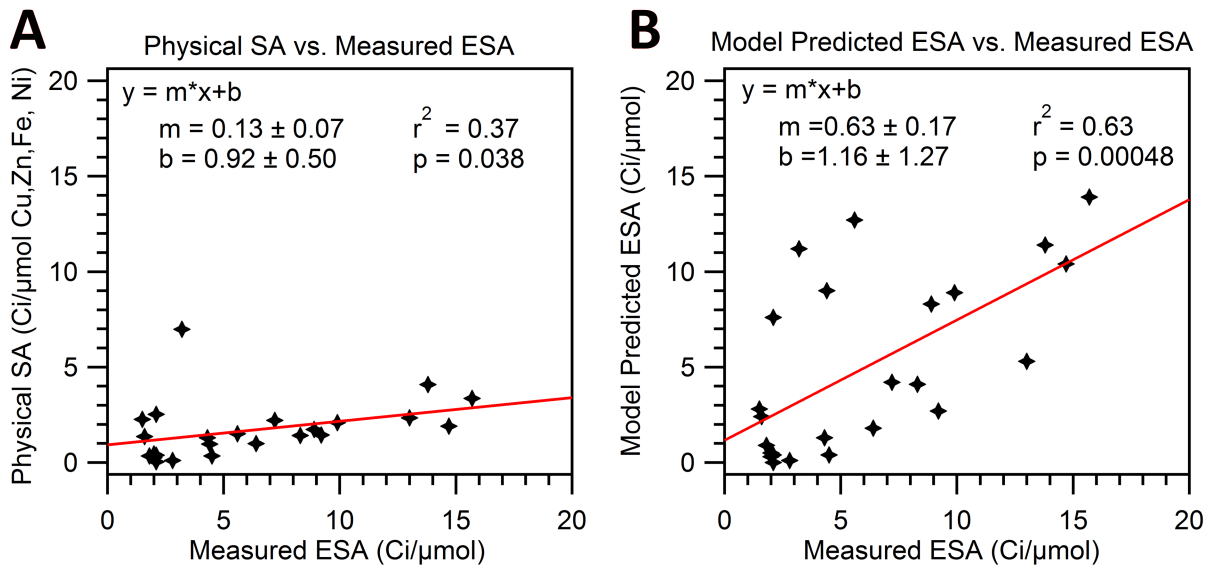

Figure 7.6: (A) Physical specific activity — the activity of a sample (Ci) divided by the sum of measured Cu, Ni, Fe, Zn impurities (µmol) — plotted against measured ESA. (B) Model-based ESA predictions plotted against measured ESA.

These results suggest that the model is more effective at predicting ESA than a physical measure of specific activity with a slope of 0.63 and correlation coefficient (r^2) of 0.63, compared to the physical specific activity plot which resulted in a slope of 0.13 and a correlation coefficient (r^2) of 0.37. Both of these plots had a significant correlation between the variables, $p = 0.038$ for the physical SA metric and $p = 0.00048$ for the model ESA metric. The physical specific activity being significantly lower than the measured ESA is expected, due to the selectivity of NOTA for Cu.

Although the model performed better than a physical estimation, the large spread

of data suggests that this model might not be a particularly robust or useful method of predicting ESA, particularly when considering that affinities must be measured under all possible labeling conditions (chelate molecule, temperature, pH) for the formation of a 'complete' model. With that said, it is also possible that our "gold standard" — competitive NOTA chelation assay — is inadequate for this type of comparison, as the measured ESA seems to depend on the amount of activity used in the competitive chelation assay (further described in Appendix E).

7.3 Conclusion

Significant advances have been made in the production of ^{64}Cu and ^{89}Zr at UW-Madison. In particular, a spot-welded ^{nat}Y target for the production of ^{89}Zr has enabled an increase in beam current of >3x compared with previous production targets. Following the production of these radiometals, the critical evaluation of chemical purity is important for informing radiolabeling strategies as well as monitoring long-term purity trends. To this end, the analytic foundation for a model of effective specific activity has been developed.

8 DIRECTIONS FOR FUTURE WORK

In this work we have explored a variety of novel applications for positron-emitting radiometals and have detailed methods for the production of several isotopes with half-lives conducive to national/international distribution. The availability of ^{52}Mn, $^{76/77}$Br, ^{64}Cu, ^{89}Zr, and ^{194}Au may enable exciting new avenues of investigation in basic science, disease biology research, and nuclear medicine at UW-Madison and abroad.

From the work described in this dissertation many directions for future research remain. Some of these possible projects are listed below.

- Critical analysis of the FitzPeaks SAMPO implementation by testing with artificially generated spectral data.
- Test of iterative back-ground subtraction method for auto-gamma counting of samples with large activity discrepancies.
- Construction of a full-size version of the linearly-filled Derenzo phantom. Compare image quality of conventional to linearly-filled Derenzo phantom. Estimate a personnel dose reduction for the linearly-filled design compared to the conventional design.
- Development of automated modules for the radiochemical isolation of ^{51}Mn, ^{52}Mn.
- Testing of ethanol-based anion exchange separation of Mn/Cr using organic acids to lower pH without introducing additional aqueous volume.

- Investigation of the clearance kinetics of radiomanganese in cardiac tissue. A close examination of differences brought about by myocardial ischemia or infarction may prove valuable.
- Examination of longitudinal functional beta cell mass using ^{51}Mn in chronic STZ–murine model of type-I diabetes.
- Investigation of the correlation of radiomanganese pancreatic accumulation, measured by PET ROI analysis, with histological measurements of beta cell mass, i.e. sectioning and insulin staining or optical projection tomography.
- Test of the multiple monitor reaction variance minimization method for proton energy determination with simpler target geometries (i.e. a single ^{nat}Al degrader) and compare experimental results against analytic and monte carlo proton transport predictions.
- Test methods for electrolytic dissolution of ^{nat}Pt or investigate binary alloys of Pt for targets which are more soluble in mineral acids.
- Investigate the formation of alternate binary alloys of selenium for the production of radiobromine. $NbSe_x$ in particular show promise.

REFERENCES

Aarnio, PA, MT Nikkinen, and JT Routti. 1992. SAMPO 90 high resolution interactive gamma-spectrum analysis including automation with macros. *Journal of Radioanalytical and Nuclear Chemistry* 160(1):289–295.

Agency, U.S. Environmental Protection. 1999. Integrated risk information system (IRIS) on chromium VI.

Ahn, B, N Parashurama, M Patel, K Ziv, S Bhaumik, SS Yaghoubi, R Paulmurugan, and SS Gambhir. 2014. Noninvasive reporter gene imaging of human Oct4 (pluripotency) dynamics during the differentiation of embryonic stem cells in living subjects. *Molecular Imaging and Biology* 16(6):865–876.

Al-Abyad, M, MNH Comsan, and SM Qaim. 2009. Excitation functions of proton-induced reactions on ^{nat}Fe and enriched ^{57}Fe with particular reference to the production of ^{57}Co. *Applied Radiation and Isotopes* 67(1):122–128.

Al-Saleh, FS, AA Al-Harbi, and A Azzam. 2006. Excitation functions of proton induced nuclear reactions on natural copper using a medium-sized cyclotron. *Radiochimica Acta* 94(8/2006):391–396.

Aleksandrov, VN, MP Semyonova, and VG Semyonov. 1987. Excitation functions for radionuclides produced by (p,x) reactions of copper and nickel. *Atomnaya Energiya* 62: 411.

Antkowiak, Patrick F. 2011. Manganese-enhanced MRI of pancreatic beta cells in mouse models of type 1 diabetes.

Antkowiak, PF, BK Stevens, CS Nunemaker, M McDuffie, and FH Epstein. 2013. Manganese-enhanced magnetic resonance imaging detects declining pancreatic β-cell mass in a cyclophosphamide-accelerated mouse model of type 1 diabetes. *Diabetes* 62(1):44–48.

Antkowiak, PF, SA Tersey, JD Carter, MH Vandsburger, JL Nadler, FH Epstein, and RG Mirmira. 2009. Noninvasive assessment of pancreatic β-cell function in vivo with manganese-enhanced magnetic resonance imaging. *American Journal of Physiology-Endocrinology and Metabolism* 296(3):E573–E578.

Antkowiak, PF, MH Vandsburger, and FH Epstein. 2012. Quantitative pancreatic β cell MRI using manganese-enhanced Look-Locker imaging and two-site water exchange analysis. *Magnetic Resonance in Medicine* 67(6):1730–1739.

Arbab, AS, C Thiffault, B Navia, SJ Victor, K Hong, L Zhang, Q Jiang, NRS Varma, ASM Iskander, and M Chopp. 2012. Tracking of In-111-labeled human umbilical tissue-derived cells (hUTC) in a rat model of cerebral ischemia using SPECT imaging. *BMC Medical Imaging* 12(1):1.

Asti, M, M Tegoni, D Farioli, M Iori, C Guidotti, CS Cutler, P Mayer, A Versari, and D Salvo. 2012. Influence of cations on the complexation yield of DOTATATE with yttrium and lutetium: a perspective study for enhancing the ^{90}Y and ^{177}Lu labeling conditions. *Nuclear Medicine and Biology* 39(4):509–517.

Atkins, HL, P Som, RG Fairchild, J Hui, E Schachner, A Goldman, and T Ku. 1979. Myocardial positron tomography with manganese-52m 1. *Radiology* 133(3):769–774.

Atwater, I, CM Dawson, A Scott, G Eddlestone, and E Rojas. 1979. The nature of the oscillatory behaviour in electrical activity from pancreatic beta-cell. *Hormone and Metabolic Research. Supplement Series* 100–107.

Au, C, A Benedetto, and M Aschner. 2008. Manganese transport in eukaryotes: the role of DMT1. *Neurotoxicology* 29(4):569–576.

Avrigeanu, M, V Avrigeanu, P Bem, U Fischer, M Honusek, K Katovsky, C Manailescu, J Mrazek, E Simeckova, and L Zavorka. 2014. Low energy deuteron-induced reactions on Fe isotopes. *Physical Review C* 89(4):044613.

Backofen, EW, and RH Herber. 1955. Half-lives of Mn52 and Mn54. *Physical Review* 97(3):743.

Bandara, N, A Zheleznyak, K Cherukuri, DA Griffith, C Limberakis, DA Tess, C Jianqing, R Waterhouse, and SE Lapi. 2016. Evaluation of Cu-64 and Ga-68 radiolabeled glucagon-like peptide-1 receptor agonists as PET tracers for pancreatic β cell imaging. *Molecular Imaging and Biology* 18(1):90–98.

Bansal, A, MK Pandey, YE Demirhan, JJ Nesbitt, RJ Crespo-Diaz, A Terzic, A Behfar, and TR DeGrado. 2015. Novel ^{89}Zr cell labeling approach for PET-based cell trafficking studies. *European Journal of Nuclear Medicine and Molecular Imaging Research* 5(1):1.

Barchuk, IF, VS Bulkin, VA Kuz'menko, PM Kurilo, Yu N Lobach, AF Ogorodnik, VS Prokopenko, VD Sklyarenko, and VV Tokarevskii. 1987. Excitation functions of reactions caused by the interaction of protons with energies of up to 67 MeV and nuclei of silicon and iron. *Atomic Energy* 63(1):528–532.

Barrandon, JN, JL Debrun, A Kohn, and RH Spear. 1975. Etude du dosage de Ti, V, Cr, Fe, Ni, Cu et Zn par activation avec des protons d'energie limitee a 20 MeV. *Nuclear Instruments and Methods* 127(2):269–278.

Bartelle, BB, KU Szulc, GA Suero-Abreu, JJ Rodriguez, and DH Turnbull. 2013. Divalent metal transporter, DMT1: A novel MRI reporter protein. *Magnetic Resonance in Medicine* 70(3):842–850.

Bernau, K, CM Lewis, AM Petelinsek, HA Benink, CA Zimprich, ME Meyerand, M Suzuki, and CN Svendsen. 2014. In vivo tracking of human neural progenitor cells in the rat brain using bioluminescence imaging. *Journal of Neuroscience Methods* 228:67–78.

Bernhardt, P, E Forssell-Aronsson, L Jacobsson, and G Skarnemark. 2001. Low-energy electron emitters for targeted radiotherapy of small tumours. *Acta Oncologica* 40(5): 602–608.

Beyer, GJ, and G Pimentel-Gonzales. 2000. Physicochemical and radiochemical aspects of separation of radioiodine from TeO_2-targets. *Radiochimica Acta* 88(3-4/2000):175.

Bianchi, A, L Calabi, C Giorgi, P Losi, P Mariani, D Palano, P Paoli, P Rossi, and B Valtancoli. 2001. Thermodynamic and structural aspects of manganese (II) complexes with polyaminopolycarboxylic ligands based upon 1, 4, 7, 10-tetraazacyclododecane (cyclen). *Journal of the Chemical Society Dalton Transactions* (6):917–922.

Blauenstein, P, R Pellikka, and PA Schubiger. 1997. Reinvestigation of a physiological eluate of the $^{52}Fe/^{52m}Mn$ generator. *Applied Radiation and Isotopes* 48(8):1097–1101.

Bock, T, B Pakkenberg, and K Buschard. 2003. Increased islet volume but unchanged islet number in ob/ob mice. *Diabetes* 52(7):1716–1722.

Bolk, A. 1961. Kirkendall effect and diffusion in the gold-platinum system-II: The concentration penetration curves and the diffusion coefficients. *Acta Metallurgica* 9(7): 643–652.

Braun, T, and G Ghersini. 1975. *Extraction chromatography*, vol. 2. Elsevier.

Brodzinski, RL, LA Rancitelli, JA Cooper, and NA Wogman. 1971. High-energy proton spallation of iron. *Physical Review C* 4(4):1257.

Brom, M, W Woliner-Van Der Weg, L Joosten, C Frielink, T Bouckenooghe, P Rijken, K Andralojc, BJ Goke, M de Jong, and DL Eizirik. 2014. Non-invasive quantification of the beta cell mass by SPECT with ^{111}In-labelled exendin. *Diabetologia* 57(5):950–959.

Brunnquell, Christina L. 2016. Molecular MRI and PET methods for detection of transplanted stem cells and cancer. Thesis.

Brunnquell, CL, R Hernandez, SA Graves, I Smit-Oistad, RJ Nickles, W Cai, ME Meyerand, and M Suzuki. 2016. Uptake and retention of manganese contrast agents for PET and MRI in the rodent brain. *Contrast Media and Molecular Imaging* in press.

Buchholz, M, I Spahn, and HH Coenen. 2015. Optimized separation procedure for production of no-carrier-added radiomanganese for positron emission tomography. *Radiochimica Acta* 103(12):893–899.

Buchholz, M, I Spahn, B Scholten, and HH Coenen. 2013. Cross-section measurements for the formation of manganese-52 and its isolation with a non-hazardous eluent. *Radiochimca Acta* 101(8):491–499.

Burgus, W. H., and J. W. Kennedy. 1950. Chemical effects accompanying the decay of Mn^{51}. *Chem. Phys.* 14(1).

Burgus, WH, GA Cowan, JW Hadley, W Hess, T Shull, ML Stevenson, and HF York. 1954. Cross sections for the reactions ^{48}Ti(d,2n)^{48}V; ^{52}Cr(d,2n)^{52}Mn; and ^{56}Fe(d,2n)^{56}Co. *Physical Review* 95(3):750.

Burkemper, JL, C Huang, A Li, L Yuan, K Rich, J McConathy, and SE Lapi. 2015. Synthesis and biological evaluation of (S)-amino-2-methyl-4-[^{76}Br] bromo-3-(E)-butenoic acid (BrVAIB) for brain tumor imaging. *Journal of Medicinal Chemistry* 58(21):8542–8552.

Cai, W, T Gao, H Hong, and J Sun. 2008. Applications of gold nanoparticles in cancer nanotechnology. *Nanotechnology, Science and Applications* 2008(1).

Calne, DB, NS Chu, CC Huang, CS Lu, and W Olanow. 1994. Manganism and idiopathic parkinsonism: similarities and differences. *Neurology* 44(9):1583–1586.

Camu, F. 1975. Impaired early insulin response to glycemic stimulus during enflurane anesthesia in dogs. *Acta Anaesthesiologica Belgica* 27:267–271.

Cherevko, S, AR Zeradjanin, GP Keeley, and KJJ Mayrhofer. 2014. A comparative study on gold and platinum dissolution in acidic and alkaline media. *Journal of The Electrochemical Society* 161(12):H822–H830.

Cherry, SR. 2001. Fundamentals of positron emission tomography and applications in preclinical drug development. *Journal of Clinical Pharmacology* 41(5):482–491.

Cianciaruso, C, A Pagani, C Martelli, M Bacigaluppi, ML Squadrito, AL Dico, M De Palma, R Furlan, G Lucignani, and A Falini. 2014. Cellular magnetic resonance with iron oxide nanoparticles: long-term persistence of SPIO signal in the CNS after transplanted cell death. *Nanomedicine* 9(10):1457–1474.

Ciarmatori, A, G Cicoria, D Pancaldi, A Infantino, S Boschi, S Fanti, and M Marengo. 2011. Some experimental studies on ^{89}Zr production. *Radiochimica Acta* 99(10):631–634.

Cogneau, M, L Gilly, and J Cara. 1966. Absolute cross sections and excitation functions for deuteron induced reactions on chromium between 2 and 12 MeV. *Nuclear Physics* 79(1):203–208.

Cotton, FA, and G Wilkinson. 1980. Advanced inorganic chemistry.

Crossgrove, J, and W Zheng. 2004. Manganese toxicity upon overexposure. *NMR in Biomedicine* 17(8):544–553.

Dabkowski, AM, SJ Paisey, M Talboys, and C Marshall. 2015. Optimization of cyclotron production for radiometal of zirconium-89. *Acta Physica Polonica A* 127(5):1479–1482.

Das, NR, and SN Bhattacharyya. 1976. Solvent extraction of gold. *Talanta* 23(7):535–540.

Daube, ME, and RJ Nickles. 1985. Development of myocardial perfusion tracers for positron emission tomography. *International Journal of Nuclear Medicine and Biology* 12(4):303–314.

Daum, E. 1997. Investigation of light ion induced activation cross sections in iron proton induced activation cross sections. *Fed Rep Germ Rep* 43(4).

De Goeij, JJM, and ML Bonardi. 2005. How do we define the concepts specific activity, radioactive concentration, carrier, carrier-free and no-carrier-added? *Journal of Radioanalytical and Nuclear Chemistry* 263(1):13–18.

Deeds, MC, JM Anderson, AS Armstrong, DA Gastineau, HJ Hiddinga, A Jahangir, NL Eberhardt, and YC Kudva. 2011. Single dose streptozotocin-induced diabetes: considerations for study design in islet transplantation models. *Laboratory Animals* 45(3):131–140.

DeGrado, TR, MK Pandey, JF Byrne, HP Engelbrecht, H Jiang, AB Packard, KA Thomas, MS Jacobson, GL Curran, and VJ Lowe. 2014. Preparation and preliminary evaluation of ^{63}Zn-zinc citrate as a novel PET imaging biomarker for zinc. *Journal of Nuclear Medicine* 55(8):1348–1354.

Derenzo, SE, TF Budinger, JL Cahoon, RH Huesman, and HG Jackson. 1977. High resolution computed tomography of positron emitters. *Nuclear Science IEEE Transactions* 24(1):544–558.

Desborough, JP, PM Jones, SJ Persaud, MJ Landon, and SL Howell. 1993. Isoflurane inhibits insulin secretion from isolated rat pancreatic islets of Langerhans. *British journal of anaesthesia* 71(6):873–876.

Diltoer, M, and F Camu. 1988. Glucose homeostasis and insulin secretion during isoflurane anesthesia in humans. *Anesthesiology* 68(6):880–886.

DiPiro, JT, and P Trouiller. 2002. *World health organization essential drug list*, 908–909. CRC Press.

Ditroi, F, F Tarkanyi, J Csikai, MS Uddin, M Hagiwara, and M Baba. 2005. Investigation of activation cross sections of the proton induced nuclear reactions on natural iron at medium energies. *AIP Conference Proceedings* 769(1):1011.

Dmitriev, PP, IO Konstantinov, and NN Krasnov. 1969. Methods for producing the mn-52 isotope. *Atomic Energy* 26(5):539–541.

Ducote, JL, Y Alivov, and S Molloi. 2011. Imaging of nanoparticles with dual-energy computed tomography. *Physics in Medicine and Biology* 56(7):2031.

Ellison, PA, HF Valdovinos, SA Graves, TE Barnhart, and RJ Nickles. 2016. Spot-welding solid targets for high current cyclotron irradiation. *Applied Radiation and Isotopes* 118: 350–353.

Emery, JF, and GW Leddicotte. 1961. *The radiochemistry of gold*, vol. 3036. National Academies.

Engelbrecht, H, M Pandey, J Byrne, A Packard, J Gruetzmacher, K Thomas, T DeGrado, V Lowe, G Curran, and T Decklever. 2013. Production of zn-63 via solution target and biodistribution in mice. *Journal of Nuclear Medicine* 54(supplement 2):386–386.

Engle, JW, H Hong, Y Zhang, HF Valdovinos, DV Myklejord, TE Barnhart, CP Theuer, RJ Nickles, and W Cai. 2012. Positron emission tomography imaging of tumor angiogenesis with a ^{66}Ga-labeled monoclonal antibody. *Molecular Pharmaceutics* 9(5): 1441–1448.

Eriksson, O, M Jahan, P Johnstrom, O Korsgren, A Sundin, C Halldin, and L Johansson. 2010. In vivo and in vitro characterization of [^{18}F]-FE-(+)-DTBZ as a tracer for beta-cell mass. *Nuclear Medicine and Biology* 37(3):357–363.

Erlandsson, B, A Marcinkowski, and N Wall. 1970. The decay and half-life of ^{51}Mn. *Arkiv for Fysik* 40:139.

Erlandsson, K, I Buvat, PH Pretorius, BA Thomas, and BF Hutton. 2012. A review of partial volume correction techniques for emission tomography and their applications in neurology, cardiology and oncology. *Physics in Medicine and Biology* 57(21):R119.

Eter, WA, D Bos, C Frielink, OC Boerman, M Brom, and M Gotthardt. 2015. Graft revascularization is essential for non-invasive monitoring of transplanted islets with radiolabeled exendin. *Scientific Reports* 5.

Fassbender, M, Yu N Shubin, and SM Qaim. 1999. Formation of activation products in interactions of medium energy protons with Na, Si, P, S, CI, Ca and Fe. *Radiochimica Acta* 84(2):59–68.

Feldman, EL, NM Boulis, J Hur, K Johe, SB Rutkove, T Federici, M Polak, J Bordeau, SA Sakowski, and JD Glass. 2014. Intraspinal neural stem cell transplantation in amyotrophic lateral sclerosis: phase 1 trial outcomes. *Annals of Neurology* 75(3):363–373.

Ferrer, JC, J Rapaport, and S Raman. 1973. Decay of ^{51}Mn. *Zeitschrift fur Physik* 265(4): 365–370.

Gambhir, SS. 2002. Molecular imaging of cancer with positron emission tomography. *Nature Reviews Cancer* 2(9):683–693.

Gargiulo, S, A Greco, M Gramanzini, MP Petretta, A Ferro, M Larobina, M Panico, A Brunetti, and A Cuocolo. 2012. PET/CT imaging in mouse models of myocardial ischemia. *BioMed Research International* 2012.

Gimi, B, L Leoni, J Oberholzer, M Braun, J Avila, Y Wang, T Desai, LH Philipson, RL Magin, and BB Roman. 2006. Functional MR microimaging of pancreatic β-cell activation. *Cell transplantation* 15(2):195–203.

Glibert, KM, and HT Easterday. 1966. The decay of ^{51}Mn. *Nuclear Physics* 86(2):279–288.

Gloris, M, R Michel, F Sudbrock, U Herpers, P Malmborg, and B Holmqvist. 2001. Proton-induced production of residual radionuclides in lead at intermediate energies. *Nuclear Instruments and Methods Section A* 463(3):593–633.

Gmmink, R, and JB Niday. 1972. Computerized quantitative analysis by gamma-ray spectrometry: Description of the GAMANAL program.

Golson, ML, AA Misfeldt, UG Kopsombut, CP Petersen, and M Gannon. 2010. High fat diet regulation of β-cell proliferation and β-cell mass. *Open Endocrinology Journal* 4.

Goorley, T, M James, T Booth, F Brown, J Bull, LJ Cox, J Durkee, J Elson, M Fensin, and RA Forster. 2012. Initial MCNP6 release overview. *Nuclear Technology* 180(3):298–315.

Gotthardt, M, DL Eizirik, M Cnop, and M Brom. 2014. Beta cell imaging-a key tool in optimized diabetes prevention and treatment. *Trends in Endocrinology and Metabolism* 25(8):375–377.

Grant, PM, RE Whipple, JW Barnes, GE Bentley, PM Wanek, and HA O'Brien. 1981. The production and recovery of ^{77}Br at Los Alamos for nuclear medicine studies. *Journal of Inorganic and Nuclear Chemistry* 43(10):2217–2222.

Graves, SA, R Hernandez, J Fonslet, CG England, HF Valdovinos, PA Ellison, TE Barnhart, DR Elema, CP Theuer, and W Cai. 2015. Novel preparation methods of ^{52}mn for immunoPET imaging. *Bioconjugate Chemistry* 26(10):2118–2124.

Graves, SA, H Valdovinos, T Barnhart, and R Nickles. 2016. Novel ^{51}Mn production methods for calcium channel transport based applications. *Journal of Nuclear Medicine* 57(supplement 2):380–380.

Greenwood, LR, and RK Smither. 1984. Measurement of Cu spallation cross sections at IPNS.

Greenwood, NN, and A Earnshaw. 1997. *Chemistry of the elements 2nd edition*. Butterworth-Heinemann.

Gregg, T, C Poudel, BA Schmidt, RS Dhillon, SM Sdao, NA Truchan, EL Baar, LA Fernandez, JM Denu, and KW Eliceiri. 2016. Pancreatic β cells from mice offset age-associated mitochondrial deficiency with reduced K_{ATP} channel activity. *Diabetes* db160432.

Greiter, MB, A Giussani, V Hollriegl, WB Li, and U Oeh. 2011. Human biokinetic data and a new compartmental model of zirconium- a tracer study with enriched stable isotopes. *Science of the Total Environment* 409(19):3701–3710.

Gross, B C, JL Erkal, SY Lockwood, C Chen, and DM Spence. 2014. Evaluation of 3D printing and its potential impact on biotechnology and the chemical sciences. *Analytical Chemistry* 86(7):3240–3253.

Grutter, A. 1982. Excitation functions for radioactive isotopes produced by proton bombardment of Cu and Al in the energy range of 16 to 70 MeV. *Nuclear Physics A* 383(1):98–108.

Ha, J, LS Satin, and AS Sherman. 2015. A mathematical model of the pathogenesis, prevention, and reversal of type 2 diabetes. *Endocrinology* 157(2):624–635.

Harper, PV, KA Lathrop, and JW Ryan. 1983. Quantitative studies in radiopharmaceutical science, A.2 production of manganese-51. *Nuclear Medicine and Imaging Research, Progress Report DOE/EV/10359-4*.

Hellman, B, E Gylfe, P Bergsten, E Grapengiesser, PE Lund, A Berts, A Tengholm, DG Pipeleers, and Z Ling. 1994. Glucose induces oscillatory Ca^{2+} signalling and insulin release in human pancreatic beta cells. *Diabetologia* 37(2):S11–S20.

Henshaw, G, I Parkin, and G Shaw. 1997. Convenient, room-temperature liquid ammonia routes to metal chalcogenides. *Journal of the Chemical Society, Dalton Transactions* (2): 231–236.

Hernandez, R, S Graves, C England, J Jeffery, R Nickles, and W Cai. 2016. Radiomanganese PET imaging of pancreatic beta cells. *Journal of Nuclear Medicine* 57(supplement 2):5–5.

Herscheid, JDM, CM Vos, and A Hoekstra. 1983. Manganese-52m for direct application: a new ^{52}Fe/^{52m}Mn generator based on a hydroxamate resin. *Applied Radiation and Isotopes* 34(6):883–886.

Heydegger, HR, CK Garrett, and A Van Ginneken. 1972. Thin-target cross sections for some Cr, Mn, Fe, Co, Ni, and Zn nuclides produced in copper by 82-to 416-MeV protons. *Physical Review C* 6(4):1235.

Hichwa, RD, and RJ Nickles. 1981. Targetry for the production of medical isotopes. *IEEE Transactions on Nuclear Science* 28(2):1924–1927.

Holland, JP, Y Sheh, and JS Lewis. 2009. Standardized methods for the production of high specific-activity zirconium-89. *Nuclear Medicine and Biology* 36(7):729–739.

Hong, H, GW Severin, Y Yang, JW Engle, Y Zhang, TE Barnhart, G Liu, BR Leigh, RJ Nickles, and W Cai. 2012. Positron emission tomography imaging of CD105 expression with ^{89}Zr-Df-TRC105. *European Journal of Nuclear Medicine and Molecular Imaging* 39(1):138–148.

Hu, TCC, RG Pautler, GA MacGowan, and AP Koretsky. 2001. Manganese-enhanced MRI of mouse heart during changes in inotropy. *Magnetic Resonance Medicine* 46(5): 884–890.

Huang, X, IH El-Sayed, W Qian, and MA El-Sayed. 2006. Cancer cell imaging and photothermal therapy in the near-infrared region by using gold nanorods. *Journal of the American Chemical Society* 128(6):2115–2120.

Huda, W, and JW Scrimger. 1989. Irradiation of volunteers in nuclear medicine. *Journal of Nuclear Medicine* 30(2):260–264.

Ido, T, A Hermanne, F Ditroi, Z Szucs, I Mahunka, and F Tarkanyi. 2002. Excitation functions of proton induced nuclear reactions on ^{nat}Rb from 30 to 70 MeV: Implication for the production of ^{82}Sr and other medically important Rb and Sr radioisotopes. *Nuclear Instruments and Methods Section B* 194(4):369–388.

Illing, AC, A Shawki, CL Cunningham, and B Mackenzie. 2012. Substrate profile and metal-ion selectivity of human divalent metal-ion transporter-1. *Journal of Biological Chemistry* 287(36):30485–30496.

Ionescu-Tirgoviste, Cn, PA Gagniuc, E Gubceac, L Mardare, I Popescu, S Dima, and M Militaru. 2015. A 3D map of the islet routes throughout the healthy human pancreas. *Scientific Reports* 5.

Ishinishi, N, and T Morishige. 1969. A study on the distribution of ^{95}Zr-^{95}Nb administered subcutaneously to rats: Comparison between young and adult rats. *Journal of Radiation Research* 10(3-4):101–106.

Jackman, KR, JW Engle, FM Nortier, KD John, ER Birnbaum, and DE Norman. 2014. Synthetic spectra for radioactive strontium production QA/QC. *Journal of Radioanalytical and Nuclear Chemistry* 302(1):347–352.

Jacobs, KE, D Behera, J Rosenberg, G Gold, M Moseley, D Yeomans, and S Biswal. 2012. Oral manganese as an MRI contrast agent for the detection of nociceptive activity. *NMR in Biomedicine* 25(4):563–9.

Janowski, M, P Walczak, T Kropiwnicki, E Jurkiewicz, K Domanska-Janik, JWM Bulte, B Lukomska, and M Roszkowski. 2014. Long-term MRI cell tracking after intraventricular delivery in a patient with global cerebral ischemia and prospects for magnetic navigation of stem cells within the CSF. *PLoS One* 9(6):e97631.

Judenhofer, MS, and SR Cherry. 2013. Applications for preclinical PET/MRI. *Seminars in Nuclear Medicine* 43(1):19–29.

Judenhofer, MS, HF Wehrl, DF Newport, C Catana, SB Siegel, M Becker, A Thielscher, M Kneilling, MP Lichy, and M Eichner. 2008. Simultaneous PET-MRI: a new approach for functional and morphological imaging. *Nature Medicine* 14(4):459–465.

Junde, H, H Su, and MA Chunhui. 2007. Nuclear data sheets for A=52. *Nuclear Data Sheets* 108(4):773–882.

Kehl, F, JG Krolikowski, B Mraovic, PS Pagel, DC Warltier, and JR Kersten. 2002. Hyperglycemia prevents isoflurane-induced preconditioning against myocardial infarction. *Journal of the American Society of Anesthesiologists* 96(1):183–188.

Kiesewetter, DO, H Gao, Y Ma, G Niu, Q Quan, N Guo, and X Chen. 2012. ^{18}F-radiolabeled analogs of exendin-4 for PET imaging of GLP-1 in insulinoma. *European Journal of Nuclear Medicine and Molecular Imaging* 39(3):463–473.

Kilimnik, G, J Jo, V Periwal, MC Zielinski, and M Hara. 2012. Quantification of islet size and architecture. *Islets* 4(2):167–172.

Kim, A, K Miller, J Jo, G Kilimnik, P Wojcik, and M Hara. 2009. Islet architecture: a comparative study. *Islets* 1(2):129–136.

Kim, K, MU Khandaker, H Naik, and G Kim. 2014. Excitation functions of proton induced reactions on ^{nat}Fe in the energy region up to 45 MeV. *Nuclear Instruments and Methods Section B* 322:63–69.

Kim, T, E Momin, J Choi, K Yuan, H Zaidi, J Kim, M Park, N Lee, MT McMahon, and A Quinones-Hinojosa. 2011. Mesoporous silica-coated hollow manganese oxide nanoparticles as positive T1 contrast agents for labeling and MRI tracking of adipose-derived mesenchymal stem cells. *Journal of the American Chemical Society* 133(9):2955–2961.

Kirsi, M, Y Cheng-Bin, F Veronica, I Tamiko, E Viki-Veikko, R Johan, J Jori, S Tiina, T Tuula, and T Marko. 2014. ^{64}Cu-and ^{68}Ga-labelled [Nle14, Lys40 (Ahx-NODAGA) NH2]-exendin-4 for pancreatic beta cell imaging in rats. *Molecular Imaging and Biology* 16(2):255–263.

Klein, ATJ, F Rosch, HH Coenen, and SM Qaim. 2002. Production of the positron emitter ^{51}Mn via the ^{50}Cr(d,n) reaction: targetry and separation of no-carrier-added radiomanganese. *Radiochimica Acta* 90(3/2002):167–177.

Klein, ATJ, F Rosch, and SM Qaim. 2000. Investigation of ^{50}Cr(d,n)^{51}Mn and ^{nat}Cr(p,x)^{51}Mn processes with respect to the production of the positron emitter ^{51}Mn. *Radiochimica Acta* 88(5/2000):253.

Knox, K. 1990. Fast and slow reactions of chromium compounds. *Journal of Chemical Education* 67(8):700.

Koehne, G, M Doubrovin, E Doubrovina, P Zanzonico, HF Gallardo, A Ivanova, J Balatoni, J Teruya-Feldstein, G Heller, and C May. 2003. Serial in vivo imaging of the targeted migration of human HSV-TK-transduced antigen-specific lymphocytes. *Nature Biotechnology* 21(4):405–413.

Koning, AJ, S Hilaire, and MC Duijvestijn. 2007. TALYS-1.0. *International Conference on Nuclear Data for Science and Technology* 211–214.

Kopecky, P. 1985. Proton beam monitoring via the Cu(p,x)^{58}Co, ^{63}Cu(p,2n)^{62}Zn and ^{65}Cu(p,n)^{65}Zn reactions in copper. *Applied Radiation and Isotopes* 36(8):657–661.

Kraus, KA, and F Nelson. 1954. Anion-exchange studies: Ion exchange in concentrated electrolytes. gold (iii) in hydrochloric acid solutions. *Journal of the American Chemical Society* 76(4):984–987.

Kung, MP, C Hou, BP Lieberman, S Oya, DE Ponde, E Blankemeyer, D Skovronsky, MR Kilbourn, and HF Kung. 2008. In vivo imaging of β-cell mass in rats using ^{18}F-FP-(+)-DTBZ: a potential PET ligand for studying diabetes mellitus. *Journal of Nuclear Medicine* 49(7):1171–1176.

Lagunas-Solar, MC, and JA Jungerman. 1979. Cyclotron production of carrier-free cobalt-55, a new positron-emitting label for bleomycin. *Applied Radiation and Isotopes* 30(1):25–32.

Lahiri, S, D Nayak, and G Korschinek. 2006. Separation of no-carrier-added ^{52}Mn from bulk chromium: A simulation study for accelerator mass spectrometry measurement of ^{53}Mn. *Analytical Chemistry* 78(21):7517–7521.

Lambrecht, RM, and AP Wolf. Cyclotron production of K-38, Mn-51, Mn-52m, and Kr-52m for positron emission tomography. In *Journal of labelled compounds and radiopharmaceuticals*, vol. 16, 129–130. John Wiley and Sons.

Lamprianou, S, R Immonen, C Nabuurs, A Gjinovci, L Vinet, XCR Montet, R Gruetter, and P Meda. 2011. High-resolution magnetic resonance imaging quantitatively detects individual pancreatic islets. *Diabetes* 60(11):2853–2860.

Landoni, G, O Fochi, and G Torri. 2008. Cardiac protection by volatile anaesthetics: a review. *Current Vascular Pharmacology* 6(2):108–111.

Lang, C, D Habs, K Parodi, and PG Thirolf. 2014. Sub-millimeter nuclear medical imaging with high sensitivity in positron emission tomography using β^+ γ coincidences. *Journal of Instrumentation* 9(01):P01008.

Lang, C, S Lehner, A Todica, G Boening, WM Franz, P Bartenstein, M Hacker, and R David. 2013. Positron emission tomography based in-vivo imaging of early phase stem cell retention after intramyocardial delivery in the mouse model. *European Journal of Nuclear Medicine and Molecular Imaging* 40(11):1730–1738.

Larobina, M, A Brunetti, and M Salvatore. 2006. Small animal PET: a review of commercially available imaging systems. *Current Medical Imaging Reviews* 2(2):187–192.

Lenzen, S. 2008. The mechanisms of alloxan-and streptozotocin-induced diabetes. *Diabetologia* 51(2):216–226.

Levin, CS, and EJ Hoffman. 1999. Calculation of positron range and its effect on the fundamental limit of positron emission tomography system spatial resolution. *Physics in Medicine and Biology* 44(3):781.

Levkovskii, VN. 1991. Activation cross sections for the nuclides of medium mass region (A=40–100) with medium energy (E=10–50 MeV) protons and alpha particles (experiment and systematics). *Inter-Vesi, Moscow, Russia*.

Lewis, CM, SA Graves, R Hernandez, HF Valdovinos, TE Barnhart, W Cai, ME Meyerand, RJ Nickles, and M Suzuki. 2015. ^{52}Mn production for PET/MRI tracking of human stem cells expressing divalent metal transporter 1 (DMT1). *Theranostics* 5(3): 227.

Li, L, W Jiang, K Luo, H Song, F Lan, Y Wu, and Z Gu. 2013. Superparamagnetic iron oxide nanoparticles as MRI contrast agents for non-invasive stem cell labeling and tracking. *Theranostics* 3(8):595–615.

Like, AA, and AA Rossini. 1976. Streptozotocin-induced pancreatic insulitis: new model of diabetes mellitus. *Science* 193(4251):415–417.

Lin, YJ, and AP Koretsky. 1997. Manganese ion enhances T1-weighted MRI during brain activation: An approach to direct imaging of brain function. *Magnetic Resonance in Medicine* 38(3):378–388.

Liu, X, Q Dai, L Austin, J Coutts, G Knowles, J Zou, H Chen, and Q Huo. 2008. A one-step homogeneous immunoassay for cancer biomarker detection using gold nanoparticle probes coupled with dynamic light scattering. *Journal of the American Chemical Society* 130(9):2780–2782.

Livingood, J. J., and G. T. Seaborg. 1938. Radioactive manganese isotopes. *Phys. Rev.* 54(6):391.

Lubag, AJM, LM De Leon-Rodriguez, SC Burgess, and AD Sherry. 2011. Noninvasive MRI of β-cell function using a Zn^{2+}-responsive contrast agent. *Proceedings of the National Academy of Sciences* 108(45):18400–18405.

Lubberink, M, V Tolmachev, S Beshara, and H Lundqvist. 1999. Quantification aspects of patient studies with ^{52}Fe in positron emission tomography. *Applied Radiation and Isotopes* 51(6):707–715.

Lundqvist, H, V Tolmachev, A Bruskin, L Einarsson, and P Malmborg. 1995. Rapid separation of ^{110}In from enriched Cd targets by thermal diffusion. *Applied Radiation and Isotopes* 46(9):859–863.

Madhusudhan, CP, S Treves, AP Wolf, and RM Lambrecht. 1979. Cyclotron isotopes and radiopharmaceuticals XXXI. improvements in ^{77}Br production and radiochemical separation from enriched $^{78}Se^{+}$. *Journal of Radioanalytical Chemistry* 53(1-2):299–305.

Mahoney, JP, and WJ Small. 1968. Studies on manganese: III. the biological half-life of radiomanganese in man and factors which affect this half-life. *Journal of Clinical Investigation* 47(3):643.

Makkar, RR, RR Smith, KE Cheng, K Malliaras, LEJ Thomson, D Berman, LSC Czer, L Marban, A Mendizabal, and PV Johnston. 2012. Intracoronary cardiosphere-derived cells for heart regeneration after myocardial infarction (CADUCEUS): a prospective, randomised phase 1 trial. *The Lancet* 379(9819):895–904.

Martin, CC, BT Christian, MR Satter, LDH Nickerson, and RJ Nickles. 1995. Quantitative PET with positron emitters that emit prompt gamma rays. *IEEE Transactions on Medical Imaging* 14(4):681–687.

Marus, LA, JW Engle, KD John, ER Birnbaum, and FM Nortier. 2015. Experimental and computational techniques for the analysis of proton beam propagation through a target stack. *Nuclear Instruments and Methods Section B* 345:48–52.

Mastren, T, BV Marquez, DE Sultan, E Bollinger, P Eisenbeis, T Voller, and SE Lapi. 2015. Cyclotron production of high-specific activity ^{55}Co and in vivo evaluation of the stability of ^{55}Co metal-chelate-peptide complexes. *Molecular Imaging* 14(10):7290.2015. 00025.

McBryde, WAE, and JH Yoe. 1948. Colorimetric determination of gold as bromoaurate. *Analytical Chemistry* 20(11):1094–1099.

McCarthy, DW, RE Shefer, RE Klinkowstein, LA Bass, WH Margeneau, CS Cutler, CJ Anderson, and MJ Welch. 1997. Efficient production of high specific activity ^{64}Cu using a biomedical cyclotron. *Nuclear Medicine and Biology* 24(1):35–43.

Mealey, J. 1957. Turn-over of carrier-free zirconium-89 in man.

Merrins, MJ, C Poudel, JP McKenna, J Ha, A Sherman, R Bertram, and LS Satin. 2016. Phase analysis of metabolic oscillations and membrane potential in pancreatic islet β-cells. *Biophysical Journal* 110(3):691–699.

Mettler, FA, W Huda, TT Yoshizumi, and M Mahesh. 2008. Effective doses in radiology and diagnostic nuclear medicine: a catalog 1. *Radiology* 248(1):254–263.

Michel, R, R Bodemann, H Busemann, R Daunke, M Gloris, H-J Lange, B Klug, A Krins, I Leya, and M LÃ¼pke. 1997. Cross sections for the production of residual nuclides by low-and medium-energy protons from the target elements C, N, O, Mg, Al, Si, Ca, Ti, V, Mn, Fe, Co, Ni, Cu, Sr, Y, Zr, Nb, Ba and Au. *Nuclear Instruments and Methods B* 129(2):153–193.

Michel, R, and G Brinkmann. 1980. On the depth-dependent production of radionuclides (44 < a < 59) by solar protons in extraterrestrial matter. *Journal of Radioanalytical Chemistry* 59(2):467–510.

Michel, R, G Brinkmann, H Weigel, and W Herr. 1979. Measurement and hybrid-model analysis of proton-induced reactions with V, Fe and Co. *Nuclear Physics A* 322(1):40–60.

Michel, R, R Stueck, and F Peiffer. 1983. Proton-induced reaction on Ti, V, Mn, Fe, Co, and Ni ions.

Miller, D. R., R. C. Thompson, and B. B. Cunningham. 1948. Products of high energy deuteron and helium ion bombardments of copper. *Phys. Rev.* 74:347.

Mills, SJ, GF Steyn, and FM Nortier. 1992. Experimental and theoretical excitation functions of radionuclides produced in proton bombardment of copper up to 200 MeV. *Applied Radiation and Isotopes* 43(8):1019–1030.

Moloto, N, MJ Moloto, NJ Coville, and S Sinha Ray. 2009. Optical and structural characterization of nickel selenide nanoparticles synthesized by simple methods. *Journal of Crystal Growth* 311(15):3924–3932.

Moore, A. 2009. Advances in beta-cell imaging. *European journal of radiology* 70(2): 254–257.

Moyer, Bruce A. 2009. *Ion exchange and solvent extraction: a series of advances*, vol. 19. CRC Press.

Murakami, T, RL Baron, MS Peterson, JH Oliver, PL Davis, SR Confer, and MP Federle. 1996. Hepatocellular carcinoma: MR imaging with mangafodipir trisodium (Mn-DPDP). *Radiology* 200(1):69–77.

Murthy, R, P Harris, N Simpson, R Van Heertum, R Leibel, JJ Mann, and R Parsey. 2008. Whole body [^{11}C]-dihydrotetrabenazine imaging of baboons: biodistribution and human radiation dosimetry estimates. *European Journal of Nuclear Medicine and Molecular Imaging* 35(4):790–797.

Nagle, RJ, and RA Meyer. 1977. Half-life of Mn-52. *Physical Review C* 16(4):1683.

Napieczynska, H, C Calaminus, GW Severin, J Fonslet, and BJ Pichler. Mn-52 as a PET neural tract tracer. In *European molecular imaging meeting*.

Nunn, AD, and SL Waters. 1975. Target materials for the cyclotron production of carrier-free ^{77}Br. *Applied Radiation and Isotopes* 26(12):731–735.

Odaka, K, I Aoki, J Moriya, K Tateno, H Tadokoro, J Kershaw, T Minamino, T Irie, T Fukumura, and I Komuro. 2011. In vivo tracking of transplanted mononuclear cells using manganese-enhanced magnetic resonance imaging (MEMRI). *PloS one* 6(10): e25487.

O'Neal, SL, L Hong, S Fu, W Jiang, A Jones, LH Nie, and W Zheng. 2014. Manganese accumulation in bone following chronic exposure in rats: Steady-state concentration and half-life in bone. *Toxicology Letters* 229(1):93–100.

Onkamo, P, S Vaananen, M Karvonen, and J Tuomilehto. 1999. Worldwide increase in incidence of type i diabetes-the analysis of the data on published incidence trends. *Diabetologia* 42(12):1395–1403.

Paty, BW, S Bonner-Weir, MR Laughlin, AJ Mcewan, and AMJ Shapiro. 2004. Toward development of imaging modalities for islets after transplantation: insights from the national institutes of health workshop on beta cell imaging. *Transplantation* 77(8): 1133–1137.

Paulus, MJ, SS Gleason, ME Easterly, and CJ Foltz. 2001. A review of high-resolution x-ray computed tomography and other imaging modalities for small animal research. *Lab Animals* 30(3):36–45.

Pautler, RG. 2004. In vivo, trans-synaptic tract-tracing utilizing manganese-enhanced magnetic resonance imaging (MEMRI). *NMR in Biomedicine* 17(8):595–601.

Pietrzyk, DJ. 1960. Anion exchange separations of metal ions in partially nonaqueous solutions. *Retrospective Theses and Dissertations* Paper 2390:119.

Pirko, I, J Gamez, E Shearier, M Raman, A Johnson, and S Macura. 2012. Manganese enhanced MRI (MEMRI) in murine cns inflammatory disease models (s21. 007). *Neurology* 78(Meeting Abstracts 1):S21. 007.

Protection, ICRP. 2007. The 2007 recommendation of the international commission on radiological protection. *ICRP*.

Raymond, J, and RE Blankenship. 2008. The origin of the oxygen-evolving complex. *Coordination Chemistry Reviews* 252(3):377–383.

Rodriguez-Porcel, M, JC Wu, and SS Gambhir. 2009. Molecular imaging of stem cells. *Harvard Stem Cell Institute*.

Rorsman, P, P-O Berggren, and B Hellman. 1982. Manganese accumulation in pancreatic β-cells and its stimulation by glucose. *Biochemical Journal* 202(2):435–444.

Rorsman, P, and B Hellman. 1983. The interaction between manganese and calcium fluxes in pancreatic β-cells. *Biochemical Journal* 210(2):307–314.

Rorsman, P, and E Renstrom. 2003. Insulin granule dynamics in pancreatic beta cells. *Diabetologia* 46(8):1029–1045.

Routti, JT. 1969. SAMPO, a fortran IV program for computer analysis of gamma spectra from Ge (Li) detectors, and for other spectra with peaks. *Lawrence Berkeley National Laboratory*.

Sanchez-Crespo, A, P Andreo, and SA Larsson. 2004. Positron flight in human tissues and its influence on pet image spatial resolution. *European Journal of Nuclear Medicine and Molecular Imaging* 31(1):44–51.

Santamaria, AB, and SI Sulsky. 2010. Risk assessment of an essential element: manganese. *Journal of Toxicology and Environmental Health, Part A* 73(2-3):128–155.

Sato, N, H Wu, KO Asiedu, LP Szajek, GL Griffiths, and PL Choyke. 2015. ^{89}Zr-oxine complex PET cell imaging in monitoring cell-based therapies. *Radiology* 275(2):490–500.

Schafer, MK-H, NR Hartwig, N Kalmbach, M Klietz, M Anlauf, LE Eiden, and E Weihe. 2013. Species-specific vesicular monoamine transporter 2 (VMAT2) expression in mammalian pancreatic beta cells: implications for optimising radioligand-based human beta cell mass (BCM) imaging in animal models. *Diabetologia* 56(5):1047–1056.

Schima, W, R Fugger, E Schober, C Oettl, P Wamser, F Grabenwoger, JM Ryan, and G Novacek. 2002. Diagnosis and staging of pancreatic cancer: Comparison of mangafodipir trisodium-enhanced MR imaging and contrast-enhanced helical hydro-CT. *American Journal of Roentgenology* 179(3):717–724.

Schmor, PW. Review of cyclotrons used in the production of radioisotopes for biomedical applications. In *Proc. of the 19th international conference on cyclotrons and their applications*, 419–424.

Schoen, NC, G Orlov, and RJ McDonald. 1979. Excitation functions for radioactive isotopes produced by proton bombardment of Fe, Co, and W in the energy range from 10 to 60 MeV. *Physical Review C* 20(1):88.

Schubert, C, MC van Langeveld, and LA Donoso. 2013. Innovations in 3D printing: a 3D overview from optics to organs. *British Journal of Ophthalmology* bjophthalmol–2013–304446.

Selvaraju, RK, I Velikyan, L Johansson, Z Wu, I Todorov, J Shively, F Kandeel, O Korsgren, and O Eriksson. 2013. In vivo imaging of the glucagonlike peptide 1 receptor in the pancreas with ^{68}Ga-labeled DO3A-exendin-4. *Journal of Nuclear Medicine* 54(8): 1458–1463.

Severin, GW, JT Jorgensen, S Wiehr, AM Rolle, AE Hansen, A Maurer, M Hasenberg, B Pichler, A Kjaer, and AI Jensen. 2015. The impact of weakly bound ^{89}Zr on preclinical studies: non-specific accumulation in solid tumors and aspergillus infection. *Nuclear Medicine and Biology* 42(4):360–8.

Shahid, Muhammad, Kwangsoo Kim, Haladhara Naik, Muhammad Zaman, Sung-Chul Yang, and Guinyun Kim. 2015. Measurement of excitation functions in proton induced reactions on natural copper from their threshold to 43 MeV. *Nuclear Instruments and Methods Section B* 342:305–313.

Shibuya, I, and WW Douglas. 1992. Calcium channels in rat melanotrophs are permeable to manganese, cobalt, cadmium, and lanthanum, but not to nickel: evidence provided by fluorescence changes in fura-2-loaded cells. *Endocrinology* 131(4):1936–1941.

Siikanen, J, TA Tran, TG Olsson, S-E Strand, and A Sandell. 2014. A solid target system with remote handling of irradiated targets for PET cyclotrons. *Applied Radiation and Isotopes* 94:294–301.

Silva, AC, JH Lee, I Aoki, and AP Koretsky. 2004. Manganese-enhanced magnetic resonance imaging (MEMRI): methodological and practical considerations. *NMR in Biomedicine* 17(8):532–543.

Simpson, NR, F Souza, P Witkowski, A Maffei, A Raffo, A Herron, M Kilbourn, A Jurewicz, K Herold, and E Liu. 2006. Visualizing pancreatic β-cell mass with [^{11}C] DTBZ. *Nuclear Medicine and Biology* 33(7):855–864.

Singhal, T, Y-S Ding, D Weinzimmer, MD Normandin, D Labaree, J Ropchan, N Nabulsi, S-F Lin, MB Skaddan, and WC Soeller. 2011. Pancreatic beta cell mass pet imaging and quantification with [^{11}C] DTBZ and [^{18}F] FP-(+)-DTBZ in rodent models of diabetes. *Molecular Imaging and Biology* 13(5):973–984.

Som, P, ZH Oster, W Lewis, RG Fairchild, and HL Atkins. 1983. Radiomanganese for positron emission tomography: a comparative study with ^{207}Tl-chloride. *Nuclear Medicine Communications* 4(1):8–16.

Stabin, MG, RB Sparks, and E Crowe. 2005. OLINDA/EXM: the second-generation personal computer software for internal dose assessment in nuclear medicine. *Journal of Nuclear Medicine* 46(6):1023–1027.

Tanaka, K, D Weihrauch, LM Ludwig, JR Kersten, PS Pagel, and DC Warltier. 2003. Mitochondrial adenosine triphosphate-regulated potassium channel opening acts as a trigger for isoflurane-induced preconditioning by generating reactive oxygen species. *Journal of the American Society of Anesthesiologists* 98(4):935–943.

Tarkanyi, F, F Ditroi, S Takacs, J Csikai, A Hermanne, MS Uddin, M Hagiwara, M Baba, Yu N Shubin, and AI Dityuk. 2004a. Activation cross-sections of light ion induced nuclear reactions on platinum: proton induced reactions. *Nuclear Instruments and Methods Section B* 226(4):473–489.

Tarkanyi, F, S Takacs, F Ditroi, A Hermanne, YN Shubin, and AI Dityuk. 2004b. Activation cross-sections of deuteron induced reactions on platinum. *Nuclear Instruments and Methods Section B* 226(4):490–498.

Tarkanyi, F, S Takacs, K Gul, A Hermanne, MG Mustafa, M Nortier, P Oblozinsky, SM Qaim, B Scholten, and YN Shubin. 2001. Beam monitor reactions. *Charged particle cross-section database for medical radioisotope production: Diagnostic radioisotopes and monitor reactions, IAEA-TECDOC-1211, Vienna* 49.

Tolmachev, V, and H Lundqvist. 1996. Rapid separation of gallium from zinc targets by thermal diffusion. *Applied Radiation and Isotopes* 47(3):297–299.

Topping, GJ. 2014. Manganese imaging with positron emission tomography, autoradiography, and magnetic resonance. *Electronic Theses and Dissertations*.

Topping, GJ, P Schaffer, C Hoehr, TJ Ruth, and V Sossi. 2013. Manganese-52 positron emission tomography tracer characterization and initial results in phantoms and in vivo. *Medical Physics* 40(4):042502.

Tornehave, D, P Kristensen, J Romer, LB Knudsen, and RS Heller. 2008. Expression of the GLP-1 receptor in mouse, rat, and human pancreas. *Journal of Histochemistry and Cytochemistry* 56(9):841–851.

Valdovinos, H, SA Graves, T Barnhart, and RJ Nickles. 2014. ^{55}Co separation from proton irradiated metallic nickel. *Xiii Mexican Symposium on Medical Physics* 1626(1): 217–220.

Valdovinos, H, R Hernandez, S Goel, S Graves, T Barnhart, W Cai, and R Nickles. 2016. Cyclotron production of ^{58m}Co for auger electron-based targeted radioimmunotherapy and pet imaging post-therapy with the daughter ^{58g}Co. *Journal of Nuclear Medicine* 57(supplement 2):332–332.

Valdovinos, HF, SA Graves, T Barnhart, and RJ Nickles. a. Co-55 separation from deuteron-irradiated electrodeposited Fe-54 targets. In *Journal of nuclear medicine: Conference proceedings*, vol. 56. Society of Nuclear Medicine.

Valdovinos, HF, R Hernandez, S Goel, S Graves, T Barnhart, W Cai, and RJ Nickles. b. Auger electron-based targeted radioimmunotherapy with ^{58m}Co, a feasibility study. In *Aip conference proceedings*, vol. 80006.

Vegas, AJ, O Veiseh, M Gurtler, JR Millman, FW Pagliuca, AR Bader, JC Doloff, J Li, M Chen, and K Olejnik. 2016. Long-term glycemic control using polymer-encapsulated human stem cell-derived beta cells in immune-competent mice. *Nature Medicine*.

Velde, GV, JR Rangarajan, R Vreys, C Guglielmetti, T Dresselaers, M Verhoye, A Van der Linden, Zeger Debyser, V Baekelandt, and F Maes. 2012. Quantitative evaluation of MRI-based tracking of ferritin-labeled endogenous neural stem cell progeny in rodent brain. *Neuroimage* 62(1):367–380.

Venkatraman, M, and JP Neumann. 1990. The Ag-Cr (silver-chromium) system. *Bull. of Alloy Phase Diagrams* 11(3):263–265.

Virostko, J, and AC Powers. 2009. Molecular imaging of the pancreas in small animal models. *Gastroenterology* 136(2):407.

Vlasov, NA, SP Kalinin, AA Ogloblin, VM Pankramov, VP Rudakov, IN Serikov, and VA Sidorov. 1957. Excitation functions for the reactions Mg21(d,α)na22, fe54(d,α)Mn52, Fe54(d,n)Co55, and Zn56(d,2n)Ga66. *Atomic Energy* 2(2):189–192.

Von Mach, MA, J Schlosser, M Weiland, PJ Feilen, M Ringel, JG Hengstler, LS Weilemann, J Beyer, P Kann, and S Schneider. 2003. Size of pancreatic islets of Langerhans: a key parameter for viability after cryopreservation. *Acta diabetologica* 40(3):123–129.

Vosburgh, GJ, LB Flexner, and DB Cowie. 1948. The determination of radioactive iron in biological material with particular reference to purification and separation of iron with iso-propyl ether, ashing and electroplating technique, and accuracy of the method. *Journal of Biological Chemistry* 175:391–404.

Watanabe SH, Ohshima Y Sugo Y Sasaki I Hanaoka H Ishioka NS, Watanabe SA. 2014. Isolation of ^{76}Br from irradiated $Cu_2{}^{76}Se$ targets using dry distillation: evaluations and improvement for routine production. *15th International Workshop on Targetry and Target Chemistry*.

Weir, GC, and S Bonner-Weir. 2004. Five stages of evolving beta-cell dysfunction during progression to diabetes. *Diabetes* 53(suppl 3):S16–S21.

Wenrong, Z, L Hanlin, and Y Weixiang. 1993. Measurement of cross sections by bombarding Fe with protons up to 19 MeV. *Chinese Journal of Nuclear Physics* 15(4): 337–340.

West, PW, P Senise, and JK Carlton. 1952. Extraction of bismuth iodide complexes as a spot test for bismuth. *Analytica Chimica Acta* 6:488–492.

Williams, IR, and CB Fulmer. 1967. Excitation functions for radioactive isotopes produced by protons below 60 MeV on Al, Fe, and Cu. *Physical Review* 162(4):1055.

Wooten, A, E Madrid, GD Schweitzer, LA Lawrence, E Mebrahtu, BC Lewis, and SE Lapi. 2013. Routine production of ^{89}Zr using an automated module. *Applied Sciences* 3(3):593–613.

Wooten, AL, BC Lewis, R Laforest, SV Smith, and SE Lapi. 2015a. Cyclotron production and PET/MR imaging of ^{52}Mn. *Internation Symposium on Radiopharmaceutical Sciences*.

Wooten, AL, BC Lewis, and SE Lapi. 2015b. Cross-sections for (p,x) reactions on natural chromium for the production of ^{52,52m,54}Mn radioisotopes. *Applied Radiation and Isotopes* 96:154–161.

Wu, Z, I Todorov, L Li, JR Bading, Z Li, I Nair, K Ishiyama, D Colcher, PE Conti, and SE Fraser. 2011. In vivo imaging of transplanted islets with ^{64}Cu-DO3A-VS-Cys40-Exendin-4 by targeting GLP-1 receptor. *Bioconjugate chemistry* 22(8):1587–1594.

Xiaolong, H. 2006. Nuclear data sheets for A= 51. *Nuclear Data Sheets* 107(8):2131–2322.

Yaffe, RP, and RA Meyer. 1977. Levels of Cr-52 populated in the decay of V-52, Mn-52g and in the sequence Fe-52 $\rightarrow$ Mn-52m $\rightarrow$ Cr-52. *Physical Review C* 16(4):1581.

Yamada, M, S Momoshima, Y Masutani, K Fujiyoshi, O Abe, M Nakamura, S Aoki, N Tamaoki, and H Okano. 2008. Diffusion-tensor neuronal fiber tractography and

manganese-enhanced MR imaging of primate visual pathway in the common marmoset: Preliminary results. *Radiology* 249(3):855–864.

Yashima, H, Y Uwamino, H Sugita, T Nakamura, S Ito, and A Fukumura. 2002. Projectile dependence of radioactive spallation products induced in copper by high-energy heavy ions. *Physical Review C* 66(4):044607.

Zaman, MR, and SM Qaim. 1996. Excitation functions of (d,n) and (d,α) reactions on ^{54}Fe: Relevance to the production of high purity ^{55}Co at a small cyclotron. *Radiochimica Acta* 75(2):59–64.

Zhang, X, JZ Xing, J Chen, L Ko, J Amanie, S Gulavita, N Pervez, D Yee, R Moore, and W Roa. 2008. Enhanced radiation sensitivity in prostate cancer by gold-nanoparticles. *Clinical and Investigative Medicine* 31(3):160–167.

Zhang, Y, H Hong, JW Engle, J Bean, Y Yang, BR Leigh, TE Barnhart, and W Cai. 2011. Positron emission tomography imaging of CD105 expression with a ^{64}Cu-labeled monoclonal antibody: NOTA is superior to DOTA. *PLoS ONE* 6(12):e28005.

Zhou, C, G Hao, P Thomas, J Liu, M Yu, S Sun, OK Oz, X Sun, and J Zheng. 2012. Near-infrared emitting radioactive gold nanoparticles with molecular pharmacokinetics. *Angewandte Chemie* 124(40):10265–10269.

Ziegler, JF. 1999. Stopping of energetic light ions in elemental matter. *Journal of Applied Physics* 85(3):1249–1272.

A FITZPEAKS CALIBRATION AND OPERATION

FitzPeaks Calibration

All calibration procedures in FitzPeaks may be accomplished with a single multi-source spectrum. For this work, point sources of ^{60}Co, ^{133}Cs ^{137}Cs, ^{152}Eu, and ^{241}Am of known activity were employed.

The sensitivity to calibration source distribution as a function of distance from the HPGe detector was not investigated in this work, but should be considered. Calibration for particularly proximal sample position geometries may necessitate acquiring individual calibration source spectra, followed by artificial superposition. To perform this operation, individual spectra would be acquired in Maestro with a preset live-time. Spectra would then be corrected for dead time and summed.

Opening a Spectrum

- Spectra for FitzPeaks analysis must be saved with the **".chn" file extension** from Maestro.
- To open a file, navigate to to the spectrum in Windows Explorer, **right click**, select **"open with"**, and select "FitzPeaks."
- **Set sample parameters**, such as counting geometry, spectral acquisition date and time, sample mass, end of bombardment date and time, etc., and then confirm these settings by clicking **"OK"**. An example configuration is shown in Figure A.1.

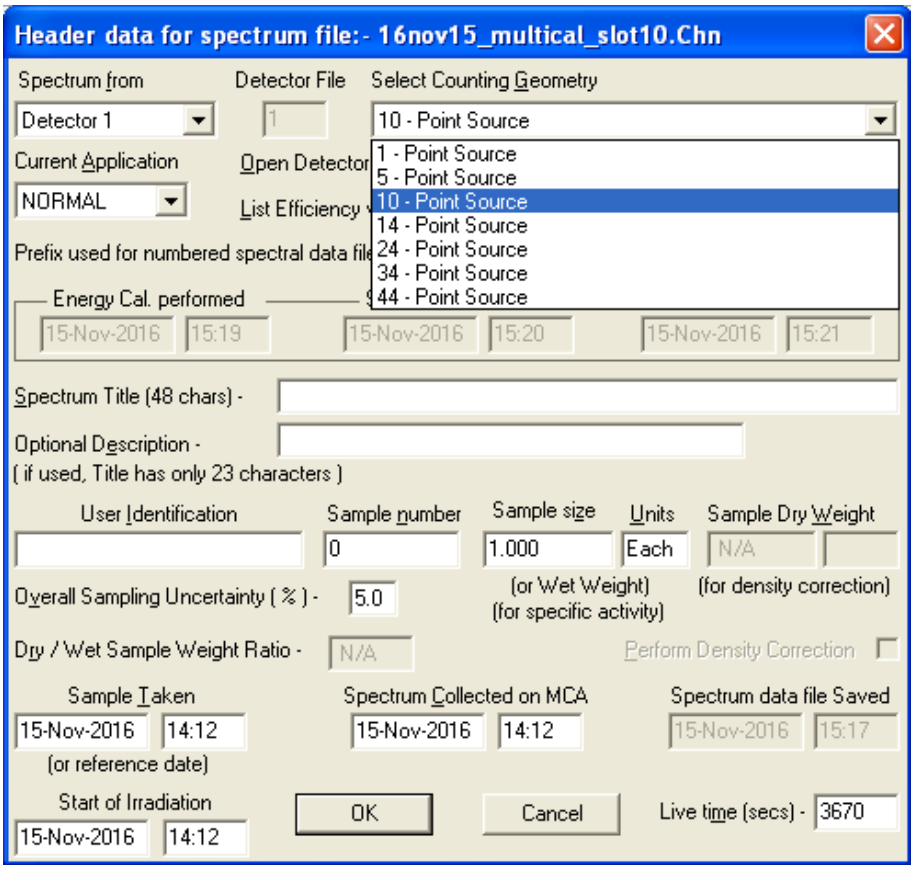

Figure A.1: Spectral file configuration example for FitzPeaks analysis.

Energy Response Calibration

- **Open a multi-source spectrum** acquired at the desired counting geometry, as described above.
- Select **"Calibrate"** from the top toolbar, and then select **"Energy"** from the drop-down menu.
- When prompted to clear the energy and shape calibration, **select "Yes."**
- If prompted to repeat the peak search, **select "Yes."**
- For the cyclotron group standard multi-source spectrum (^{60}Co, ^{133}Cs ^{137}Cs, ^{152}Eu, and ^{241}Am), **open "energycal.enc"** in the FitzPeaks main program directory. For

other calibration source combinations, create an text file containing the desired calibration energies with the file extension ".enc".

- An energy response calibration is automatically generated and presented in the form of a residual plot. The "Goodness of Fit" is also displayed in the left-hand menu. **Select the desired order of fit (1st or 2nd) and press "OK."** An example energy calibration setup is shown in Figure A.2.

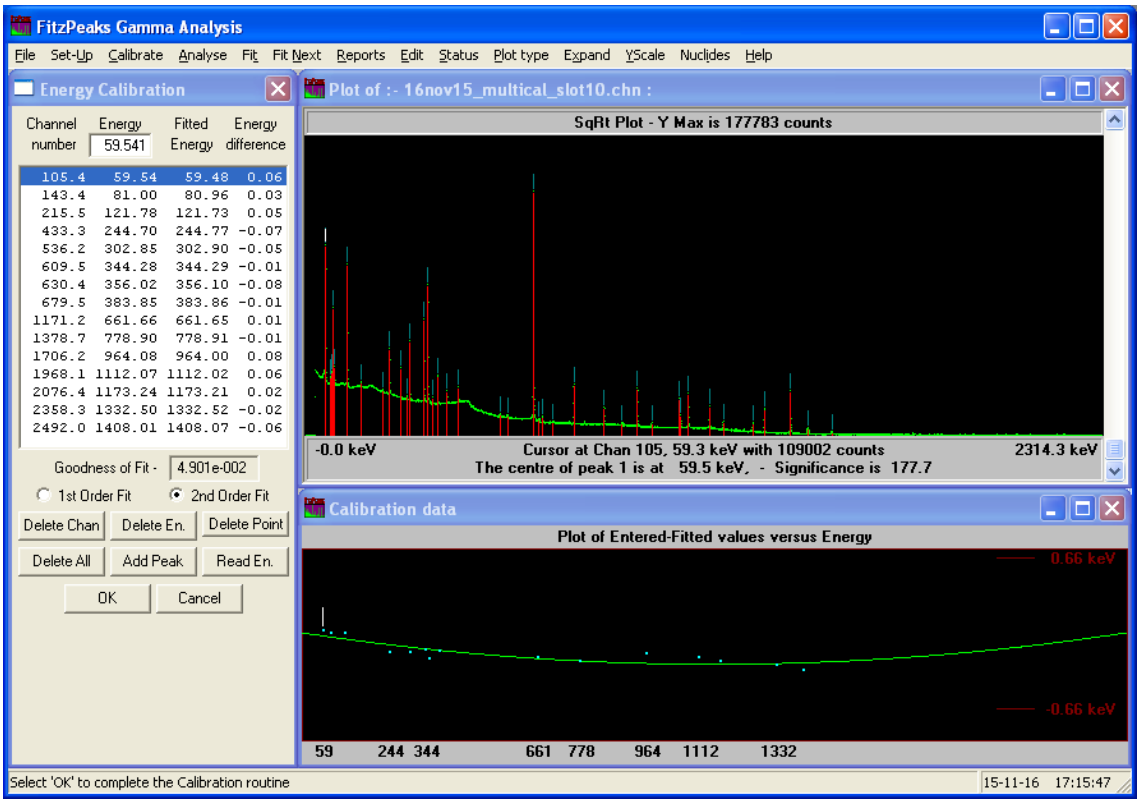

Figure A.2: A second-order model provides the best fit, but may create greater inaccuracies when extrapolating.

Peak Shape Calibration

- **Open a multi-source spectrum** acquired at the desired counting geometry, as previously described.

- Select **"Calibrate"** from the top toolbar, and then select **"Peak Shape"** from the drop-down menu.
- For the cyclotron group standard multi-source spectrum (^{60}Co, ^{133}Cs ^{137}Cs, ^{152}Eu, and ^{241}Am), **open "shapefit.shp"** in the FitzPeaks main program directory. For other calibration source combinations, create an text file containing the desired calibration energies with the file extension ".shp".
- An energy response calibration is automatically generated and presented in the form of a residual plot. The "Goodness of Fit" is also displayed in the left-hand menu. **Select the desired order of fit (1st or 2nd) and press "OK."** An example energy calibration setup is shown in Figure A.2.
- **Press "Fit All"** and wait until peak shape fitting is completed. If desired, **select "Perform High Energy Tailing Calibration" from the left-hand menu.**
- View the resulting plots of peak width vs. energy, high-side tail vs. energy, and low-side tail vs. energy by switching views under "Display function" in the left-hand menu. Evaluate the performance and **select the desired order fo fit (1st or 2nd) for each parameter (width, high, low) and press "OK".** An example peak shape calibration setup is shown in Figure A.3

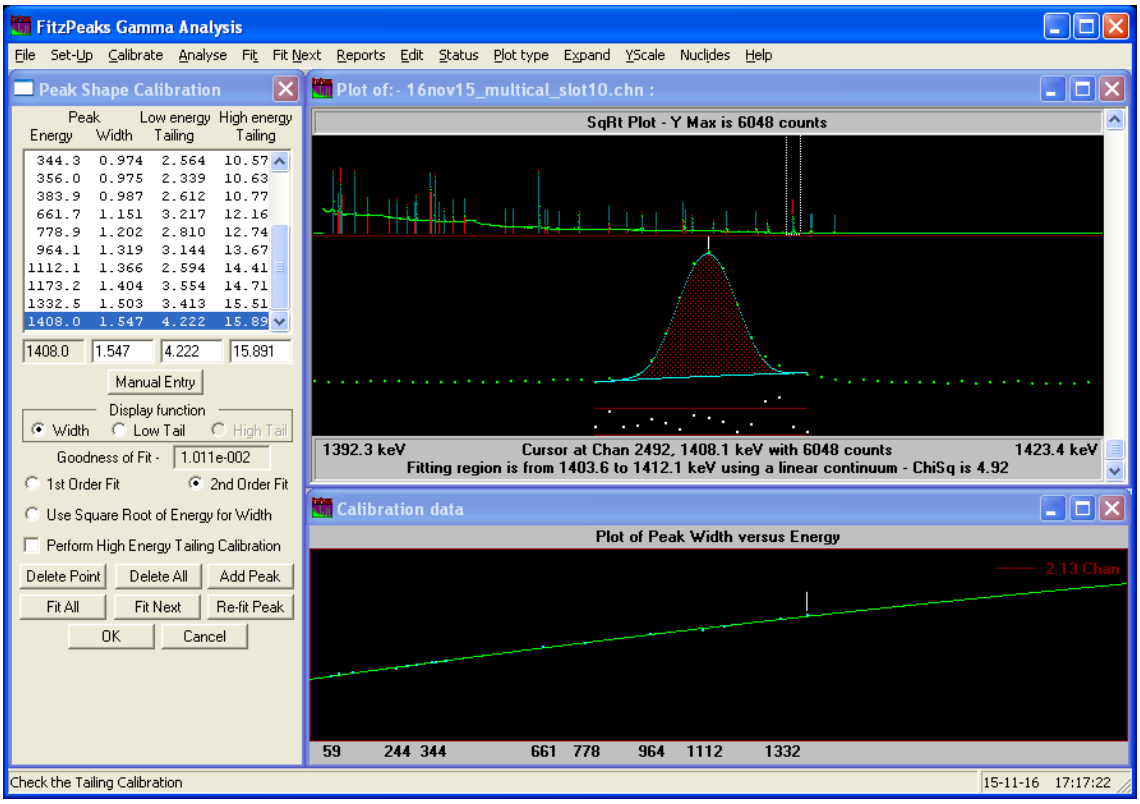

Figure A.3: FitzPeaks calibration of peak shape as a function of energy.

Efficiency Calibration

- **Open a multi-source spectrum** acquired at the desired counting geometry, as previously described.
- Select **"Calibrate"** from the top toolbar, and then select **"Efficiency"** from the drop-down menu.
- When prompted to perform a peak search and fitting **select "Yes".**
- **Wait for the peak search and fitting to complete.** During fitting, if prompted to add a new peak, use judgment to decide if a new peak is warranted.
- For the cyclotron group standard multi-source spectrum (^{60}Co, ^{133}Cs ^{137}Cs, ^{152}Eu, and ^{241}Am), **open "effcal.efc"** in the FitzPeaks main program directory. For other

calibration source combinations, create an text file containing the desired calibration energies, source activities, and activity measurement date and time, with the file extension ".efc".

- When prompted with efficiency calibration source data file, as shown in Figure A.4, **press "Close".**

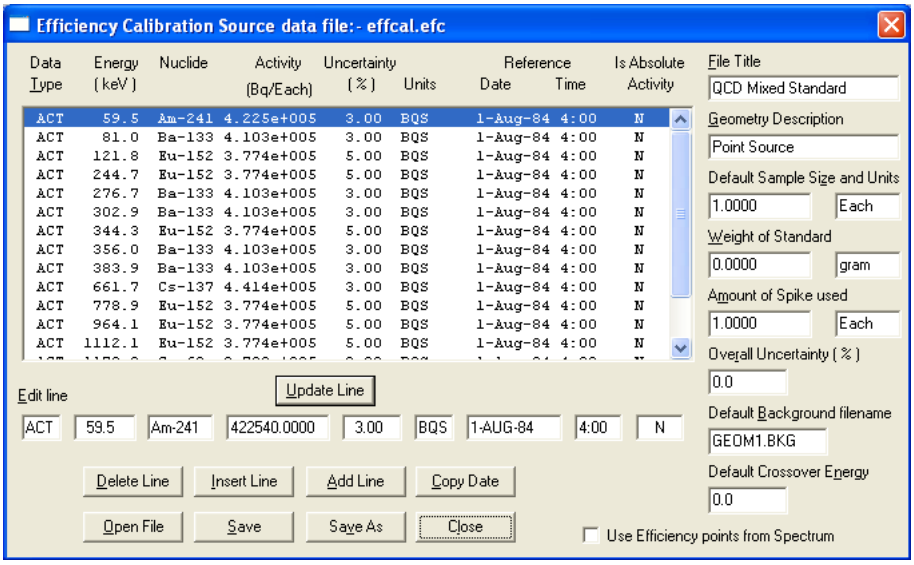

Figure A.4: FitzPeaks calibration source data file showing the energy of each peak, corresponding isotope, activity, reference date and time. Branching ratio data is built into the analysis library.

- In the left-hand menu, **change "High Energy Order of Fit" to '6'**, and **check the box next to "Use Linear Energy Polynomial".** These setting seem to provide the best efficiency curve fit, but setting may be modified depending on fit performance. Once the desired settings have been configured, **press "Calibrate".** (Sometimes you have to press "Calibrate" twice.) An example configuration menu is shown in Figure A.5.
- Evaluate the efficiency vs. energy fit performance. If satisfied **press "OK".**

- If satisfied with the results of the efficiency calibration, when prompted to save changes to a detector file **press "Yes".** The default detector file is "Det_01.cal", so **press "Save."** to modify this file. When prompted whether to uptdate the calibration file Det_01, **press "Yes".** When prompted whether to update the calibration geometry for your desired position, select **"Yes".**

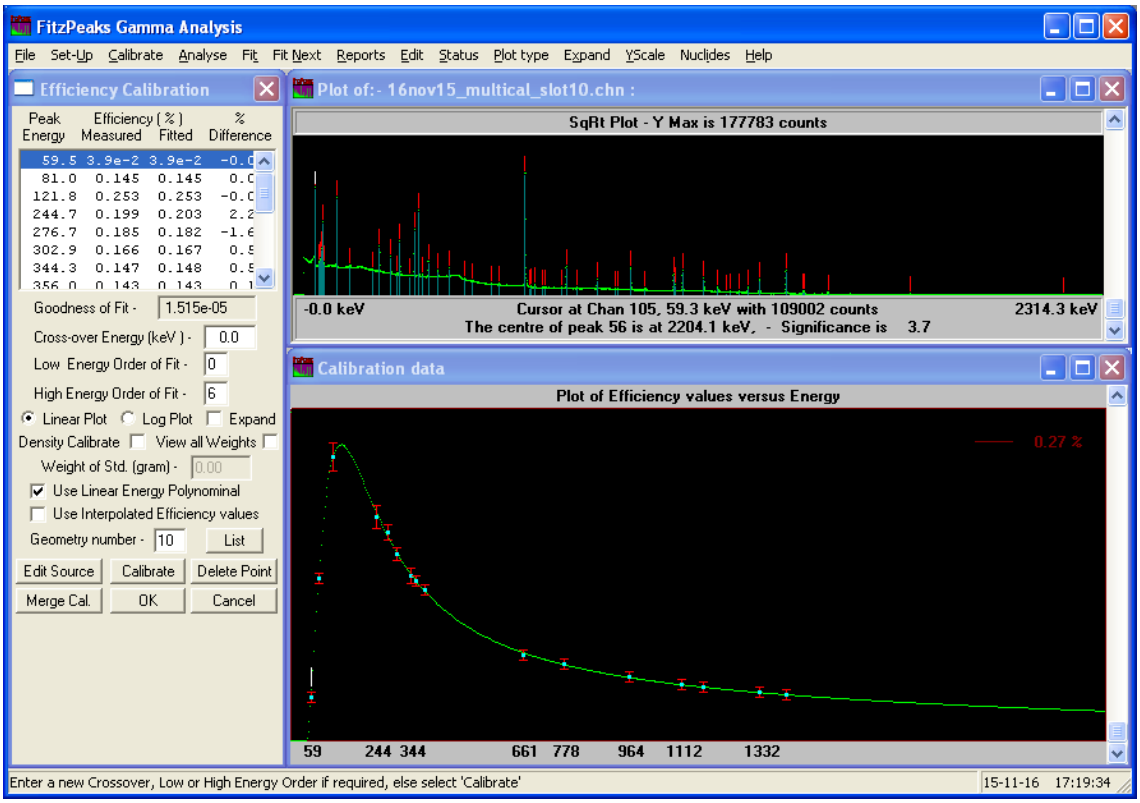

Figure A.5: FitzPeaks calibration of efficiency as a function of energy.

FitzPeaks Operation

Once all desired geometry positions have been calibrated, a spectrum may be analyzed in the following way:

- Open the desired spectrum (.Chn) by **right clicking, selecting "Open with", and selecting "FitzPeaks".**
- **Select the counting geometry** which was used for the sample, and modify any acquisition details if incorrectly populated. **Press "OK".**
- From the top toolbar, **press "Analyse", then select "Full Analysis"** from the drop-down menu.
- **Wait for the peak search and fitting to complete.** During fitting, if prompted to add a new peak, use judgment to decide if a new peak is warranted.
- When peak fitting has completed, a **Main Report** will be automatically presented. This main report represents an attempt to automatically identify and quantify the nuclides contained within your spectrum. Quantified activities are given in units of Bq, and are based on the nuclear decay data within the analysis library, and the efficiency calibration for the selected geometry. Decay corrected quantifications are based on user-defined EoB times.
- To view individual peak information, in the top toolbar **select "Peak Fit".** This document contains information regarding individual peaks, including energy, FWHM, peak area, peak area uncertainty, and efficiency-corrected gammas per second and associated uncertainty.
- Both the Main Report and Peak Fit documents may be saved as '.txt' files for further analysis.

B ^{51}MN SUPPLEMENTAL DATA

Tissue	Number of ^{51}Mn disintigrations (MBq-h/MBq)	Number of ^{51}Cr disintigrations (MBq-h/MBq)
Adrenals	0.00×10^{0}	0.00×10^{0}
Brain	4.43×10^{-3}	3.93×10^{0}
Breasts	0.00×10^{0}	0.00×10^{0}
Gallbladder Contents	0.00×10^{0}	0.00×10^{0}
LLI	0.00×10^{0}	0.00×10^{0}
Small Intestine	0.00×10^{0}	0.00×10^{0}
Stomach	0.00×10^{0}	1.23×10^{1}
ULI	6.42×10^{-3}	5.70×10^{0}
Heart Contents	0.00×10^{0}	0.00×10^{0}
Heart Wall	2.37×10^{-2}	2.10×10^{1}
Kidneys	6.91×10^{-2}	6.12×10^{1}
Liver	6.30×10^{-2}	5.58×10^{1}
Lungs	1.68×10^{-2}	1.49×10^{1}
Muscle	2.18×10^{-3}	1.93×10^{0}
Ovaries	0.00×10^{0}	0.00×10^{0}
Pancreas	4.11×10^{-2}	3.64×10^{1}
Red Marrow	0.00×10^{0}	0.00×10^{0}
Cortical Bone	8.40×10^{-4}	7.48×10^{-1}
Trabecular Bone	0.00×10^{0}	0.00×10^{0}
Spleen	9.16×10^{-3}	8.12×10^{0}
Testes	0.00×10^{0}	0.00×10^{0}
Thymus	0.00×10^{0}	0.00×10^{0}
Thyroid	0.00×10^{0}	0.00×10^{0}
Urinary Bladder Contents	0.00×10^{0}	0.00×10^{0}
Uterus/Uterine Wall	0.00×10^{0}	0.00×10^{0}
Total Body	8.70×10^{-1}	7.20×10^{2}

Table B.1: Source organ integrated disintigrations for ^{51}Mn and ^{51}Cr used in OLINDA dose calculations.

Time (min)	Heart (SUV)	Liver (SUV)	Kidneys (SUV)	Muscle (SUV)	Pancreas (SUV)	Salivary gland (SUV)
0.04	0.00 ± 0.00	0.00 ± 0.00	0.00 ± 0.00	0.00 ± 0.00	0.00 ± 0.00	0.00 ± 0.00
0.13	0.00 ± 0.00	0.00 ± 0.00	0.00 ± 0.00	0.00 ± 0.00	0.00 ± 0.00	0.00 ± 0.00
0.21	2.73 ± 0.58	1.32 ± 0.50	0.04 ± 0.05	0.00 ± 0.00	0.00 ± 0.00	0.00 ± 0.00
0.29	14.48 ± 0.53	6.73 ± 2.32	3.62 ± 0.03	0.00 ± 0.00	1.56 ± 0.35	0.90 ± 0.35
0.38	13.12 ± 1.58	7.21 ± 1.90	6.91 ± 0.63	0.26 ± 0.36	3.13 ± 0.22	2.93 ± 1.57
0.46	9.48 ± 0.58	6.99 ± 1.17	8.41 ± 0.85	0.46 ± 0.63	3.63 ± 0.07	2.97 ± 0.70
0.54	7.47 ± 0.06	7.33 ± 0.67	9.69 ± 1.36	0.39 ± 0.53	4.43 ± 0.42	3.32 ± 0.87
0.63	6.16 ± 0.24	7.49 ± 0.51	10.53 ± 1.61	0.41 ± 0.52	4.71 ± 0.03	3.08 ± 0.89
0.71	5.27 ± 0.20	7.50 ± 0.30	10.75 ± 1.30	0.36 ± 0.46	5.08 ± 0.12	2.83 ± 0.45
0.79	4.59 ± 0.19	7.97 ± 0.38	11.02 ± 1.27	0.32 ± 0.40	5.28 ± 0.72	3.14 ± 0.65
0.88	4.63 ± 0.24	7.98 ± 0.34	11.18 ± 1.26	0.26 ± 0.31	5.06 ± 0.09	3.18 ± 0.83
0.96	4.46 ± 0.31	8.33 ± 0.11	11.65 ± 1.32	0.20 ± 0.25	5.31 ± 0.50	3.16 ± 0.14
1.08	3.88 ± 0.41	8.34 ± 0.16	11.94 ± 1.55	0.49 ± 0.35	5.14 ± 0.32	2.57 ± 0.24
1.25	3.72 ± 0.25	8.70 ± 0.13	12.21 ± 1.83	0.45 ± 0.31	5.53 ± 0.43	2.81 ± 0.14
1.42	3.79 ± 0.60	9.27 ± 0.24	12.72 ± 1.45	0.45 ± 0.35	5.72 ± 1.06	2.94 ± 0.41
1.58	3.71 ± 0.46	9.10 ± 0.17	12.57 ± 1.42	0.47 ± 0.41	5.78 ± 0.50	2.73 ± 0.18
1.75	3.73 ± 0.45	9.57 ± 0.07	12.67 ± 1.51	0.38 ± 0.34	6.02 ± 0.54	2.66 ± 0.20
1.92	3.92 ± 0.55	10.06 ± 0.32	13.06 ± 1.68	0.48 ± 0.26	6.14 ± 1.41	2.71 ± 0.39
2.25	3.81 ± 0.41	10.01 ± 0.29	12.89 ± 1.73	0.50 ± 0.17	6.19 ± 0.61	2.58 ± 0.20
2.75	3.78 ± 0.41	10.23 ± 0.46	13.16 ± 1.93	0.48 ± 0.11	6.20 ± 0.59	2.56 ± 0.24
3.25	3.79 ± 0.36	10.37 ± 0.49	13.01 ± 1.68	0.44 ± 0.11	6.38 ± 0.53	2.58 ± 0.03
3.75	3.65 ± 0.29	10.46 ± 0.58	13.20 ± 1.95	0.43 ± 0.08	5.98 ± 0.79	2.58 ± 0.06
4.25	3.80 ± 0.33	10.51 ± 0.61	13.15 ± 1.88	0.49 ± 0.11	6.30 ± 0.81	2.65 ± 0.04
4.75	3.83 ± 0.44	10.53 ± 0.66	13.02 ± 1.88	0.44 ± 0.10	6.40 ± 1.22	2.69 ± 0.15
5.5	3.96 ± 0.38	10.77 ± 0.84	12.97 ± 1.90	0.41 ± 0.12	6.38 ± 0.79	2.60 ± 0.31
6.5	4.10 ± 0.31	11.11 ± 1.14	13.13 ± 2.08	0.42 ± 0.15	6.48 ± 1.05	2.57 ± 0.21
7.5	4.20 ± 0.12	11.24 ± 1.30	12.95 ± 2.09	0.42 ± 0.11	6.49 ± 1.21	2.65 ± 0.02
8.5	4.37 ± 0.10	11.26 ± 1.41	12.85 ± 1.98	0.43 ± 0.15	6.43 ± 0.63	2.75 ± 0.01
9.5	4.43 ± 0.09	11.47 ± 1.40	13.09 ± 2.21	0.42 ± 0.14	6.56 ± 0.96	2.69 ± 0.03
10.5	4.51 ± 0.03	11.44 ± 1.32	12.97 ± 2.25	0.42 ± 0.14	6.65 ± 1.18	2.67 ± 0.20
11.5	4.49 ± 0.07	11.35 ± 1.44	12.92 ± 2.21	0.40 ± 0.14	6.75 ± 1.16	2.67 ± 0.08
12.5	4.53 ± 0.03	11.50 ± 1.55	13.00 ± 2.32	0.40 ± 0.11	6.58 ± 1.06	2.60 ± 0.02
13.5	4.50 ± 0.05	11.51 ± 1.43	13.13 ± 2.30	0.44 ± 0.11	6.52 ± 1.12	2.69 ± 0.03
14.5	4.56 ± 0.05	11.41 ± 1.38	13.02 ± 2.31	0.41 ± 0.12	6.59 ± 0.90	2.76 ± 0.14
16.25	4.59 ± 0.07	11.53 ± 1.46	13.17 ± 2.39	0.40 ± 0.14	6.62 ± 0.84	2.64 ± 0.17
18.75	4.59 ± 0.01	11.59 ± 1.45	13.20 ± 2.47	0.39 ± 0.14	6.52 ± 0.86	2.73 ± 0.20
21.25	4.61 ± 0.07	11.71 ± 1.51	13.38 ± 2.43	0.41 ± 0.12	6.58 ± 0.80	2.77 ± 0.18
23.75	4.68 ± 0.02	11.74 ± 1.57	13.42 ± 2.49	0.42 ± 0.13	6.46 ± 0.89	2.77 ± 0.19
26.25	4.73 ± 0.01	11.81 ± 1.65	13.40 ± 2.38	0.40 ± 0.15	6.49 ± 0.56	2.69 ± 0.10
28.75	4.72 ± 0.06	11.89 ± 1.64	13.55 ± 2.33	0.40 ± 0.16	6.60 ± 0.58	2.77 ± 0.05
31.25	4.72 ± 0.02	12.02 ± 1.75	13.65 ± 2.50	0.42 ± 0.14	6.62 ± 0.58	2.75 ± 0.16
33.75	4.72 ± 0.02	12.06 ± 1.73	13.74 ± 2.59	0.40 ± 0.13	6.67 ± 0.47	2.69 ± 0.13

Table B.2: Tabulated time activity curves (TACs) measured by dynamic PET for isoflurane anaesthetized ICR mice (n=2) injected with a rapid intravenous bolus of $^{51}MnCl_2$.ROIs were hand-drawn on composite images and applied to all frames. Values represent mean ± SD. A blood-clearance half-life of 7.7 ± 0.7 s was measured by weighted exponential least-squares regression.

Tissue	Uptake (SUV)
Heart	3.53 ± 0.25
Liver	4.63 ± 0.91
Kidney	7.70 ± 1.06
Muscle	0.47 ± 0.07
Pancreas	5.93 ± 0.93
Salivary Gland	3.90 ± 0.75

Table B.3: ^{51}Mn uptake in non-anaesthetized ICR mice (n=3) 1 hour following a rapid intravenous bolus of $^{51}MnCl_2$, quantified by hand-drawn static PET ROIs.

Tissue	Uptake (SUV)
Blood	0.09 ± 0.02
Skin	0.28 ± 0.06
Muscle	0.45 ± 0.16
Bone	0.52 ± 0.11
Heart	5.64 ± 1.75
Lung	2.57 ± 1.28
Liver	3.66 ± 0.78
Kidney	9.23 ± 0.70
Spleen	1.62 ± 0.18
Pancreas	7.03 ± 1.28
Stomach	2.47 ± 1.43
Intestine	3.37 ± 2.84
Tail	0.12 ± 0.10
Brain	0.38 ± 0.03
Salivary Gland	3.18 ± 1.30

Table B.4: ^{51}Mn uptake in ICR mice immediately following PET imaging (~90 min post-injection), quantified by ex vivo gamma counting.

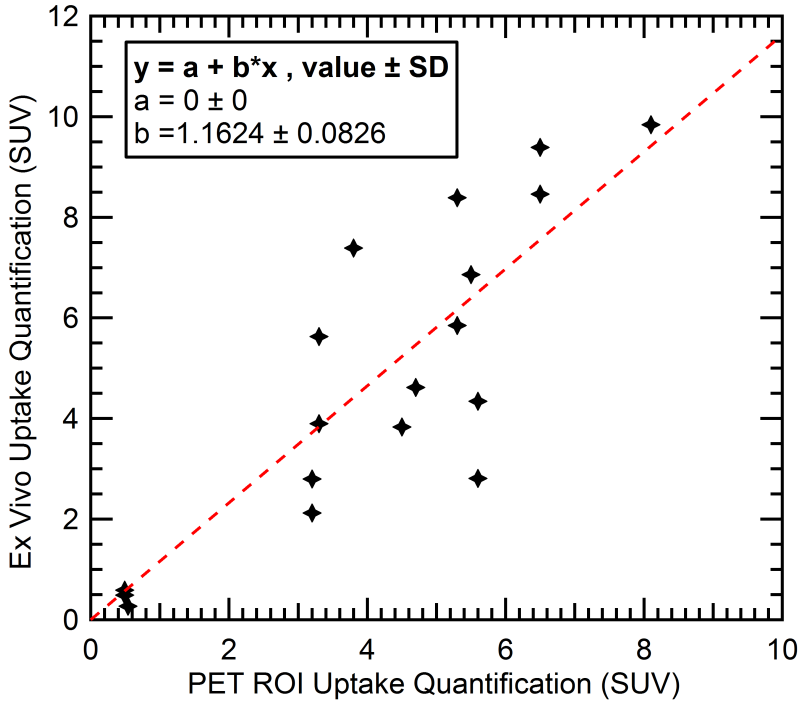

Figure B.1: *Ex vivo* ^{51}Mn uptake quantifcation compared against *in vivo* PET ROI-based quantification. Reasonable agreement is seen with a slope of 1.16 $\pm$ 0.08. The difference of ~16% might be attributable to the removal of low-activity blood compared with *in vivo* volumes.

C BETA CELL MASS SUPPLEMENTAL DATA

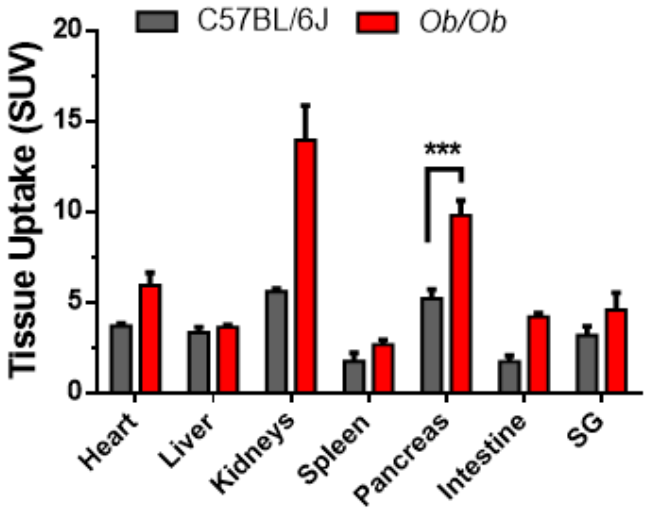

Figure C.1: Ex vivo biodistribution of lean (C57BL/6J) and obese (ob/ob) mice, one-hour post injection of $^{52}Mn^{2+}$. Significantly higher $^{52}Mn^{2+}$ uptake can be noted in obese mice compared to the lean controls (***P < 0.0001; n=3).

	Organ/tissue uptake					
Time (days)	Heart/blood	Liver	Kidneys	Muscle	Pancreas	S Gland
0.042	2.11 ± 0.20	3.27 ± 0.34	5.13 ± 0.02	0.38 ± 0.03	5.13 ± 0.37	2.30 ± 0.26
0.125	1.88 ± 0.19	3.37 ± 0.47	5.21 ± 0.32	0.38 ± 0.02	5.11 ± 0.50	2.53 ± 0.44
0.5	1.21 ± 0.16	3.51 ± 0.29	4.90 ± 0.19	0.35 ± 0.05	4.89 ± 0.17	2.77 ± 0.19
1	0.93± 0.11	3.15 ± 0.28	4.59 ± 0.27	0.33 ± 0.03	4.84 ± 0.18	2.69 ± 0.05
3	0.80 ± 0.08	1.94 ± 0.17	3.32 ± 0.14	0.27 ± 0.05	4.40 ± 0.34	2.85 ± 0.09
5	0.72 ± 0.05	1.49 ± 0.05	2.60 ± 0.03	0.26 ± 0.03	3.65 ± 0.37	3.18 ± 0.33
7	0.69 ± 0.00	1.08 ± 0.10	1.96 ± 0.21	0.20 ± 0.02	2.98 ± 0.25	3.02 ± 0.13
9	0.64 ± 0.02	0.83 ± 0.06	1.56 ± 0.20	0.18 ± 0.02	2.26 ± 0.23	2.70 ±0.10
11	0.58 ± 0.03	0.70 ± 0.02	1.28 ± 0.14	0.19 ± 0.01	1.80 ± 0.23	2.63 ± 0.15
13	0.54± 0.03	0.62 ± 0.01	1.13 ± 0.06	0.19 ± 0.01	1.65 ± 0.31	2.50 ±0.08
Mean ± SD values are reported as standardized uptake value (SUV)						

Table C.1: Quantitative results of longitudinal PET imaging studies in ICR mice administered a $^{52}Mn^{2+}$ intravenous bolus (n = 4)

Organ/tissue	$^{52}Mn^{2+}$ uptake (SUV)*
Blood	0.01 ± 0.01
Skin	0.16 ± 0.05
Muscle	0.26 ± 0.04
Bone	0.50 ± 0.09
Heart	1.19 ± 0.08
Lung	0.22 ± 0.06
Liver	0.72 ± 0.04
Kidney	1.85 ± 0.04
Spleen	0.35 ± 0.10
Pancreas	2.62 ± 0.44
Stomach	0.76 ± 0.18
Intestine	0.14 ± 0.02
Salivary	2.84 ± 0.13
Tail	0.14 ± 0.01
Brain	0.52 ± 0.01
	*Mean $\pm$ SD

Table C.2: Ex vivo biodistribution of $^{52}Mn^{2+}$ at day 13 after intravenous administration in healthy ICR mice. (n = 4)

Organs	Baseline	Diazoxide	Nifedipine	Glibenclamide	STZ-diabetic
	(n=3)	(n=3)	(n=3)	(n=4)	(n=3)
Heart/blood	2.11 ± 0.20	2.58 ± 0.22	2.61 ± 0.30	2.50 ± 0.60	1.97 ± 0.50
Liver	3.27 ± 0.34	3.11 ± 0.50	2.06 ± 0.56	3.20 ± 0.87	2.89 ± 1.70
Kidneys	5.13 ± 0.02	4.66 ± 1.48	3.52 ± 0.43	5.70 ± 1.35	3.80 ± 0.78
Muscle	0.38 ± 0.03	0.40 ± 0.07	0.44 ± 0.07	0.44 ± 0.04	0.23 ± 0.06
Pancreas	5.13 ± 0.38	2.85 ± 0.92	2.36 ± 0.61	6.47 ± 1.36	2.04 ± 0.81
Salivary Gland	2.30 ± 0.26	2.46 ± 0.97	2.15 ± 0.22	2.25 ± 0.14	1.51 ± 1.01
	Mean ± SD values are reported as standardized uptake value (SUV)				

Table C.3: Quantitative results of PET imaging in ICR mice 1 h post administration of $^{52}Mn^{2+}$ under various conditions to stimulate or inhibit insulin release.

Organs	Baseline	Diazoxide	Nifedipine	Glibenclamide	STZ diabetic
	(n=3)	(n=3)	(n=3)	(n=4)	(n=3)
Heart	4.01 ± 0.26	4.96 ± 0.46	5.42 ± 0.81	5.29 ± 1.19	1.97 ± 0.50
Liver	3.63 ± 0.13	3.17 ± 0.83	1.84 ± 0.45	3.26 ± 0.70	2.89 ± 1.70
Kidneys	8.12 ± 0.88	6.42 ± 2.67	4.55 ± 0.84	8.10 ± 1.22	3.80 ± 0.78
Spleen	1.74 ± 0.22	1.75 ± 0.47	0.52 ± 0.13	1.68 ± 0.40	0.23 ± 0.06
Pancreas	6.31 ± 0.51	4.43 ± 1.08	3.20 ± 0.61	7.53 ± 1.29	2.04 ± 0.81
Intestine	1.96 ± 0.32	2.40 ± 0.99	1.94 ± 0.14	2.25 ± 0.64	1.51 ± 1.01
Salivary Gland	2.90 ± 0.67	2.97 ± 0.62	2.35 ± 0.16	2.68 ± 0.46	1.97 ± 0.50
	Mean ± SD values are reported as standardized uptake value (SUV)				

Table C.4: One-hour post injection ex vivo biodistribution data in ICR mice administered $^{52}Mn^{2+}$ under various conditions to stimulate or inhibit insulin release.

In vivo PET Data			Ex vivo biodistribution		
Organs	**C57BL/6J (n=3)**	**Ob/Ob (n=3)**	**Organs**	**C57BL/6J (n=3)**	**Ob/Ob (n=3)**
Heart/blood	1.93 ± 0.10	3.32 ± 0.13	**Heart**	3.68 ± 0.15	5.93 ± 0.69
Liver	3.40 ± 0.73	3.68 ± 0.25	**Liver**	3.33 ± 0.29	3.63 ± 0.10
Kidneys	5.08 ± 0.37	9.43 ± 0.44	**Kidneys**	5.58 ± 0.16	13.94 ± 1.91
Muscle	0.38 ± 0.06	0.26 ± 0.09	**Spleen**	1.74 ± 0.46	2.65 ± 0.27
Pancreas	4.89 ± 0.68	7.27 ± 1.03	**Pancreas**	5.19 ± 0.52	9.79 ± 0.83
Salivary Gland	2.40 ± 0.20	3.11 ± 1.05	**Intestine**	1.72 ± 0.33	4.17 ± 0.21
			Salivary Gland	3.18 ± 0.49	4.57 ± 0.95

Table C.5: In vivo PET and ex vivo biodistribution data in C57BL/6J and obese (ob/ob) mice one-hour after intravenous administration of $^{52}Mn^{2+}$. (n = 3)

D MEASURED FE+P AND CU+P CROSS SECTIONS

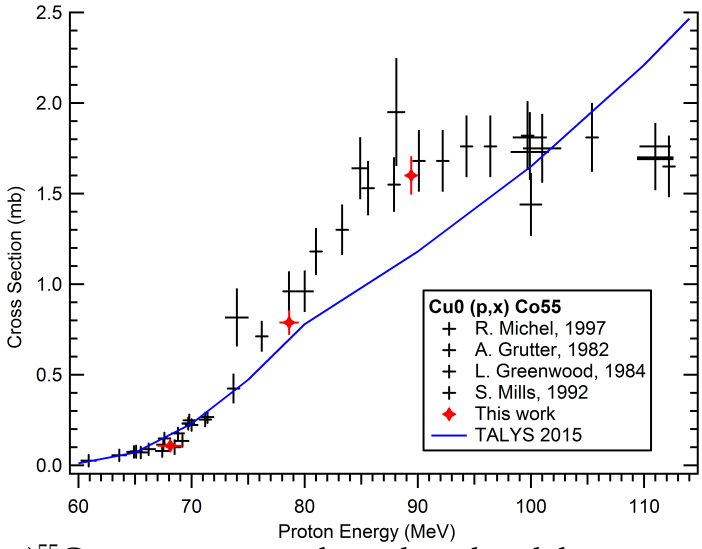

Measured $^{nat}Cu(p,x)^{55}Co$ cross section values plotted with literature data and theoretical TALYS 2015 results.

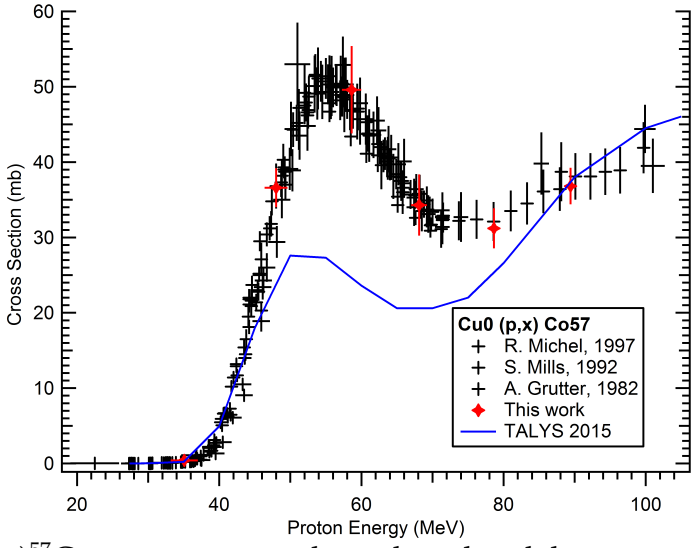

Measured $^{nat}Cu(p,x)^{57}Co$ cross section values plotted with literature data and theoretical TALYS 2015 results.

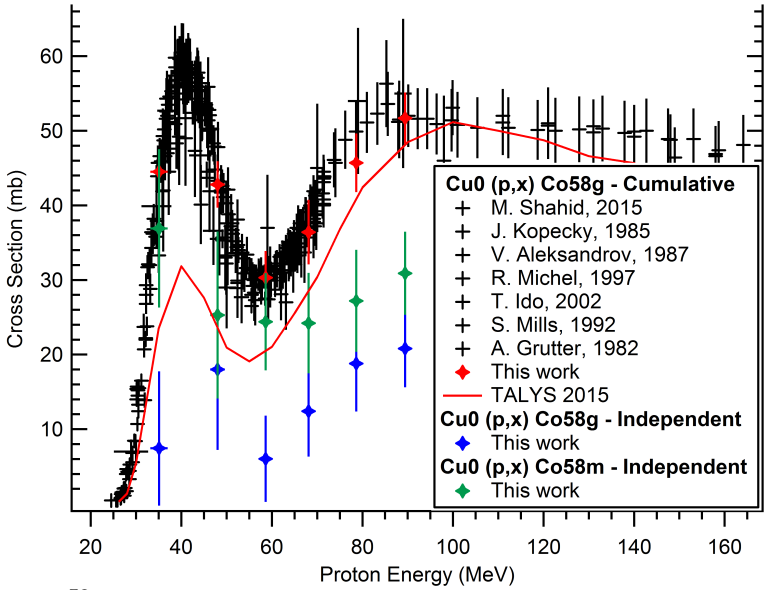

Measured $^{nat}Cu(p,x)^{58}Co$ cross section values plotted with literature data and theoretical TALYS 2015 results.

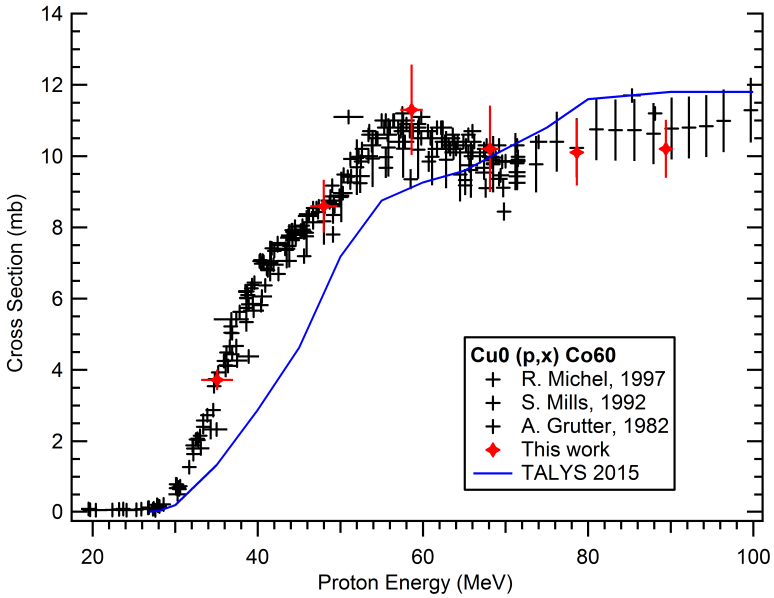

Measured $^{nat}Cu(p,x)^{60}Co$ cross section values plotted with literature data and theoretical TALYS 2015 results.

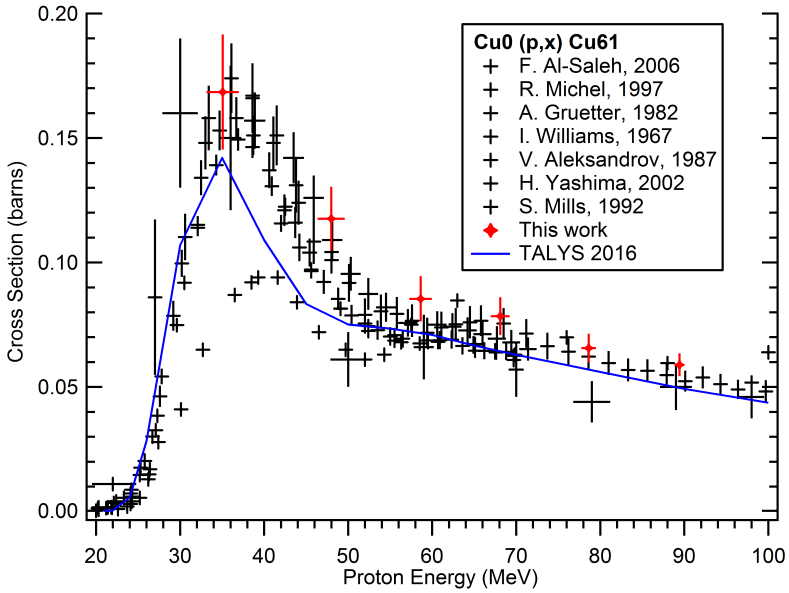

Measured $^{nat}Cu(p,x)^{61}Cu$ cross section values plotted with literature data and theoretical TALYS 2015 results.

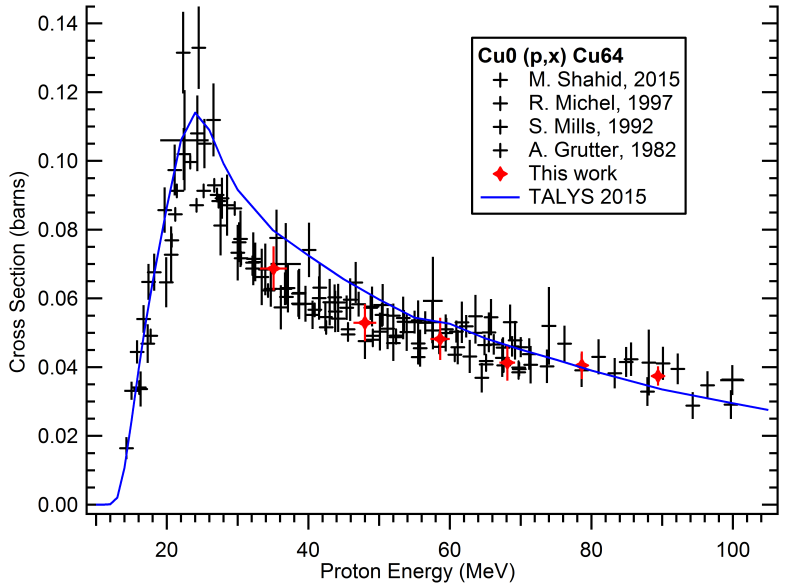

Measured $^{nat}Cu(p,x)^{64}Cu$ cross section values plotted with literature data and theoretical TALYS 2015 results.

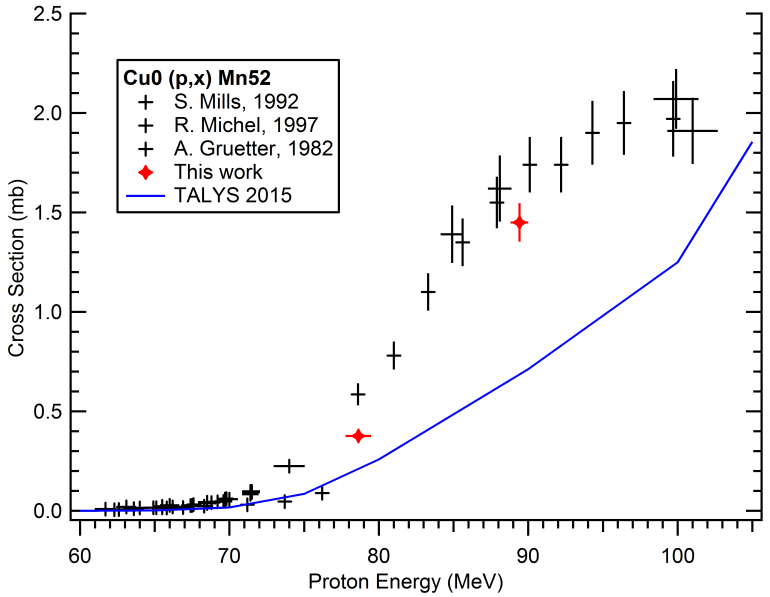

Measured $^{nat}Cu(p,x)^{52}Mn$ cross section values plotted with literature data and theoretical TALYS 2015 results.

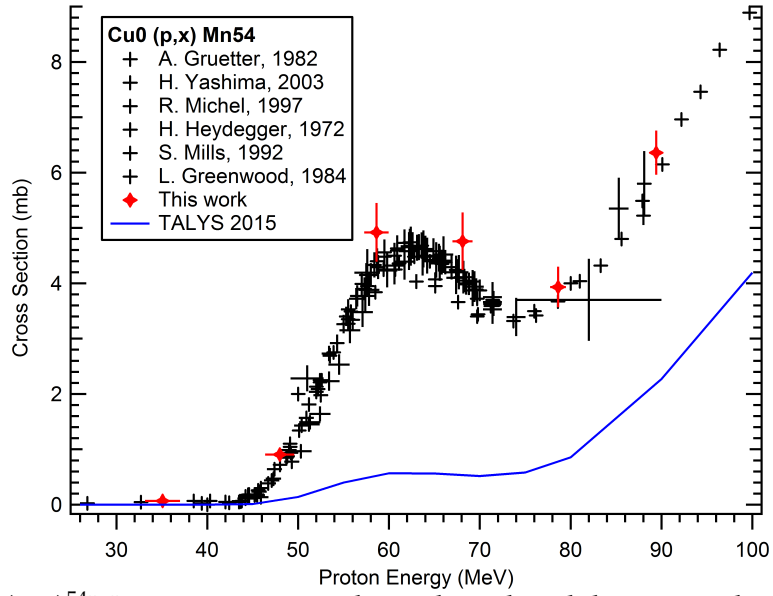

Measured $^{nat}Cu(p,x)^{54}Mn$ cross section values plotted with literature data and theoretical TALYS 2015 results.

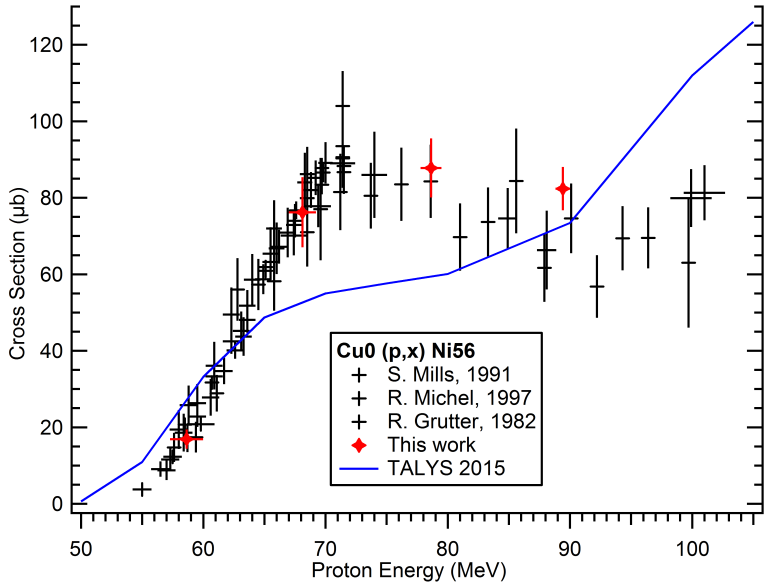

Measured $^{nat}Cu(p,x)^{56}Ni$ cross section values plotted with literature data and theoretical TALYS 2015 results.

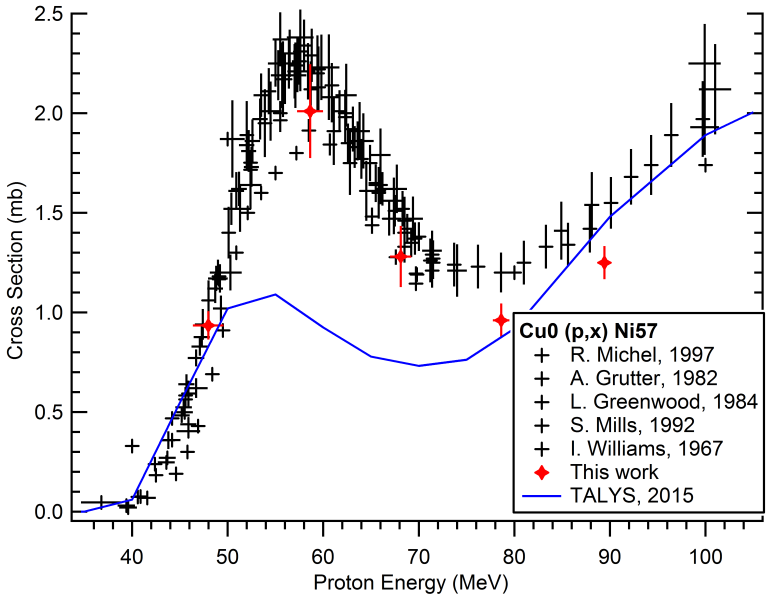

Measured $^{nat}Cu(p,x)^{57}Ni$ cross section values plotted with literature data and theoretical TALYS 2015 results.

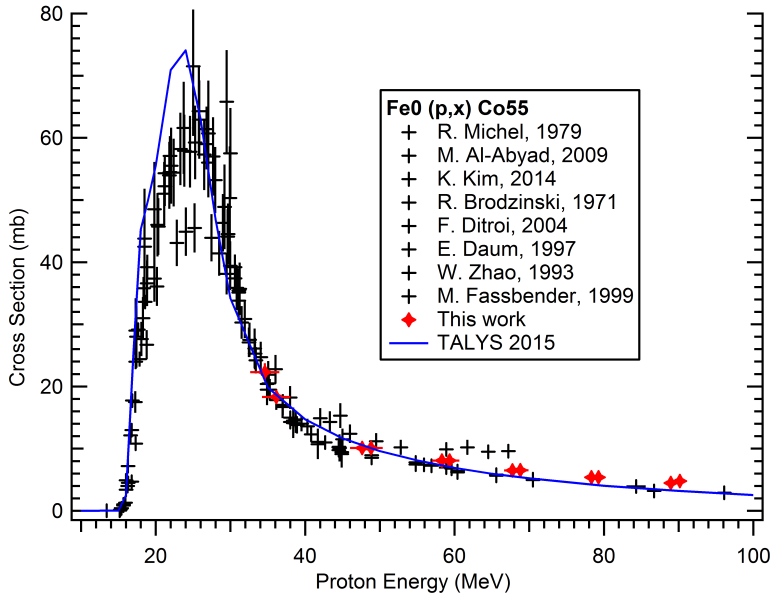

Measured $^{nat}Fe(p,x)^{55}Co$ cross section values plotted with literature data and theoretical TALYS 2015 results.

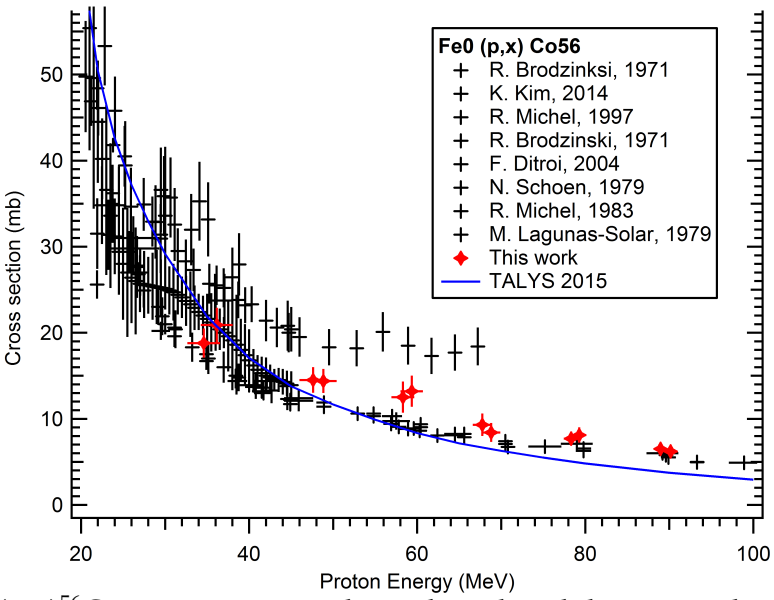

Measured $^{nat}Fe(p,x)^{56}Co$ cross section values plotted with literature data and theoretical TALYS 2015 results.

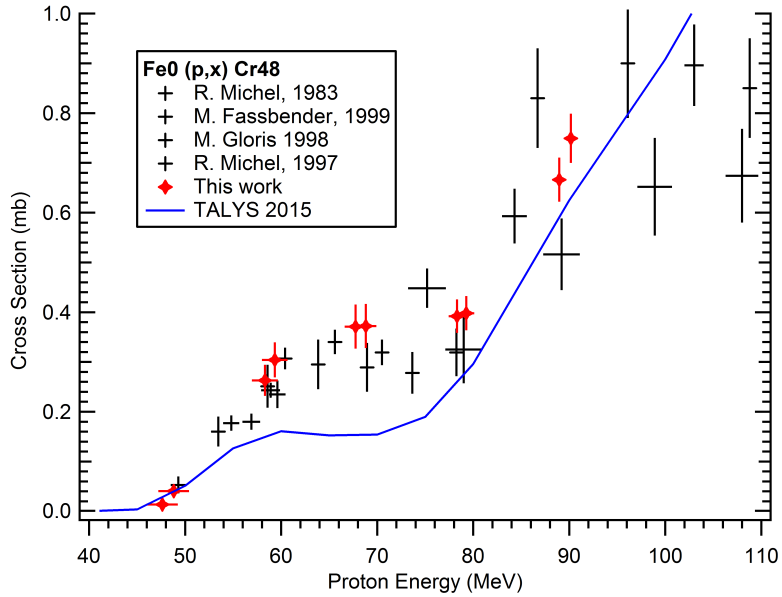

Measured $^{nat}Fe(p,x)^{48}Cr$ cross section values plotted with literature data and theoretical TALYS 2015 results.

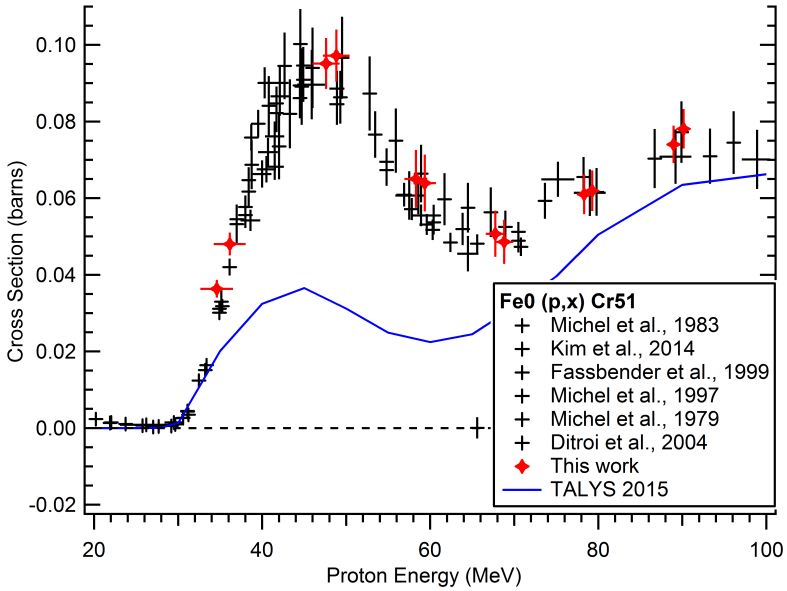

Measured $^{nat}Fe(p,x)^{51}Cr$ cross section values plotted with literature data and theoretical TALYS 2015 results.

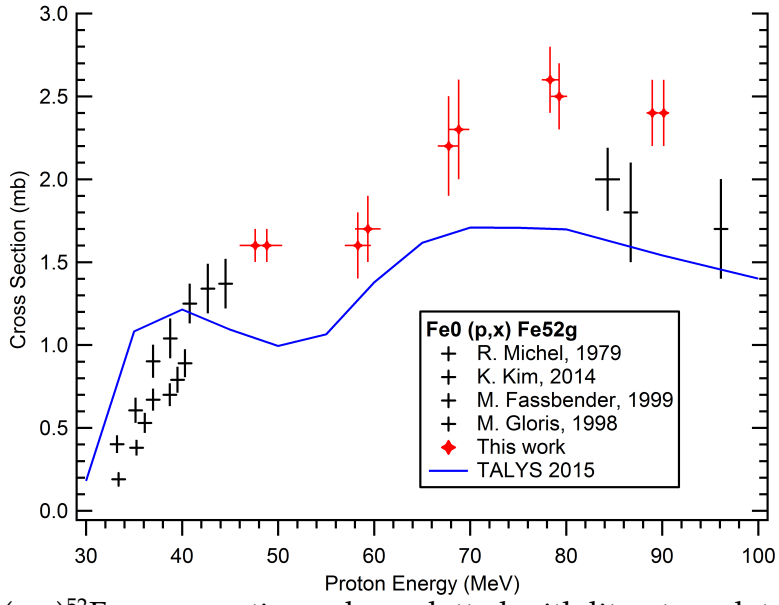

Measured $^{nat}Fe(p,x)^{52}Fe$ cross section values plotted with literature data and theoretical TALYS 2015 results.

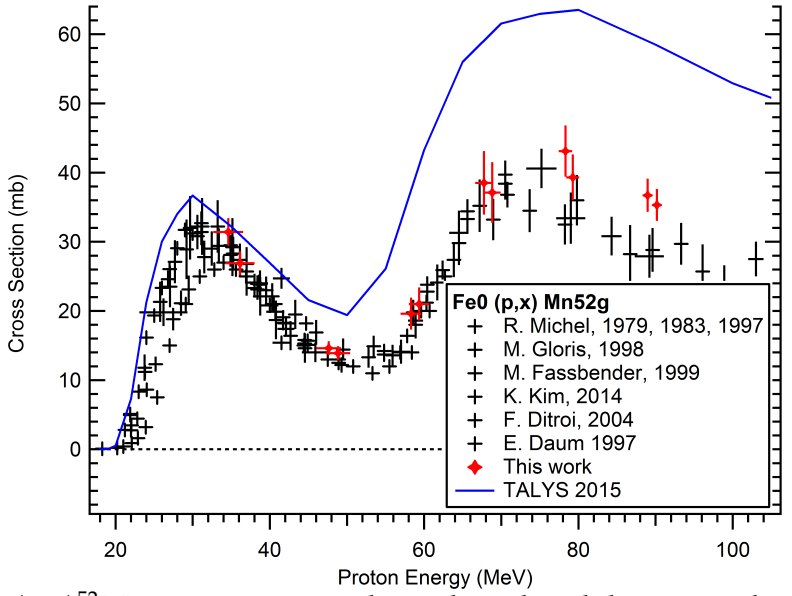

Measured $^{nat}Fe(p,x)^{52}Mn$ cross section values plotted with literature data and theoretical TALYS 2015 results.

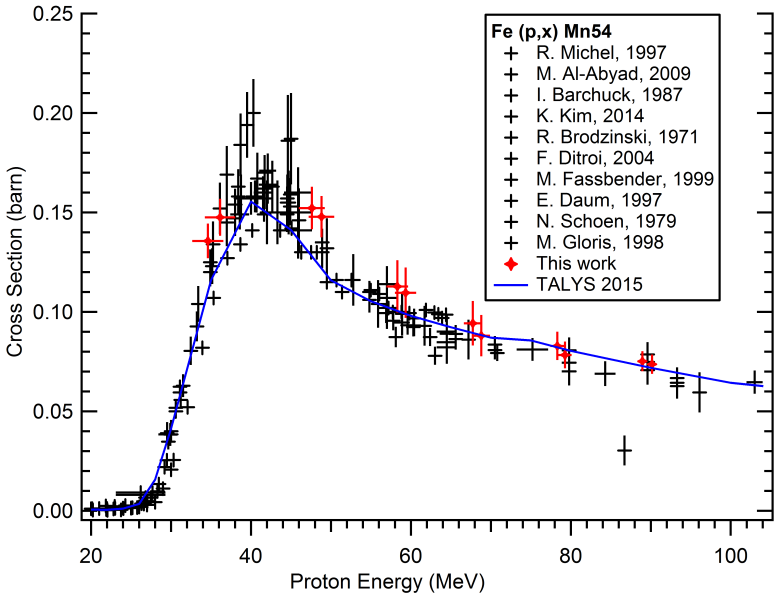

Measured $^{nat}Mn(p,x)^{54}Mn$ cross section values plotted with literature data and theoretical TALYS 2015 results.

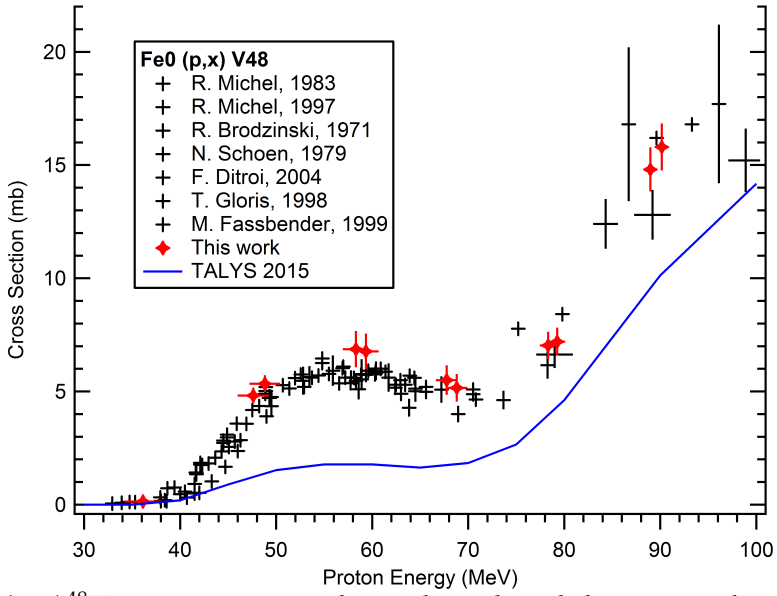

Measured $^{nat}Fe(p,x)^{48}V$ cross section values plotted with literature data and theoretical TALYS 2015 results.

E ^{64}CU EFFECTIVE SPECIFIC ACTIVITY HISTORY AND ANALYSIS

The effective specific activity of weekly ^{64}Cu productions was measured using NOTA according to the methods described in Chapter 7. A history of these measured values is listed in Table E.1. A histogram of these values, Figure E.1, reveals that the distribution is significantly skewed right, with a maximum value of 74 Ci/μmol, a minimum value of 0.3 Ci/μmol, a median value of 8.3 Ci/μmol NOTA, and a mean of 9.8 Ci/μmol.

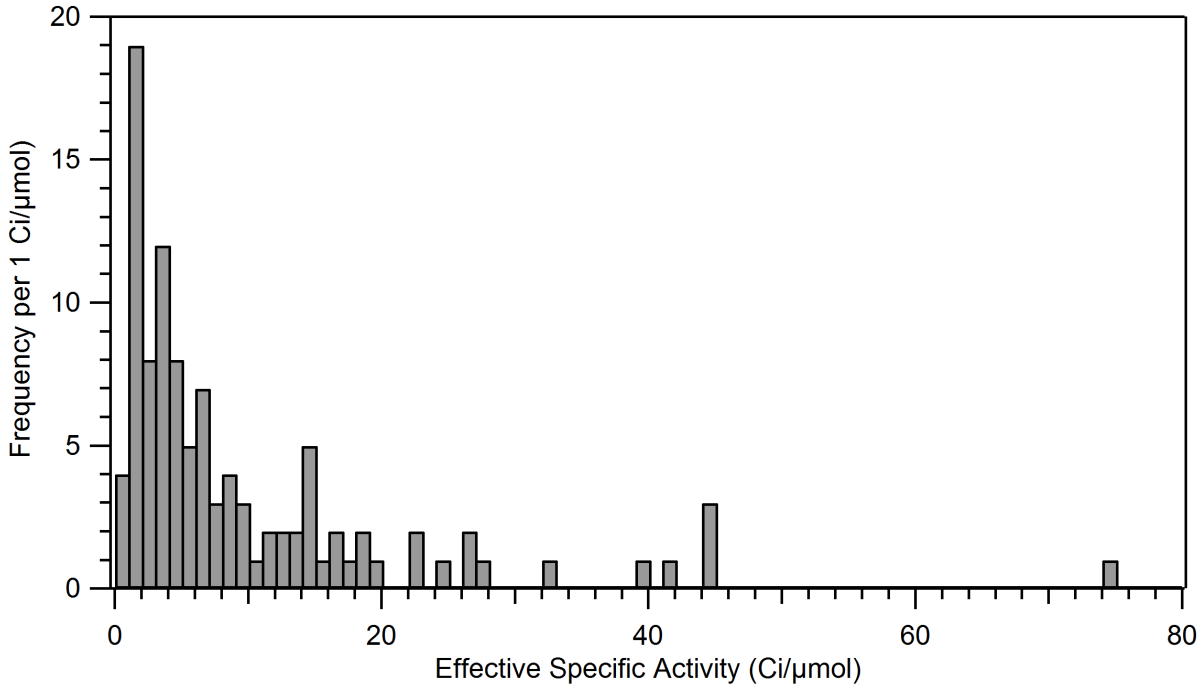

Figure E.1: ^{64}Cu effective specific activity measured by NOTA chelation assays from June 24th, 2013 to Nov. 14th, 2016. The average was found to be 9.8 ($n = 104$).

Date	ESA (Ci/μmol)	Date	ESA (Ci/μmol)	Date	ESA (Ci/μmol)
6/24/2013	2.2	11/3/2014	1.5	9/9/2015	12.3
7/15/2013	3.1	11/10/2014	2.0	9/14/2015	14.3
7/17/2013	2.9	11/17/2014	1.1	9/22/2015	9.0
7/29/2013	6.0	11/24/2014	2.6	9/28/2015	14.2
7/31/2013	1.6	12/1/2014	1.3	10/12/2015	2.9
8/12/2013	0.3	12/8/2014	1.4	10/27/2015	27.3
9/3/2013	2.8	12/15/2014	1.0	11/3/2015	7.6
9/23/2013	4.6	1/12/2015	1.2	11/10/2015	6.7
11/11/2013	4.4	2/16/2015	3.2	11/17/2015	12.9
1/6/2014	5.6	2/23/2015	3.3	11/23/2015	11.2
3/17/2014	3.0	2/23/2015	10.0	12/7/2015	8.3
4/7/2014	0.7	3/2/2015	11.4	12/28/2015	6.6
4/14/2014	3.6	3/9/2015	44.5	1/12/2015	1.1
4/21/2014	3.4	3/16/2015	44.5	2/9/2015	5.7
5/5/2014	5.0	3/23/2015	24.0	3/28/2016	5.8
5/13/2014	4.0	4/6/2015	22.0	4/4/2016	4.8
5/19/2014	7.0	4/13/2015	6.9	4/11/2016	4.1
6/24/2014	3.2	4/20/2015	9.6	4/26/2016	16.9
6/30/2014	1.2	4/27/2015	39.0	5/2/2016	22.0
7/7/2014	1.8	5/4/2015	74.0	5/9/2016	14.6
7/14/2014	0.5	5/11/2015	32.5	5/17/2016	6.5
7/22/2014	1.1	5/18/2015	13.7	5/31/2016	16.9
7/28/2014	4.1	5/25/2015	9.6	6/6/2016	14.3
8/4/2014	3.4	6/1/2015	7.0	6/20/2016	44.9
8/11/2014	1.3	6/15/2015	19.9	7/27/2016	13.4
8/25/2014	3.1	6/22/2015	8.9	8/8/2016	5.2
9/2/2014	2.7	6/22/2015	6.1	8/15/2016	2.3
9/3/2014	1.4	6/30/2015	1.0	8/22/2016	1.4
9/8/2014	1.9	7/6/2015	8.6	9/6/2016	41.1
9/15/2014	3.6	7/13/2015	0.8	9/13/2016	3.1
9/22/2014	4.0	7/21/2015	17.3	10/3/2016	2.0
9/30/2014	3.8	7/27/2015	26.2	10/10/2016	7.5
10/13/2014	1.5	8/3/2015	18.8	10/17/2016	10.0
10/20/2014	1.2	8/10/2015	26.1	11/7/2016	15.7
10/27/2014	4.9	8/17/2015	18.3	11/14/2016	14.8

Table E.1: Tabulated history of ^{64}Cu effective specific activity measurements by NOTA assay.

Over time, it was found that the measured effective specific activity of ^{64}Cu had an

apparent dependence on the amount of activity used for the assay. To investigate this possibility the measured ^{64}Cu ESA was plotted against the amount of activity used per sample, shown in Figure E.2. There is a clear positive relationship between these two variables which suggests that our assay is not a robust test of the true effective specific activity.

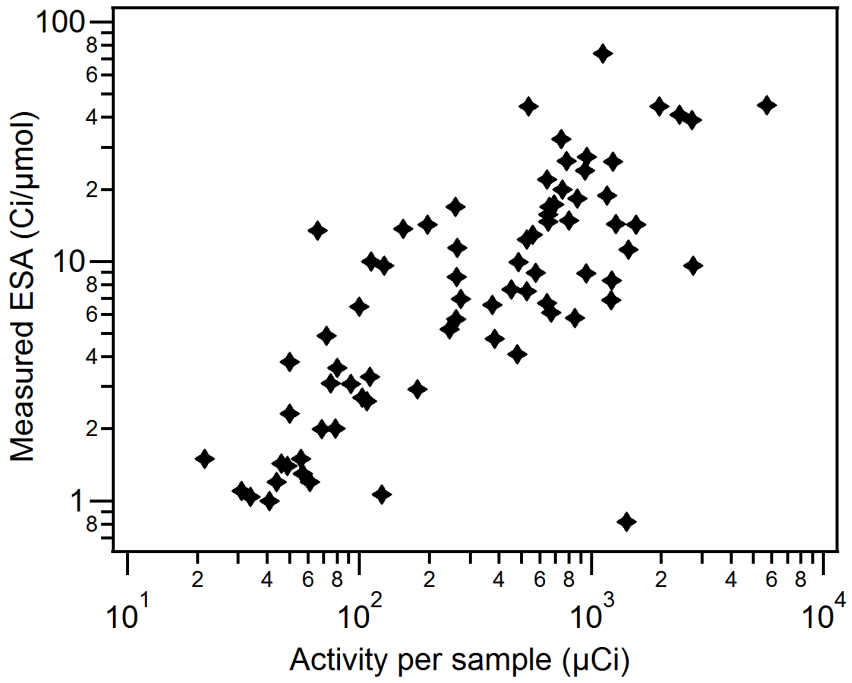

Figure E.2: Measured effective specific activity by NOTA chelation as a function of the amount of ^{64}Cu activity used in each assay sample. Ideally there would be no relationship between these variables. This trend suggests that the assay is only setting a "lower bound" on the true effective specific activity.

We hypothesize that as the stock NOTA solutions are stored, over time trace metals are introduced through pipetting and through leaching from the walls of the 50 mL plastic container. This effect is likely NOTA concentration independent due to different stocks having a similar pH. These contaminating metals over time occupy available chelate molecules adding a "constant offset" to the amount of available chelate. This

theory is consistent with seeing a positive correlation between ESA and sample activity, as it means we are overestimating the amount of chelate required to bind 50% of the ^{64}Cu activity. Larger quantities of ^{64}Cu however have the ability to diminish this effect comparatively.

With these findings, we believe it is prudent to describe this assay as setting a "lower bound" on the ESA of our ^{64}Cu product. This conclusion can be arrived at simply by way of the statement "if we use more ^{64}Cu for the assay, we could observe a higher ESA measurement." Without using an amount of ^{64}Cu which carries *true* contaminating metals which significantly overwhelm the "background contaminants," it is not possible to say we are providing an accurate measurement.

One potential way to mitigate this effect is to use a smaller volume of chelate per assay sample (i.e. 10 μl vs. 100 μl) while taking these volumes from more concentrated NOTA stocks. This should reduce the relative impact of "background contamination," effectively shifting the trend in Figure E.2 left one order of magnitude. If this theory is correct, one might expect to see a "leveling off" at high-activity assays implying that we are asymptotically approaching a true measure of ESA.